UNIVERSITY *of York*

This is a repository copy of *Nuclear Fission::A Review of Experimental Advances and Phenomenology*.

White Rose Research Online URL for this paper:
https://eprints.whiterose.ac.uk/id/eprint/119672/

Version: Accepted Version

Article:

Nuclear Fission: A Review of Experimental Advances and Phenomenology

Nuclear Fission: A Review of Experimental Advances and Phenomenology

A.N. Andreyev[1,2]**, K. Nishio**[2]**, K.-H. Schmidt**[3]

[1] Department of Physics, University of York, York, YO10 5DD, United Kingdom
[2] Advanced Science Research Center, Japan Atomic Energy Agency, Tokai, Iberaki, 319-1195, Japan
[3] Rheinstr. 4, D 64390 Erzhausen, Germany

Abstract In the last two decades, through technological, experimental and theoretical advances, the situation in experimental fission studies has changed dramatically. With the use of advanced production and detection techniques both much more detailed and precise information can now be obtained for the traditional regions of fission research and, crucially, new regions of nuclei have become routinely accessible for fission studies.

This work first of all reviews the recent developments in experimental fission techniques, in particular the resurgence of transfer-induced fission reactions with light and heavy ions, the emerging use of inverse-kinematic approaches, both at Coulomb and relativistic energies, and of fission studies with radioactive beams.

The emphasis on the fission-fragment mass and charge distributions will be made in this work, though some of the other fission observables, such as prompt neutron and γ-ray emission will also be reviewed.

A particular attention will be given to the low-energy fission in the so far scarcely explored nuclei in the very neutron-deficient lead region. They recently became the focus for several complementary experimental studies, such as β-delayed fission with radioactive beams at ISOLDE(CERN), Coulex-induced fission of relativistic secondary beams at FRS(GSI), and several prompt fusion-fission studies. The synergy of these approaches allows a unique insight in the new region of asymmetric fission around ^{180}Hg, recently discovered at ISOLDE. Recent extensive theoretical efforts in this region will also be outlined.

The unprecedented high-quality data for fission fragments, completely identified in Z and A, by means of reactions in inverse kinematics at FRS(GSI) and VAMOS(GANIL) will be also reviewed. These experiments explored an extended range of mercury-to-californium elements, spanning from the neutron-deficient to neutron-rich nuclides, and covering both asymmetric, symmetric and transitional fission regions.

Some aspects of heavy-ion induced fusion-fission and quasifission reactions will be also discussed, which reveal their dynamical features, such as the fission time scale. The crucial role of the multi-chance fission, probed by means of multinucleon-transfer induced fission reactions, will be highlighted.

The review will conclude with the discussion of the new experimental fission facilities which are presently being brought into operation, along with promising 'next-generation' fission approaches, which might become available within the next decade.

Contents

CONTENTS 2

1. Introduction

Nuclear fission, discovered in 1938 [1], provides one of the most dramatic examples of a nuclear decay, whereby the nucleus splits preferentially into two smaller fragments releasing a large amount of energy. Fission is a unique tool for probing the nuclear potential-energy landscape and its evolution, as a function of elongation, mass asymmetry, spin, and excitation energy, from the single compound-nucleus system over the top of the fission barrier and further to the scission point, culminating in the formation of fission fragments. This transition involves a subtle interplay of collective (macroscopic) and single-particle (microscopic) effects, such as shell effects and pairing, all of which considered both for the initial nucleus and for the final fission fragments and at large deformations.

In Fig. 1, the fission process is illustrated as the collective motion of the nucleus in deformation space.

CONTENTS   3

Figure 1. (Color online) a) Macroscopic, $V_{\text{macro}}(\text{LDM})$, and b) total, $V_{\text{total}} = V_{\text{macro}}(\text{LDM}) + V_{\text{micro}}(\text{Shells})$ potential-energy surface for the ^{238}U nucleus as a function of elongation and fission-fragment mass asymmetry. The most probable fission paths (or 'fission valleys'), which follow the lowest energy of the nucleus, are shown by the red lines with arrows. While in the LDM approach only symmetric fission can happen along the single 'symmetric' valley, the introduction of microscopic shell effects produces the asymmetric fission valleys. Figure modified from [2].

The nuclear potential energy for a ^{238}U nucleus is shown as a function of elongation and mass asymmetry, which are the most important collective degrees of freedom in fission. Fig. 1(a) shows the simplified concept, initially proposed in 1939 [3], to explain fission based on the so-called 'Liquid Drop Model' (LDM). Within the LDM-approach the nucleus is considered as a classical incompressible 'macroscopic' liquid drop, whereby the competition between the repulsive Coulomb force (due to the protons in the nascent fission fragments) and the attractive surface energy of two fission fragments creates a smooth potential-energy surface (PES) with the minimum, denoted as the ground state in the plot. During the fission process, the nucleus elongates along the line of zero mass asymmetry, shown by the red line in Fig. 1,(a), thus initially increasing its potential energy, until at some moment the maximum of the potential energy is reached, which is called the saddle point (the top of the fission barrier). Afterwards, at even further elongation, the nucleus reaches the scission point and splits in two equal fission fragments (mass asymmetry =0). While the LDM approach was able to qualitatively explain why fission is one of the main decay modes of heavy nuclei, it failed to describe the experimental observation available at that time that the fission happens predominantly asymmetrically, in two un-equal fragments. Following the recognition of the quantum nature of the atomic nucleus and the development of the shell-model approach in nuclear physics, the need to include the microscopic shell corrections in the description of the fission process was realized in [4, 5, 6], whereby the

total potential energy becomes the sum of macroscopic (LDM) and misroscopic (shell effects) energy: $V_{\text{total}} = V_{\text{macro}}(\text{LDM}) + V_{\text{micro}}(\text{Shells})$. This naturally led to the appearance of the asymmetric fission valleys, as shown in Fig. 1,(b), thus to the asymmetric fission-fragment mass distribution (FFMD). As the microscopic shell effects depend strongly on specific neutron and proton numbers, their influence on the PES will differ among the nuclei, often leading to an even more complex fission potential-energy landscape with several fission valleys (or fission modes [7]), each characterized by its unique saddle and scission points, FFMDs and other properties, as will be extensively discussed in this review. As a final remark to this introductory picture, it is important to note the strong dependence of microscopic effects on the temperature (or, excitation energy) of the nucleus. In particular, there is compelling evidence that the shell effects are 'washed out' at sufficiently high excitation energies, which leads to the disappearance of asymmetric fission valleys on the PES, reverting it to the smooth LDM-like surface. Due to the latter, the nucleus will again fission predominantly symmetrically, as in the pure LDM. This explains the strong need for fission studies as a function of excitation energy.

On the other hand, specifically the low-energy fission, in which the nuclear shell effects are expected to be preserved, is a crucial source of our understanding of the complex process of fission and of the subtle interplay between collective and single-particle degrees of freedom‡. However, while low excitation energies are reached in spontaneous fission (SF), in the β-delayed fission (βDF), or in thermal-neutron-induced reactions [8], the situation is very different when the fissionning nucleus is produced in reactions with charged particles, in particular with heavy ions. Indeed, in the latter case the Coulomb barrier between the two colliding nuclei prevents them from forming a low-excited fissioning composite system, leading to typical excitation energies of at least $E^* \sim 35$ MeV even at the Coulomb barrier. Due to this, one preferentially observes symmetrical fission from a range of highly excited states even by using incident energies in the vicinity of the Coulomb barrier. Furthermore, the exponential drop of the fusion cross section below the Coulomb barrier leads to strongly reduced production rates in the experiments at sub-barrier energies, which makes such experiments less practically feasible.

‡ In most cases throughout this review, we assume the 'low-energy' fission regime when the excitation energy of the fissioning system is lower or close to the height of the fission barrier, $E^* \sim B_f$. However, due to widely different fission-barrier heights across the Chart of Nuclei, see the discussion of Fig. 2 further in the text, this will lead to different absolute excitation energies which can be considered as 'low' or 'high' as far as fission in different regions is concerned.

CONTENTS 4

The situation is better in the case of multi-nucleon transfer (MNT) reactions, where excited states can be populated starting from low excitation energies, sometimes from around the top of the fission barrier or even slightly below, up to highly excited states.

To set the scene in respect of 'low-' vs 'high-' energy fission, Fig. 2 shows an overview of calculated fission-barrier heights within the macroscopic-microscopic model by Möller et al [9]. A highly changeable landscape with the fission-barrier heights ranging from just a few MeV for heavy and superheavy elements with $Z > 100$§, up to ~ 25 MeV in the vicinity of the doubly magic ^{208}Pb can be noted. In respect of the fission barriers of the neutron-deficient nuclei in the lead region, which are discussed in detail in Section 4.1, several important conclusions can be drawn. Firstly, there exists a large group of nuclei above $Z \sim 78$ and around neutron numbers $N = 100$–115, for which the typical fission barriers are below $B_f \sim 12$ MeV. Due to this, these nuclei are particularly suitable for low-energy fission studies by means of βDF (only odd-odd cases [10]) and/or by Coulex-induced fission [11]. Secondly, as mentioned above, particle-induced fission reactions that can also be used in this region typically result in relatively high excitation energies well above the fission barrier, even if a beam energy close to the Coulomb barrier is selected. As one particular example, relevant for the follow-up discussions in Section 4.1, we notice the smoothly decreasing fission barriers in the chain of the neutron-deficient Hg isotopes: from ~ 24 MeV close to the neutron shell closure at $N = 126$, to ~ 10 MeV in the region of ^{180}Hg. This explains, why so far only charged-particle-induced reactions were used in the vicinity of $N = 126$, see e.g. [12, 13, 14, 15], while both βDF and Coulex-induced fission recently became the methods of choice to study low-energy fission by approaching the mid-shell at $N = 104$ and beyond [10, 16, 17].

While the fission-fragment mass distributions, which are most intensively studied so far, are closely linked to the structure of the potential-energy surface as illustrated in Fig. 1, other observables carry valuable information on additional degrees of freedom. For example, the effects of nuclear dissipation on the way to scission are very important, as such data contain unique information on dynamical aspects of the fission process like the fission times, the interplay between collective and single-particle degrees of freedom and the degree of equilibration on the fission path. Such effects are probed by e.g. the characteristics of the fission-fragment distribution [18, 19, 20, 21] prompt-particle emission (neutrons, γ rays, charged particles), see e.g. [22, 23], or by atomic methods, see e.g. [24,

25, 26, 27] and references therein. An odd-even staggering in the yields [28], angular momenta [29], kinetic energies, and prompt-neutron multiplicities [30] for fission fragments with even or odd numbers of protons and neutrons reflects the influence of pairing correlations on the fission process. Moreover, fragment-mass-dependent data on prompt-neutron and prompt-gamma emission after scission reveal how much of the available energy release ends up in the excitation energies of the individual fragments.

There were several previous comprehensive reviews covering the fission research up to ~ 1995 [31, 32, 8, 33]. Several recent reviews discussed some of the fission aspects, studied in reactions with charged particles and in the traditional regions of fission in transactinide and superheavy nuclei, see e.g. [34, 35, 36]. The recent one by Heßberger [37] is specifically dedicated to spontaneous fission. The present work will therefore summarize the experimental fission data and new or improved techniques emerging from ~ 1995, including extensive novel research based on the use of inverse kinematics and radioactive ion beams, which was not possible in the previous studies.

The outline of the review is as follows: first, Section 2 provides a general classification of different production mechanisms relevant for fission studies, in particular in respect of the reaction-kinematics type - 'direct' or 'inverse'. The follow-up Section 3 shows selected examples of experimental facilities for both methods, while the discussion of specific results is given in Section 4. Section 5 will further review a range of several fission facilities being presently under construction or being considered for future fission studies. The work concludes with Section 6, where a discussion of some of the open questions in fission research will be given.

2. General features of fission experiments in direct and inverse kinematics

Historically, several different types of reaction mechanisms were used to study the fission process. An attempt to summarize the main methods is given in Table 1, which provides the classification based both on the reaction kinematics type ('direct' or 'inverse') and on the beam type (stable or radioactive). For several decades since the discovery of induced fission in reactions with neutrons in 1938 [1] and of spontaneous fission in 1940 [38], the reactions in the so-called 'direct kinematics' were used. Here, a stable (or a long-lived) light projectile (e.g. electron, photon, neutron, proton or light ion) is shot on a heavy target to produce fissioning nuclei and study their decay. The predominance of this method was due to the relative easiness to accelerate light ions and electrons or

§ The zoom-in for the region of superheavy elements will be discussed in detail in Section 4.4 and in Fig. 55
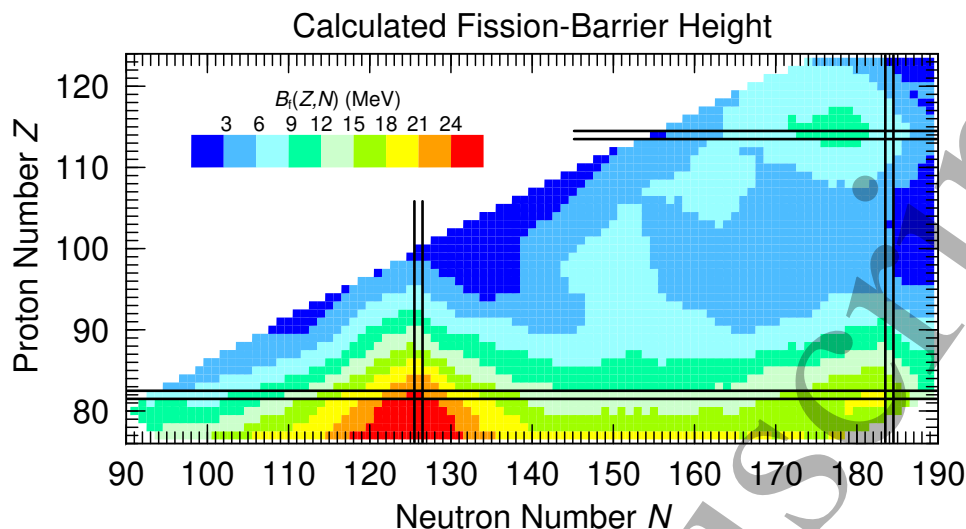
Figure 2. (Color online) Calculated fission-barrier heights for 2891 nuclei derived from the macroscopic-microscopic model by Möller *et al.* The highly-variable structure is mostly due to ground-state shell effects. Figure modified from [9].

to get neutrons from a power reactor or a suitable light-ion-induced reaction. Following the progress in the accelerator and detection techniques, the use of 'inverse kinematics' became possible, in which a heavy nucleus is shot on a light target, as e.g. in the recent experiments at VAMOS(VAriable MOde high acceptance Spectrometer) at GANIL [39]. Furthermore, within the last two decades, the use of short-lived radioactive ion beams (RIBs) for fission research was introduced at ISOLDE [10] and GSI [11, 40, 41], which revolutionized the whole field of fission studies. As shown in Table 1, presently both stable and radioactive beams can be employed in both kinematics; the future technical developments will further blur the boundaries between different methods, see Section 5. The following subsections 2.1- 2.2 briefly discuss the main advantages and drawbacks of both approaches.

2.1. Fission experiments in direct kinematics

In order to produce fissioning nuclides of interest, initial experiments in direct kinematics used different reaction mechanisms, e.g. complete fusion, transfer-induced fusion, spallation/fragmentation‖ to name a few. Fig. 3 shows a simplified diagram for two most commonly used methods to produce fissioning nuclides at beam energies close to the Coulomb barrier by means of complete fusion or MNT-induced reactions with light or heavy ions, denoted by a common

‖ In this work, the term "spallation" is used to characterize reactions induced by light particles at beam energies per nucleon well above the Fermi energy, that proceed essentially by an internuclear cascade [43], see Section 4.7. "Fragmentation" denotes reactions induced by heavy ions, in which the scenario of a geometrical abrasion with a distinction of participants and spectators is applicable [44].
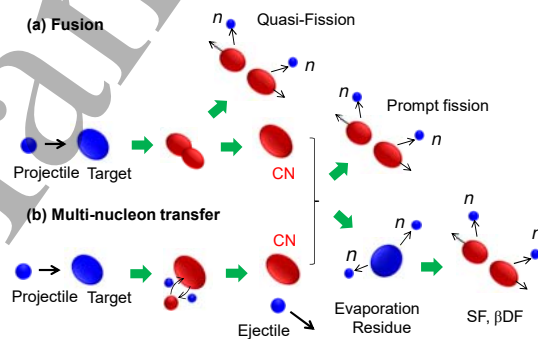
Figure 3. (Color online) Two most common reaction mechanisms which occur in the light/heavy-ion-induced reactions in direct kinematics at beam energies in the vicinity of the Coulomb barrier: (a) Complete fusion which proceeds via the formation of an excited compound nucleus (CN), followed by prompt fission (the whole process is often called 'fusion-fission' in the literature and in this review). Often, a competition with the so-called quasifission (QF) occurs in reactions with heavy ions, which is the prompt fission from a non-fully equilibrated composite system, shown in the figure, before the CN is formed; (b) Multi-nucleon transfer (MNT) reactions, whereby one or several nucleons can be transferred to (or picked up from) the target nucleus to produce an excited CN and an outgoing ejectile. In both cases a) and b), the excited CN further decays either by prompt fission or evaporates several neutrons (also γ rays) to form an evaporation residue (ER), which can then decay by spontaneous fission or by βDF.

name 'fusion/transfer-induced fission' in Table 1. In the following, we will explicitly distinguish the two types of fission - the prompt fission from excited CN (called 'prompt' fusion/transfer-induced fission) and the fission of a residual nucleus, after the particle-evaporation cascade. The latter usually happens in the form of spontaneous fission (broadly including the fission of shape isomers) and βDF.

CONTENTS   6

Table 1. Classification of reactions types, used for fission studies. Selected examples of facilities are mentioned for some cases and will be discussed in relevant sections in the text.

Beams	Direct Kinematics	Inverse Kinematics
Stable Beams, up to ^{238}U (n, p, light/heavy ions, γ, e$^-$)	Prompt fusion/transfer-induced fission SF, βDF	Prompt fusion/transfer-induced fission, VAMOS at GANIL [39]
	Future/Proposed	
	photofission with brilliant γ-ray beams at e.g. ELI [42], SF, βDF with S3 at GANIL	
Radioactive Ion Beams (RIBs) (fragmentation/spallation of ^{238}U)	βDF of low-energy 30-60 keV beams at ISOLDE [10]	Coulex of relativistic secondary beams SOFIA at GSI [11, 40, 41]
	Future/Proposed, see Section 5	
	prompt fusion/transfer-induced fission with post-accelerated RIBs	p,2p/Coulex with SAMURAI at RIKEN e$^-$-RIBs with SCRIT at RIKEN, ELISe at GSI

In direct-kinematics experiments, the choice of the target material is very limited, as only very few nuclides above ^{209}Bi are found on Earth, e.g. the primordial nuclides ^{232}Th, ^{235,238}U, ^{244}Pu and some of their long-lived decay products, e.g. ^{226}Ra. Only several more can be produced in sufficient quantity in a nuclear reactor, including e.g. ^{243}Am ($T_{1/2} = 7370$ years), ^{248}Cm ($T_{1/2} = 3.5 \times 10^5$ years), ^{249}Bk ($T_{1/2} = 320$ d), ^{249}Cf ($T_{1/2} = 333$ d), ^{254}Es ($T_{1/2} = 275$ d). Specifically, the ^{249}Bk and ^{249}Cf materials were used extensively in the recent experiments to identify new superheavy elements [36]. However, such short-lived nuclides may pose the problem of high radioactivity that complicates the target preparation and can also impose extra limitations on the fission detectors, in e.g. the prompt-fission experiments.

Figure 4 gives an overview of the fissioning systems, for which FFMDs or nuclear-charge distributions were known at the end of the 20th century. Besides the systems accessible by neutron-induced fission, the low-energy charged-particle-induced prompt fusion/transfer-fission reactions were predominantly used to access nuclei in the regions around stable isotopes near ^{208}Pb, e.g. [12, 13, 14, 15] and long-lived ^{226}Ra ($T_{1/2} = 1600$ y), see e.g. [45, 46]. The large gap in between is due to the absence of suitable targets to produce low-energy fission. Furthermore, the studied nuclei concentrated very much in a narrow band close to the β-stability valley. Only in the upper part of the chart of the nuclides, βDF and, predominantly, SF of very heavy nuclei produced in complete-fusion or transfer-induced reactions with light and heavy ions, gave access to nuclei in a broader range of N/Z values, in particular on the neutron-deficient side, see e.g. [32, 47, 48]. An ultimate example of such studies was the FFMDs measurements for SF of ^{259}Fm, produced in the (t,p)-transfer reaction of an intense 10μA triton beam with a unique $(0.9$-$1.3) \times 10^9$ atoms target of ^{257}Fm ($T_{1/2} = 100$ d) [49]. As will be shown in Section 4.3, the modern MNT-induced experiments with heavy ions and very exotic radioactive actinide targets up to the element einsteinium with $Z = 99$ (^{254}Es) al-

low to substantially broaden the region of nuclei available for fission studies, e.g. towards the most neutron-rich nuclei.

After the production of fission fragments either in QF, or in the prompt fusion-fission of the excited CN, or eventually in the SF/βDF of the fully de-excited fissioning evaporation residue, one of the greatest challenges is the unambiguous determination of mass A and atomic number Z of the fission products. The following three identification/detection techniques are mainly used for such measurements:

- Identification of characteristic γ-ray radiation following the series of β decay of the fission products, often complemented with the radiochemical pre-separation of the suitably long-lived initial fission fragments. An advantage of this method is that the measurements can be performed at a place distant from the irradiation point, thus eliminating the background which occurs at the in-beam irradiation spot. In the past, this was the only technique that allowed unambiguous identification of fission products in both Z and A [50, 51, 52, 53, 54], In most cases, only cumulative yields, that means the yields after some β-decay stages were accessible, while no information on prompt neutron emission and FFs kinematic properties, e.g fragment energies and/or the total kinetic energy could be obtained. Due to the above limitations, this method is not so frequently used nowadays. Recent examples of the application of this method include e.g. photofission and neutron-induced fission of ^{238}U [55, 56] and proton-induced fission of ^{232}Th [57].

- In-beam (prompt) fission experiments, in which the fission detectors directly face the thin reaction target, allowing the observation of fission fragments in a compact geometry. Silicon detectors, multi-wire proportional chambers (MWPC), or time-of-flight (TOF) detectors are often used for FFs detection, see Section 3.1. With a proper choice of ancillary detectors, this method can further allow an access to a wide range of fission ob-

servables, including prompt neutron [58, 59] and γ-ray multiplicities [60, 61, 62, 63]. We note that similar detection methods are also exploited in the SF and βDF studies, but some sort of pre-separation (chemical or electromagnetic) of the fissioning *parent* nucleus is often used in such cases, see Sections 4.4 and 4.1.

- A FFs pre-separation with a spectrometer, e.g. the LOHENGRIN recoil separator [64, 65] at the high-flux reactor of the ILL, Grenoble, whereby the fission fragments after the thermal-neutron-induced fission are separated in-flight by mass and energy by an ion-optical system before being measured by the detection system. The mass yields are readily obtained by ion counting and integration over the ionic-charge-state and kinetic-energy distributions. For the light fragments, a mass resolving power of $A/\Delta A = 250$ (full-width at $1/10$ maximum) was achieved. The determination of isotopic yields requires a nuclear-charge identification in addition. Traditionally this is obtained by the ΔE-E method with a split-anode ionization chamber. However, for fission fragments with typical energies of the order of $\sim 1\,A\,\text{MeV}$ this method reaches its limit at about $Z \approx 42$, thus it can only cover the light fission peak. In the heavy fission peak, isotopic yields are instead measured by γ-ray spectrometry, using Ge clover detectors surrounding the focal plane, see recent examples from LOHENGRIN in Refs. [66, 67]. γ-ray spectrometry enables also the determination of isomeric yields [68] and of the isomer population as function of the kinetic energy of the fission fragments [69]. Still, the accuracy of the absolute-yield determination may be limited by the knowledge of the γ-ray intensities per decay, and this method is not applicable for the yield measurement of very long-lived or stable fission fragments. Thus, at present, an independent development is pursued to push the limits of the ΔE-E method, namely by using very homogeneous Si_3N_4 membranes as passive absorbers combined with calorimetric low-temperature detectors for a pulse-height-defect-free determination of the residual energy [70]. Other examples of the FFs pre-separation method, but in inverse kinematics, which boosts the FFs energies, include the fission experiments at the VAMOS [39] at GANIL and at FRS(FRagment Separator) at GSI [40, 41, 71, 11], see Section 3.5.

In most fission techniques in direct kinematics, the momentum/energy of the initial fissioning system induced by the reaction is low, or even zero, as in case of SF/βDF. Therefore, the kinematical properties, in particular the energies of the fission fragments, are
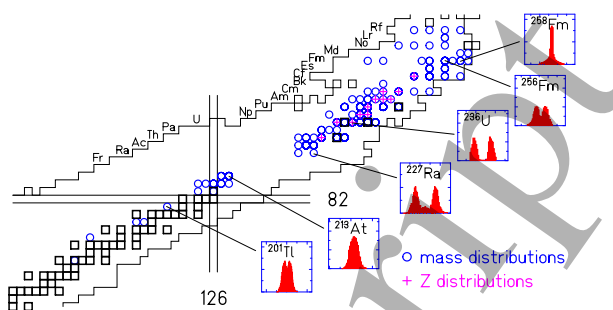
Figure 4. (Color online) Overview of fissioning nuclei investigated in low-energy fission up to $\sim$1995, before the first systematic measurements in inverse kinematics at FRS(GSI) and of βDF at ISOLDE were performed. Mass distributions (circles) and Z distributions (crosses) were measured for nuclei marked by symbols at excitation energies up to 10 MeV above the fission barrier (or in SF). Several examples of measured FFMDs are shown, data from Refs. [12, 46, 72, 73]. For orientation, the primordial isotopes are indicated by squares. The figure is a slight modification of Fig. 1 in Ref. [40].

either uniquely defined by the fission process itself (as in SF/βDF), or allow a relatively simple kinematical correction for the transferred momentum. However, as mentioned above, the relatively low energies of FFs in such studies result in certain difficulties for their Z and A identification, see examples in Sections 3.1 and 4.1. In particular, straggling phenomena severely hamper an unambiguous Z identification of fission products by energy-loss measurements at FFs kinetic energies. This is one of the main drawbacks of the fission experiments in direct kinematics.

Returning now back to Fig. 4, one notices that the lighter systems, up to ^{213}At show an essentially single-humped mass distribution. Interesting enough, a double-humped structure in a nearly symmetric fission was reported for ^{201}Tl at an excitation energy of 7.6 MeV above the fission barrier by Itkis *et al* in 1988 [12] in α-particle-induced fission. However, a more extended study of this feature further away from the β-stability line was not possible at that time.

In the range from $A = 227$ to $A = 256$, where most of the previously investigated systems are situated, asymmetric fission prevails. The heavy mass FFs peak was found to be centered close to $A = 140$ [76]. This implies that the light mass peak approaches the heavy peak with increasing mass of the fissioning nucleus, until there is a sharp transition to symmetric fission with a narrow mass distribution and high total kinetic energy (TKE) between ^{256}Fm and ^{258}Fm. The same feature was also observed for several isotopes of other neighboring elements of similar mass [47, 48, 32, 77]. In fact, already in the earlier fission studies further complex features in the FFMDs, TKE, and prompt-neutron multiplicity were observed in asymmetric

CONTENTS   8

Figure 5. (Color online) Updated overview of fissioning systems investigated up to ∼2016 in low-energy fission with excitation energies up to 10 MeV above the fission barrier. In addition to the systems for which FFMDs have previously been obtained in particle-induced and spontaneous fission (○), the nuclei for which fission-fragment Z distributions after electromagnetic excitations were measured in the 1996 experiment [40] in inverse kinematics at the FRS at GSI (×) and the fissioning daughter nuclei studied in βDF (◇) are shown. Full diamonds mark systems for which FFMD were measured, the data are from [10, 17] and references therein. Furthermore, 25 nuclei are marked (+), including FFMDs obtained from MNT-induced fission with ^{18}O+^{232}Th [74] and ^{18}O+^{238}U target [75]. Several examples of measured FFMDs are shown, data from Refs. [12, 46, 72, 73]. For orientation, the primordial isotopes are indicated by squares. The figure is a modification of Fig. 1 in Ref. [40] and of Fig. 1 in Ref. [10].

fission and were interpreted as due to contribution from different fission channels or fission modes [7]. In the seminal scission-point model by Wilkins *et al* [78], the most important fission channels, named Standard 1 and Standard 2 in the nomenclature of Brosa *et al* [7],

were attributed to the influence of shell effects near the doubly magic ^{132}Sn and a deformed shell around the neutron number $N=88$ in the heavy fragment, respectively.

Furthermore, a few systems, such as ^{225,227}Ra,

CONTENTS   9

^{226,227,228}Ac and ^{227,228,229}Th that were investigated with radioactive ^{226}Ra and ^{227}Ac targets [45, 79, 80] revealed also a transitional region of multimodal fission (coexistence of symmetric and asymmetric fission) due to the gradual appearance of symmetric fission around $A = 226$ with decreasing mass of the fissioning system. In the past, the detailed study of this transitional region was very much hampered by the non-availability of suitable target material between ^{209}Bi and ^{226}Ra.

A survey on the status of this field before the development of the novel experimental approaches based on inverse kinematics (see Section 3.5) reveals, on the one hand, a wealth of often very detailed experimental results, which are comprehensively reviewed in the textbook by Wagemans [8] and recent reviews on neutron-induced fission by Gönnenwein [33] and on charged-particle-induced fission by Kailas and Mahata [34]. On the other hand, it became clear that the use of the traditional method of direct kinematics with light projectiles results in a quite incomplete coverage of fissioning systems, especially at low excitation energies, which is further aggravated by severe technical difficulties in measuring some of the key experimental fission quantities that could never be fully overcome.

Figure 5 shows the present status of low-energy fission studies, in which the mass and/or charge distributions were measured. Most of the newest data (in respect of Fig. 4) were obtained by using the new techniques, which are described further in the text¶.

2.2. Boosting the fission-fragment energies for improving the mass/charge resolution in inverse-kinematics fission studies

During the last two decades, new types of fission studies have been developed by employing inverse-kinematics reactions. At GSI (Darmstadt), the electromagnetically induced (Coulex) fission of short-lived radioactive isotopes produced by fragmentation of relativistic $1\,A$ GeV ^{238}U ions on a Be target was exploited [81, 40]. This method and its latest development in the SOFIA (Studies On Fission with ALADIN) experiment [11], discussed in details in Section 3.5.1, allowed to considerably expand the region of nuclei, accessible for *low-energy* ($E^* \sim 14$ MeV) fission studies, towards the scarcely studied (by fission) neutron-deficient Hg-Th nuclei, see green crosses in Fig. 5. Due to its specific excitation

¶ Although the progress in fission research imparted by comparing Figs. 4 and 5 is impressive, the development in fission research shown in Fig. 5 is represented only to some part. This is due to the excitation-energy limit that has been applied to this figure, in order to keep it comparable to Fig. 4. More higher-energy fission data, obtained via charged-particle-induced reactions, became available in the last two decades, see e.g. Fig. 32 for the neutron-deficient lead region.

mechanism (see Section 3.5.1), this method suits well for nuclei whose fission barrier is less than $\sim$15 MeV. However, this method does not allow to study the nuclei beyond $A = 238$, due to the present non-availability of beams heavier than ^{238}U$^+$.

At VAMOS [83], prompt fission of several nuclei close to and above ^{238}U was studied by means of MNT reactions of ^{238}U ions with a ^{12}C target at Coulomb energies [84, 39, 85], see the detailed discussion in Section 3.5.2.

A very important feature of both types of experiments is that due to the high momentum/kinetic energy of the initial fissioning system (due to inverse kinematics used), the fission fragments achieve a large kinematical boost in forward direction, e.g. $\sim$700 A MeV for the reactions with the relativistic secondary beams at GSI (see Table 1) or $\sim$6 A MeV in the experiments at VAMOS. This effect makes their Z and A identification much easier. For example, values of $\delta Z \sim 0.35$ and $\delta A \sim 0.6$ to 0.8 were obtained in the recent SOFIA experiment [71, 28].

A common difficulty of these methods is that the choice of accessible systems strongly depends on the primary beams and on the characteristics of the reaction. At present, they can only be used at laboratories that provide beams of very heavy nuclei (e.g. ^{238}U) with energies above the Coulomb barrier (VAMOS-type experiments) or with appreciably higher energies (GSI-type). Moreover, suitable detection devices, including large powerful spectrometers, must be available for the identification of the fission products.

3. Selected examples of experimental fission techniques

3.1. Measurements of fission-fragment mass distributions in prompt-fission studies in direct kinematics at near-Coulomb-barrier energies

In this section, in-beam (prompt) fission experiments with heavy ions in direct kinematics at energies close to the Coulomb barrier will be discussed, with an emphasis on the measurements of the fission-fragment mass distributions. In this type of experiments, the fission-fragment detectors directly face the reaction point (target). Compared to n/γ/e$^-$ or light-ion-induced fission, the use of heavier projectiles allows to study fission of nuclei further away from the β-stability line, especially on the proton-rich side and in the region of superheavy nuclei, in addition to SF/βDF (see, Sections 4.4 and 4.1 [16, 86, 87, 17, 88]).

The accessible nuclei are determined both by the projectile-target combination and also by the reaction

$^+$ Efforts to provide a ^{242}Pu beam are presently undertaken at GSI [82].

CONTENTS

type, e.g. fusion-fission, quasifission or MNT-induced fission, see Fig. 3. One of the characteristic differences between fusion-fission/QF (Fig. 3(a)) on the one hand and MNT reactions (Fig.3(b)) on the other hand is that a full momentum transfer (FMT) happens in the former case, whereas only a partial momentum is transferred in the latter, thus the recoil momenta (velocities) of the compound nuclei in two reactions are different. This, in turn, results in different folding angles θ_{fold} of fission fragments in the laboratory frame, where θ_{fold} is defined as the sum of the emission angles θ_1 and θ_2 of the fragments relative to the beam direction. As both mechanisms can occur in a given reaction, the difference in the folding angle is often used in the follow-up data analysis to differentiate the two contributions. Figure 6 provides an example of a double-humped folding-angle distribution measured with the JAEA fission setup (further discussed in Fig. 7) in the reaction ^{30}Si+^{238}U [89]. While the FMT folding angle (indicated by a red arrow) remains nearly constant for the range of projectile energies used in the study, the folding angle for the multi-nucleon-transfer channels shows a characteristic dependence on the beam energy. Namely, at the lower energies (e.g. below $E_{\text{lab}} = 168$ MeV in Fig. 6), the backward scattering of the ejectile dominates, boosting the velocity of the fissioning nucleus, which results in a smaller folding angle. With an increase of the projectile energy, the ejectile is preferentially scattered to forward angles, which makes the recoil velocity smaller, thus the folding angle enhances accordingly.

For heavy-ion reactions characterized by $Z_p \times Z_t > 1600$ [90], where Z_p and Z_t are the projectile and target proton numbers, the competing channel of quasifission can open and might even become the dominant one for the very heavy systems (see Section 4.5.1). Quasifission is a non-fully equilibrated process, thus should have different properties relative to fusion-fission in such observables, as e.g. the angular distribution and kinetic energies of resulting fission fragments, and also the fission time scale, see e.g. [18] and refs therein. On the other hand, the quasifission is categorized by the FMT-like folding-angle distribution type, because the projectile and the target nucleus amalgamate to a one-body composite system, albeit for a short time only.

3.1.1. Typical setups for prompt fusion-fission experiments. In a typical prompt-fission experiment, the FFMDs are derived based on the kinematical analysis of the reaction itself and of subsequent coincident fission fragments, by what is known as the 'kinematic coincidence method' [91, 92]. In this method, both fission fragments are detected in coincidence to determine their masses and kinetic energies from the mass- and momentum-conservation
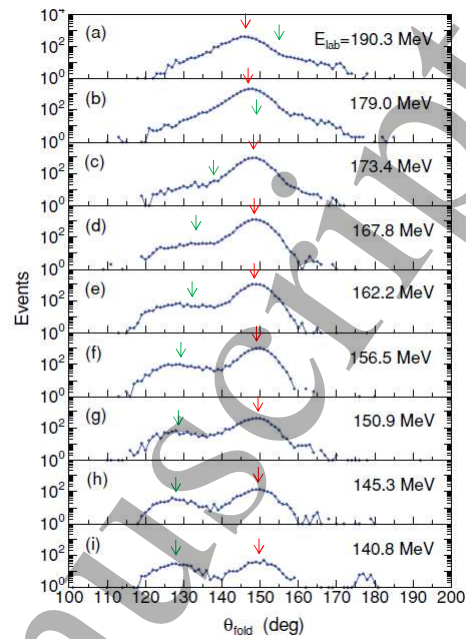
Figure 6. (Color online) Folding-angle distributions of fission fragments in the reaction of ^{30}Si + ^{238}U [89], measured at the projectile energies, indicated in each panel. The red and green arrows mark the positions of the folding angle, corresponding to fusion-fission (FMT) and to MNT-induced fission, respectively.

laws. Usually, the mass of the fissioning nucleus is treated to be equal to the sum of the masses of projectile and target nuclei for the fusion-fission reactions. However, the influence of prompt neutron emission [58, 59] should be carefully considered case-by-case, see e.g. the discussion of reactions in the mercury region in Section 4.1.3 and also in the actinide region in Figs. 49–50 in Section 4.3.1. For the MNT-induced reactions, the mass of the fissioning compound nucleus can be determined only when the mass of the ejectile nucleus is identified by using charged-particle detectors. To apply the method of kinematical coincidences, a fission setup should be able to measure some (ideally - all) of the following properties of both fragments: velocities, energies, azimuthal and polar angles with respect to the beam direction (or positions of registration) of the fission fragments. In case the velocities of the fission fragments are measured (the so-called $2v$ or 'double velocity' method), no corrections for the neutron evaporation is needed [35, 91], as the isotropic neutron emission only broadens the velocity distribution, without shifting it. However, this method requires a setup with very good timing properties, see examples in the next section. On the contrary, when the kinematic analysis relies only on the energy measurement of the FFs, the knowledge of the number of prompt neutrons emitted from the individual fission fragments is needed [93]. The latter requires a

CONTENTS   11

more elaborate setup for the correlation measurement between FFs and neutrons, see the recent study [59].

The following main types of fission detectors are extensively used in current prompt-fission studies:

- Silicon detectors are often exploited in fission experiments including light-particle (n, p, α, ^{3}He) induced fission, see recent examples in Refs. [94, 14, 15, 95, 96, 97, 98]. However, when used to detect heavy ions, these detectors suffer considerably from the pulse-height defect, which strongly depends on the mass and charge values of the fission fragments, see e.g. [99, 93, 100]. Also the timing signal from a silicon detector exhibits a characteristic delay depending on energy and mass of the ion [101], and on the detector design [102]. While the silicon detectors can be made position-sensitive to allow the position (thus direction) of the FFs to be measured, the rate capabilities and radiation hardness sometimes limit the application of these detectors. On the other hand, thin (several tens of micrometers) silicon detectors can be used as ΔE detectors in transfer-induced fission experiments to identify the ejectile nuclei, rather than the FFs themselves, see Section 3.1.2 for examples. In passing we note that Si detectors are often used in SF [103, 49, 48, 104, 105, 106] and βDF [107, 16, 10, 17, 108, 88] studies for the FFs' energy determination.

- Frisch-gridded ionization chambers (GICs) are still frequently used in modern neutron-induced fission experiments [109, 60, 61, 62, 110, 111, 112, 113]. Their main advantage is the large detection efficiency, approaching $\sim 4\pi$ in cases when the target material is situated inside the chamber, usually on its cathode. The emission angles of the fragments can be obtained by measuring the drift time of the electrons, generated along the fragment track, over the cathode and grid region. Furthermore, it was shown that the pulse-height deficit within a gas is smaller than that in silicon [114], thus the GIC can provide a better resolution for determining fragment energy/mass under good operation conditions [115, 114]. The GIC can be easily coupled with neutron and/or γ-ray detectors for correlation measurements with FFs. Examples are ^{252}Cf(SF) for neutron [113] and n+^{241}Pu for γ-ray [61] measurements (also see Section 4.6).

- Multiwire proportional counters (MWPCs) can be designed with a large size, and can be made position-sensitive in two dimensions. They usually provide a sufficiently fast timing signal (on the order of ~ 1 ns), which is suitable for time-of-flight measurements, can cope with high counting rates and are radiation-resistant, if

a gas flow is provided. Due to the above properties, this is one of the most frequently used detectors for prompt-fission studies, particularly for heavy-ion-induced fission. A similar type of fast-timing gas detectors, called parallel-plate avalanche counter (PPAC), uses uniform thin-layer electrodes (rather than multiple wires), as used in e.g. a setup where the electrodes are directly exposed to the neutron beam, for example as in fission cross-section measurements in the studies [116, 117]. Hereafter, we refer to these types of detector as MWPC/PPAC, except for specific cases.

- Fast-timing detectors, based on micro-channel plates, for amplification of secondary electrons emitted by a thin foil during the passage of a fission fragment. Such detectors are often used for the velocity measurements of fission fragments with the TOF method, where a start detector with a very good timing response (up to ~ 100 ps) is necessary. The MCP-based start timing detectors can be combined with large-area MWPC/PPACs or silicon detectors, used as a stop detector, to achieve overall good timing resolution that is needed for velocity measurements, in particular for the so-called 'double-velocity double energy' ($2v$-$2E$) method*.

- Recently, attempts to use poly-crystalline and single-crystal chemical vapor-deposited (pCVD and sCVD, respectively) diamond detectors for the detection of fission fragments were undertaken, see e.g. Ref. [118, 119]. This is due to their several promising properties, such as high radiation hardness, an expected faster timing response in comparison with silicon detectors and much easier operation compared to the MCP-based timing detectors. Unfortunately, while a sufficiently good timing resolution was obtained (up to 100 ps), the energy resolution proved to be not yet sufficient for FFMDs measurements due to a severe pulse-height deficit [118]. Another issue to be solved is the largely varying quality of the diamond material, resulting in high costs. Despite the present issues, such detectors look as a promising alternative for future fission setups.

Several research groups are presently active in the studies of different aspects of prompt fission, in particular of the FFMD measurements, by means of reactions with heavy ions at the following facilities:

- 20UR tandem at the Japan Atomic Energy Agency (JAEA) in Tokai [120, 89, 121, 122, 123, 124, 74, 125]

* See Section 3.2 for further details and examples for this method.

CONTENTS   12

- 14UD tandem accelerator at the Australian National University (ANU) in Canberra using the CUBE fission spectrometer [126, 127, 128, 129, 18, 130, 131, 132, 133, 134],

- Flerov Laboratory for Nuclear Reactions (FLNR) in Dubna, Russia, using the CORSET setup [135, 136, 137, 138, 139, 140, 141, 142, 143, 144, 145, 146, 35],

- 15UD Pelletron at the Inter University Accelerator Centre (IUAC) in New Delhi, India [147, 148, 149, 150, 151, 152, 153, 154, 155, 156, 157, 158, 159]

- Pelletron LINAC facility in collaboration between BARC (Bhabha Atomic Research Centre) and Tata Institute of Fundamental Research (TIFR) in Mumbai, India [160]

In the following, selected examples of applied techniques are presented in some details.

Fission set-up at the JAEA tandem facility at Tokai. Figure 7 shows an example of the setup for prompt fusion-fission and MNT-induced fission experiments at the JAEA tandem facility. Here, up to four position-sensitive (in X- and Y- directions) MWPCs can be used to detect fission fragments in coincidence. A silicon ΔE-E detector array is used only for MNT-induced fission [75, 74, 125] (see Section 3.1.2), and is removed for fusion-fission/quasifission experiments. The positions of the MWPCs are optimized for each experiment to increase the detection efficiency as a function of the momentum of the fissioning nucleus, which is determined by the target-projectile combination and the incident-beam energy. The MWPCs have an active area of $200{\times}120\,\mathrm{mm}^2$ [120] or $200{\times}200\,\mathrm{mm}^2$ [75] each, and are located at a distance of $210{-}224\,\mathrm{mm}$ from the target center. One MWPC can cover the emission angle of fission fragments of about $\Delta\theta_{Lab} = 50°$ relative to the beam direction. Due to the continuous nature of the beam at the JAEA tandem, no start signal can be derived from the beam itself; therefore, the FFs masses and kinetic energies are determined from the kinematical analysis by measuring the time difference, ΔT, between the signals from two coincident MWPCs, and the positions of registration (X_1, Y_1, X_2, Y_2) of both fragments. Additionally, the charges $\Delta Q_{1,2}$ induced on the cathodes of the respective MWPCs are also deduced, which allows to distinguish the FFs events both from the elastically scattered projectile and target nuclei, and also from the target- and projectile-like fragments, in case of QF.

A peculiar feature of the JAEA tandem, which is not available at other tandems, should be emphasized - its ability to deliver the beams of noble gases, due to the presence of an ECR ion source mounted on the
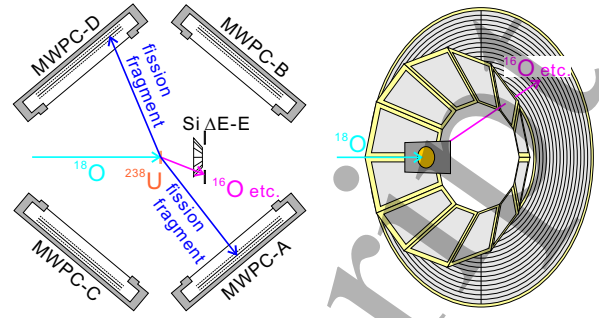
Figure 7. (Color online) A typical detection setup for in-beam MNT-induced fission experiments at JAEA. In the case shown, the MNT reaction $^{18}O + ^{238}U$ was studied, whereby four MWPCs - MWPC-A - MWPC-D - were used to detect the coincident fission fragments, while a silicon ΔE-E telescope array was exploited to determine the transfer channel. In case of the fusion-fission experiments, the ΔE-E telescope array is removed. Figure is taken from [74].

terminal [161]. Fig. 8 gives an example of raw data from the JAEA setup obtained in the fusion-fission reaction $^{36}Ar + ^{144}Sm \rightarrow ^{180}Hg^*$ [124]. Two MWPCs were used in this study; therefore, the panel a) shows a plot of $\Delta Q_1 + \Delta Q_2$ vs ΔT signals for coincident events measured in the MWPCs. Coincident fission events, marked by the red-colored polygon, are located in between the peaks corresponding to the elastically scattered target ^{144}Sm and projectile ^{36}Ar nuclei, which are also measured in coincidence. Fig. 8(b) shows the same data as in Fig. 8(a), but in the coordinates $\theta_1 + \theta_2 (= \theta_{\mathrm{fold}}$, See Fig. 6) vs $\phi_1 + \phi_2$ in the laboratory frame, where $\theta_i (i = 1,2)$ are the emission angles of the fission fragments projected on the plane defined by the beam direction Z and the horizontal X-axis (see Fig. 1 of Ref. [120]). The out-of-plane angles ϕ_i $(i=1,2)$ were the projections of the emission angles on the X-Y plane. The fission-fragment masses and total kinetic energies are obtained by analyzing the events enclosed by the red polygons in Fig. 8, whereas the elastic-scattering events can be used for the mass calibration. The typical mass resolution obtained in the fusion-fission experiments at JAEA is about $6\,\mathrm{u}$ (FWHM).

CUBE facility at the ANU's tandem at Canberra. A conceptually similar setup, called CUBE, shown in Fig. 9(a), is used in the experiments at the ANU. The CUBE utilizes two large-area position-sensitive MWPCs with dimensions of $284{\times}357\,\mathrm{mm}^2$ [91], installed at a distance of $180\,\mathrm{mm}$ from the target and covering an acceptance angle of up to $\Delta\theta_{Lab} \sim 75°$, being the largest among all presently operating in-beam setups. As for the JAEA setup, the MWPCs positions can be optimized depending on the reaction to be studied. The large angular coverage is advanta-

CONTENTS
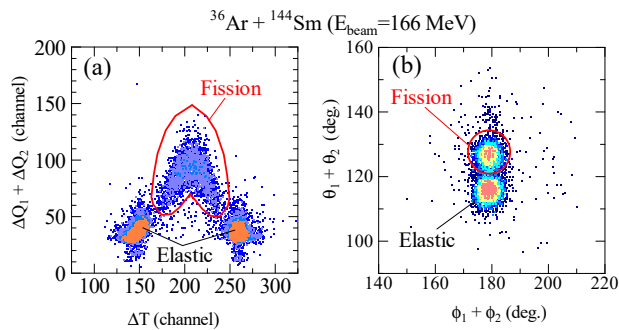
Figure 8. (Color online) a) Events from the fusion-fission reaction ^{36}Ar+^{144}Sm→^{180}Hg*, mapped on the $\Delta Q_1 + \Delta Q_2$ vs ΔT axes. Fission events within the polygon and elastic-recoil events are clearly separated. (b) Same as in (a) but in the coordinates $\theta_1 + \theta_2$ vs $\phi_1 + \phi_2$. Figure is taken from [124].

geous to obtain mass-angle distributions (MADs) of the fission fragments, especially in case of the QF mechanism, due to the asymmetry of the angular distribution in comparison to the fission of a fully equilibrated CN. An important feature of the 14UD pelletron at ANU is that it delivers a pulsed beam with a typical pulse width of $0.7-1.5$ ns, which can be used as a start signal for the independent measurement of velocities (thus, masses) for both fragments. From the measured masses of the FFs, A_i ($i=1,2$), the mass ratio $M_R = A_1/(A_1 + A_2)$ can be obtained. A typical resolution for M_R is reported as <0.02 [129].

Fission set-up at the IUAC Pelletron facility at Delhi. At the IUAC facility, two fission chambers have been developed for in-beam prompt-fission measurements [162]. In the General Purpose Scattering Chamber (GPSC), two MWPCs ($200{\times}100$ mm^2 each) are mounted on the rotating arms to cover a wide range of fission-fragment angles. To extract TOF information, a pulsed beam from the IUAC tandem with a bunch width of $\sim$1.1 ns is used [162, 158]. The second chamber hosts two MWPCs ($125{\times}75$ mm^2 each) covering the scattering angle of $\pm14°(X)$ and $\pm8°(Y)$ [162]. The TOF measurement for fission fragments can be performed by referring to the rf of the tandem-LINAC. This chamber can be coupled with the National Array of Neutron Detectors (NAND)[159], which consists of 100 liquid organic scintillators (12.7 cm-diameter, 12.7 cm-thickness), located at a distance of 175 cm from the target.

Fission set-up at the BARC-TIFR Pelletron LINAC facility, Mumbai. In the fission experiments at this facility, the coincident fission fragments are measured by two MWPC detectors, each of $126{\times}76$ mm^2 area, by exploiting the TOF method and referring to the rf of the accelerator as the start signal (width
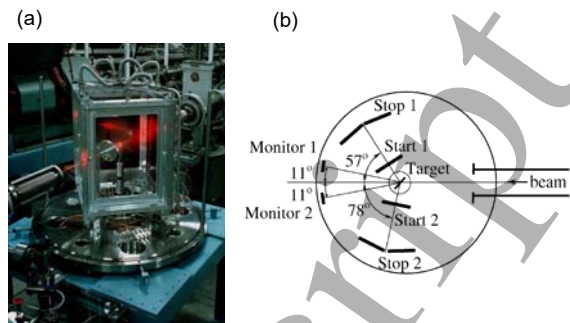
Figure 9. (Color online) Arrangements for the in-beam fission experiments at (a) CUBE at ANU and (b) CORSET at FLNR, see text for further details. The CUBE set-up consists of two large-area MWPCs [91]. The CORSET is a two-arm velocity-measurement system which uses small-area MCP-based start detectors (Start1 and Start2) and larger-area MCP-based detectors with a position-sensitive readout as the stop detectors (Stop1 and Stop2). Figure is taken from [143].

$\sim$1 ns) [160].

CORSET setup at FLNR, Dubna. The CORSET setup [144, 137], shown in Fig. 9(b), is a double-arm fission time-of-flight spectrometer which uses MCP-based timing detectors to provide both the start and stop signals in the double-velocity method. While a small-size start detector in the close vicinity to the target is used, a large-area MCP detector ($70{\times}90$ mm^2) coupled with a position-read-out scheme is exploited, which allows to determine also the emission angles of the fission fragments. The typical angular acceptance of the setup is $\Delta\theta_{Lab} \sim 28°$ [142, 144]. Due to the good timing resolution of $\sim$150 ps [144], the velocities of the fragments are determined independently with high accuracy. Taking advantage of the fast timing properties of the MCPs, the system provides a mass resolution of $\sim$3 u (FWHM), even with a relatively short flight distances of around $10-20$ cm.

3.1.2. Prompt multi-nucleon transfer-induced fission technique. The method of a direct few-nucleon transfer-induced fission by means of e.g. (d,pf), (^{3}He,pf) or (^{6}Li,df) reactions was introduced in fission research more than forty years ago [45, 163, 164, 165]. The initial studies concentrated predominantly on the measurements of fission probabilities and their excitation-energy dependence. In this method, the type, energy and scattering angle of the outgoing ejectile have to be measured in coincidence with the fission fragments, to determine the specific transfer channel, thus the fissioning nuclide. Under certain assumptions, the kinematic analysis of the reaction allows to determine the excitation energy of the fissioning nucleus. This approach is still actively used in the so-called 'sur-

CONTENTS 14

rogate' fission measurements, see recent examples in [166, 167, 168, 169, 170, 171] and the comprehensive review in [172].

One of the first examples of FFMD measurements via direct few-nucleon transfer was reported in [45] for the isotopes ^{227,228}Ac, studied with the ^{226}Ra(^{3}He,df)^{227}Ac and ^{226}Ra(^{3}He,pf)^{228}Ac reactions.

The development of heavy-ion accelerators capable of delivering heavier projectiles, coupled with the increased sensitivity of the detection systems to isolate specific transfer channels, allowed to extend the fission studies to more exotic nuclei, lying further away from stability. Several research groups around the world are active in this type of studies; below we will present the general ideas of the method by using an example from the JAEA research group, with a more detailed discussion of the results given in Section 4.3.

Since several years, a dedicated program to study MNT-induced fission is being conducted at the JAEA tandem facility by using the fission setup shown in Fig. 7 [75, 74]. The incident-beam energy is typically chosen at $\sim$1.7–1.8 times the Coulomb barrier, where the MNT reactions preferentially occur at forward scattering angles, which defines the geometry of the setup. The specific example of the ^{18}O+^{238}U reaction at the beam energy of 157.7 MeV was chosen for the follow-up discussion.

To identify the energy and the angle of the outgoing ejectile, a silicon ΔE-E telescope array is used. The energy loss in a relatively thin (75 μm/cm^2) ΔE detector with a very good thickness uniformity together with the registration of the residual energy E_{res} in a thicker 300 μm E detector allows to determine the type of the ejectile. Sufficient energy resolution for the kinetic-energy measurement of the outgoing particle is required to determine the excitation energy of the fissioning nucleus and the FFs masses from the subsequent kinematical analysis. For example, a $\sim$1% energy resolution of the ΔE detector is required to distinguish different oxygen isotopes (see Fig. 10), thus the same level of the thickness's uniformity of the silicon wafer is necessary, which is not easy to achieve for very thin detectors.

In the JAEA setup, twelve ΔE detectors are conically mounted around the beam axis. Each ΔE detector defines the range of azimuthal angle (φ) with an acceptance $\Delta\varphi = 22.5°$. The E detector has 16 annular strips with inner and outer radii of 24.0 mm and 48.0 mm, respectively, corresponding to the acceptance of $\theta = 16.7°$–31.0° with respect to the beam direction (the angular coverage is adjustable by moving the $\Delta E - E$ telescope along the incident beam axis).

Figure 10 shows an example of a two-dimensional ΔE-E_{total} spectrum for ejectile particles, measured at a forward angle of about 25° relative to the beam direction, where E_{total} is the sum of the energies ΔE and E_{res}. The spectrum clearly demonstrates several important features:

- Many transfer channels are open in such type of reactions, which allows to study the fission of $\sim$15 different fissioning nuclides in a single experiment at a single beam energy.

- Not only different ejectile elements, e.g. Li-O, can be easily distinguished, but also a clear separation of isotopes for each element can be reliably achieved, e.g. ^{16,17,18}O or ^{14,15,16}N, as examples. By assuming a binary process also in the exit channel and no emission of other light particles instantaneously during the reaction phase, one can therefore identify the isotope of the fissioning compound nucleus. For example, the observation of three oxygen isotopes ^{16,17,18}O as ejectiles indicates the population of the respective compound nuclei ^{240,239,238}U*. Overall, fission of a series of nuclei up to curium isotopes ($Z = 96$) was studied in this particular reaction by selecting specific oxygen, nitrogen, carbon, boron and beryllium isotopic lines.

- A wide range of kinetic energies of the ejectiles indicates a similarly wide range of the excitation energies reached by the compound nuclei. The maximum initial excitation energy reached in this study is about $60-80$ MeV, depending on the transfer channel, see Section 4.3. By selecting a specific narrower range of ejectile energies allows to determine a more narrow range in the excitation energy, which in turn allows to study the dependence of the FFMDs and/or of the fission probability on the excitation energy (see Section 4.3). The typical excitation-energy resolution in the JAEA experiments is $\sim$0.9 MeV (FWHM), which is mainly determined by the energy resolution for the ejectiles.

The latter point is illustrated by Fig. 11, which shows the fission events of ^{239}U* populated in the one-neutron pick-up reaction ^{238}U(^{18}O,^{17}O)^{239}U*, by gating on the isotopic line of the ^{17}O ejectile in Fig. 10. At the lower excitation energies, two localized regions are observed, corresponding to the light and the heavy fragment, while the structure is smeared out with the increase of the excitation energy. The FFMDs extracted from these data are shown in Fig. 12, where the data are plotted for a series of excitation-energy intervals of $\sim$10 MeV width. The latter are selected as a compromise between the statistics within each interval and the necessity to keep a reasonably narrow excitation-energy range to allow a reliable evaluation of the excitation-energy dependence of the FFMD's.
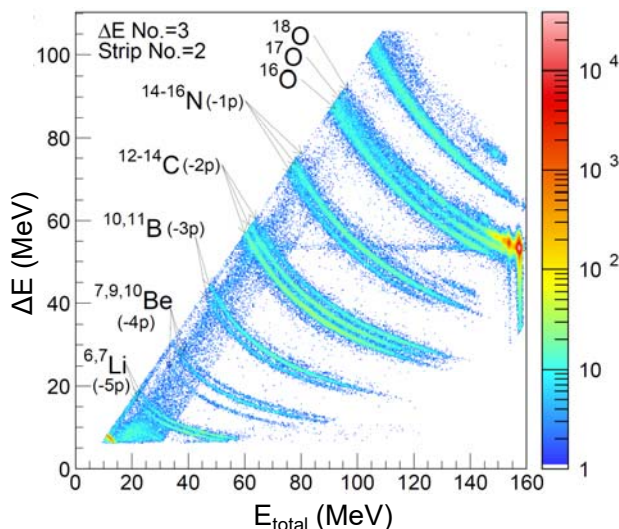
Figure 10. (Color online) ΔE-E_{total} spectrum for the reaction of ^{18}O + ^{238}U at $E_{beam} = 157.7$ MeV, measured at an angle of about $25°$ relative to the beam direction (defined by the strip of the annular silicon detector). Figure taken from [125].
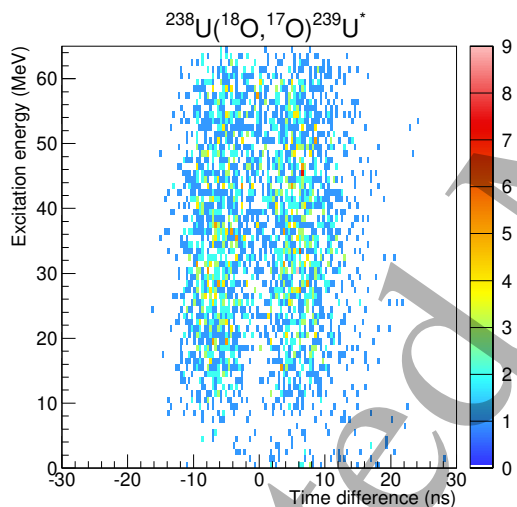
Figure 11. (Color online) The excitation energy of ^{239}U* versus the time difference ΔT between the fission fragments measured in the one-neutron pick-up reaction ^{18}O+^{238}U→^{17}O+^{239}U* [125].

To perform the benchmarking of the JAEA mass distributions, they are compared with the literature data from the reaction n+^{238}U [173], obtained at similar excitation energies. This comparison shows a fairly good agreement with the neutron-induced data, proving that the transfer reaction (^{18}O,^{17}O) can provide the FFMD data as a surrogate to the neutron-induced fission. Results for other transfer-reaction channels will be discussed in Section 4.3.
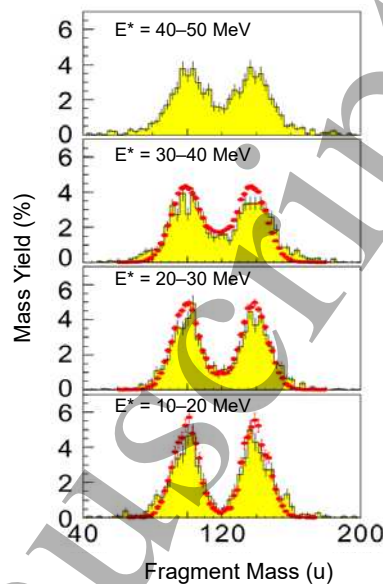
Figure 12. (Color online) The FFMD for ^{239}U* obtained from the one-neutron pick-up data ^{238}U(^{18}O,^{17}O)^{239}U* (black-line histogram) [125], projected from Fig. 11. The excitation-energy range is indicated in each spectrum. The red symbols show the data from the n+^{238}U reaction from [173]. Figure taken from [125].

3.2. Spontaneous and neutron-induced fission, the measurements of prompt fission γ rays and neutrons.

3.2.1.   2v- 2E 'double velocity - double energy' method for fission-fragment measurements.   This section briefly summarizes several techniques, which are applied in the studies of spontaneous fission and neutron-induced fission, where the fission-fragment energies are not distorted (or only weakly distorted) by the reaction mechanism itself. This is in contrast to fission studies in direct kinematics with heavy ions, as discussed in Section 3.1 and with reactions in inverse kinematics, further reviewed in Section 3.5.

A natural development of the above-mentioned $2v$ (double velocity) fission technique is the so-called $2v$- $2E$, 'double velocity - double energy' method, whereby the kinetic energies of both fragments are measured in addition to their velocities [174, 175, 176]. From the velocities, pre-neutron fragment masses can be determined, whereas those after the neutron emission (post-neutron masses) are derived from the energies. The FFs mass difference before and after the neutron emission gives the neutron multiplicity, $\bar{\nu}(A)$, as a function of fragment mass A. The advantage of this method is that no neutron detectors are required. This approach is usually applied only for fission at relatively low excitation energies, such as SF or neutron-induced fission, where the pre-scission neutron emission and/or 2nd (and higher-

CONTENTS　　　　　　　　　　　　　　　　　　　　　　　　　　　　　　　16
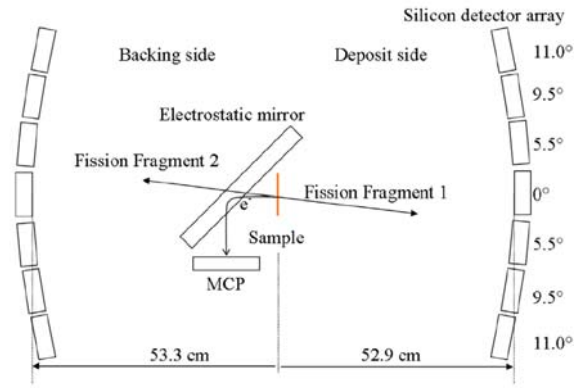
Figure 13. (Color online) The $2v$-$2E$ setup VERDI. Shown are the central FIssion Electron Time-of-flight Start (FIETS) detector and the two energy silicon detector spheres at the end of each time-of-flight section (not to scale). Fission fragments are detected by one of the silicon detector pairs, while the electrons, emitted by the target, are deflected by the electrostatic mirror into the micro-channel-plate (MCP) detector. Figure is taken from [98].

order) chance fission do not happen and thus do not contribute to the total uncertainty of the $\bar{\nu}$-value determination. However, to get sufficiently precise $\bar{\nu}(A)$ values via the FFs pre-neutron and post-neutron mass differences, high-precision measurements of both the velocities and energies are mandatory. In the past, a $2v$-$2E$ spectrometer, dubbed Cosi-fan-tutte [174], was operated with the neutron beams at ILL (Grenoble) and reached an excellent mass resolution of $\delta A/A = 0.6$ %, partially at the expense of a rather low efficiency of 4×10^{-5} [177]. The fragment velocities were measured using a start and stop time-of-flight system with channel-plate detectors in both arms of the spectrometer, while the fragment energies were measured with ionization chambers.

Nowadays, a revival in the development of the $2v$-$2E$ setups for (n,f) studies is clearly underway. As just one recent example, Fig. 13 shows the $2v$-$2E$ VERDI spectrometer (VElocity foR Direct mass Identification, [98]), built at the Joint Research Center-Institute for Reference Materials and Measurements (JRC-IRMM). VERDI uses a unique approach to provide the start signal, by using secondary electrons produced by FFs when they penetrate the fissioning target. A silicon-detector array is used to provide the stop timing signal and the energies. The design goal is to achieve a mass resolution of $A/\Delta A \sim 130$. Other recently developed $2v$-$2E$ spectrometers are the STEFF (SpecTrometer for Exotic Fission Fragments), built by the University of Manchester [178], and the SPIDER (SPectrometer for Ion DEtermination in fission Research) [179] at LANSCE (Los Alamos), which are exploited in neutron-induced-fission experiments, see Section 3.2.3 for further details.

3.2.2. *Measurements of prompt neutron and γ-ray decays from fission fragments.* The measurements of prompt fission neutrons and γ rays (e.g. energy spectra and multiplicities) provide very important nuclear data for atomic-energy applications. Recently, such experiments got a renewed interest following the needs for more precise data and also in view of the developments of the Generation-IV reactors. The advent of highly-efficient, multi-detector arrays both for the neutron and γ-ray measurements is one of the advanced features of modern fission studies, which substantially enhances the quality of the obtained data.

The γ-ray energy/multipolarity and multiplicity carry information on the spins of the fragments, which are important for understanding the mechanism of spin generation during fission. The sensitivity of the γ-ray measurements was significantly improved when the highly-efficient, multi-detector, $\sim 4\pi$ γ-ray calorimeters started to be used in fission studies. One of such systems is the Heidelberg-Darmstadt Crystall Ball (CB) [180, 181], built in the middle of 1980'ies, which consists of 162 large NaI(Tl) (20 cm long) detectors with high γ-ray detection efficiency ($>90\%$). Prompt fission γ-rays and neutrons can be distinguished via the time-of-flight measurements with a start signal from the fission detectors. For the latter, Frisch-gridded 4π twin ionization chambers were used [181, 182] for correlation measurement between fission fragments and γ-rays.

At ILL, the single-arm spectrometer LOHEN-GRIN detects only one fragment per fission event, and information on the population of excited states of the fission fragments is limited to states with at least $0.5\,\mu$s half-life that reach the focal plane before decaying. For a more holistic approach, a different type of spectrometer is required that can detect all prompt γ rays from both fission fragments, e.g. to extract complete excitation energy and spin distributions in both fragments and their correlations. As a first step in this direction, the recent EXILL campaign combined a well-collimated cold neutron beam, incident on ^{235}U or ^{241}Pu targets, with an efficient Ge detector array consisting of EXOGAM clovers from GANIL, LOHEN-GRIN clovers and GASP detectors from Legnaro [183]. Besides a wealth of new nuclear-spectroscopy information, this campaign also provided new data on the population of excited states in the fission fragments [184].

Several experiments use smaller set-ups, consisting of a few (2-4) γ-ray detectors of various sizes and properties, see specific examples in Sec. 4.6.2.

3.2.3. *Fission with neutron spallation sources at n_TOF at CERN, LANSCE at LANL, JSNS at J-PARC.* Since recently, powerful spallation neutron sources, based on a high-energy proton driver, became

CONTENTS 17

available for fission studies. Examples are the J-PARC at Japan Atomic Energy Agency/KEK (Japan) [185], LANSCE at LANL(US) [186] and the n_TOF facility at CERN (Geneva, Switzerland) [187], which are briefly described in this section. In these facilities, the spallation neutrons, after production in a heavy target, are directed to an external target of interest, where the γ-ray radiation and/or fission following capture reactions on the target are measured by relevant sets of detectors.

One of the main advantages of spallation neutron sources in respect of fission studies is that the fission properties can be measured as a function of incident-neutron energy using the time-of-flight technique; that is why the technique is usually called 'n-TOF'. The time-of-flight is usually derived from a start signal provided by the proton time-pulse structure (the moment of the proton impact on the target), while the stop signal is provided by the fission event itself. The maximum energy of the neutrons depends on the incident-proton energy, but the overall spectrum shape can be changed by a moderator, thus, it can be tuned for specific applications.

n_TOF facility at CERN. The n_TOF facility at CERN is a pulsed neutron source coupled to a 185 m flight path (EAR1) designed to study neutron-nucleus interactions for neutron kinetic energies ranging from a few meV to several GeV, the upper limit being defined by the initial proton beam energy of up to 20 GeV from the PS-CERN. A lead spallation target is usually used. The number of neutrons per a typical proton pulse varies between 5.5×10^5 and 1.2×10^7, depending on the collimator/moderator configuration [188]. Recent examples of fission cross-section measurements for the reactions n+^{245}Cm and n+^{237}Np can be found in references [189, 190]; the fission fragments were measured with a Fast Ionization Chamber [117]. In some cases, PPACs were used, which allow to measure the FFs angular distribution relative to the neutron-beam direction, in addition to the cross-section measurements. For capture (n,γ) reactions, a 4π total-absorption calorimeter consisting of 40 BaF$_2$ crystals is used [191].

For measurements with very exotic target materials, which are difficult to produce in a large quantity, a shorter beam line with a flight path of 18.5 m (EAR2 beam line) was recently developed [192], which allows a much higher neutron flux on the target, at the expense of a more limited neutron-energy range. Several measurements were already performed since 2014 at EAR2, including fission cross-section measurements for n+^{240}Pu, while those for n+^{237}Np are planned for 2016.

Some experiments at n_TOF use the recently developed two-arms 2v-2E fission spectrometer STEFF [178], which is presently installed at the EAR2 flight path. A single common start signal for the fragments's TOF measurements is provided by a single MCP detector in one of the arms, while the stop signals are given by two MWPC secondary-electron mirror stop detectors. At the end of each arm (behind the MWPCs), Bragg ionization chambers are mounted to determine both the kinetic energy and the nuclear charge of the fragments. A resolution of $\Delta Z = 2$ (FWHM) [193] was obtained for the light group of FFs, while the mass and energy resolutions were reported as $\Delta A \sim 4$u and $\Delta E \sim 1$ MeV, respectively [178]. The central fission chamber is surrounded by a symmetric array of 12 NaI detectors to measure prompt fission γ rays. The first experiments with STEFF have already started with the n+^{235}U reaction.

LANSCE at LANL(Los Alamos) The Los Alamos Neutron Science Center (LANSCE) [194] uses a 800 MeV pulsed proton linear accelerator to produce spallation neutrons for basic and applied science at two target stations. At the Weapons Neutron Research facility (WNR), the neutron beam is generated by impinging the accelerated protons (with nominal current of 4 μA) into an unmoderated tungsten spallation target, which produces a "white" neutron spectrum with a usable range from about 100 keV to hundreds of MeV [195]. At the Lujan Center, moderated spallation is used to generate neutrons from subthermal energies up to a few hundreds of keV [195]. Several fission experiments have been performed at LANSCE, including for example fission-cross-section measurements for the reactions n+^{240,242}Pu [195], using parallel-plate ionization chambers. An another example of fission measurements is an ongoing study of total kinetic energy (TKE) in the fission of actinides and its dependence on incident-neutron energy. Recent work on TKE for the reaction ^{235}U(n,f) [108] was performed at WNR using silicon PIN photodiodes.

In addition to the compact radiation detectors mentioned above, several unique setups are available at LANSCE for nuclear-science programs [196], offering various types of fission measurements, as summarised below.

- A highly-efficient, highly-segmented Detector for Advanced Neutron Capture Experiments (DANCE) [197, 198, 199, 200] is one of the most advanced detector systems in the world for γ-ray measurements following neutron-capture and/or fission. DANCE is a γ-ray calorimeter, consisting of a spherical array of 160 BaF$_2$ crystals, covering a total solid angle of approximately 3.5π steradians. The array has a single-γ-ray efficiency of 85–88% and a cascade efficiency of

over 95%. Despite having an inferior energy resolution in comparison to some other types of modern γ-ray detectors, DANCE is well suited for a better characterization of the full γ-ray emission spectrum and γ-ray multiplicity. The fission trigger is given by a compact PPAC installed inside the BaF_2 array [201]. The PPAC has the advantage that it can handle high α-decay rates ($\sim 2.4 \times 10^8$ /s), and provides good timing resolution (~ 1.7 ns) for the measurement of the time difference between the fission signals from the PPAC and the γ-ray signals from DANCE.

- The SPIDER (SPectrometer for Ion DEtermination in fission Research) is a two-arm $2v$-$2E$ fission spectrometer [179]. Each arm of the spectrometer consists of two MCP-based timing detectors (the larger stop detector is position sensitive) - for FFs's velocity measurements and an ionization chamber for their energy determination. The intrinsic mass resolution of SPIDER is expected to reach $\Delta A = 1$ u. A new, 16-arm version of SPIDER is currently being constructed, and will be used to study fast-neutron-induced fission at LANSCE [202].

- The Chi-Nu [203, 204] consists of two neutron-detector arrays installed at WNR to measure the prompt fission-neutron spectra as a function of incident-neutron energies. One array consists of 54 organic liquid scintillators [196] and is used to measure fission neutrons with energies in excess of 500 keV, while the other array includes 22 ^{6}Li-glass detectors to detect low-energy neutrons below 1 MeV [204] down to ~ 50 keV. The Chi-Nu detector system uses double time-of-flight to measure the incident and emitted neutron energies. The time-of-flight of the prompt fission neutrons are obtained from a PPAC which provides a start signal when fission occurs, and a 'stop' signal from the neutron scintillation detectors. The time-of-flight distance is 100 cm for the liquid-scintillator array and 40 cm for the ^{6}Li glass scintillator array.

- A GErmanium Array for Neutron-Induced Excitations (GEANIE), located at a 20-meter flight path port at the WNR, consists of 20 high-purity germanium detectors with BGO escape-suppression shields [196]. The time-of-flight technique is used to make measurements such as capture cross sections in the energy range from hundreds of keV to hundreds of MeV.

- The time-projection chamber (TPC) at LANSCE (diameter ≤ 15 cm$\times$length 30 cm) [205] is exploited for high-precision fission-cross-section measurements. This is a particle-tracking detector that uses fission-product tracking information

to reduce systematic uncertainties compared to more conventional detectors used for fission-cross-section measurements.

JSNS facility at J-PARC, Tokai, Japan. The Japan Spallation Neutron Source (JSNS) [206] at the J-PARC facility started its operation in 2008. A 3 GeV proton beam bombards a mercury target at a repetition rate of 25 Hz to generate spallation neutrons. One of the neutron beam lines, called Accurate Neutron-Nucleus Reaction measurement Instruments (ANNRI) [207, 208], is designed for neutron-induced reaction studies as well as other applications. Measurement stations are located at 21.5 m and 27.9 m from the moderator. For the measurement of capture cross sections, an array of Ge detectors (shorter-distance TOF path) [209] and two large-volume NaI crystals (longer-distance TOF path) [210, 211] are installed.

Presently, due to J-PARC's safety requirements any radioactive target material must be sealed in a capsule, which makes FFs detection impossible. Still, the measurements of fission cross sections can be performed by detecting prompt fission neutrons escaping the sealed target. This was demonstrated in the reaction n+^{241}Am using liquid scintillation detectors mounted at the 21.5 m-station, where the pulse-shape-discrimination technique was applied to separate prompt fission neutrons and prompt γ rays [212]. An advantage of this method is that this method allows to perform the measurements in the presence of very strong background from α decays of short-lived isotopes. In the future, after getting the licence to use open sources of actinide materials, it is planned to measure fission data (e.g. fragment mass and angular distributions) for resonances with different J^π values.

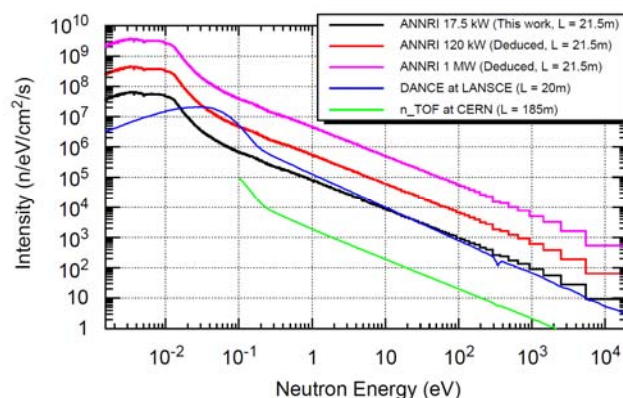**Figure 14.** (Color online) Available neutron intensity at the sample positions at ANNRI(J-PARC), n_TOF at CERN [191] and DANCE at LANSCE [213]. The ANNRI spectra, which were deduced under the 120 kW operation in the 2009 Japanese fiscal year and the expected spectrum under the future 1 MW operation, are shown also. The figure is taken from [208].

Figure 14 shows the energy dependence of the

CONTENTS   19

neutron intensity obtained at the ANNRI's target station. Several curves show the proton-beam-power dependence of the neutron flux, which is expected to reach a maximum at 1 MW in future. In this figure, also the neutron intensity at n_TOF(185 m) [191] and DANCE at LANSCE (20 m, neutron flight path 14 (FP14) in Lujan Center) [213] are shown.

3.3. Current photofission experiments with γ-ray beams, Compton-backscattered γ-ray sources for fission.

Absorption of a photon by a nucleus can trigger the fission of the latter via the process dubbed 'photofission'. Historically, the bremsstrahlung-induced fission of actinides has often been exploited, but this approach does not allow the tuning of the γ-ray energy, see e.g. the recent bremsstrahlung-induced fission study of ^{232}Th by using a recoil catcher and an off-line γ-ray spectrometric technique [55]. In such experiments, only integral fission yields could typically be measured, whereby the fission cross section has to be convolved with the spectral intensity of the γ-ray beam, resulting in a typical effective γ-ray bandwidth $\Delta E/E$ in a range of $(4-6)\times10^{-2}$, as quoted in Ref. [214].

The recent progress in accelerator and laser physics has provided an opportunity to obtain tunable, high-flux, quasi-monoenergetic γ-ray beams via Compton backscattering (CBS) of eV-range photons from powerful lasers off a relativistic electron beam. This technique allows to overcome most of the previous limitations in terms of beam intensity and energy resolution.

CBS γ-ray beam sources in the MeV energy region have been developed for example at the NewSUBARU, Hyogo, Japan [215, 216] and HIγS at Triangle Universities Nuclear Laboratory (TUNL, Durham, US) [217].

In a recent ^{238}U(γ,f) experiment at the HIγS facility, the photofission cross section of ^{238}U was measured at sub-barrier energies [214]. The CBS γ-ray beam had a relatively modest bandwidth of $\Delta E = 150-200$ keV and a spectral flux of about $10^2 \gamma/$(eV s). An array of PPACs, comprising 23 electrolytically deposited ^{238}UO$_2$ (2 mg/cm^2) targets was used to measure the photofission cross section.

One of the advantages of the CBS γ-ray beams is a possibility to reach an almost 100% linearly polarized beam. Using the HIγS source, the polarization asymmetry, being the difference between the in-plane and out-of-plane prompt-fission-neutron yields relative to the polarization of the γ-ray beam, was recently measured [218, 219] by using an array of 18 liquid scintillation detectors. Polarization asymmetries were found to be almost zero for the photofission of ^{233,235}U,
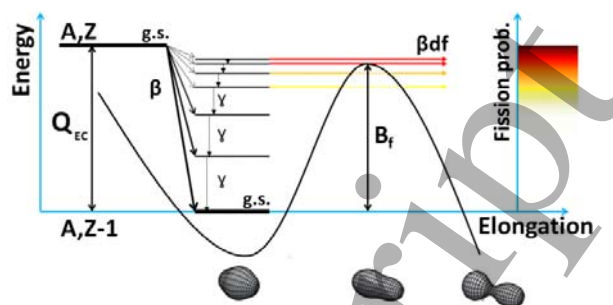
Figure 15. (Color online) Schematic representation of the βDF process on the neutron-deficient side of the Nuclidic Chart. The Q_{EC} value of the parent (A, Z) nucleus is indicated, while the curved line shows the potential energy of the daughter $(A, Z-1)$ nucleus with respect to nuclear elongation, displaying also the fission barrier B_f. The color code on the right-hand side represents the probability for excited states, with excitation energies close to B_f, to undergo fission; the darker colors correspond to higher probabilities.

^{237}Np, and ^{239}Pu, whereas significant asymmetries were detected for ^{232}Th, ^{238}U and ^{240}Pu.

3.4. β-delayed fission with stable and radioactive beams

β-delayed fission is another mechanism, which can provide low-energy fission data for nuclei far away from the β-stability line, see the recent review in Ref. [10]. Since this review, several new developments happened, which will be briefly discussed in this section.

βDF is a two-step nuclear decay process, see Fig. 15, in which the parent nucleus first undergoes β decay, populating excited state(s) in the daughter nuclide. In the case of neutron-deficient nuclei, electron capture (EC) and/or β^+ decay are considered (referred further as β^+/EC), while β^- decay happens on the neutron-rich side of the Nuclidic Chart. If the excitation energy of these states, E^*, is comparable to or greater than the fission-barrier height, B_f, of the daughter nucleus $(E^* \sim B_f)$, then fission may happen instantaneously in competition with other decay modes, e.g. γ decay and/or particle emission (neutron, proton or α), depending on which side of the β-stability valley the parent nucleus is situated. A special feature of βDF is that fission proceeds from excited state(s) of the daughter nuclide, but the observed time behavior of the βDF events is determined by the half-life of the parent nucleus (as with e.g. β-delayed γ and particle decays). As in most cases the β-decay half lives are longer than tens of ms, it makes βDF more easily accessible for experimental studies.

In βDF, the *maximum* excitation energy of the daughter nucleus is limited by the Q_{EC} ($Q_{\beta-}$ in case of neutron-rich nuclei) of the parent. The typical Q_{EC} ($Q_{\beta-}$) values are in the range of $3-6$ MeV and $9-12$

CONTENTS 20

MeV for the known βDF nuclei in the trans-uranium and lead regions, respectively. Thus, the distinctive importance of βDF is highlighted by its ability to provide *low-energy* fission data for very exotic nuclei, which do not decay by SF and which are difficult to access by other techniques.

The calculated fission-barrier heights for the corresponding daughter isotopes are typically in the range of $5-8$ MeV and $8-12$ MeV in the respective uranium and lead regions, see Fig. 2. This means that most of the presently studied βDF nuclei have negative Q_{EC}(Parent)-B_f(Daughter) values, see Table 1 of Ref. [10], whereby mostly excited states below the top of the fission barrier are populated by the β decay. This leads to a predominantly sub-barrier fission, which is one of the reasons why the βDF probabilities are typically quite low, often in the $10^{-6}-10^{-2}$ range [220]. The other reason for this could be the specific β-decay feeding pattern (the β-decay strength function S_β). The strong sensitivity of the βDF probability on the Q_{EC}(Parent)-B_f(Daughter) value can be used to estimate the fission-barrier height, see the recent study in Ref. [221] for details and references to this method, and also on its application to βDF of ^{180}Tl.

One particular drawback of the βDF studies is that only odd-odd (thus, even-A) nuclides are expected to have this decay mode. Indeed, so far the βDF of 29 odd-odd isotopes was observed [10], including the recent identification of βDF in ^{230}Am at the gas-filled separator GARIS (RIKEN) [222, 223], and in ^{236}Bk and ^{240}Es at the gas-filled separator RITU (JYFL) [224]. This is, first of all, due to the odd-even staggering in the masses which makes the Q_{EC} values of the odd-odd isotopes larger than those of their odd-A or even-even neighbors. Secondly, after the β decay of an odd-odd parent, an even-even daughter is produced, which usually has a higher probability to fission in comparison to its odd-A or odd-odd neighbouring isotopes ♯

In the last decade, a substantial progress was achieved in the βDF studies in the neutron-deficient lead region, some of the results will be reviewed in Section 4.1. As mentioned above, the recent Coulex-induced fission experiments by the SOFIA collaboration also provided first complementary low-

♯ Nuclei with odd numbers of protons and/or neutrons are known to have longer spontaneous-fission half-lives than their even-even neighbours [225, 226]. This observation has been attributed to three different effects: (i) An extra energy (specialization energy [227, 228]) that is required to find a transition state at the barrier with quantum numbers (spin, parity and spin projection on the symmetry axis), matching those of the ground state, (ii) an increase in the inertial parameter with the number of unpaired nucleons [228], and (iii) an increase in the pairing gap at the barrier top compared to the energy gap in the ground state.

energy fission data in the same region, see Fig. 22 and Ref. [11]. Finally, the fusion-fission reactions with heavy ions can also be used to study the same nuclides, but the accessible excitation energies are higher, starting from typically $\sim$30 MeV, due to the Coulomb barrier in the entrance channel. However, they allow to probe the excitation-energy dependence of the FFMDs [124, 229], which is hardly possible in βDF and Coulex-induced fission studies. The complementarity of the three approaches will be further highlighted in Section 4.

β**DF with stable beams in direct kinematics.** Since $\sim$1995, βDF studies by the Berkeley group with stable beams in direct kinematics allowed to perform investigations of the neutron-deficient isotopes ^{242,244,246,248}Es [230, 107, 231]. In particular, the FFMD measurements for the neutron-deficient nuclides ^{242,244}Es could be achieved, confirming their asymmetric mass split, as for most of the nuclei in this region. The discovery of βDF of ^{186,188}Bi [232] and ^{192,194}At [233] was reported in experiments at the velocity filter SHIP (GSI). In the recent experiments at the gas-filled separator GARIS (at RIKEN, Wako), four βDF decays of the new isotope ^{230}Am were reported, which was produced after α decay of ^{234}Bk, studied via the complete-fusion reaction ^{40}Ar+^{197}Au$\rightarrow$^{234}Bk+3n [222]. In a follow-up dedicated experiment at GARIS, ^{230}Am was directly produced in the reaction ^{27}Al+^{207}Pb$\rightarrow$^{234}Am+4n [223]. The nuclei of interest were implanted in a position-sensitive silicon detector, where their subsequent decays were measured. Nineteen events attributed to βDF of ^{230}Am could be identified, and the βDF probability of $P_{\beta DF}(^{230}$Am$)=0.3(1)$ was reported, being the highest so far among all measured βDF nuclei. By using a similar technique, the βDF of ^{236}Bk and ^{240}Es were recently discovered at the RITU gas-filled separator [224].

β**DF with low-energy radioactive beams at ISOLDE(CERN).** Since about one decade, a new technique to study βDF nuclei in the lead region was developed at the mass separator ISOLDE [234], by using the low-energy $30-60$ keV radioactive beams. This method allows to extend low-energy fission studies to very exotic neutron-deficient (in the future, also neutron-rich) nuclei, which are difficult to access by other techniques, see however the above comment on the recent Coulex-induced fission experiment by the SOFIA collaboration.

For consistency of the discussion, only a short description of these experiments is given here, we refer the reader to Ref. [10] for a detailed discussion, and in particular to the recent studies by Ghys *et al* [17, 220]
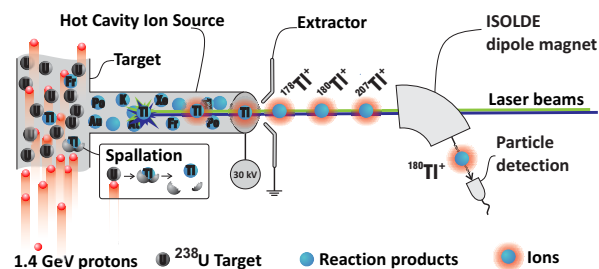
CONTENTS   21

Figure 16. (Color online) Schematic view of the ISOLDE and RILIS operation as applied in the βDF study of ^{180}Tl [16]. The 1.4-GeV 2 μA proton beam impinges on a thick 50 g/cm^2 ^{238}U target, producing a variety of reaction products via spallation and fission reactions. The neutral reaction products diffuse towards the hot cavity, where the thallium atoms are selectively ionized to the 1^+ charge state by two overlapping synchronized laser beams, precisely tuned to provide thallium ionization in a two-color excitation and ionization scheme. The ionized thallium ions are extracted by the high-voltage potential of 30 kV, followed by the $A = 180$ mass separation with the ISOLDE dipole magnet. The mass-separated ^{180}Tl ions are finally implanted in the carbon foils of the Windmill system, for subsequent measurements of their decays with the silicon and germanium detectors, as described in the main text. Plot modified from [237].

which were published since the review work.

As an example, Fig. 16 provides a brief overview of the production method of the isotope ^{180}Tl in the pilot βDF study at ISOLDE [16]. A novel and unique feature of this βDF experiment was the combination of selective ionization of a specific element (Tl, in this case) with the Resonance Ionization Laser Ion Source (RILIS) [235, 236] and subsequent mass separation at $A = 180$ with ISOLDE. This allowed to obtain a uniquely clean source of the desired parent nucleus with fully determined Z and A values. After selective ionization, acceleration up to 30 keV, and mass separation, a pure beam of ^{180}Tl with an intensity of $\sim$150 ions/s was analyzed by the Windmill (WM) detection system [16]. Here, the radioactive beam was deposited on a thin carbon foil, surrounded by two silicon detectors (Si1 and Si2), along with HPGe detectors for coincident particle–γ-ray measurements. The use of two silicon detectors in a compact geometry allowed both singles α/fission decays and double-fold fission-fragment coincidences to be efficiently measured. The same method was later used for βDF studies of ^{178}Tl [87], ^{192,194,196}At [233, 17, 88] and of ^{200,202}Fr [17]. A detailed discussion of the results will be given in Section 4.

3.5. Fission in inverse kinematics

3.5.1. Coulomb-induced fission with secondary relativistic beams at GSI The description in this section is essentially valid for all low-energy fission experiments performed up to now with secondary projectile frag-

ments at relativistic energies, although the detection set-up was continuously developed and extended to improve the resolution and to cover additional observables.

When ^{238}U beams with sufficiently high energies (around 1 A GeV) became available at the BEVALAC of LBNL, Berkeley (in 1982) and at the SIS18 synchrotron of GSI Darmstadt (in 1990), several exploratory experiments were performed to develop suitable experimental methods for studying the fission process. These earlier experiments mainly aimed to determine the fission cross sections by electromagnetic and nuclear interactions in different targets and to measure the corresponding fission-fragment nuclide production cross sections [238, 239, 240, 241, 242, 243, 244, 245, 246, 247, 248].

The first comprehensive experiment on low-energy fission induced by electromagnetic excitation in inverse kinematics on 70 fissioning systems was performed in 1996 with relativistic secondary beams, produced from a 1 A GeV ^{238}U primary beam [40] at GSI, Darmstadt. In 2012, following a series of technical developments, this method was further extended in the SOFIA experiment by using a large dipole analyzing magnet [71, 11]. The SOFIA detector equipment, in particular the time-of-flight and tracking detectors, was considerably upgraded. A position resolution of 200 μm (FWHM) and a time resolution of 40 ps (FWHM) were obtained [71]. This experiment also profited from a higher ^{238}U primary-beam intensity, which amounted to several 10^9 projectiles per second, compared to a few times 10^7 projectiles per second in the preceding experiment. The higher beam intensity allowed measurements with higher statistics and the investigation of a larger variety of fissioning systems.

While the 1996 experiment mentioned above [40] has been fully analyzed, and all results have been published, the SOFIA experiments [71, 11, 28] are still under analysis, and, therefore, only some first results are presented in this review.

Reaction mechanisms. Fission experiments with relativistic heavy-ion beams often have to consider or even explicitly make use of several reaction mechanisms. For example in the SOFIA experiment, a two-stage scenario is employed, with the aim to exploit specific characteristics of different reactions pertinent to each stage. Firstly, the nuclear interactions with the nuclei in the first (production) target serve to produce relativistic secondary beams of a large number of fragmentation residues. In the second stage, these secondary products are excited in the Coulomb field of a heavy nucleus at impact parameters that are large enough to avoid nuclear interactions. The excitation-energy distribution induced by the electromagnetic

excitation is given by the Fourier transform of the time-dependent Coulomb field of the target nucleus seen by the projectile and the energy-dependent photo-absorption cross section of the projectile. The total calculated initial excitation-energy distribution and the one of events ending up in fission are shown in Fig. 17 for the case of a relativistic ^{236}U secondary beam impinging on a ^{238}U target in the SOFIA set-up. The mean initial excitation energy of fission events amounts to about 14 MeV. Thus, this method is well suited for low-energy fission studies of nuclei with fission barriers below this value. Large part of the distribution which has a width of 5 MeV (standard deviation) is below the threshold of multi-chance fission.
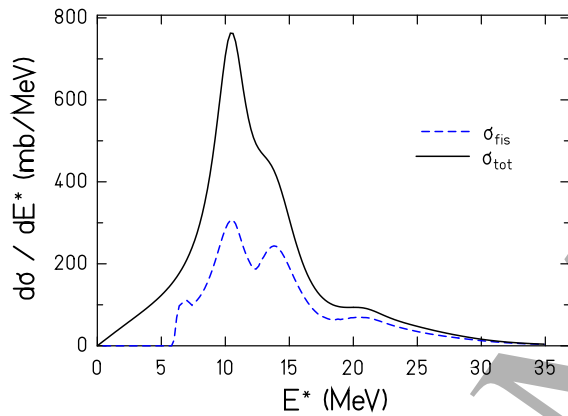

Figure 17. (Color online) Calculated excitation-energy distribution of the secondary projectiles ^{236}U, induced by electromagnetic excitation in a ^{238}U target at an energy of 670 A MeV (full line). In addition, the calculated distribution that leads to fission is shown (dashed line). Higher-chance fission (after emission of one or several neutrons) is included. The calculation has been performed by L. Grente [249].

Experimental set-up. Fig. 18 shows the production of the secondary beams at the FRS of GSI as it was used in the SOFIA experiments on low-energy fission in inverse kinematics [71, 11, 28]. This part of the experimental set-up is very similar to the one used in the 1996 experiment [40], except that in that experiment the fission set-up was mounted directly behind the FRS.

The secondary projectiles with a typical energy of about 700 A MeV, after leaving the FRS, impinge on a high-Z secondary target, where they are Coulomb-excited and fission in-flight. In the 1996 experiment, this target consisted of five lead plates, while two plates of depleted uranium and one lead plate were used in the SOFIA experiment. In the SOFIA experiment, additional aluminum plates were mounted

for subtracting the contributions from nuclear-induced fission that also occur in the high-Z targets, while in the 1996 experiment a scintillator detector was used for this purpose. Because the fission fragments are emitted in a narrow cone in forward direction, both fragments are measured in coincidence with a high efficiency, which amounted to 90% in the most recent SOFIA experiment [11].

The set-up used for the SOFIA experiment [71, 11] is shown in Fig. 19. Compared to the previous GSI experiment [40], the additional analysis of the deflection in the large dipole magnet ALADIN allowed to determine the masses of the fission fragments in addition to their nuclear charge.

Identifying fission induced by nuclear interactions. For exploiting the *low-energy* electromagnetic excitations in fission experiments, *higher-energy* excitations by nuclear interactions must be suppressed in the data analysis, because the impact parameter cannot directly be measured. Most part of the nuclear interactions leads to a loss of nucleons. The loss of protons prior to fission can be detected by summing up the proton numbers of the two detected fission fragments Z_1+Z_2, because the probability for the emission of protons from the excited fragments after scission is very low in most cases. Thus, a condition that $Z_1 + Z_2$ is equal to the Z value of the initial fissioning secondary nucleus eliminates most of the fission events induced by nuclear interactions. Moreover, the nuclear interactions in the regime of limiting fragmentation depend only weakly on the size of the target nucleus, while the electromagnetic excitations grow strongly with increasing nuclear charge of the target nucleus. For light targets, such as beryllium or aluminum, nuclear interactions dominate largely, and electromagnetic interactions are negligible. Thus, the remaining fraction of nuclear-induced fission events that fulfill the condition on Z_1+Z_2 can be subtracted by determining the height of the $Z_1 + Z_2$ distribution measured with the light target, after adjusting this distribution in the lower-Z part to the distribution measured with the heavy target. This procedure is illustrated in Fig. 20.

The $Z_1 + Z_2$ filter was also applied by Rubehn *et al* at the ALADIN dipole magnet for determining the fission contributions from nuclear and electromagnetic interactions [242, 243], and for determining the cross sections for charge pick-up and consecutive fission [244], for ^{238}U projectiles at 600 and 1000 A MeV in different targets.

We would also like to mention that the abrasion process in fragmentation reactions produces highly excited exotic nuclei with rather low angular momenta. The excitation energy amounts to about 27 MeV per abraded nucleon on the average [250], and the angular-
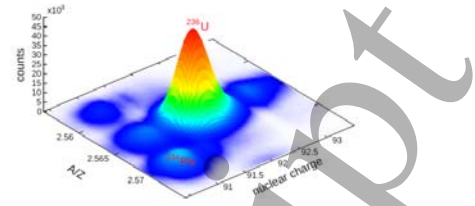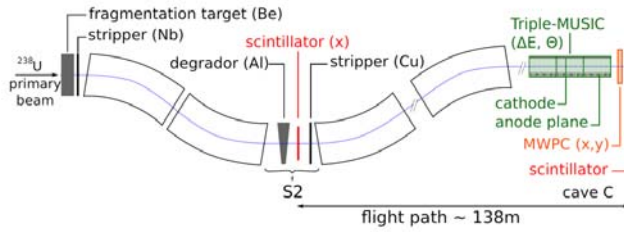
Figure 18. (Color online) Left part: Schematic view of the FRS that provided the radioactive beams for the experiments in inverse kinematics at GSI, Darmstadt [40, 71, 11, 28]. A multitude of different radioactive nuclides is produced by the fragmentation of a $1\,A\,\text{GeV}$ ^{238}U primary beam in a thick beryllium target. The isotopes of interest are separated and identified by the FRS, and are further sent to a dedicated set-up for the actual secondary-beam experiment. The figure refers to the SOFIA experiments, where the fission set-up is located in another experimental area (Cave C). Right part: Two-dimensional identification diagram of the secondary beam for an ion-optical setting on ^{236}U. The figure is taken from Ref. [28].
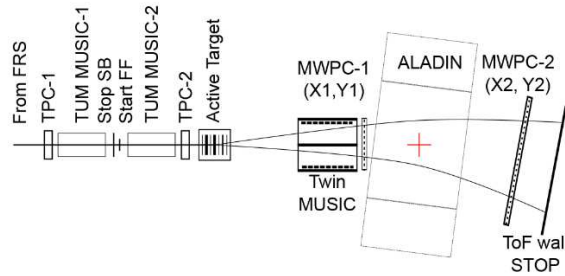

Figure 19. (Color online) Experimental set-up of the SOFIA experiment on low-energy fission in inverse kinematics [71], performed with secondary beams from the fragment separator FRS of GSI, Darmstadt. Two time-projection chambers (TPC1 and TPC2) are installed for tracking the secondary-beam projectiles, two multiple-sampling ionization chambers (MUSIC-1 and MUSIC-2) provide energy-loss measurements and additional tracking information, and an active target, consisting of several depleted uranium, lead and aluminum target plates mounted in an ionization chamber, allows confining the analysis to fission induced in specific target layers. Two multi-wire proportional chambers measure the vertical and the lateral positions of the fission fragments, and the twin MUSIC gives energy-loss and additional tracking information. The start detector (Start FF) and the ToF wall provide start and stop signals of the time-of-flight measurement for determining the velocities of the fission fragments. The figure is taken from Ref. [11] with kind permission of The European Physical Journal (EPJ).
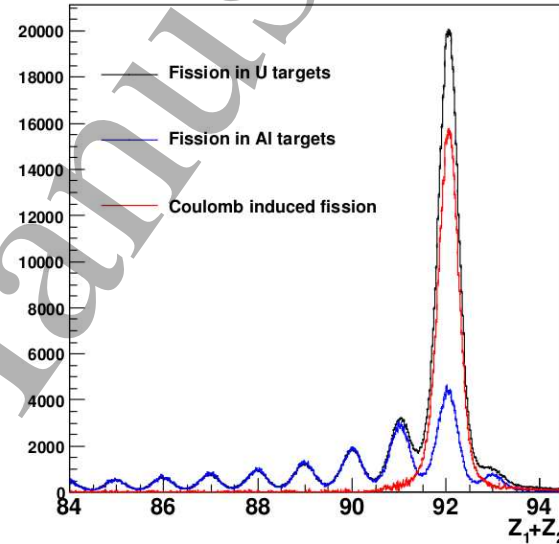
Figure 20. (Color online) Charge-sum $Z_1 + Z_2$ spectrum of the fission fragments produced in the aluminum targets (blue histogram) and in the uranium targets (black histogram) from a ^{236}U secondary beam in the SOFIA experiment. The blue histogram has been normalized in order to represent the fraction of nuclear-induced fission in the uranium targets at $Z_1 + Z_2 = 92$. The difference spectrum (red histogram) is the deduced contribution from electromagnetically induced fission in the uranium targets. The figure is taken from Ref. [252].

momentum distribution hardly reaches values above $20\,\hbar$ [251]. These conditions are well matched for investigating fission as a function of excitation energy up to very high values without being disturbed by the additional influence of high angular momenta that is unavoidably introduced in heavy-ion fusion reactions. This is an important aspect for studying the influence of dissipation on the fission process. Experiments of this kind are discussed in Section 4.7.

Choice of fissioning systems. A primary beryl- lium target was used for the production of the sec- ondary projectiles, because it provides a large interac-

tion rate for a given energy loss of the primary beam. The nuclides produced by fragmentation in a heavy tar- get material cover practically all known isotopes of all elements over the whole chart of the nuclides [248, 253] up to the mass of the primary ^{238}U projectile.

An impression of the variety of nuclides, available as secondary projectiles for the SOFIA experiment with a ^{238}U primary beam, is obtained from Fig. 21. This figure shows the measured production cross sections of spallation products from the reaction $^{238}\text{U} + {}^2\text{H}$ at $1\,A\,\text{GeV}$ [254]. According to model calculations with INCL4 [255] coupled with ABLA07 [256], the cross sections of nuclei with $Z \approx 78$ and
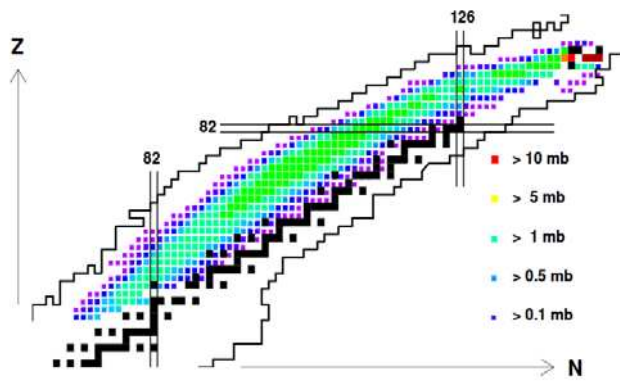
Figure 21. (Color online) Measured formation cross sections of spallation residues, produced in the reaction ^{238}U $(1\,A\,\mathrm{GeV})$ + ^{2}H, are shown on a chart of the nuclides, see text for details. Primordial nuclides are marked by black squares. A few neutron-rich isotopes of uranium, protactinium and thorium (altogether four) with large cross sections were not measured. The figure is taken from Ref. [254].

Figure 22. (Color online) Excerpt of the nuclide chart. Primordial nuclides are marked by black squares, colored squares represent fissioning systems measured during the first SOFIA experiment. The warmer the color, the higher the statistics. Most of the time was invested in the uranium region, while only short test runs were performed for the lighter systems. The experiment revealed good experimental conditions for all systems for studying electromagnetic-induced fission. The figure is taken from Ref. [11] with kind permission of The European Physical Journal (EPJ).
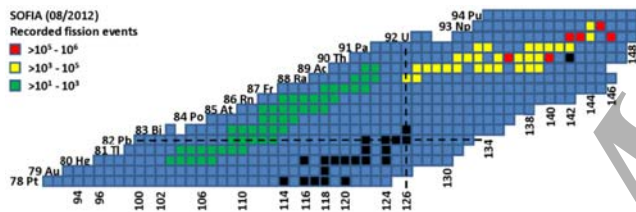
heavier are very close to the ones produced in a beryllium target, for which comprehensive data are not available.

Figure 22 shows the specific regions of nuclei, which were studied with SOFIA. So far, the main focus of the SOFIA experiment was on the Ac to Np region with $N \geq 126$, were data with good statistics have been obtained for several tens of nuclides. Only a limited time was spent on lighter systems in the neutron-deficient lead region, which are also produced with high intensities as secondary beams according to Fig. 21. Already this first study showed that the Coulex-induced fission experiments at SOFIA are feasible with a large number of nuclides in this region of the chart of the nuclides, which further extends and enriches the data provided by the βDF and prompt-fission studies, see discussion in Section 4.
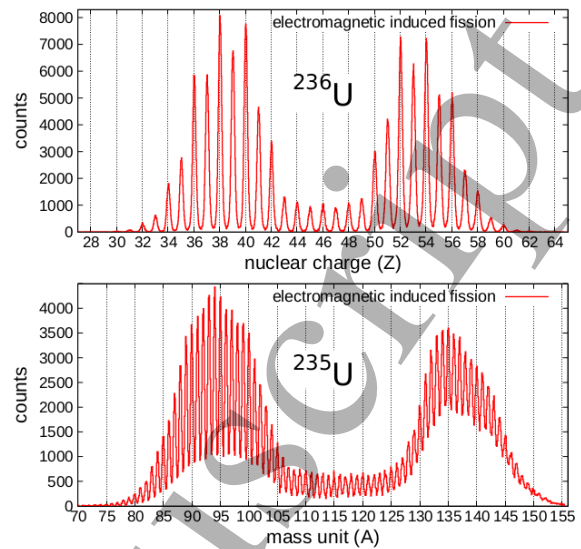
Figure 23. (Color online) Upper part: Element distribution obtained for the ^{236}U(γ,f) reaction [249]. Lower part: Mass distribution obtained for the ^{235}U(γ,f) reaction [11]. The figure is taken from Ref. [28].

Resolution of kinematical measurements. The measurement of the nuclear charge of all fission fragments with their full resolution can only be obtained using inverse kinematics at relativistic energy. Since at such high energy all ions are fully stripped, their ionic charge obtained by the energy-loss ΔE gives a direct measurement of the nuclear charge Z. Moreover, the energy loss is not affected by fluctuations caused by ionic-charge-changing processes.

The Z resolution in such experiments with ions at relativistic energies also strongly profits from the fact that δ electrons, which are produced with velocities up to about twice the ion velocity, do not contribute to the ionization signal [257], because their long ranges exceed the size of the Twin MUSIC, and from an additional suppression of the ionization via primary high-energetic electrons by appropriate pulse shaping.

The main difficulty of the SOFIA experiment lies in the measurement of the mass number, since it requires a large-scale detection system to combine the energy-loss measurement of the heavy ion (a fission fragment) with its time-of-flight (TOF) and its tracking through a magnetic field that yields the magnetic rigidity $B\rho$. With these three observables, the mass A of the fission fragment can be deduced using the so-called ΔE - TOF - $B\rho$ method, based on the following equation: $A/Z \propto B\rho/(\beta\gamma)$, where β is the ion velocity relative to the speed of light and γ is the Lorentz factor. The immense effort that was invested to obtain a good mass resolution is documented in Ref. [71].

In the most recent SOFIA experiment [28], the

CONTENTS   25
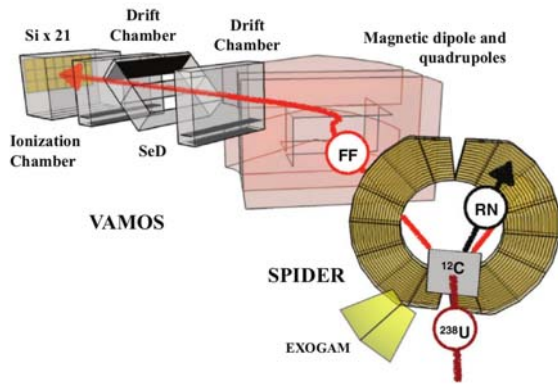
Figure 24. (Color online) Set-up of the fission experiments in inverse kinematics at the VAMOS spectrometer after transfer and fusion reactions using a 6.1 A MeV beam of ^{238}U. The figure is taken from Ref. [84].

Figure 25. (Color online) Identification of target-like nuclei in the SPIDER telescope in the VAMOS fission experiments. The energy loss in the ΔE detector is plotted on the vertical axis. The factor $\cos(\theta)$ accounts for the different effective thicknesses crossed by the target-like nuclei emitted at different angles θ. The total kinetic energy is represented on the horizontal axis. Experimental data are shown in coincidence with the detection of a fission fragment in VAMOS. The figure is taken from Ref. [39].

elemental distribution of the system ^{236}U$(\gamma,$f$)$ was measured with a resolution (FWHM) of 0.35 charge units. The mass distribution was measured with a resolution (FWHM) of 0.6 mass units in the light fragment group and 0.8 mass units in the heavy fragment group. The upper part of Fig. 23 shows the measured element distribution, while the mass distribution from this experiment is not yet available, and the distribution for the system ^{235}U$(\gamma,$f$)$ originating from the previous experiment [11] is shown in the lower part of Fig. 23 instead.

3.5.2. Multi-nucleon-transfer-induced fission with a ^{238}U beam at VAMOS(GANIL) The MNT-induced fission technique, presented in Section 3.1.2, has recently also been employed in inverse kinematics. It was the idea of Fanny Farget to perform fission studies with this technique at GANIL in inverse kinematics using a ^{238}U beam at Coulomb energies. The aim was to identify the fission fragments in Z and A with appreciably better resolution than it can be achieved with a system that fissions essentially at rest as e.g. in SF/βDF or at low energy as in reactions in direct kinematics induced by light particles. To widen the choice of fissioning systems to be studied, a carbon target was used as light reaction partner instead of hydrogen and helium isotopes that are often exploited in experiments in direct kinematics.

Experimental set-up Figure 24 shows the set-up of the experiment that was performed at GANIL. A primary ^{238}U beam of 6.1 A MeV impinges on a ^{12}C target, resulting in both prompt fusion-fission and transfer-induced fission. The VAMOS spectrometer [83] is used to isotopically identify one fission fragment per fission event. Similar to the MNT detection

setup at JAEA, described in Section 3.1.2, a ΔE-E telescope SPIDER (Silicon Particle Identification DEtector Ring), is used to select the outgoing ejectile, which both determines the fissioning nucleus (from U to Cf), and allows to deduce its excitation energy. This is demonstrated in the $\Delta E - E$ spectrum shown in Fig. 25. Compared to a similar identification plot shown in Fig. 10, measured in direct kinematics at JAEA, the resolution of different isotopes is less pronounced. A new measurement with an active target that provided a much better resolution [258] showed that this difference can be attributed to the quality of the detection system, e.g. to inhomogeneities of the SPIDER ΔE detector.

This set-up corresponds in an ideal way to the kinematical properties of the reaction products: the annular $\Delta E - E$ telescope covers most part of the angular range that is populated by the light transfer (target-like) residues, while its central hole lets pass most of the fission fragments, which are kinematically forward-focused. The VAMOS spectrometer covers part of the angular distribution populated by the fission fragments that contains fragments over the whole range of mass and kinetic energy, according to its large acceptance.

Choice of fissioning systems In a specific projectile-target combination, a limited number of nuclides (about 10 nuclides with a ^{12}C target) is produced by strong transfer channels, which makes them accessible to fission experiments. While the choice of heavy primary projectiles is limited to ^{238}U and eventually very few other (primordial) cases, post-accelerated
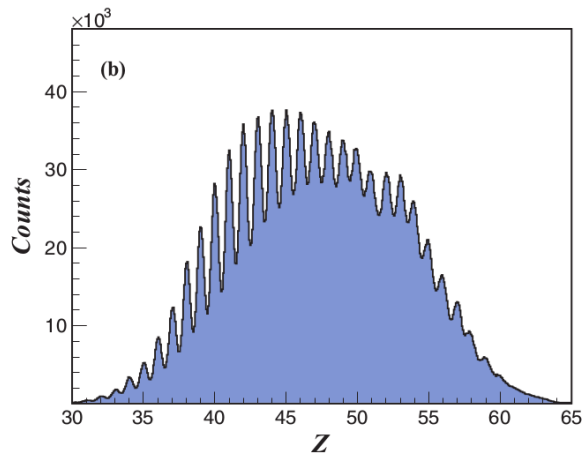
Figure 26. (Color online) Z resolution obtained for fission fragments from the fusion of $6.1\,A\,\mathrm{MeV}$ ^{238}U projectiles with ^{12}C, measured at the VAMOS spectrometer. The Z distribution is summed over the contributions from all ionic charge states. The figure is taken from Ref. [84].

beams of heavy radioactive nuclides provided in future by an ISOL-based secondary-beam facility could appreciably extend the choice of fissioning nuclei to be studied by transfer-induced fission in inverse kinematics (see Section 5).

Definition of excitation energy   Like in the MNT reactions in direct kinematics (see Section 3.1.2), by determining the kinetic energy and the angle of the light residue (target-like) product, the total excitation energy of the system can be deduced with a good precision by momentum conservation and energy balance.   In the present experiment, the annular $\Delta E - E$ detector provides this information and allows to determine the total excitation energy with an uncertainty of 2.7 MeV. The probability that part of this excitation energy appears in the light target-like residue grows with its mass, because the number of levels in the corresponding energy range increases. This causes an additional uncertainty on the excitation energy of the fissioning system. This problem has been tackled by measuring the γ-ray radiation emitted from the excited light transfer product by a Ge detector array mounted close to the target [39].

Resolution of kinematical measurements.   In VAMOS measurements, the mass distributions were obtained with a resolution below 0.8 mass unit (FWHM) and elemental distributions with a resolution around $\Delta Z/Z = 1.5\%$ (FWHM) [84]. As an example, the Z distribution of fission fragments from the fusion-fission reactions, summed over all ionic charge states, is shown in Fig. 26. The resolution deteriorates slightly
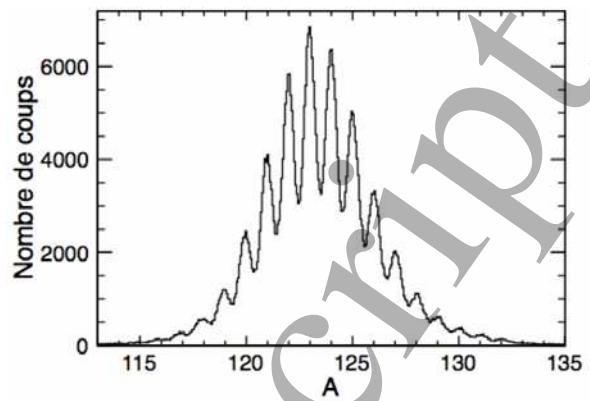
Figure 27. Mass resolution obtained for fission fragments with $Z = 50$ from the fusion of $6.1\,A\,\mathrm{MeV}$ ^{238}U projectiles with ^{12}C, measured at the VAMOS spectrometer. The figure is taken from Ref. [259].

towards the heavier fragments. Fig. 27 shows the mass resolution for fragments with $Z = 50$. Despite different Z and A are not fully resolved, the yields can be determined from a fit to the corresponding measured distributions.

Due to good resolution in Z and A of the fission fragments and with the help of the excitation-energy measurements in the MNT reactions, this experimental approach is the first one to allow studies of the charge polarization (the N/Z degree of freedom) and the odd-even effect in fission-fragment nuclide distributions (in Z and N) as a function of excitation energy over the whole fission-fragment range.

4. Discussion

This section provides a review of selected results on fission, which were obtained since $\sim$1995. Four main regions of interest will be discussed (see also Fig. 5), each of them characterized by a different extent of the previous knowledge, different requirements to the fission data and experimental techniques applied.

- The neutron-deficient nuclei in the lead region (Au-Fr isotopes), with the neutron-to-proton ratio of $N/Z \sim 1.25 - 1.4$, which is quite different from that for the typical fissile nuclei in the heavy actinides (e.g. $N/Z \sim 1.56$ for ^{236}U). This region was barely studied so far by the fission techniques, therefore any fission data, even with a relatively poor mass resolution, are very much welcome. The complementary fission data provided by the low-energy βDF at ISOLDE and Coulex-induced fission at SOFIA(GSI) on the one hand and higher-energy fusion-fission reactions at a number

CONTENTS   27

of facilities around the world (see Section 4.1) on the other hand became available in the last decade.

- The nuclei in the vicinity of ^{235}U. This is by far the most-studied region of fission, where extensive data (also calculations and evaluations) exist, including on FFMDs, on γ-ray and neutron multiplicity, and energy-spectra measurements. Driven mostly by the requirements of the nuclear-reactor industry, the higher-precision data are the goal of the modern fission studies in this region. The SOFIA experiment is one of the key new facilities which is able to provide such data. Some of the present and future facilities will be discussed in Section 5.

- The region of the minor actinides lying somewhat north-east of ^{235}U. The understanding of their properties is of importance both for the future Accelerator Driven Systems (ADS) and also to the nuclear-waste management. While a number of isotopes was already studied in some details, the advances in the experimental techniques, e.g. the use of surrogate and/or MNT reactions will allow to extend these investigations to even more exotic, neutron-rich nuclei (see Section 4.3.)

- The broad region above ^{235}U, up to the heaviest nuclei with $Z = 118$ presently known, where several important fission phenomena occur. In particular, the recent data on SF and superheavy elements (SHE) will be summarised in Section 4.4. These data allow to probe the predictions of different theory models at the furthest limits of the nuclei existence, crucially mapping the borders of deformed and spherical shell effects in this region. The modern recoil separators utilizing high-intensity heavy-ion beams along with sensitive detection systems are used in these experiments [36, 260]. At present, complete-fusion reaction in heavy-ion collision is the only mechanism to produce superheavy elements, where fusion-fission and quasifission compete in the reaction. Orientation effects †† on the quasifission process will be discussed in Section 4.5.

4.1. Mapping fission in the neutron-deficient lead region by means of βDF, relativistic Coulex and prompt-fission techniques

4.1.1. New island and a new mechanism of asymmetric fission around ^{180}*Hg.* In this section, the recent results of the βDF experiments at ISOLDE will be discussed, in which βDF of ^{178,180}Tl [16, 262, 87], ^{194,196}At and ^{202}Fr [17, 88] was studied, resulting in the

††Orientation effect, see [261] for a review, refers to the influence of the deformation of the target nucleus on the reaction mechanism.

low-energy fission data for the daughter (after β decay) isotopes ^{178,180}Hg, ^{194,196}Po and ^{202}Rn, respectively.

Historically, the first βDF study at ISOLDE was performed for the isotope ^{180}Tl, whose production method was described in Section 3.4. The available $Q_{EC}(^{180}\text{Tl}) = 10.44$ MeV, while the calculated fission barrier is $B_f(^{180}\text{Hg}) = 9.81$ MeV, thus $Q_{EC}(^{180}\text{Tl})$-$B_f(^{180}\text{Hg}) = 0.63$ MeV, allowing for some above-barrier fission to happen. Despite this, a rather low βDF probability of $P_{\beta DF}(^{180}\text{Tl}) = 3.2(2) \times 10^{-5}$ was deduced [10]. The top panel in the leftmost column of Fig. 28 shows the two-dimensional Si1-Si2 energy plot of coincident FFs of the daughter isotope ^{180}Hg. The dominant asymmetric fission of ^{180}Hg is clearly demonstrated by a double-humped structure seen in this plot, with practically no events in between the peaks, which would otherwise correspond to the symmetric mass split. The respective single-peaked and quite narrow Gaussian-like TKE distribution, depicted in the middle panel of the same column, indicates that a single fission mode dominates in ^{180}Hg. Finally, the deduced clearly asymmetric FFMD is depicted in black in the bottom panel, whereby the most probable fission fragments were found in the vicinity of ^{80}Kr and ^{100}Ru. In a follow-up experiment [87], the βDF of ^{178}Tl was studied, whereby the mass-asymmetric fission of the daughter ^{178}Hg was observed. These two experiments established the new region of mass-asymmetric fission in the extremely neutron-deficient mercury isotopes, in addition to the previously known one in the transactinides.

This discovery caused an intense interest from the theory community, whereby very different approaches, such as the macro-microscopic model by Möller *et al* [16, 263, 264], two modern versions of the scission-point model [265, 266, 267, 268] and two fully self-consistent models, HFB-D1S and HFB-SkM* [269, 270], were used to shed light on the observed phenomenon. A new mechanism for the asymmetric fission of ^{178,180}Hg was proposed [16, 263], which is not driven by the strong shell effects of the final fragments. The latter is the typical situation in the fission of transactinides, where the strong shell effects in the range of the heavy fragments are responsible for the asymmetry.

In the following, a few selected examples of calculations are discussed in some details, while we refer the reader to the respective studies for a full description of the models used. In the βDF study of ^{180}Tl [16], the five-dimensional (5D) macroscopic-microscopic model [271] was applied to explain the observed asymmetric mass split of the fission fragments of ^{180}Hg. In a follow-up study [263], the two-dimensional potential-energy surfaces (PES) for ^{180}Hg and ^{236}U, extracted from the 5D-model, were discussed to analyze the differences in the nature of asymmetric
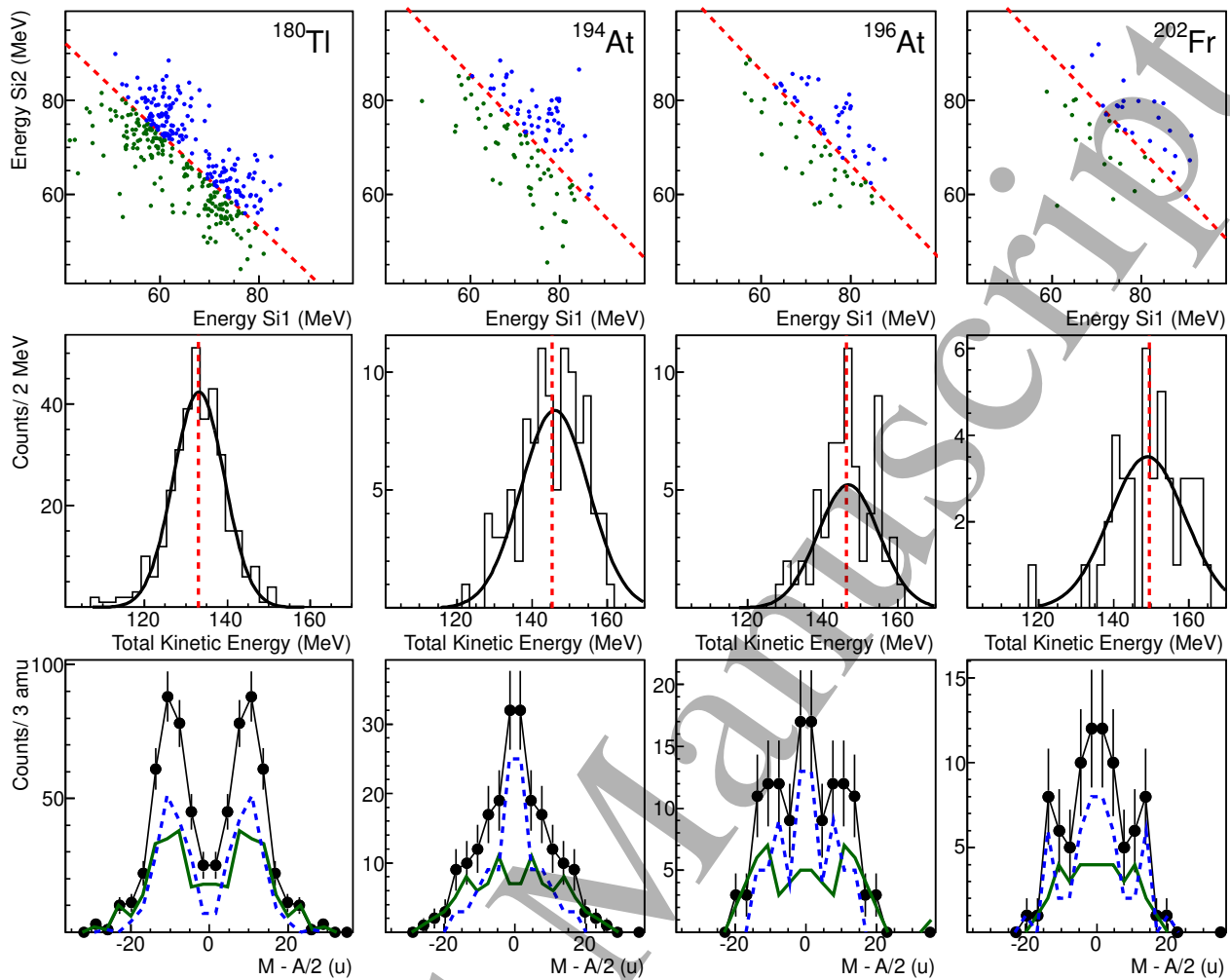
Figure 28. (Color online) Summary plot of the ISOLDE experiments to study βDF of ^{180}Tl, ^{194,196}At and ^{202}Fr. 2D energy distribution of coincident FFs in 2 silicon detectors (top), total kinetic energy (middle) and mass distributions (bottom) of investigated nuclei are shown. The green and blue curves represent data below and above the average TKE values for each case shown by the red dashed lines in the first and second rows of the plot. Details are given in the main text. Figure is taken from [17].

fission for proton-rich nuclei in the lead region compared to the more familiar actinide region, see Fig. 29.

The PES for ^{236}U shows features common to many actinide nuclei with $226 \leq A \leq 256$ (compare also to the PES of ^{238}U from another calculation shown in Figure 1), such as a deformed ground state, a relatively low two- or three-humped fission barrier, and most prominently, well-separated symmetric ($\alpha_g = 0$) and asymmetric ($\alpha_g \sim 0.2$) valleys. The latter valley is usually attributed as being due to the strong shell effects (spherical and/or deformed) of fission fragments in the vicinity of the double-magic ^{132}Sn. Fission starts from the left at the hexadecapole-deformed ground state, passes through the nearly symmetric first saddle point to the symmetric fission-isomer minimum. Then the mass asymmetry begins to increase as the nucleus passes over the mass-asymmetric second saddle point,

through a shallow third minimum, and finally over a third asymmetric saddle at the head of the asymmetric valley to a shape near the asymmetric scission point The higher symmetric saddle reduces the probability of entering the symmetric valley by requiring barrier penetration for systems with near-threshold energies.

For ^{180}Hg, shown in the bottom panel of Fig. 29, the PES is very different, with only a single pronounced symmetric valley corresponding to separated semi-magic ^{90}Zr nuclei, and no deep asymmetric valley extending to scission. The dominant symmetric valley is inaccessible due to the high barrier along the symmetric path from the ground state. The symmetric valley remains separated from a shallow asymmetric valley by a high ridge in the potential. A similar result can also be seen in Fig. 30, which shows the PES calculations within the HFB-SKM* approach [270], which will be further discussed in Section 4.1.3.
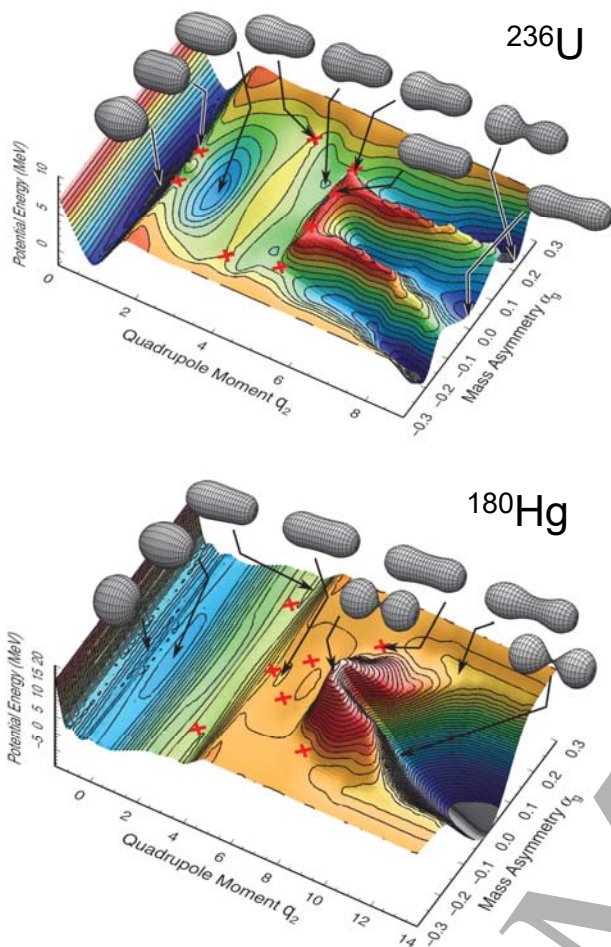
Figure 29. (Color online). Calculated PES surfaces for ^{180}Hg and ^{236}U, as a function of the dimensionless quadrupole moment and the mass asymmetry. The shapes of the nuclei at several key deformations are drawn, connected to the points on the surface by arrows. The plots are modified from [263].

Figure 30. (Color online) Ground-state potential-energy surfaces for (a) ^{180}Hg and (b) ^{198}Hg in the (Q_{20}, Q_{30}) plane calculated in HFB-SkM*. The static fission pathway aEF corresponding to asymmetric elongated fragments is marked. The figure is taken from [270].

Further extensive calculations of the mass yields for 987 nuclides were performed in Ref. [272] by using the Brownian shape-motion method [273] and performing random walks on the previously calculated five-dimensional potential-energy surfaces [271]. One of the aims of this study was to establish theoretically whether ^{178,180}Hg represent separate cases of asymmetric fission in this region, or whether they belong to a broad contiguous region of asymmetric fission, and if so, its extent. Fig. 31 shows the map of expected asymmetric and symmetric fission, whereby a broad island of asymmetric fission in the neutron-deficient lead region is predicted. In agreement with the experimental data, this new region of asymmetric fission also includes ^{178,180}Hg, though they are predicted to lie on its left-most border, with a smooth transition to symmetric fission expected for lightest Hg isotopes. Furthermore, this island is separated from the classical location of asymmetric fission in the actinides by an extended area of symmetric fission.
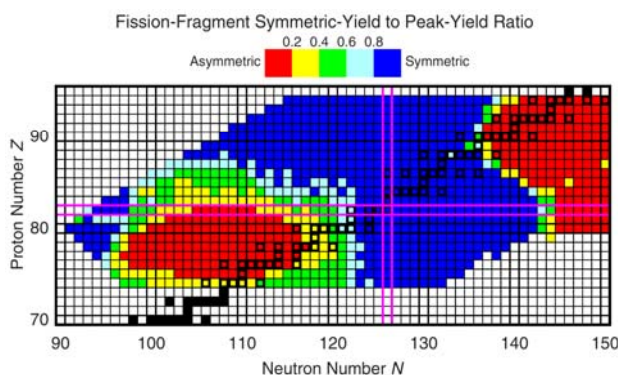
Figure 31. (Color online) Calculated symmetric-yield to peak-yield ratios for 987 fissioning systems. Black squares (open in colored regions, filled outside) indicate β-stable nuclei. Two extended regions of asymmetric fission are drawn in the red color, the one in the left bottom corner is the predicted region of a new type of asymmetric fission and includes ^{178,180}Hg, while the previously known asymmetric fission region in the heavy actinides is seen in the top right corner. The region of predominantly symmetric fission in between is shown in blue. The figure is taken from [272].

For a comparison with the measured FFMDs in the neutron-deficient lead region, Fig. 32 shows a

CONTENTS   30

subset of the calculated data from Fig. 31, but in the mass-yield representation, with selected examples (solely due to the space limitation) of the measured FFMDs. A good agreement between measured and calculated FFMDs can be noted for many nuclides, shown in the plot, e.g. for ^{180}Hg, ^{201}Tl, ^{210}Po, ^{204,208}Rn, ^{210}Ra. On the other hand, one also notices a clear discrepancy for e.g. ^{195}Au, for which a strongly asymmetric mass division is predicted, while experimentally a symmetric mass split was observed, see also [17] for further details. We will repeatedly come back to the discussion of different aspects of Figs. 31 and 32 further on in the text.

The asymmetric mass split of ^{178,180}Hg also raised the following four questions, addressed in details in Sections 4.1.2-4.1.3.

• How does the transition from the asymmetric fission of ^{178,180}Hg happen by moving along the mercury chain to the heavier isotope ^{198}Hg, for which a predominantly symmetric mass split was observed in the earlier light-particle-induced fission experiments by Itkis et al [13, 14, 15], see Figs. 5 and 32.

• How does the asymmetric FFMD of ^{180}Hg change with an increase of the excitation energy? This and the above question led to the complementary in-beam fusion-fission experiments at JAEA [124] and ANU [229] along the mercury isotopic chain.

• How does the transition from the asymmetric fission of ^{178,180}Hg occur by moving along the diagonal line in Fig. 32 towards the region of the heavier nuclides ^{204,208}Rn and ^{210}Ra, for which a predominantly symmetric mass split was observed in the first Coulex-induced low-energy fission experiment at FRS [40, 41]. To answer this question, the low-energy fission studies of nuclei in the thallium-to-astatine region with the neutron numbers around $N\sim102$–116 were recently performed by further βDF experiments at ISOLDE [17, 88] and via the Coulex-induced fission at SOFIA [11].

• How will the FFMDs evolve by moving 'down south' from ^{180}Hg, e.g. along the $N=100$ isotones, which can be investigated by complete-fusion reactions with heavy ions, see the recent study of ^{179}Au in Ref. [160].

4.1.2. $Multimodal$ $fission$ and $asymmetric$-to-$symmetric$ $transition$ in the $region$ $between$ ^{180}Hg and $^{210}Ra.$ To answer the third question, the βDF studies of ^{194,196}At and ^{202}Fr were subsequently performed at ISOLDE [17, 88]; the results are shown in the second-to-fourth columns in Fig 28. Similar to the above-discussed case of ^{180}Hg, the top row of these columns

shows the two-dimensional Si1-Si2 energy plots of co-incident FFs of ^{194,196}Po and ^{202}Rn. The respective full kinetic-energy spectra and the deduced mass distributions are shown in the middle and bottom rows of Fig. 28, respectively. In contrast to ^{180}Hg, a single broad hump is seen in the 2D energy distribution of ^{194,196}Po and ^{202}Rn. In addition, TKE distributions are significantly broader compared to the ^{180}Hg reference, as can be concluded from the standard deviation values, extracted from single-Gaussian fits, see [17] for details. Mass spectra, drawn in black, exhibit a mixture of symmetry with asymmetry.

The indication of triple-humped FFMDs and the breadth of the extracted TKE distributions suggest the presence of at least two distinct fission modes in these nuclei, each having different mass and TKE distributions. This feature was therefore further investigated by discriminating between fission events with high or low TKE, similar to the method used in Refs. [47, 48] to illustrate the bimodal fission in the transfermium region. In Fig. 28, FFMDs of fission events with respectively higher or lower TKE in comparison to a certain threshold energy E_{thres} are shown by respectively the dashed blue and full green lines. The value E_{thres} was arbitrarily taken as the mean TKE value and is indicated by a dashed red line on the TKE distributions and the 2D energy plots. Remarkably, the ^{194,196}Po cases exhibit a narrow symmetric distribution for fragments with higher TKE, while a broader, possibly asymmetric structure is observed for lower TKE. In contrast, this feature is absent in ^{180}Hg in which only one asymmetric fission mode was identified. In the case of ^{202}Rn, statistics prohibit drawing definitive conclusions.

These results establish a multimodal fission for these three isotopes, lying in the transitional region between the asymmetry of ^{178,180}Hg and symmetry of e.g. ^{204,208}Rn and ^{210}Ra. Self-consistent PES calculations performed within the HBF-D1S framework [270] provide a clear insight in the underlying reasons for the occurrence of the multimodal fission in this region. As an example, Fig. 33 shows PES for ^{196}Po, where two distinct competing paths - an asymmetric and symmetric - are marked. Beyond $Q_{20} = 250$ b, the PES flattens in such a way that a mildly asymmetric fission pathway competes with the symmetric pathway, which allows multimode fission to happen.

Such a flat, relatively structure-less PES is expected to represent quite a general behavior of PES's in this region of nuclei, and it is very different from the typical PES's in the actinides, where a dominant asymmetric valley is usually present, as discussed in respect of Fig. 29. Clearly, the outcome of any FFMD calculations on such flat PES's will strongly depend
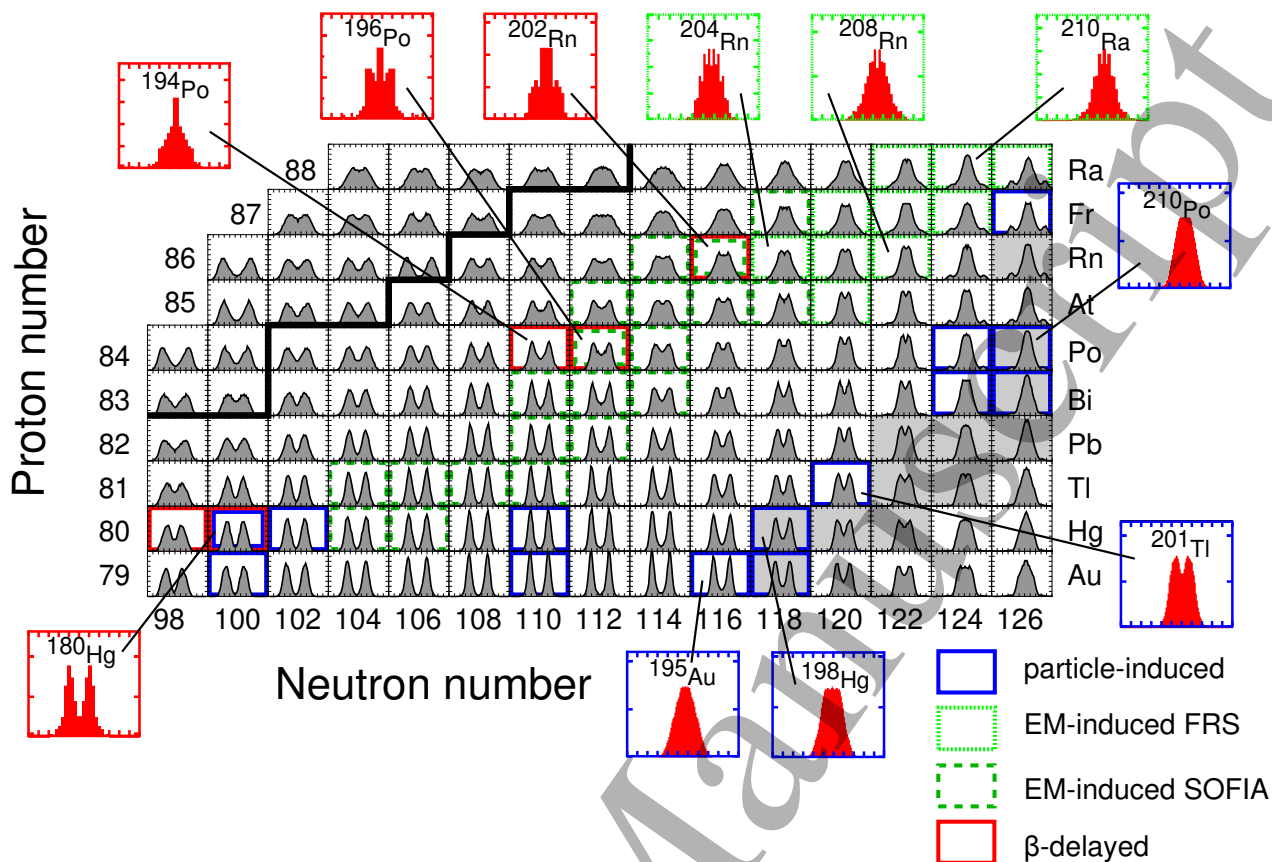
Figure 32. (Color online) Calculated FFMDs (gray), with fission-fragment masses on the horizontal and their relative yields on the vertical axis, for even-N neutron-deficient isotopes between gold and radium at excitation energies slightly above the theoretical fission-barrier heights $B_{f,th}$ from Ref. [9]. The calculated yields are compared with selected experimental MDs from particle-induced (blue symbols, [14, 15]), βDF (red, [16, 87, 17]) and EM-induced fission from FRS (green, [40, 41]) and SOFIA (dashed light green, [11]. The isotopes ^{180,190}Hg [124], ^{182}Hg [229] and ^{179,189}Au [160], recently measured by fusion-fission reactions are also marked in blue. The border of the lightest known isotopes is shown by the thick solid line, β-stable nuclei are shown on a gray background. Figure is modified from [17].

on specific details of a subtle and complex interplay between several degrees of freedom, including a yet not fully understood dependence on the excitation energy.

Unfortunately, due to relatively low fission rates of only up to some tens fissions per hour in the present βDF experiments at ISOLDE, no further details could be extracted, unless much longer experiments are performed. In this respect, experiments at the SOFIA setup [11] have all potential to establish a complementary way for fission studies in this region. One of the main advantages of SOFIA is its access to all types of nuclides - odd-odd, even-even and odd-A, while only the odd-odd cases can be studied via βDF, see Section 3.4. The feasibility of this approach was already confirmed by the first SOFIA campaign, which reached some of the neutron-deficient Hg isotopes, see Figs. 22 and 32.

4.1.3. Asymmetric-to-symmetric transition along the chain of mercury isotopes, from ^{180}Hg to ^{198}Hg To
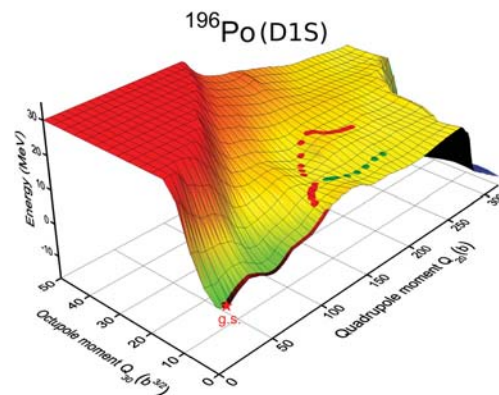
Figure 33. (Color online) Ground-state PES for ^{196}Po in the (Q_{20},Q_{30}) plane calculated in the HFB-D1S approach. Two competing fission pathways corresponding to different mass asymmetries are marked. The figure is taken from [270].

study the evolution and excitation-energy dependence of the FFMDs along the mercury chain, the
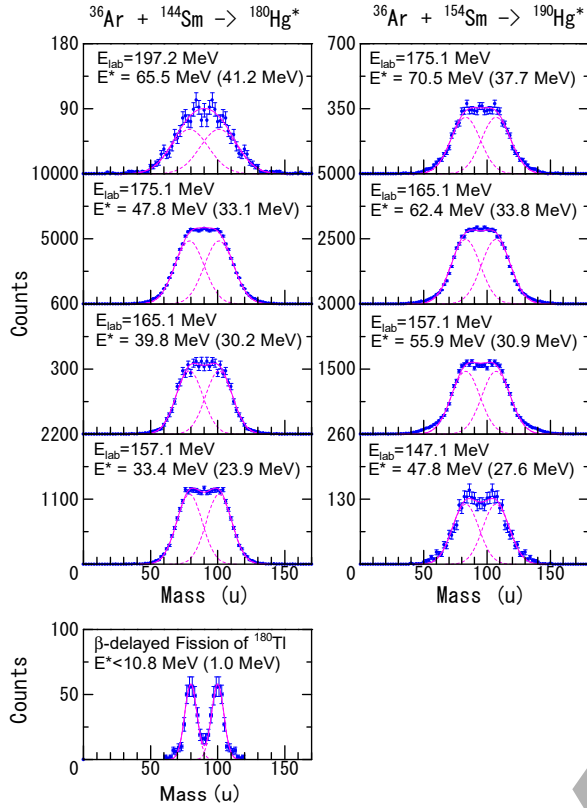
Figure 34. (Color online) FFMDs from fission of ^{180,190}Hg* at different beam energies E_{lab} obtained in the ^{36}Ar $+^{144,154}$Sm reactions at JAEA. The full excitation energies E^* are indicated in each panel. The effective excitation energy above the fission barrier $E^*_{Eff,B_f(l)}$ is shown in parentheses. Solid curves are the results of the double-Gaussian fitting by assuming only a single asymmetric fission mode, with respective Gaussian contributions for the light and heavy mass peaks shown by the dashed curves. The bottom panel in the left column: the FFMD for ^{180}Hg from the βDF of ^{180}Tl at ISOLDE ($E^*_{max}(^{180}$Hg$) < 10.4$ MeV) from [16, 86]. The figures are compiled from [16, 86, 124].

Figure 35. (Color online) The fragment mass-ratio (M_R) distribution obtained in the reactions of (a) ^{40}Ca+^{142}Nd→^{182}Hg* and (b) ^{13}C+^{182}W → ^{195}Hg*, taken from the ANU study [229]. The excitation energy of the CN is indicated in the parentheses. The other values in parenthesis are the scaling factors applied to the number of events.

dedicated campaigns have been performed by the JAEA and ANU groups, in which the fusion-fission reactions ^{36}Ar+^{144,154}Sm→^{180,190}Hg* (JAEA) and ^{40}Ca+^{142}Nd→^{182}Hg* and ^{13}C+^{182}W→^{195}Hg* (ANU) were studied in a broad range of excitation energies. Their respective fission detectors, shown in Figs. 7 and 9(a), were exploited. The resulting FFMDs are presented in Figs. 34 [124] and 35 [229], respectively, as a function of initial excitation energy E^*. By analogy with earlier studies by Itkis et al [14, 15], an effective excitation energy above the fission barrier of a rotating nucleus, $E^*_{Eff,B_f(l)}$, was derived in the JAEA analysis and is shown in parentheses. This is the excitation energy above the top of the fission barrier, determined by taking into account the pre-neutron emission multiplicity and energy, and a change of the fission barrier from those calculated by Möller et $al.$ [9] due to the angular momentum introduced by the projectile and

respective nuclear rotation [274].

For comparison, the FFMD of ^{180}Hg from the low-energy βDF of ^{180}Tl at ISOLDE is also shown in the bottom left-most panel of Fig. 34 (the same data as in the left-most bottom panel of Fig. 28).

While we refer the reader to the original papers [124, 229] for the comprehensive discussion of the data shown in in Figs. 34 and 35, a brief summary of the most salient features and conclusions is provided below.

First, we consider the case of ^{180}Hg*, in the left-hand column of Fig. 34. The flat-topped shapes of the measured FFMDs remain practically unchanged through the studied excitation-energy range and do not transit to a single-Gaussian shape, which would correspond to a symmetric liquid-drop-like fission. Two peaks can be discerned, especially at the lowest measured excitation energies, with the light and heavy fragment masses of $A_L/A_H = 79/101$. The latter values were derived from a free fit with two Gaussians corresponding to the light and heavy mass peaks, see the red dashed lines in Fig. 34. The positions of the light and heavy mass peaks are in a good agreement with those derived from the low-energy fission of ^{180}Hg at ISOLDE (the bottom leftmost panel of the figure), but show much larger FWHM

values. A quite similar picture can also be seen for ^{190}Hg* in the right-hand column of Fig. 34, for which the maxima at $A_L/A_H = 83/107$ were derived from the fits. The data for ^{182}Hg* from the ANU work, shown in Fig. 35, seem to confirm the above inference, with a clear signature of asymmetry at the lowest measured excitation energy can be seen, while flat-top distributions, resembling those in ^{180,190}Hg from the JAEA study, were measured at the higher excitation energies, see details in Ref. [229]‡.

Therefore, an important conclusion on the survival of the mass asymmetry in ^{180,182,190}Hg* even up to $E^* \sim 66$–70 MeV ($E^*_{Eff,B_f(l)} \sim 40$ MeV) can be drawn, which also proves the survival of the underlying microscopic effects even at such high excitation energies. This inference is quite different from what is known in the fission in the transuranium region, where the shell effects are quickly washed out as a function of the excitation energy. A thorough microscopic analysis of this important phenomenon in respect of the isotopes ^{180,198}Hg and ^{196}Po is given in Ref. [270].

On the other hand, no sign of asymmetry was observed in the heavier ^{195}Hg in the ANU study, whose FFMD resembles well to the predominantly symmetric mass split of ^{198}Hg, deduced by Itkis et al in [14], see also Fig. 32. Thus, a transition from the asymmetric fission in the vicinity of ^{178,180}Hg to a symmetric one around ^{198}Hg is clearly demonstrated by the JAEA and ANU studies.

To probe the evolution of FFMDs by moving to lighter elements, two fusion-fission reactions ^{35}Cl+^{144,154}Sm$\rightarrow^{179,189}$Au* were studied at several excitation energies at the BARC-TIFR Pelletron LINAC facility [160]. The deduced FFMDs for ^{179}Au* do not show a simple Gaussian shape, especially at the lowest excitation energy $E^* = 36.7$ MeV, see Fig. 36, and a contribution from the mass-asymmetric fission mode was needed when fitting the data. Furthermore, the analysis of the FFMD for ^{179}Au* showed a good agreement with the fission of ^{182}Hg* produced in the reaction ^{40}Ca+^{142}Nd at ANU.

It is therefore confirmed from the in-beam fission experiments of ^{36}Ar+^{144,154}Sm$\rightarrow^{180,190}$Hg*, ^{40}Ca+^{142}Nd$\rightarrow^{182}$Hg* and ^{35}Cl+^{144}Sm$\rightarrow^{179}$Au*, that there is a somewhat extended area of mass-asymmetric fission in the region of $^{180-190}$Hg, originally found in the low-energy fission of ^{180}Hg [16]. It is important to continue to map the FFMD mass-asymmetry in proton-rich nuclei by using a wider variety of target-projectile combinations. Still a challenge to be considered in this approach is that rather highly excited states are populated in fusion, so that the shell

‡ The authors of [229] also considered a possible admixture in the measured FFMD of asymmetric fission due to ^{180}Hg, produced after the neutron emission from ^{182}Hg*, see the ideas in respect of Figs. 49–50 in Section 4.3.1.
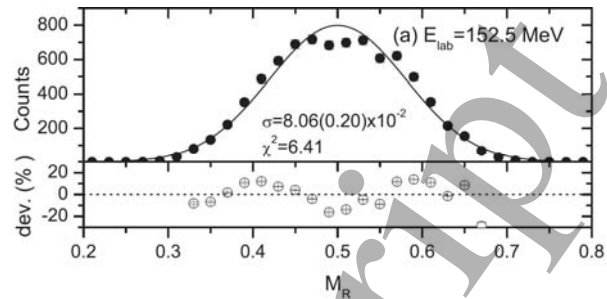
Figure 36. Fission fragment mass distribution in the reaction ^{35}Cl+^{144}Sm$\rightarrow^{179}$Au* at $E_{lab} = 152.5$MeV ($E^* = 36.7$ MeV), measured at the BARC-TIFR facility. The filled symbols are experimental data, and the solid lines are fit to the data. The deviation of the experimental data from the fit is shown in the panel below the respective mass distribution. The plot is taken from [160].

structure responsible for the mass asymmetry could be smeared out to a certain extent.

The asymmetry-to-symmetry transition seems to be a robust feature in different theory approaches, see e.g. [264, 265, 266, 267, 269, 270]. As one example, Figure 30 compares the PES's for ^{180,198}Hg calculated within the HFB-SKM* model in [270]. As mentioned earlier, the PES of ^{180}Hg is dominated by an asymmetric fission pathway, which is clearly separated from the symmetric fission pathway by a barrier. The situation is different in ^{198}Hg, where the PES is rather flat in the pre-scission region, whereby the symmetric and asymmetric fission paths have almost equal energy, see also a detailed discussion in [269].

Finally, it is instructive to re-iterate that neither βDF, not Coulex-induced fission experiments can reach nuclei with the fission barriers above $\sim$12 MeV. Thus, presently, charged-particle-induced fusion-fission reactions remain the only method to study fission of nuclei from higher excited states. On the contrary, this type of reactions does not allow to reach low excitation energies of the CN, due to the energy balance determined from the reaction Q-value and the Coulomb barrier between the colliding nuclei.

4.2. New results on fission in the astatine-to-californium region from inverse kinematics experiments

This section provides an overview of some of the recent results and improved understanding of fission emerging from the experiments in inverse kinematics.

4.2.1. *Overall variation of fission channels* A pronounced feature of fission-fragment distributions is the appearance of fission channels due to the influence of shell effects on the fission process [7]. As demonstrated in Fig. 5, double-humped (asymmetric)

CONTENTS   34
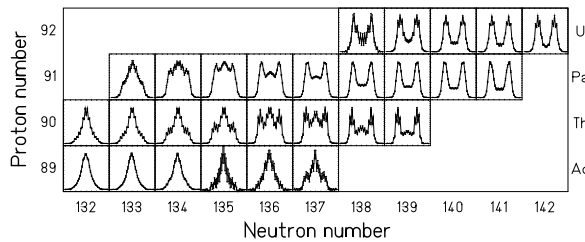
Figure 37. Element distributions after electromagnetic-induced fission of several secondary projectiles on the chart of the nuclides, part 1. The figure is taken from Ref. [40].
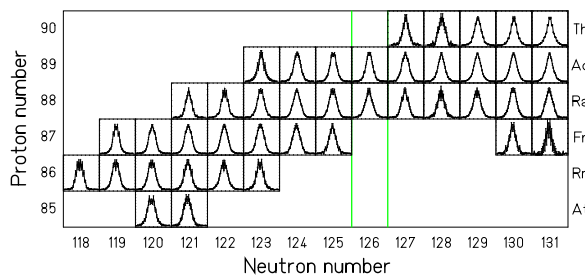
Figure 38. Element distributions after electromagnetic-induced fission of several secondary projectiles on the chart of the nuclides, part 2. The figure is taken from Ref. [40].

fission prevails over a large range of the actinides, and a constant position of the heavy component at $A \approx 140$ had been observed [76] in asymmetric fission of systems up to $A \approx 256$. Appearance of symmetric fission had been observed in lighter [45] and in heavier systems [276], see also discussions in Ref. [35] for even heavier systems. These general features were already addressed very early in theoretical studies, see for example Refs. [277, 278], when the two-centre shell model became available [279], whereas experimental information remained fragmentary, especially for lighter actinides. It was the aim of the first extended experiment on low-energy fission with secondary beams at FRS [40] to reveal the evolution of the fission channels in the range of $A \approx 210-230$ and to study the position of the heavy component of the asymmetric fission channels over long isotopic chains.

Figs. 37 and 38 show the measured fission-fragment Z distributions of 70 nuclides that were prepared as secondary beams from a $1\,A\,\mathrm{GeV}$ ^{238}U primary beam. Since the number of protons and neutrons in the fission fragments are strongly correlated, one can expect that the mass distributions show almost the same shape. This has been corroborated by the results of the later SOFIA experiment that was able to determine the fission-
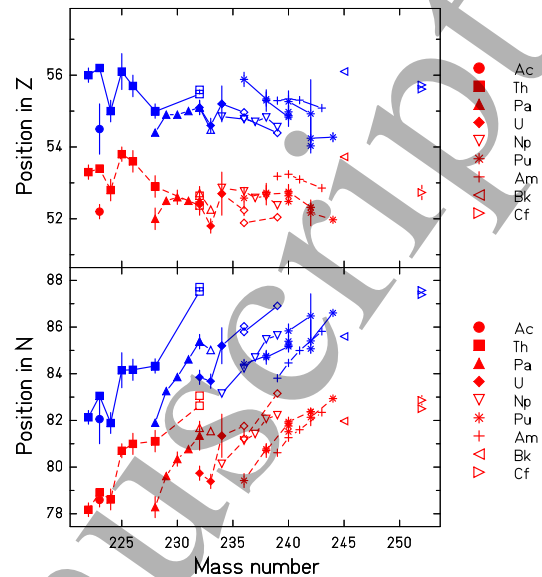
Figure 39. (Color online) Mean positions of the Standard 1 and Standard 2 fission channels in atomic number (upper part) and neutron number (lower part) deduced from measured fission-fragment A and Z distributions. The values of Standard 1 (Standard 2) for the isotopes of a given element are connected by dashed (full) lines and marked by red (blue) symbols. Values were converted from measured atomic numbers or mass numbers using the unchanged-charge-density assumption and neglecting neutron evaporation. Different symbols denote the elements as given in the legend of the figure. Data from the secondary-beam experiment [40] are marked by solid symbols. Open symbols mark results from experiments in direct kinematics, partly from spontaneous fission. The figure is taken from Ref. [275], see also the same work for the reference to the data.

fragment masses of several systems in this region as well [11].

The most prominent feature of the measured Z distributions is the presence of multi-modal fission (co-existence of symmetric and asymmetric fission) in a broad region from $A \approx 223$ to $A \approx 230$, evidenced by triple-humped distributions. The relative weights of the two fission modes vary gradually, favoring asymmetric fission (centered at $Z \approx 54$, which corresponds roughly to $A \approx 140$) towards the heavier $(A > 230)$ nuclei and symmetric fission towards the lighter $(A < 223)$ systems, the latter extending all the way down to ^{204}Rn. The shape of the Z distributions varies systematically along isotopic ($Z = $ constant) and isotonic ($N=$constant) sequences. The sequence ^{224}Pa-^{225}Th-^{226}Ac, which show similar shapes, suggests that $N+2Z$ is better suited as ordering parameter for the transition from single-humped to triple-humped distributions. These data, together with several FFMDs, measured previously [45, 79, 80] by other means in the transition region and marked in Fig. 4, fit nicely in the general trend of the data as shown in

CONTENTS   35

Fig. 5.

These data are also qualitatively consistent with two-dimensional fission-fragment mass – total-kinetic energy (A-TKE) distributions, measured by Itkis *et al.* [280] at appreciably higher excitation energies of generally more than 10 MeV above the fission barrier in proton- and α-particle induced fission of eight pre-actinides, reaching from ^{201}Tl to ^{213}At. All these data [45, 79, 80, 280, 40] shed some light on the relative yield, the mass (or Z) and TKE distribution of the asymmetric fission mode, localized around $A=140$ in the heavy fragment, as a function of the mass of the fissioning system and its excitation energy.

The width of this component decreases from about 15 mass units (FWHM) for ^{234}U to 5 mass units for ^{204}Pb. Future experiments that reach down to lower excitation energies, for example the SOFIA experiment, will be able to investigate the properties of this asymmetric fission mode in the pre-actinides in more detail with much higher yield.

A plausible explanation for the gradual vanishing of the asymmetric fission mode with decreasing mass of the fissioning system has been suggested by Itkis et al. [280]: While the region of predominantly asymmetric fission is rather abruptly limited for higher masses (around $A=258$) when two fragments close to the doubly magic ^{132}Sn can be formed, asymmetric fission is gradually weakened towards lighter systems by the influence of the macroscopic potential. Because the light and the heavy peak move more and more apart, the macroscopic energy expense in asymmetric fission grows and tends to favor symmetric fission. Recent stochastic calculations of Möller *et al.* [272] reproduce the main features of the measured Z distributions shown in Figs. 37 and 38 quite well (see also Fig. 31). Fission in the pre-actinides shows a rich variety of interesting phenomena. In this region, pronounced structures appear near symmetry, see Section 4.1.2, where the macroscopic potential is flat, and relatively small shell effects can have a decisive effect on the fission path [272]. But also the traditional asymmetric fission valley, appearing at larger asymmetry near $A=140$ in the heavy fragment due to strong shell effects, still exists in rather light systems.

The FRS data of Ref. [40] that include also data on total kinetic energies [281] allowed for a refined and extended analysis of the characteristics of the fission channels [275]. As an example, the deduced mean positions of the heavy fission-fragment component of the Standard 1 and Standard 2 fission channels in Z and N are shown in Fig. 39. The positions of both fission channels turned out to be essentially stable, with mean values of $Z \sim 52$ for Standard 1, and $Z \sim 55$ for Standard 2 mode, for all systems

investigated. On the contrary, the mean number of neutrons varies considerably along the different isotopic chains. Obviously, this is in contradiction to the observation of a constant position at $A \approx 140$ stated in Ref. [76], probably because the data at that time were limited to rather short isotopic sequences close to the β-stability line.
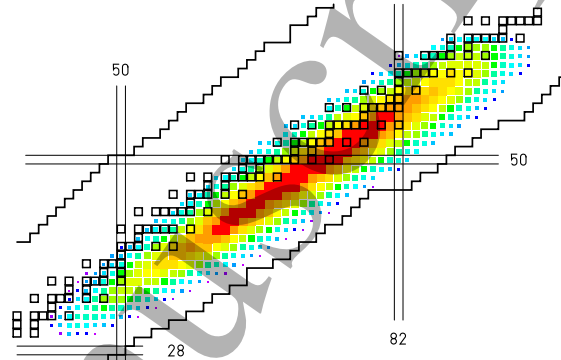
Figure 40. (Color online) Measured fission-product yields from the complete fusion reaction ^{238}U + ^{12}C→^{250}Cf* at 6.1 A MeV (E^*=45 MeV) from Ref. [84] are shown on the chart of the nuclides. The sizes of the clusters are proportional to the logarithm of the cross sections. The primordial nuclei are marked by black open squares, and the limits of know nuclides and the main spherical shells are shown for orientation.
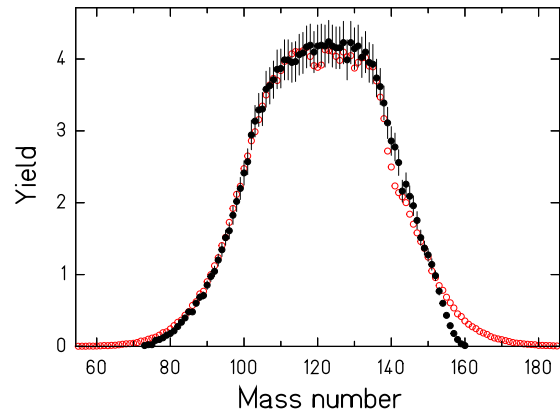
Figure 41. (Color online) Black symbols - projection on the mass number from Fig. 40. The data are compared with the result of the GEF code [282, 283] (red symbol). The deviations in the heavy wing are mainly caused by a known acceptance cut of the experimental set-up. The figure is taken from Ref. [283].

In the GANIL inverse-kinematics experiment with the VAMOS spectrometer, the full identification of all fragments in Z and A from the fission of ^{250}Cf at an excitation energy of 45 MeV, produced by the complete fusion of ^{238}U and ^{12}C, has been achieved [84]. Fig. 40 shows the measured fission-product distribution on a chart of the nuclides. The projected mass distribution

CONTENTS   36

is shown in Fig. 41. These are the first data on fully identified fission fragments, emitted in the de-excitation process of a specific compound nucleus with a well defined excitation energy in this high-energy range. This was achieved only due to the use of inverse kinematics. The flat top of the mass distribution can be interpreted as a sign for a sizable contribution of double-humped asymmetric fission in addition to the dominant contribution of single-humped symmetric fission, even at this high excitation energy. Due to multi-chance fission, the observed distribution is the sum of contributions from several nuclei that fission at different excitation energies (see discussion of Figs. 49–50 in Section 4.3.1.)

The evolution of the average N/Z degree of freedom was also determined for several transfer residues, such as ^{238}U, ^{239}Np, ^{240}Pu and ^{244}Cm, at different mean excitation energies, see Fig. 42. In order to assure a reasonable statistics, no cut on the distribution of excitation energies, induced in the reaction, was applied. These data show a strong variation of the influence of nuclear shell structure on the neutron excess of the fission fragments. It is known that the fission-fragment mass distributions in low-energy fission (spontaneous or thermal-neutron-induced) are strongly influenced by shell effects for all these systems. It is expected that the same is true for the charge-polarization degree of freedom. Therefore, the evolution of the structure in the neutron excess may primarily be attributed to the variation of the excitation energy. A clear structure is present at the low excitation energies, while it becomes weak at $\langle E^* \rangle = 23$ MeV in ^{244}Cm and completely disappears at $E^* = 45$ MeV in ^{250}Cf. A relatively large $\langle N \rangle/Z$ value around $Z = 50$–52 indicates the preferential formation of ^{132}Sn-like ($N/Z = 1.64$) fragments, which is realized particularly for low excitation energies.

These data represent a unique test for nuclear-reaction models. In particular, the data are sensitive to the influence of initial excitation energy and angular momentum on the yields of the fission channels and the shape of their contribution to the mass distribution, the relative contributions of the fission chances, the charge polarization at scission and the mass-dependent neutron multiplicities. The latter strongly depends on the division of the excitation energy between the nascent fragments, for example via the proposed process of energy sorting in the superfluid regime [284].

The experiments in inverse kinematics at GANIL and GSI provide valuable information not only on the nature but also on the kinematical properties of one or both fragments of a fission event, respectively. Besides the measurement of individual fission-product atomic numbers, masses and kinetic energies after prompt-neutron emission [84, 28, 252], also mean pre-neutron
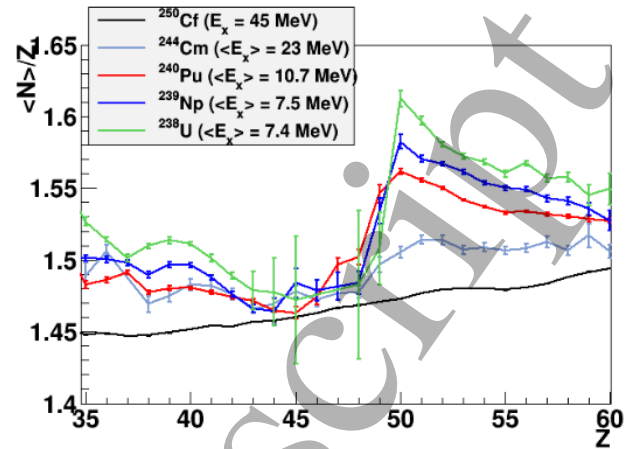
Figure 42. (Color online) Neutron excess of post-neutron-evaporation fission fragments as a function of their atomic number. The figure is taken from Ref. [285].

fragment masses were derived from the mean velocities of complementary fission products [85]. Moreover, properties of the scission configuration such as the distance between fragments, the neutron multiplicity, the total excitation energy, and the proton- and neutron-number sharing during the emergence of the fragments are reported [85].

4.2.2. General characteristics of odd-even structures The enhanced production of even-even fission fragments is another salient feature of the fission-fragment distributions [286]. The data on this feature from experiments in direct kinematics are scarce, partly due to the insufficient Z resolution in kinematical experiments, partly due to the uncertainties in the absolute determination of fission yields from radiochemical measurements. Most of the available results originate from measurements at the LOHENGRIN spectrograph. Note that a good mass resolution is not sufficient for determining neutron-number distributions, if the Z determination is not unique.

Influence of asymmetry on the odd-even effect in proton number. The secondary-beam experiment at FRS [40] also showed that some features previously observed for a few systems in direct kinematics [289], proved to be generally present for all nuclei investigated in that work. As illustrated in Fig. 43, an odd-even staggering in the Z distributions is present for fissioning systems with both even and odd number of protons. The magnitude of this staggering is usually measured by the local odd-even effect, definded for integer Z_{low} values as [290]

$$\delta_p(Z) = \frac{1}{8}(-1)^{Z_{low}}[\ln Y(Z_{low+3} - \ln Y(Z_{low})$$
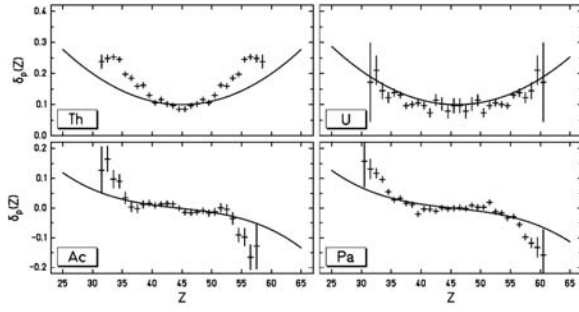
Figure 43. Local odd-even effect $\delta_p(Z)$ (defined by equation (1)) in the element distributions for electromagnetic-induced fission of $^{231-234}$U, $^{224-232}$Pa, $^{220-229}$Th, and $^{214-223}$Ac, averaged over the different isotopic chains. The lines represent theoretical estimations of Ref. [287] that are based on the statistical weight of the single-particle levels in the two nascent fragments. The figure is taken from Ref. [287].
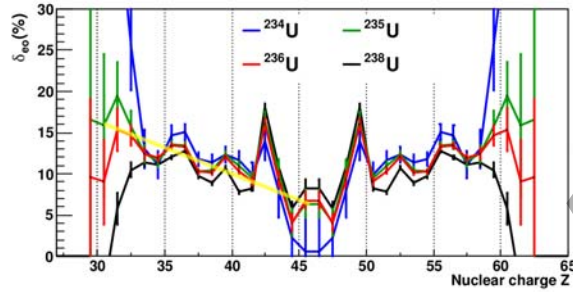
Figure 44. (Color online) Local odd-even effect $\delta_p(Z)$ (defined by equation (1)) in the element distributions for electromagnetic-induced fission of ^{234,235,236,238}U measured in the SOFIA experiment, given in percent. The yellow line indicates the average increase of the odd-even effect as a function of asymmetry. The figure is taken from Ref. [252].
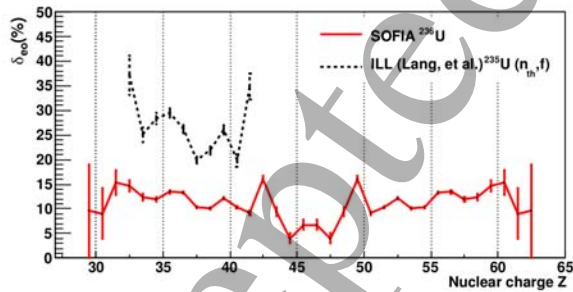
Figure 45. (Color online) Local odd-even effect $\delta_p(Z)$ (defined by equation (1)) in the fission-fragment element distribution for electromagnetic-induced fission of ^{236}U measured in the SOFIA experiment and in thermal-neutron-induced fission of ^{235}U [72], given in percent. The figure is taken from Ref. [252].

$$- 3(\ln Y(Z_{low} + 2) - \ln Y(Z_{low} + 1))] \qquad (1)$$

with

$$Z = Z_{low} + 3/2.$$
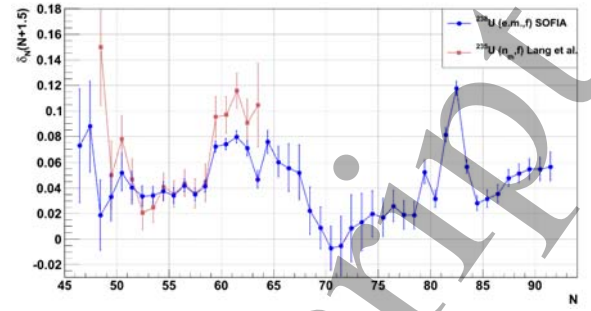
Figure 46. (Color online) Local odd-even effect $\delta_n(N)$ (defined in analogy to equation (1)) in the fission-fragment neutron-number distribution for electromagnetic-induced fission of ^{236}U measured in the SOFIA experiment and in thermal-neutron-induced fission of ^{235}U [72]. The figure is taken from Ref. [288].

The staggering in neutron number can be expressed in a similar way. The local odd-even effect in Fig. 43 is generally positive in the light fission-fragment group, and grows strongly with increasing asymmetry. This suggests that the preference for producing even-Z fragments is connected with the light fragment, while the heavy fragment plays only a minor role. This explains also the fundamentally different shapes of the Z-dependent odd-even effect for even-Z and odd-Z fissioning systems. While in the former case both fragments have an even or an odd number of protons, in the latter case one even-Z fragment is always formed together with an odd-Z fragment.

These results were essentially corroborated in the SOFIA experiment, see Fig. 44, although there is a local peak at $Z = 49.5$ and at its light partner at $Z = 42.5$, and there are some deviations for extremely asymmetric splits that appear with very low yields. Note that Fig. 43 shows the absolute odd-even effect, while percentage values are given in Fig. 44.

Fig. 45 demonstrates that the odd-even effect in Z is sensitive to the excitation energy of the fissioning system: it decreases by about a factor of two in electromagnetic fission (relatively broad excitation-energy distribution with a mean value of $E^* \sim 14\,\mathrm{MeV}$) if compared to the thermal-neutron-induced fission of the same compound nucleus ($E^* = 6.55\,\mathrm{MeV}$). This effect had already been observed previously, for example in bremsstrahlung-induced fission [291].

Robustness of the fine structure in neutron number. The fine structure in neutron number behaves very differently. As demonstrated in Fig. 46, the fine structure in electromagnetic fission is almost identical to the fine structure in thermal-neutron-induced fission. This is true for both the amplitude and the details of the structure. Besides a clear odd-even effect, one observes a strong enhancement of nuclides

CONTENTS   38

with $N = 82$. The SOFIA experiment is the first study that was able to provide such kind of data for higher excitation energies than reachable in thermal-neutron-induced fission

The robustness of this fine structure in neutron number is an indication that it is not produced at scission, because one would expect the same kind of sensitivity to the initial excitation energy of the system as observed in the Z distribution. It is probably created during the prompt-neutron emission and reflects the influence of the neutron threshold energy on the nuclide cross sections in the last stage of the evaporation process as suggested by Ricciardi et al [292, 293] to explain the odd-even structure in the light fragmentation products.

4.2.3. Nuclear dissipation from inverse-kinematics experiments Due to dissipation, the fission process is expected to be strongly influenced by transient effects that delay the onset of the fission flux [294], by a reduction of the stationary fission flux over the fission barrier [294] and by an increased saddle-to-scission time [295]. Several observables, for example the emission of pre-fission neutrons [22, 296], charged particles [297], GDR γ-ray radiation [23], and fission probabilities [298] have been studied in order to deduce the viscosity of nuclear matter. However, the results did not yield a consistent picture [26], whereby the magnitude of the dissipation strength and its dependence on excitation energy and deformation obtained from different observables and with different models used for the analysis (see e.g. [299]) diverge appreciably. Particularly strong discrepancies have been reported for the overall fission time derived from atomic technique experiments (e.g. [24, 25, 26, 27]) and from kinematical measurements [18], which are further emphasized in the recent study [300]. Experimental signatures that are sensitive to the dissipation on a specific stage of the fission process, for example pre-saddle effects, are particularly interesting. In Refs. [301, 302, 303, 304] it is argued that the manifestation of pre-saddle dissipation is only possible under favorable experimental conditions. These are primarily high excitation energy and low angular momentum of the fissioning system. Fission in the course of the de-excitation process after a relativistic nuclear collision is particularly well suited for studies of pre-saddle dissipative effects, because the excitation energies induced in the abrasion process are high, and side effects due to high angular momenta are small [304]. As already mentioned earlier, the excitation energy amounts to about 27 MeV per abraded nucleon [250], and the angular momentum hardly exceeds $20 \hbar$ [251]. Experiments in inverse kinematics at relativistic energies offer another important advantage:

They provide the experimental information on the composition of the fission fragments in A and Z.
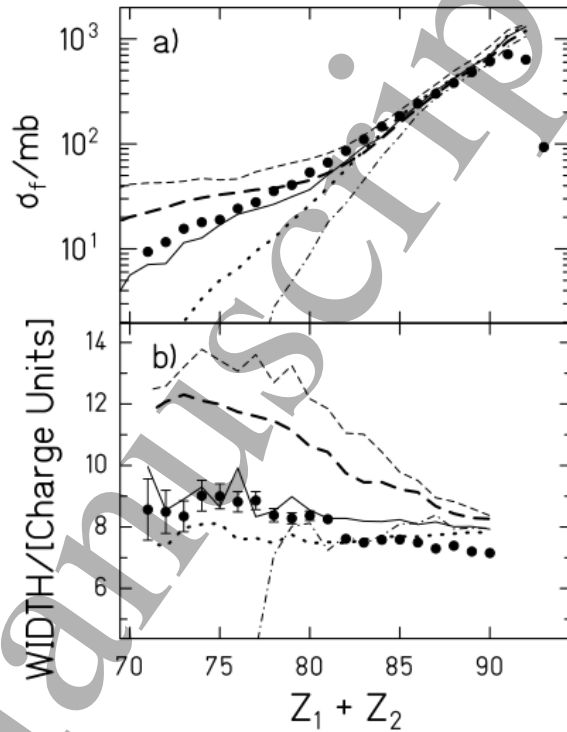
Figure 47. (a) Partial fission cross sections and (b) partial widths of the fission-fragment element distributions for the reaction of ^{238}U at $1\,A\,\mathrm{GeV}$ on $(\mathrm{CH2})_n$ in comparison with several calculations. The thin dashed and the thick dashed lines are obtained by applying the Bohr-Wheeler transition-state model and Kramers' stationary solution with $\beta = 6\times10^{21}\,\mathrm{s}^{-1}$, respectively. The solid, the dotted, and the dashed-dotted lines show calculations including transient effects [305] with $\beta = 2\times10^{21}\,\mathrm{s}^{-1}$, $0.5\times10^{21}\,\mathrm{s}^{-1}$, and $5\times10^{21}\,\mathrm{s}^{-1}$, respectively. The staggering in these curves and the abrupt decrease of the dashed-dotted curve below $Z_1 + Z_2 = 78$ are due to statistical fluctuations of the Monte Carlo calculations. The figure is taken from Ref. [306].

In the past two decades, a series of experiments was performed with primary and secondary relativistic beams at GSI, Darmstadt, with the aim to deduce the dissipation strength from fission observables. Ignatyuk et al [307] inferred a strong reduction of the total fission cross section in the reaction ^{238}U + Cu at $950\,A\,\mathrm{MeV}$ due to dissipative effects. Benlliure et al [308] reproduced the completely measured residue cross sections in the reaction ^{197}Au + ^{1}H at $800\,A\,\mathrm{MeV}$ with a model calculation by using a dissipation strength of $\beta = 2\times10^{21}\,\mathrm{s}^{-1}$. A similar result $(\beta = 2\times10^{21}\,\mathrm{s}^{-1})$ was obtained by the same kind of analysis for the systems ^{238}U + ^{1}H and ^{238}U + ^{2}H at $1\,A\,\mathrm{GeV}$ [309].

Jurado et al [306] introduced the width of the fission-fragment charge distribution as a function of the fissioning element, besides the partial fission

cross sections, as a very sensitive measure of the dissipation strength and inferred a dissipation strength of $\beta = 2 \times 10^{21}\,\mathrm{s}^{-1}$, see Fig. 47, by using a realistic description of the transient effects [305], assuming an initial sperical shape of the fissioning system. This kind of analysis requires the coincident measurement of both fission fragments. These studies by the use of secondary projectiles demonstrated the influence of the initial deformation of the fissioning system on the transient effects. A refined and extended analysis was performed by Schmitt *et al* [310]. Considering the influence of the initial shape of the secondary projectiles, determined by their ground-state deformation and, for the first time, by the abrasion process, a large number of systems could be described with a single dissipation strength of $\beta = (4.5 \pm 0.5) \times 10^{21}\,\mathrm{s}^{-1}$. The larger value compared to Refs. [306, 311] is explained by the influence of the ground-state deformation of ^{238}U and the abrasion-induced shape distortion that was not considered before. In the most recent experiment, the fission of ^{208}Pb induced by spallation in a hydrogen and a deuterium target was studied [312] with this approach. Also these data are well described with a dissipation strength of $\beta = 4.5 \times 10^{21}\,\mathrm{s}^{-1}$.

The authors of these studies concluded that in particular the partial widths of the fission-fragment charge distributions (see Fig. 47) or more complete information on fission-fragment nuclidic yields from more recent experiments on fragmentation or spallation reactions, obtained in inverse kinematics, give reliable and consistent results on the dissipation strength between ground-state and the saddle. This observable measures the time that the nucleus has available to cool down by neutron evaporation before fission. It is argued that, in contrast to many other observables, e.g. the fission probabilities, the deduced dissipation strength is only weakly model-dependent. They could not observe an excitation-energy-dependent variation of the dissipation strength that is discussed in detail in e.g. [313].

4.3. Fission studies by means of few- and multi-nucleon transfer reactions

4.3.1. Fission-fragment mass distributions of the heavy actinides measured at JAEA The multi-nucleon transfer reactions provide a complementary method to study a variety of compound nuclei, including those on the neutron-rich side, which are difficult, if impossible, to access by particle capture and/or heavy-ion fusion reactions using available target-projectile combinations. Furthermore, this reaction mechanism can populate excited states in a broad range of excitation energy, allowing the excitation-energy dependence of fission properties to be studied

in a single experiment. The latter is advantageous in respect of particle capture/fusion reactions, where the incident-beam energy must be changed to populate different excitation-energy ranges.

This subsection will review selected results obtained in the recent experiments at the JAEA tandem in direct kinematics in the MNT-induced reactions of an ^{18}O beam with targets of ^{232}Th, ^{238}U, ^{237}Np and ^{248}Cm, while we refer the reader to Fig. 7 for details of the respective experimental set-up. Most of the data are presently under analysis; therefore, only the reaction ^{18}O+^{232}Th will be discussed here [74].

Figure 48 shows the FFMDs for fourteen nuclei studied in this reaction, whereby the FFMDs for the isotopes ^{231,234}Th* and ^{234,235,236}Pa* were obtained for the first time. For the other nuclides, the previously known FFMDs data were systematically extended to excitation energies as high as 60 MeV. The figure clearly demonstrates that the mass-asymmetric fission dominates at low excitation energies for all the measured nuclei. The yield in the mass-symmetric fission region increases with excitation energy, whereby the FFMDs become increasingly structure-less at excitation energies in excess of 40–50 MeV, presumably due to the weakening of shells responsible for asymmetric fission. It should be pointed out that the actual excitation energies leading to fission (as compared to those calculated just from the energy/mass balance of the reactions, shown in Fig. 48) will be reduced by neutron evaporation before fission, when the initial CN is excited above the threshold for multiple-chance fission, see the discussion below.

It is also interesting to note that the measured FFMDs seem to reveal a larger peak-to-valley ratio by increasing the isospin (the N/Z ratio) of the isotopes of the same element, compared at the same excitation energy (see, for instance, the FFMDs for the isotopic chains for $E^* = 20-40\,\mathrm{MeV}$). This might be explained by the growing influence of the doubly magic nuclide ^{132}Sn on the mass division, which is expected due to a better match in the N/Z-ratio between ^{132}Sn and the increasingly heavier fissioning isotopes.

The measured FFMDs were compared with the calculations within the fluctuation-dissipation model based on the Langevin equations, see Ref. [314], where an attempt to include the excitation-energy dependence was also undertaken. The applied model is the same as discussed in context of Fig. 59. In particular, the potential energy is calculated within the two-center shell model [315] as the sum of the liquid-drop energy V_{LD} and the excitation-energy-dependent shell-correction energy $V_{shell}(E^*) = V_{shell}(0) \times \exp(-E^*/E_d)$, where the shell-correction energy at the zero temperature $V_{shell}(0)$ and the shell-damping parameter $E_d = 20\,\mathrm{MeV}$ were

CONTENTS　　　　　　　　　　　　　　　　　　　　　40
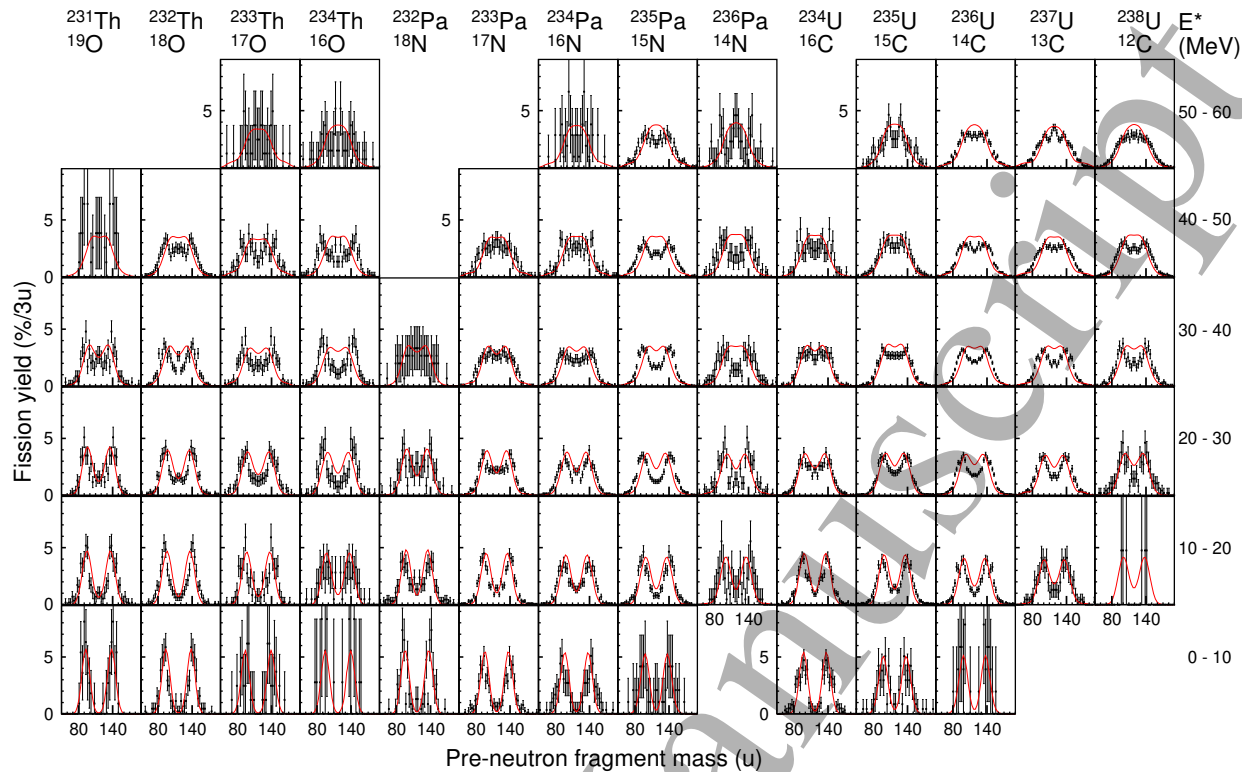
Figure 48. (Color online) FFMDs obtained in the MNT-induced channels of the reaction ^{18}O+^{232}Th (data points with error bars)[74]. The fissioning nucleus and the corresponding ejectile are indicated on the top of the plot. The data are shown for sequential excitation-energy intervals of 10 MeV, indicated on the right side. The red curves are the results of Langevin calculations [74] (see text) after a convolution with the experimental mass resolution, where the initial CN excitation energy is used to start the calculation, but effects of multi-chance fission (neutron evaporation before fission) were not included as discussed in the context of Fig. 50.

used. The calculated FFMDs are shown by the red solid curves in Fig. 48. One can see that the calculations reproduce reasonably well both the global shape of the experimental mass distributions and also the positions of the light- and heavy-fragment peaks for most of the studied nuclides, at least at the excitation energies below $\sim$30 MeV. This demonstrates the reasonable treatment of the shell-correction energy at these excitation energies, and confirms the validity of the shell-damping energy of $E_d = 20$ MeV, originally introduced in [316], in contrast to a recently suggested value of $E_d = 60$ MeV [317].

With increasing excitation energy, however, the contribution from multi-chance fission becomes increasingly important. Thus, the fission observables, in particular FFMDs, become a superposition of several contributions, originating from fission at different excitation energies. The underlying idea is illustrated by Fig. 49, where the different contributions, as a function of the neutron energy are shown, for the fission cross section of the reaction ^{239}Pu(n,f) [318]. The figure clearly illustrates the fact that only at the energies below $E_n \sim 5$ MeV, the first-chance fission is dominant and fission happens at low excitation energy, where the
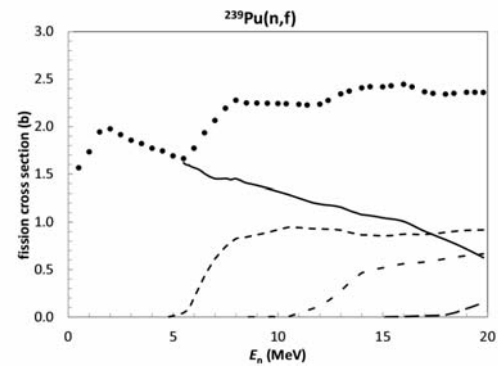
Figure 49. Total ^{239}Pu(n,f) cross section (symbols), as evaluated in ENDF/B-VII, along with the corresponding contributions due to first- (solid curve), second- (short-dashed), third- (dashed), and fourth-chance fission (long-dashed) cross sections. The figure is taken from [318].

shell effects are preserved, which leads to an asymmetric mass split, observed experimentally. On the contrary, at e.g. $E_n = 20$ MeV, the contribution of first-chance fission is less than each of the second- and third-

CONTENTS   41

chance fission§. These features are demonstrated by Fig. 50 from [319], based on the recent MNT-induced studies at JAEA. This figure compares the experimental data for fission of ^{238}U* at the initial excitation energy $E^* = 35$ MeV with the Langevin calculation taking into account multi-chance fission. According to calculations, at *this initial energy*, the 1st- and 2nd-chance fission happen with somewhat lower probabilities (calculated by the GEF code [283]) from respective higher excitation energies, which results in more symmetric-like fission. On the contrary, the higher-chance fissions, after emission of several neutrons (3–5, in this case), occur at lower excitation energies, thus they lead predominantly to an asymmetric mass split. The final calculated FFMD, shown by the solid red line, is the sum of the FFMDs over the possible multi-chance fissions; it is seen that the measured asymmetric FFMD predominantly comes from the higher-chance fission. In passing we mention the recent work by Möller and Schmitt [320] which considered the effects of multi-chance fission within the macro-microscopic approach. Several fission observables show structures that are evidently associated with multi-chance fission. One of the examples is the incident-neutron-energy dependence of the total kinetic energies (TKEs), $TKE(E_\mathrm{n})$ [321], where a step-like structure appears at the neutron energy where 2nd chance fission sets in. The average energy of prompt neutrons also exhibits a dip structure [322] at the same energy.

Apart of FFMDs, the fission probabilities as a function of excitation energy will be deduced from the same data for all studied nuclei from the JAEA MNT-fission setup.

Clearly, this experimental technique has a large potential to explore fission of neutron-rich heavy actinide nuclei. The use of radioactive targets such as ^{244}Pu, ^{249}Cf and, eventually, ^{254}Es is promising for this purpose. Also heavier projectiles such as ^{22}Ne could be employed by improving the quality of the ΔE-E detectors. Finally, provided the necessary beam intensities of post-accelerated radioactive neutron-rich beams, such as ^{20,22}O, could be reached in the future, they could be used to access even more neutron-rich actinide nuclei.

4.3.2. Resonance structures in the superdeformed and hyperdeformed minima of the fission barrier
It is long known that due to the coupling between the states in the normal and super-deformed (SD)

§ It is, however, important to stress for didactic purposes that at the respective higher excitation energy, the nature of the 1st chance fission will change as it will now happen from higher-excited states, thus leading predominantly to symmetric fission. The higher-chance fission, on the other hand, will now happen at the respectively lower excitation energies, thus leading to asymmetric fission.
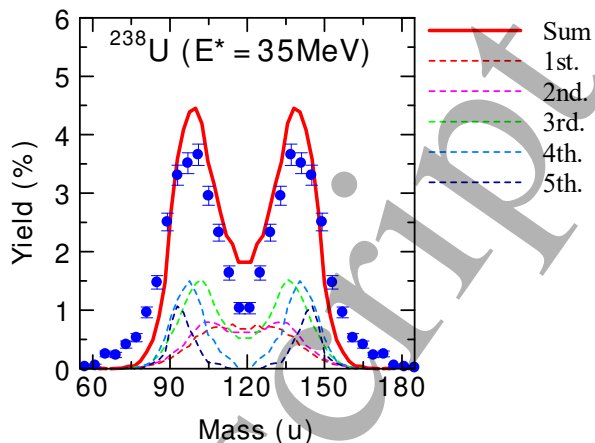
Figure 50. (Color online) Experimental FFMD of ^{238}U* (blue symbols) measured at the initial excitation energy of 35 MeV, obtained from the inelastic scattering channel of the reaction ^{238}U(^{18}O,^{18}O)^{238}U*(ff) [319], is compared with the Langevin calculation [314] taking into account multi-chance fission. The solid red curve shows the final calculated FFMD, where the contributions from every multi-chance fission are shown by the dashed curves with different colors.

minima in the PES of some heavy actinides, the fission cross sections may exhibit intermediate structures (e.g. fission resonances) below the fission threshold, associated with the resonance tunneling through the complex multi-humped fission barriers, see e.g. review papers [226, 323, 324]. Transfer reactions such as (d,p) have often been used in the past to explore these intermediate structures, by means of the measurements of the kinetic energy of an outgoing particle in coincidence with the fission fragments. This allows to determine the excitation energy of the fissioning residual nucleus, similar to the MNT reactions described in Section 3.1.2. An obvious advantage of transfer reactions in the earlier studies, compared to the neutron-induced fission, was a wider excitation-energy-range coverage in a single experiment, from below the fission threshold up to well above.

However, following the discussion in Sections 3.2.3–3.3, we remind that with the recent advent of approaches based on the neutron time-of-flight measurements and on the use of γ-ray beams, such types of experiments can presently be performed with alternative methods.

In the earlier studies, silicon ΔE-E detectors were frequently used to determine the energy of the outgoing ejectile in the (d,p) reaction with an energy resolution of $\sim$50 keV. To achieve a better energy resolution, magnetic spectrographs were frequently used for the ejectile measurements. As an example, by using a Browne-Buechner-type magnetic spectrograph at Chalk River, a resolution of $\sim$18 keV (FWHM) was reached in one of the first experiments of this

type in the reaction ^{239}Pu(d,pf) [325] to study structures associated with the SD minimum in ^{240}Pu. The same reaction was later investigated with the Q3D magnetic spectrograph at the Munich tandem accelerator, whereby an energy resolution of 3 keV (FWHM) in Ref. [326] or $\sim$7 keV in Ref. [327] was achieved. The studies of the resonance structures in the SD minimum were reviewed in [323].

In some actinide nuclei, in addition to the second (superdeformed) minimum in the PES, a third, strongly elongated (hyperdeformed, HD) reflection-asymmetric minimum with characteristic quadrupole and octupole deformations of $\beta_2 \approx 0.90$ and $\beta_3 \approx 0.35$, respectively, was predicted already forty years ago, see e.g. [328, 329]. Since then, several theoretical approaches were used to study the HD minima, e.g. the macroscopic-microscopic method [330, 331, 332, 333], the constrained Hartree-Fock model with D1S interaction [334], relativistic mean field calculations [335], or, the self-consistent finite-temperature superfluid nuclear density functional theory (FT-DFT) as in the recent study [336]. In spite of a quite general appearance of the HD minimum in different approaches, there are often quantitative discrepancies among the models in respect of the third-barrier height as well as the depth of the HD minimum, showing that the prediction of the HD's properties remains a challenging subject for modern fission theory. The latter is primarily caused by insufficient knowledge on nuclear properties at extreme nuclear deformations as well as the need for a larger number of degrees of freedom for extremely deformed and reflection asymmetric nuclear shapes, including their temperature dependence. As one example, the study by McDonnell et al [336] used a FT-DFT with two Skyrme energy density functionals - a traditional SkM* and a recently developed UN-EDF1 [337] optimized for fission studies. It was shown that, in contrast to predictions of most macroscopic-microscopic approaches, either only very shallow or no third minima in the PES's of ^{232}Th and ^{232}U are expected. On the other hand, a better-developed third minimum was suggested in the lighter Th and U isotopes with $N = 136$ and 138.

Figure 51 shows a schematic example of the PES for ^{236}U as deduced from the measurements in [338] (see also below), in which three minima can be seen: normal (or ground state), superdeformed and hyperdeformed. In order to obtain the evidence for the HD minimum from the measurements of the transmission resonances, it is necessary that the states in the ground state minimum (class-I) are strongly mixed with the class-II states in the SD minimum, and further on - with the states in the HD minimum. Otherwise, the narrow class-II states in general will not overlap with the isolated class-III states. According to

different predictions, these conditions are expected to be realized for several isotopes of Th, Pa and U.
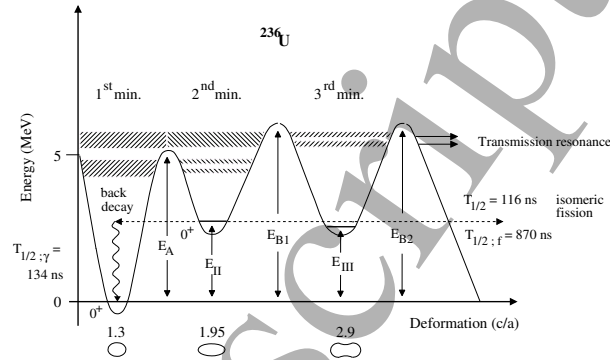
Figure 51. The triple-humped potential-energy surface of ^{236}U as a function of deformation, with damped class-I, class-II and class-III compound-nucleus states shown in the three minima. For strongly mixed class-I and class-II states, transmission resonances of class-III states can occur in fission. The figure is taken from [338].

Since about two decades, systematical studies of the HD states are being carried out by the Munich-Debrecen collaboration using the Q3D magnetic spectrograph at Munich, e.g. in the reactions ^{233}U(d,pf)^{234}U* [339], ^{235}U(d,pf)^{236}U* [340, 338], ^{231}Pa(^{3}He,df)^{232}U* [341], ^{231}Pa(d,pf)^{232}Pa* [171], and ^{239}Pu(d,pf)^{240}Pu* [327]. In these experiments, the fission fragments are detected by position-sensitive avalanche detectors [339] in coincidence with the ejectile particle measured with the Q3D spectrometer. As just one example to illustrate the experimental and analysis method used, Fig. 52 shows the fission probability, $P_f(^{236}$U$^*)$ as a function of excitation energy in the region below the fission threshold, obtained in the reaction ^{235}U(d,pf) [338]. The structures at 5.27, 5.34, and 5.43 MeV were proposed to be due to HD resonances already in 1998 [340], where an energy resolution of 3 keV (FWHM) was achieved by using the Q3D magnetic spectrometer. In the latest measurements and analysis in [338], as shown in Fig. 52, the measured P_f spectrum was reasonably well reproduced with the assumption of the existence of several rotational bands, build on bandheads with different K-values, with large moments of inertia, arising from very large quadrupole and octupole moments as the characteristic properties of the HD minima.

In addition to the studies of the fission probabilities, as described above, it is also important to measure the FFMDs, TKE, and $\bar{\nu}(A)$ distributions from the intermediate resonance SD and HD states. For the SD states, the FFMDs for fission through the β-vibrational states were measured for the first time at JAEA [342] in the ^{239}Pu(d,pf) reaction, which exhibits nearly the same distributions as ^{239}Pu(n$_{th}$,f). On the other hand,
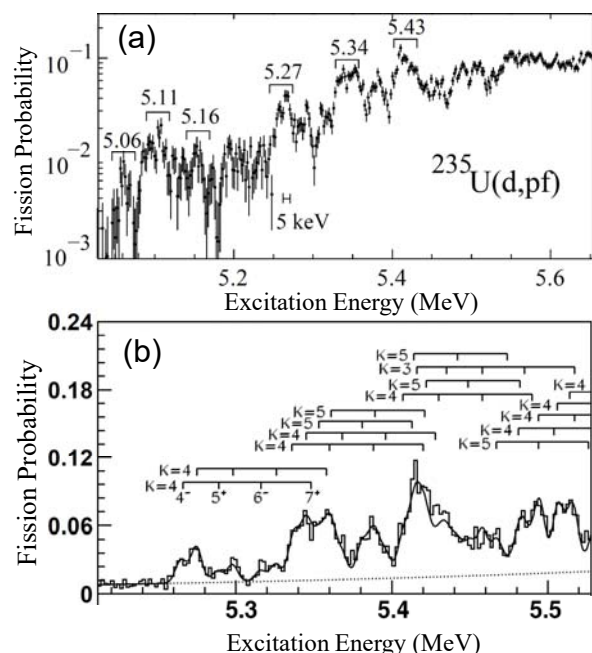
Figure 52. (a) Prompt-fission probability, P_f, obtained for the reaction ^{235}U(d,pf) [338]. The ejectile-energy resolution is 5 keV(FWHM). (b) Expanded view of the spectrum (a) at the excitation energy above ~5.2 MeV. The solid line shows a fit to the data assuming alternating-parity rotational bands starting with $J=K$, where the background component is included in the analysis (dotted curve). The picket-fence structures indicate the positions of the rotational-band members used in the fit with the K values as indicated for each band. The figures are taken from [338].

the characteristic difference between the SD and HD shapes is that the latter is expected to be somewhat octupole-deformed, and, since the HD shape is closer to the shape of the scission configuration, the fission from the HD states could lead to significant differences in FFMDs in comparison to fission from normal or SD states.

To conclude this section, we mention that recently the sub-barrier structures in ^{238}U have been studied by the same collaboration via the photofission technique, by using a monochromatic Compton-backscattered γ-ray beam [214], see also Section 3.3.

4.3.3. Fission probabilities via the surrogate method: spin mismatch issues and the use of inverse kinematics at VAMOS. Since several decades, the light-ion-induced transfer reactions were often used in what is called the "surrogate reactions method" to determine neutron-induced fission cross sections, (n,f), see the recent (2012) comprehensive review in Ref. [172]. Some recent applications of this method in the reactions with ^{3,4}He beams include: ^{235,238}U(^{3}He,α)[343], ^{236,238}U(^{3}He,p)[344], ^{234,235,236,238}U,^{239}Pu(α,α') [345, 346, 347]. Also (p,p′), (p,d), (p,t) reactions with ^{239}Pu,

^{235,238}U, ^{243}Am targets [169, 170] were investigated. In addition, lithium beams were bombarded to ^{232}Th and ^{238}U samples to populate CNs in the (^{6}Li,d), (^{6}Li,α), (^{7}Li,t), (^{7}Li,α) reactions [348, 168, 349, 350, 351].

After the review on the surrogate-reaction method [172], an important progress in deriving the fission probabilities in surrogate reactions has been made in two different aspects. The first one concerns the influence of the mismatch in spin and parity on fission and capture cross sections, while the second one is related to the recent application of the inverse-kinematic technique.

Spin-parity mismatch Neutron-induced and transfer reactions could lead to different distributions in spin and parity. Therefore, it is not obvious, whether unmeasured fission probabilities or capture cross sections for neutron-induced reactions can reliably be deduced from surrogate reactions using the Weisskopf-Ewing approximations, as extensively discussed in the 2012 review [172].

As shown in Ref. [172], in a few cases a direct comparison of experimental surrogate-reactions data with those from neutron-induced reactions is possible. It was found that fission probabilities from these two reaction types generally agree quite well. In contrast, appreciable discrepancies were found for capture cross sections, by comparing the surrogate reaction ^{156}Gd(p,p′γ) [352] with the capture reaction ^{155}Gd(n,γ) [353, 354]. In a recent experiment that was not yet considered in Ref. [172], deviations as large as a factor 10 were obtained for radiative capture cross sections in the rare-earth region with the surrogate method (^{174}Yb(^{3}He,^{4}Heγ)^{173}Yb and ^{174}Yb(^{3}He,pγ)) [355] in comparison with the corresponding neutron-induced data (^{172}Yb(n,γ) [356, 357] and ^{175}Lu(n,γ) [358, 359]. On the empirical side, these observations gave confidence to the fission probabilities obtained by the surrogate or the surrogate-ratio method and motivated considerable activity in the field, e.g. Refs. [169, 170]. But a better understanding of the different behavior of fission and capture requires more dedicated studies.

The previous results suggest that the fission probability is much less sensitive to differences in the entrance channel than the γ-ray emission probabilities, but to prove this it is necessary to measure simultaneously fission and γ-ray emission probabilities for the same nucleus at the same excitation energy.

Recently, the CENBG collaboration measured for the first time simultaneously the fission and γ-decay probabilities of ^{239}U induced by the ^{238}U(d,p) reaction, which was used to simulate the n+^{238}U reaction for which good-quality neutron-induced data on fission and capture cross sections exist. The details of

CONTENTS　　　　　　　　　　　　　　　　　　　　　　44

the experiment, the data analysis and the applied corrections are given in Ref. [360]. The measurement of the γ-decay probability at excitation energies, where the fission channel is open, is challenging, because of the background of γ rays emitted by the fission fragments. As can be seen in Fig. 53, in the excitation energy region, where the γ-ray emission and fission compete, the fission probability obtained with the (d,p) reaction is in good agreement with the neutron-induced data, whereas the γ-decay probability is several times higher than the neutron-induced one.
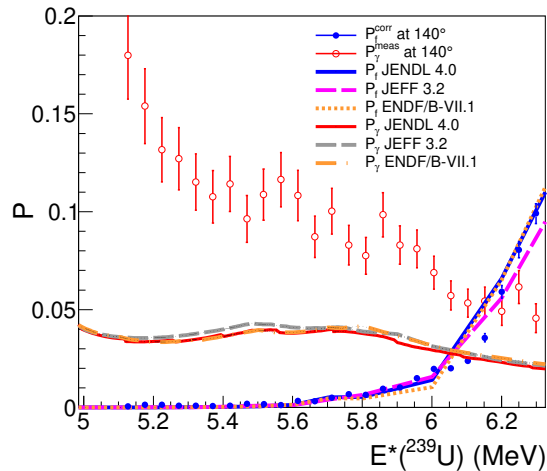
Figure 53. (Color online) Fission (full blue circles) and γ-decay (empty red circles) probabilities as a function of excitation energy measured for the ^{238}U(d,p) reaction compared to the corresponding neutron-induced decay probabilities according to different evaluations (colored lines). The fission probability has been corrected for the deuteron breakup effect, see [360]. The figure is taken from ref. [360].

Calculations performed with the model of Ref. [361] predict that the average angular momentum populated in the ^{238}U(d,p) reaction is about 70% larger than in the n+^{238}U reaction near the neutron separation energy ($E^* = 4.8$ MeV). This difference decreases with E^* and amounts to about 25% at $E^* = 6.3$ MeV. Therefore, the results of [360] show that the significant change in the initial spin distribution caused by the different entrance channel has a much stronger impact on the γ-emission probability than on the fission probability. Further theoretical work is in progress to understand these results by coupling a Hauser-Feshbach calculation of the decay probabilities with the initial spin and parity distribution populated by the ^{238}U(d,p) reaction that will result from the model of Ref. [361].

Inverse-kinematics technique The transfer-induced fission experiment in inverse kinematics, conducted at GANIL by Farget *et al* [84, 39] was also exploited to determine the fission probabilities of the nuclei ^{238}U,

^{239}Np, $^{240-242}$Pu and ^{244}Cm as a function of excitation energy. The results are compared in Fig. 54 with previous data from normal-kinematics experiments and with TALYS calculations. Some discrepancies appearing near the threshold may be explained by the limited excitation-energy resolution of 2.7 MeV (FWHM). It is expected to be improved in future experiments. In general, the fission probabilities obtained in this experiment agree well with the results obtained in neutron-induced reactions. This is in line with the results of other surrogate experiments using transfer reactions in direct kinematics as discussed in Section 4.3.3.
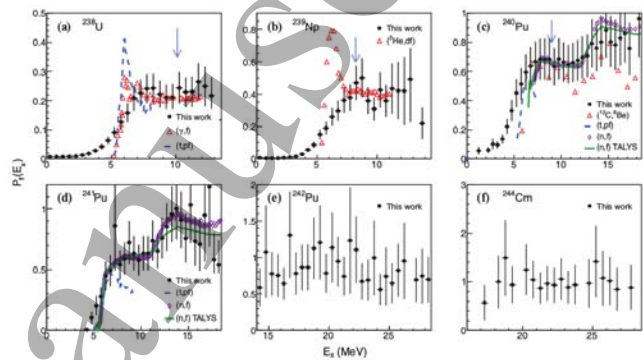
Figure 54. (Color online) Fission probabilities as a function of the total excitation energy. Results are presented for ^{238}U + ^{12}C inelastic scattering (a) and transfer-induced fission reactions (b)−(f). The fissioning nucleus is indicated in each figure. Earlier γ -, transfer-, and neutron-induced fission data are included for comparison, as well as TALYS calculations of neutron-induced fission probabilities. The corresponding references are given in Ref. [39]. Arrows point to excitation energies equal to the sum of the fission barrier and the energy of the first excited state of the light transfer partner. The figure is taken from Ref. [39].

By using radioactive beams in future experiments, it will be possible to appreciably extend the choice of fissioning systems to be studied by the surrogate method in transfer-induced reactions by overcoming the limited availability of targets for direct-kinematic experiments.

4.4. Recent results on spontaneous fission

Spontaneous fission is one of the major decay modes of many nuclides above $Z = 92$. Since the 1995' review on spontaneous fission, see [32] and references therein, about 20 new spontaneously fissioning isotopes were discovered, and the properties of many previously known ones were re-studied and improved. Nowadays, the SF is known up to the element Flerovium, see the recent comprehensive review by Heßberger [37]. Fig. 55 shows the presently known SF isotopes, overlaid on the map of fission-barrier heights, calculated within the macroscopic-microscopic model

by Möller *et al* [9]. Most of the new SF isotopes originate from recent heavy-ion-induced complete-fusion-reaction experiments, which resulted in the discovery of several new superheavy elements with $Z = 114$ - 118, see recent detailed reviews [36, 260].

As seen in Fig. 55, some of these isotopes allow the unique probe (together with α-decay properties, where known) of two important regions, where an increased stability in respect of SF is expected, due to the respective increase in the fission-barrier heights. The first group, with atomic numbers $Z = 104$-106 and neutron numbers around $N = 162$ are in the bottom part of the predicted island of deformed nuclei, centered around $^{270}_{108}\mathrm{Hs}_{162}$. Another ten new spontaneously fissioning isotopes with $Z \geq 108$ and neutron numbers $N \geq 168$ are found on the approach to the predicted island of spherical nuclei, shown in the red color, with expected center at $^{298}_{114}\mathrm{Fl}_{184}$.

Figure 56 shows SF half-life systematics for even-even nuclides with $Z = 98$–114. First of all, one notices a well-documented increase of T_{SF} for the $N = 152$ isotones of the elements with $Z = 98,100,102$ [31], which is due to the strong shell effects around these Z and N numbers and the resulting increase of the fission barriers, as seen in Fig. 55. A decreasing trend of the fission barriers from $Z = 100$ to 104 at $N = 152$ is consistent with the sudden drop of T_{SF} toward $Z = 104$. The recent data for the $Z = 104,106,108$ elements provide first proof for the increased stability by approaching $N = 162$, in agreement with higher fission barriers expected from Fig. 55. Finally, the most recent data for $Z = 112,114$, though still being far from $N = 184$, seem to also show the increased stability in respect of SF. Fig. 56 also shows the calculated SF half lives based on another version of the macroscopic-microscopic model by Smolańczuk *et al* [362, 363], which follows the similar trends of increased stability implied by the other fission barrier calculation [9].

In passing we note that the recent reexamination of the shell structure of SHE in covariant density functional theory (CDFT) also reveals an important role played by the $N = 184$ shell gap [364], which is in contrast to earlier inferences from this approach.

4.5. Fusion-fission and quasifission phenomena in heavy-ion-induced reactions

4.5.1. Orientation effect and its importance for the fusion-fission versus quasifission competition. At present, complete-fusion reactions provide the only mechanism to produce superheavy elements and to study their decay, including their spontaneous fission [366]. Apart of this important goal, they also open up a possibility to study fission of nuclei located far away from the β-stability line, also as a function of the excitation energy.

It has already been known since 1980'ies that the fusion probability in a complete-fusion reaction could be strongly influenced by the static deformation of the target nucleus, which can lead to the so-called 'sub-barrier' fusion cross-section enhancement. This so-called 'orientation' effect was extensively investigated in respect of the fusion probability in various reactions using deformed target nuclei, for example $^{154}\mathrm{Sm}$ ($\beta_2 = 0.270$[367]), see e.g. Refs. [368, 369]. A comprehensive review can be found in Ref. [261].

Furthermore, around the same period, it was also found that in the heavy-ion-induced reactions characterized by $Z_p \times Z_t > 1600$ fusion-fission and quasifission compete, with the QF probability becoming dominant for heavier system [370, 371, 92, 372, 373]. This competition results in the reduction of the fusion probability to form a compound nucleus, which is important especially for the synthesis of superheavy nuclei, see the recent comprehensive review [35].

Due to the importance of quasifission for the production of superheavy elements, within the last two decades several research groups carried out systematic studies of the orientation effect and its possible link to quasifission. In this subsection, we will summarize some of these efforts and discuss the evolution of the nuclear shape from the projectile-target contact point in a heavy-ion reaction towards the final fission fragments, where the competition between the fusion-fission and quasifission can play a decisive role. To explain the underlying mechanisms, Fig. 57 shows the calculated potential-energy surface of $^{274}\mathrm{Hs}^*$, following its production in the reaction of $^{36}\mathrm{S}$ ions with a target of $^{238}\mathrm{U}$. The potential energy was calculated with a two-center shell model [315], which is also used for the Langevin calculations [374] to determine the fission time scale and FFMDs as explained in Fig. 59 and Fig. 60. Due to the large prolate deformation of the target nucleus $^{238}\mathrm{U}$ ($\beta_2 = 0.215$ [367]), two extreme entrance projectile-target orientations should be considered: a) the contact of a spherical $^{36}\mathrm{S}$ projectile with the tip (or polar) of the prolate $^{238}\mathrm{U}$, resulting in a more elongated configuration, and b) a more compact equatorial-side contact. They are characterized by lower and higher Coulomb barriers, respectively, thus also by the different available excitation energies at the respective barriers. For example, the lower-energy polar-side configuration may lead to a contact point outside of the fusion barrier, as shown in the plot, whereby the system does not evolve towards the complete fusion (formation of a true CN) and instead proceeds via a separate QF valley to an asymmetric fission with the FFs mass values driven by the shell effects of nuclei in the vicinity of $^{208}\mathrm{Pb}$ (or $^{78}\mathrm{Ni}$), in agreement with the experimental results, shown in Fig. 58. On the contrary, by
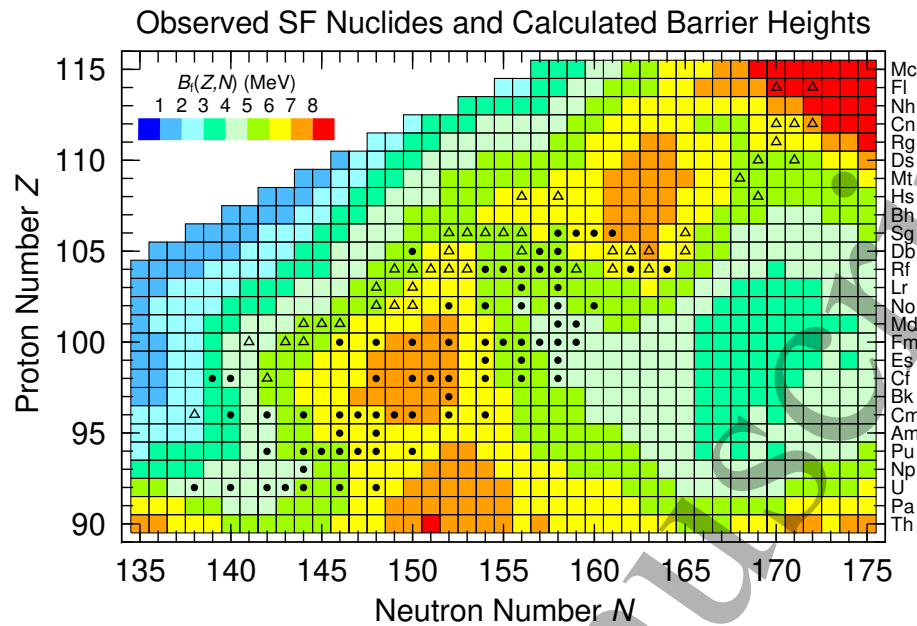
Figure 55. (Color online). Presently known spontaneously fissioning isotopes (symbols) overlaid on the map of fission-barrier heights for the region above $Z = 90$, calculated within the macroscopic-microscopic model by Möller *et al* [9]. Open triangles and thick dots show the isotopes for which SF was discovered or their properties were re-studied since or before ∼1995, respectively. The highly variable fission-barrier heights are mostly due to the ground-state shell effects, which are particularly strong in the deformed regions around $^{252}_{100}$Fm$_{152}$, $^{270}_{108}$Hs$_{162}$ and in the nearly spherical region in the red right-hand upper corner of the plot, near the next doubly magic nuclide postulated to be at $^{298}_{114}$Fl$_{184}$ (not shown in the plot). The figure is modified from [9].
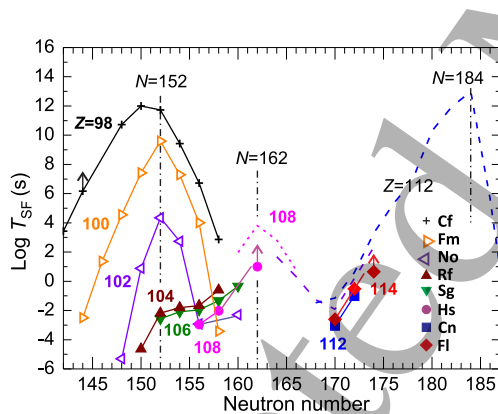
Figure 56. (Color online) Logarithm of partial SF half-lives versus neutron number for even-even isotopes of elements with $Z = 98$–114. Dashed lines show the theoretical half-life values for even-even $Z = 108$ (in magenta), 110 (in violet) and 112 (in blue) isotopes from [362, 363]. The value for ^{284}Fl is taken from [365]. The figure is modified from [36], see also the same work for the reference to the data.

increasing the beam energy, the equatorial-side contact becomes eventually possible with larger geometrical fraction than the polar-side configuration‖, which leads

‖ It should be noted that at a higher energy which is enough to reach an equatorial-side contact, the tip-side collisions also happens. This should be considered in a model calculation.
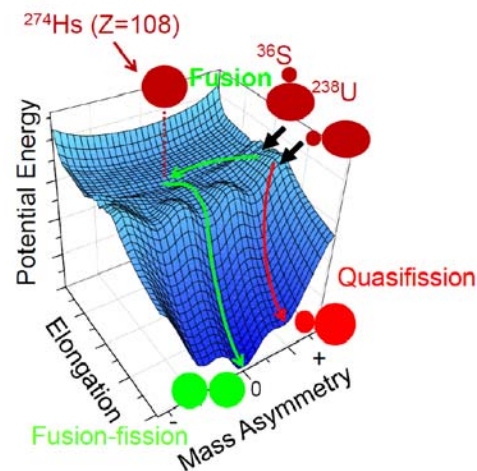
Figure 57. (Color online) Potential-energy landscape of ^{274}Hs plotted as a function of the elongation and mass asymmetry, taken from [120]. The red arrow shows the expected evolution of the nuclear shape starting from the collision of ^{36}S to the polar side of the deformed ^{238}U, producing a composite system which further disintegrates by quasifission by generating mass-asymmetric fragments. On the other hand, the more compact collisions at the equatorial side at the higher beam/excitation energies lead first to the compound-nucleus shape (CN), followed by prompt symmetric fission (green arrows).

to a contact point inside the fusion barrier. This would

CONTENTS   47

make the equatorial-side collision to evolve towards a true CN, which fissions symmetrically.

To investigate these phenomena, the JAEA group performed a series of experiments at their setup at the tandem (Section 3.1.1) to measure FFMDs in the reactions between spherical ^{30}Si, ^{31}P, ^{34,36}S, ^{40}Ar, ^{48}Ca projectiles and a deformed ^{238}U target, leading to excited superheavy nuclei ^{268}Sg*, ^{269}Bh*, ^{272,274}Hs*, ^{278}Ds*, ^{286}Cn* [120, 89, 121, 123, 375]; the obtained results are summarized in Fig. 58. For each reaction, the data for four incident energies are shown in each column, with the respective excitation energies of the compound nucleus also indicated.

The FFMD at the highest measured excitation energy of $E^* = 60.5$ MeV in the reaction ^{30}Si+^{238}U $\rightarrow$ ^{268}Sg* ($Z_p \times Z_t = 1288$) shows a relatively narrow Gaussian shape, which suggests that a symmetric liquid-drop-like fission happens in this case. On the other hand, a triple-humped structure is visible at the lowest measured excitation energy of $E^* = 35.5$ MeV. The trend is opposite to the expectation of the liquid-drop model [376], whereby the standard deviation σ_m should increase with excitation energy. Thus, it is interpreted that the asymmetric mass peaks observed at $\bar{A}_L/\bar{A}_H \sim 90/178$ originate from quasifission.

Further inspection of Fig. 58 shows that the reactions with projectiles of larger mass and/or charge numbers have larger yields of quasifission, and also the mass asymmetry of quasifission changes. For example, the shapes of FFMDs become quite different already in the reaction ^{36}S+^{238}U $\rightarrow$ ^{274}Hs* (third column) at comparable excitation energies to those in the reaction ^{30}Si+^{238}U. In particular, the width of the FFMD becomes larger at $E^* = 61.5$ MeV in the reaction with ^{36}S, and the shape of the peak clearly deviates from a Gaussian. By reducing the excitation energy, the symmetric component quickly disappears, with a dominant QF asymmetric mass distribution seen at the lowest measured energy. The quasifission peaks are now located at $\bar{A}_L/\bar{A}_H \sim 74/200$, which are also different from those seen in the reaction with ^{30}Si and should most probably be linked to the influence of shell effects of the doubly magic nuclei around ^{78}Ni and ^{208}Pb, as hinted by the calculations in Fig. 57.

Finally, in the reactions with even heavier beams, such as ^{40}Ar and ^{48}Ca, the mass-asymmetric quasifission dominates at all the measured energies. The centers of the heavy and light fragment masses for QF are located at $\bar{A}_L/\bar{A}_H \sim 78/208$.

To further understand the trends in Fig. 58, the reactions ^{30}Si+^{238}U $\rightarrow$ ^{268}Sg* and ^{36}S+^{238}U $\rightarrow$ ^{274}Hs* were studied within the fluctuation-dissipation framework, in which the evolution of the nuclear shape is calculated by solving the Langevin equation, see for example [377, 378, 374]. Fig. 59 shows the time depen-

dence of the nuclear-shape distribution on the mass asymmetry (α) and charge-center distance (z) for the lowest incident energies (in respect of Fig. 58). At the very beginning of the reactions [$t = (0-5) \times 10^{-21}$s], both systems show the same probability distributions. The difference already appears in the next time range, $t = (5-10) \times 10^{-21}$s, whereby the flux of the ^{30}Si+^{238}U reaction moves towards the compound-nucleus shape, whereas most of the flux in the reaction ^{36}S+^{238}U goes to quasifission with fragment masses around 74/200. In the next time range, $t = (10-30) \times 10^{-21}$s, a small fraction of quasifission starts to also appear in ^{30}Si+^{238}U leading to fragment masses $\sim 88/180$, which are in agreement with the experimental values. At $t = (30-50) \times 10^{-21}$s, the reaction ^{36}S+^{238}U already finishes. On the contrary, fission from the compound nucleus produced by ^{30}Si+^{238}U continues up to the time domain of $t > 50 \times 10^{-21}$s.

Figure 60 compares the experimental FFMDs with the Langevin calculation for the reactions ^{30}Si+^{238}U [89] and ^{34}S+^{238}U [121]. In the calculation, orientation effects are considered to generate the incident-energy dependence of the FFMDs. The calculated distributions reproduce the measured data quite well and include both fusion-fission and quasifission events, see explanations for Fig. 57. Furthermore, in the calculations by tracing each trajectory (shape evolution) obtained by solving the Langevin equation, it is possible to separate the 'pure' fusion-fission (CN fission) events as those for which the shape of the system reached the CN shape, defined as a rectangular box in Fig. 59. The obtained FFMDs of 'pure' CN fission are also shown in Fig. 60 by filled histograms. The latter have a single Gaussian shape with a narrow width and are similar for both reactions, ^{30}Si+^{238}U and ^{34}S+^{238}U.

By using the CORSET setup (Section 3.1.1), the Dubna group also studied the orientation effects in the reactions between lighter projectiles and heavier strongly-deformed actinide target nuclei, such as ^{248}Cm and ^{249}Cf [146]. Importantly, despite having a relatively low value of $Z_p \times Z_t = 1152$ in the reaction ^{26}Mg+^{248}Cm $\rightarrow$ ^{270}Hs*, the obtained FFMDs at the lower energies still showed a mass-asymmetric component around $A_L/A_H \sim 94/180$ arising from quasifission. This further proves that the onset of QF is strongly influenced by the target deformation, and can happen also for relatively light projectiles, even for the reactions with quite low values of $Z_p \times Z_t \sim 1000$. We note, however, that e.g. in the reaction ^{22}Ne+^{249}Cf $\rightarrow$ ^{271}Hs* ($Z_p \times Z_t = 980$), the FFMDs has the Gaussian-shape characteristic of CN fission for all the measured energies, indicating that fusion-fission is the dominant source to generate fission fragments.

The Dubna group also studied the orientation
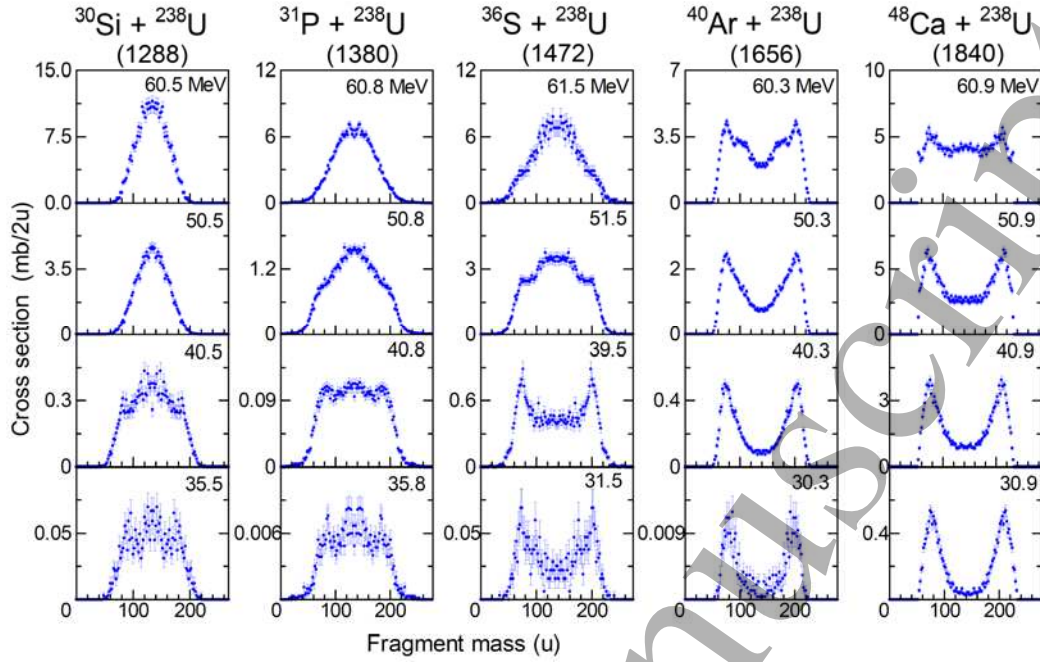
Figure 58. (Color online) FFMDs for the reactions between five spherical projectiles and deformed ^{238}U target nuclei taken at four excitation energies, shown in each panel. Data are from [120, 89, 123, 375]. The $Z_p \times Z_t$ value for each reaction is shown in brackets.

effect in reactions with lighter deformed target nuclei, e.g. with ^{154}Sm in comparison with the spherical ^{144}Sm. Fig. 61(a) shows the fission-fragment mass-TKE distribution for the reaction ^{48}Ca+^{144}Sm ($Z_p \times Z_t = 1240$), where a dominant symmetric CN-like fission can be seen in the middle of the plot, the same trend was observed at all measured incident energies [142].

In the reaction of ^{48}Ca with a deformed ^{154}Sm target (see, Fig. 61(b)), obviously having the same $Z_p \times Z_t = 1240$ value, additionally an asymmetric fission channel with the mass peaks around $\bar{A}_L/\bar{A}_H \sim 61/141$ appears, and the probability of the mass-asymmetric component increases at lower energies. The quasifission origin for the observed mass-asymmetric fission events in this case was proven by measuring the fission-fragment angular distributions, see details in [142]. By assuming the neutron-to-proton ratio being equilibrated in QF in the reaction ^{48}Ca+^{154}Sm, the FFs neutron and proton numbers should correspond to $(Z_L, N_L) = (25,36)$ and $(Z_H, N_H) = (57,84)$. This suggests the influence of the neutron shell at $N = 82$ in the heavy fragment as the main reason for the observed mass peaks in QF in this case.

Figures 61(d) and (c) reveal the difference between the actinide-based reaction ^{48}Ca+^{238}U$\rightarrow$ ^{286}Cn* and the cold-fusion reaction ^{48}Ca+^{208}Pb $\rightarrow$ ^{256}No*. The latter exploits the spherical ^{48}Ca and ^{208}Pb nuclei, thus no orientation effect is expected. Indeed, despite

having a value $Z_p \times Z_t = 1690$, the reaction ^{48}Ca+^{208}Pb shows a single Gaussian-shape FFMD [379, 380, 145], typical for the CN fission. On the contrary, the reaction ^{48}Ca+^{238}U ($Z_p \times Z_t = 1840$) is dominated by quasifission, with no clear evidence for the CN-like fission seen in the middle of the plot.

Finally, the difference between deformed ^{154}Sm and ^{238}U targets can be seen by comparing the spectra in Figs. 61(b) and (d). The former reaction shows both symmetric and asymmetric fission modes corresponding to fusion-fission and quasifission, respectively, whereas the latter reaction is largely dominated by quasifission.

4.5.2. Mass-angle correlation in quasifission and fusion-fission, fission time scale. The growth of the QF probability for reactions with increasing $Z_p \times Z_t$ values can also be demonstrated by e.g. fission-fragment mass-angle correlations. As quasifission is a fast decay process, fission fragments are emitted with forward-backward angular asymmetry relative to the beam direction. This asymmetry can be revealed by the so-called mass-angle distribution (MAD) plot, which shows the center-of-mass fragment emission angle, $\theta_{c.m.}$ (with respect to the beam direction) versus the mass ratio $M_R = A_1/(A_1 + A_2)$, defined from the fragment masses A_i ($i=1,2$). Fig. 62 summarises the recent systematical studies of the MADs for an extended series of target-projectile combinations by the Canberra group with their CUBE setup [131]. In

CONTENTS
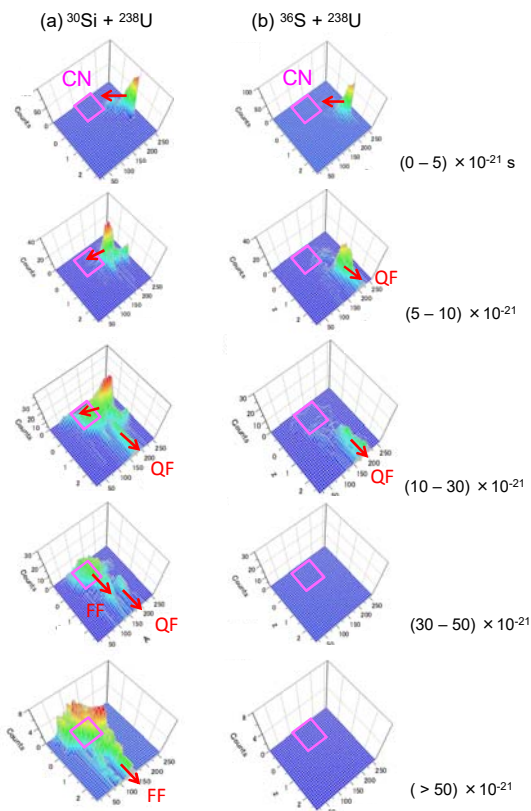
Figure 59. (Color online) Calculated probability distribution of the nuclear shape plotted as a function of mass asymmetry (α) and charge-center distance (z) [374] for reactions (a) ^{30}Si+^{238}U → ^{268}Sg* and (b) ^{36}S+^{238}U → ^{274}Hs* The time ranges are indicated. The positions of the respective compound nuclei are marked by rectangles. Quasifission (QF) and fusion-fission (FF) flux flows are indicated.

Figure 60. (Color online) Comparison between the experimental FFMDs (solid blue circles) and Langevin-type calculations (open magenta histograms) in the reactions of ^{30}Si+^{238}U → ^{268}Sg* [89] and ^{34}S+^{238}U → ^{272}Hs* [121]. Filled magenta histograms show the calculated fission from the compound nucleus, as defined in the text. The fusion probability, P_{fus}, is determined from the calculated ratio of CN fission to all fission events, the results are shown in % in each panel of the figure. The geometrical shapes on the right-hand-side demonstrate the predominant equatorial-side collisions at the higher incident-beam energies and the polar-tip collisions at the lower energies.

the reactions with the carbon and oxygen beams, no correlations were observed between the mass ratio M_R and the angle $\theta_{\text{c.m.}}$ for all the target nuclei used. A slight difference is visible for the reactions involving actinide target nuclei (^{232}Th and ^{238}U) on the one hand and lighter target isotopes (Hg, Pt, Os, and W) on the other hand, whereby the former cases have somewhat larger widths of their FFMDs.

The differences between the actinide- and lighter-target nuclei are more clearly visible, when the heavier projectiles, e.g. from sulfur on, are employed. For example, the reaction ^{32}S+^{232}Th [127] exhibits a mass-angle correlation, which is not evident for reactions using lighter targets, such as lead and mercury. The heavier projectiles (e.g. titanium and nickel) generate strong mass-angle correlations even for the reactions with the lighter target isotopes.

The conclusion on systematically wider fragment-mass distributions in reactions between heavier projectiles and actinide targets is consistent with the

trend observed in Fig. 58, see Section 4.5.1.

Recently, the MADs were theoretically studied using the TDHF model in the reactions of ^{40}Ca+^{238}U [382], ^{54}Cr+^{186}W, ^{50}Cr+^{180}W, and ^{54}Cr+^{186}W [133]. One of the features of the TDHF calculations is an exact treatment of the incident angle between the deformed nuclei in the approaching phase. The calculations show that the collision on the equatorial side have a larger probability to generate mass-symmetric fission fragments, thus resulting in smaller mass-angle correlations.

To conclude this section, we also mention that the MADs can be used for the determination of the fission time scale, see e.g. the studies of reactions of ^{34}S, ^{48}Ti, and ^{58,64}Ni with the targets of ^{184,186}W at the ANU [18]. The extracted short mean scission times of $\leq 10^{-20}$ s for quasifission in the reactions with ^{48}Ti and ^{64}Ni were compared with the mean scission times measured in similar reactions by the crystal blocking technique in Ref. [24], where the much longer fission times were deduced. The authors of [18] strongly emphasized this discrepancy and called for further efforts to clarify this issue, which could be very important for the synthesis of new superheavy
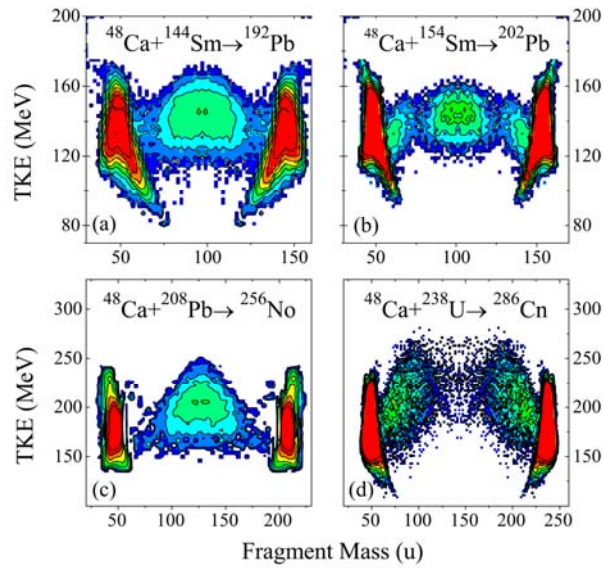
Figure 61. (Color online) Mass-energy distributions of fission fragments in the ^{48}Ca-induced reactions with the targets of (a) spherical ^{144}Sm ($Z_p \times Z_t$=1240), (b) deformed ^{154}Sm (1240), (c) spherical ^{208}Pb (1640), and (d) deformed ^{238}U (1840). Figure is taken from [145]. The peak in the middle of each panel is due to the fusion-fission of excited fully equilibrated CN, while the two strong peaks on the left- and right-hand sides are due to the scattered beam and target nuclei. The events in between the areas of the scattered nuclei and fusion-fission events are due to quasifission.

eleements, see also the recent study [300].

4.6. Prompt-neutron and γ-ray emission in fission: selected recent results.

4.6.1. Prompt-neutron emission from fission fragments.

Prompt-fission-neutron multiplicities. Prompt neutron emission from fission fragments is a well established phenomenon, whereby the deformation energy of the nascent fragments at the scission point is considered as the main source for the respective excitation in low-energy fission, such as SF or thermal-neutron-induced fission. Thus, the average neutron multiplicity from an individual fragment with a mass A, $\bar{\nu}(A)$, carries an important information on how the fissioning system evolves along the different paths on the potential-energy surface. Prompt-neutron and γ-ray measurements until $\sim$1974 were summarized in Refs. [383, 384], while the comprehensive book [8] reviewed the data up to $\sim$1990. In our work, selected examples of more recent studies will be presented.

Prompt-fission setups described in Section 3.1 can be easily combined with neutron detectors for the correlation measurements of fission fragments and
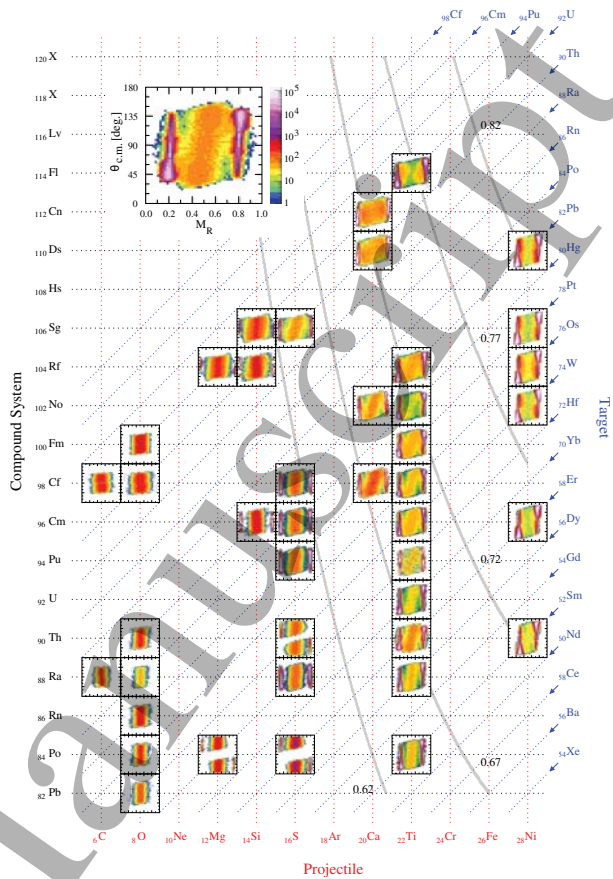
Figure 62. Fission-fragment mass-angle distributions (MADs)[131]. All miniature plots have the same axes as the large MAD (top left, ^{48}Ti+^{170}Er at $E_{\text{beam}} = 225.0$ MeV). The full gray lines correspond to the noted constant values of the effective entrance-channel fissility parameter x_{eff} [381]. The intensity scale represents counts per pixel in the MAD, proportional to $d^2\sigma/d\theta_{\text{c.m.}}.dM_{\text{R}}$.

neutrons to obtain $\bar{\nu}(A)$. Since neutrons are strongly kinematically focused to the fragment directions in the laboratory frame in the reactions in direct kinematics, the assignment to one of the fragments as a neutron-emitter is easily possible, when neutrons are detected along the fragment flight axis within a limited solid angle. By using this method, $\bar{\nu}(A)$ data for thermal-neutron-induced fission of ^{233,235}U and ^{239}Pu were re-measured [385, 386, 387] at the Kyoto University Research Reactor [388]. A liquid scintillation detector (127 mm-diameter$\times$ 51 mm-thickness) was mounted on the axis defined by two fission-fragment detectors, which comprised a multi-wire proportional counter and a silicon detector ($1v$-$1E$ method) [389]. In the measurement, also the neutron-energy spectra from individual fragments were obtained. An example of data for ^{233}U(n$_{\text{th}}$,f) [385] is shown in Fig. 63. While the $\bar{\nu}(A)$ values demonstrate a well-known sawtooth distribution, the average neutron energies $\bar{\eta}(A)$ have a mirror-symmetric distribution around the symmetric

CONTENTS   51

fission split at slightly below $A = 120$. The neutron energies are especially high for the symmetric and large-asymmetric fission fragments. The different shapes of the $\bar{\nu}(A)$ and $\bar{\eta}(A)$ spectra can be explained by nuclear-structure effects of the fission fragments as follows below.

Figure 63(c) shows the level-density parameter, $a(A)$, for fission fragments from the reaction ^{233}U(n_{th}, f), obtained with the formula $\bar{E}^* = aT^2$. The average excitation energy $\bar{E}^*$ and the nuclear temperature T [390] of the fission fragments were determined from the values of $\bar{\nu}$ and $\bar{\eta}$ given in Figs. 63(a) and (b), respectively. The data in Fig. 63(c) exhibit a strong variation as a function of the fragment mass, with sudden drops around the fragments in the vicinity of $A = 125$ and 75. The trend is largely different both from the trend for stable isotopes (shown by the open blue circles) [391] and from the linearly increasing function $a(A) \propto A$ (dashed line), often used in statistical-model calculations. The $a(A)$ values from the neutron-induced fission, ^{233}U(n_{th}, f), confirmed the originally reported similar trend from the ^{252}Cf(sf) measurements [392] carried out at the Central Bureau for Nuclear Measurement (CBNM) in Belgium (now called JRC-IRMM). For the quantitative understanding, the data are compared with the Gilbert-Cameron predictions from [393], where the level-density parameter takes into account the shell-correction energies for neutrons and protons (the red solid line in Fig. 63(c)). Significantly smaller values for nuclei around $A = 125$ can be explained by the large negative shell-correction energies around ^{132}Sn. This analysis provides that simulation of prompt neutron-evaporation requires information on the structure of neutron-rich fission fragments.

Two new detailed measurements of the neutron multiplicity as a function of fragment mass and TKE have recently been performed by the JRC-IRMM group for ^{252}Cf(sf). In the first experiment, reported in [113], a gridded Frisch ionization chamber and a liquid scintillator were used, thus the neutron multiplicity could be measured directly. The second experiment [98] was performed with the $2v$-$2E$ VERDI spectrometer (see Fig. 13 in Section 3.1.1), whereby the neutron multiplicity was derived via an indirect method by calculating the difference between the pre-neutron and post-neutron FFs's masses. The comparison of the measurements in Fig. 64 shows that while the shapes of both distributions are very similar, the indirect values from the $2v$-$2E$ measurement are 15 % larger than those from the direct detection method. Interestingly, the $\bar{\nu}(A)$ data for ^{233}U(n_{th}, f)(Fig. 63(a)) and ^{252}Cf(sf) (Fig. 64) show that the hump at $A \sim 138$ is commonly observed for both reactions.
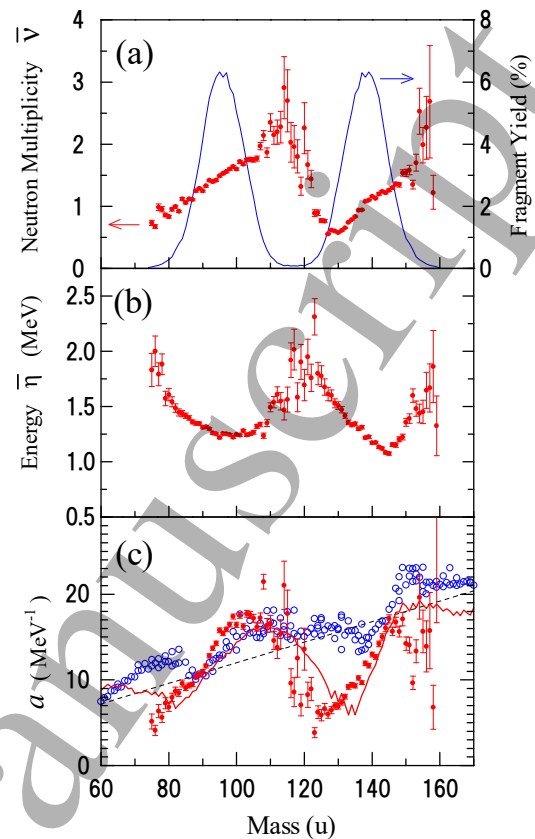
Figure 63. (Color online) Red symbols - the data for the reaction ^{233}U(n_{th}, f) [385]. (a) The prompt-neutron multiplicity $\bar{\nu}(A)$ as a function of the FFs mass (see left ordinate). The respective FFMD is schematically shown by the blue line (right ordinate); (b) Average neutron energy in the c.m. frame, $\bar{\eta}$; (c) The level-density parameter obtained from the fragment-neutron correlation data. The red solid line is the prediction by Gilbert and Cameron [393]. The black dashed line is the linear expression $a(A) = 0.12A$. Open blue circles are the level-density parameters for the stable isotopes [391].

Excitation energy dependence of $\bar{\nu}(A)$. There are only a few experiments that studied the variation of $\bar{\nu}(A)$ as a function of excitation energy. The most precise data have been reported around years 1984-1986 by Müller *et al.* [394] and Naqvi *et al.* [395]. Fig. 65 shows the $\bar{\nu}(A)$ data for neutron-induced fission of ^{237}Np at incoming neutron energies of 0.8 MeV and 5.55 MeV. The total neutron multiplicity increases from 2.73±0.11 to 3.46±0.11 [395]. More importantly, Fig. 65 reveals that this increase appears only in the heavy fragment group, while the prompt-neutron multiplicity in the light fragment group is unchanged within the experimental uncertainties. The same result was obtained in the reaction ^{235}U(n,f) with $E_n = 0.5$ MeV and 5.5 MeV [394]. Furthermore, it was found that the fission-fragment yields remain almost constant, except for an increase of the symmetric fission channel that still stays around the 1% level at

CONTENTS 52
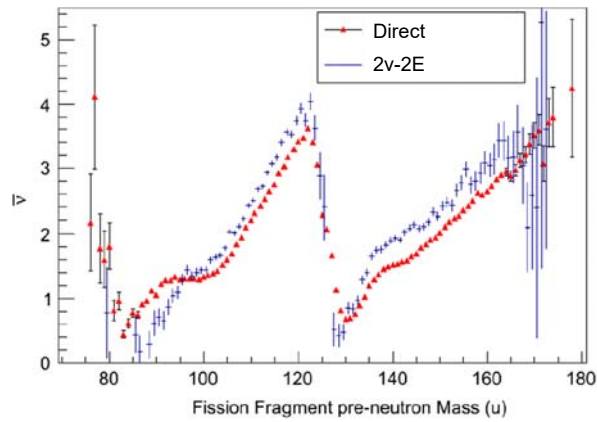
Figure 64. (Color online) Average neutron multiplicity as a function of fission-fragment mass, $\bar{\nu}(A)$ for ^{252}Cf(sf). Filled triangles display the data from the direct neutron-detection method using a liquid organic scintillation detector [113]. The crosses show the results from the $2v$-$2E$ indirect method employed with the VERDI spectrometer [98] with a mass resolution $A/\Delta A \sim 80$. Figure is taken from [98].

the higher energy.

Mainly due to its importance for higher-energy fission in e.g. reactors with fast neutrons, the evolution of $\bar{\nu}(A)$ as a function of excitation energy has recently attracted a renewed interest.
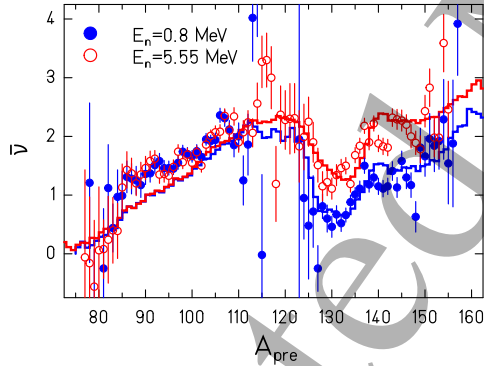
Figure 65. Color online) Measured prompt-neutron multiplicity in ^{237}Np(n,f) as a function of pre-neutron mass at two different incident-neutron energies [395] (colored data points) in comparison with the result of the GEF model (red and blue histograms). The figure is taken from [395].

Figure 66 shows a recent example of prompt-neutron-multiplicity measurements in the reaction $p + {}^{242}\text{Pu} \rightarrow {}^{243}\text{Am}^*$ at three beam energies, leading to appreciably higher excitation energies. The experiment was performed by the Dubna group at the Accelerator Laboratory, University of Jyväskylä, by using the CORSET setup coupled to the time-of-flight neutron-detector array DEMON [396] composed of eight liquid scintillators. Similar to Fig. 65, the

plot demonstrates that as a function of the beam energy (thus, as a function of E^*) the prompt-neutron multiplicities increase only for heavy fragments in the mass region of $120-150$ u, whereas those for the light fragments remain almost unchanged. A similar conclusion was also derived for the reaction $p + {}^{238}\text{U} \rightarrow {}^{239}\text{Np}^*$ in the same study.
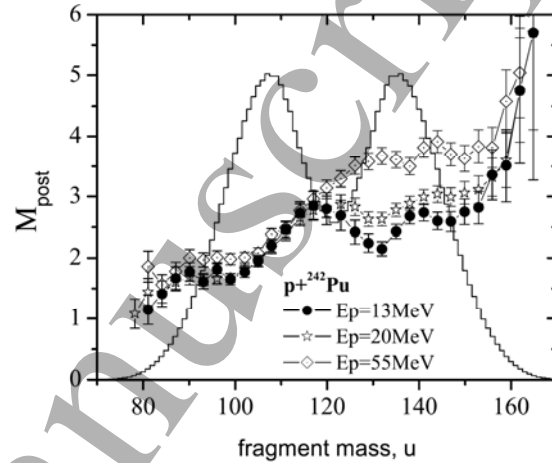
Figure 66. Post-scission neutron multiplicity, M_{post}, as a function of pre-neutron fragment mass for the reaction $p + {}^{242}\text{Pu} \rightarrow {}^{243}\text{Am}^*$ at three proton beam energies. The histogram shows the mass distribution at a proton energy of 20 MeV. The figure is taken from [140].

Energy-sorting hypothesis. Recently, Schmidt and Jurado [284] interpreted the insensitivity of the prompt-neutron yield in the light fission-fragment group to the initial excitation energy found in ^{237}Np(n,f) [395] at $E_n = 0.8$ MeV and 5.55 MeV (see Fig. 65) as a consequence of the peculiar thermodynamical properties of the di-nuclear system before scission. In this energy regime, pairing correlations are expected to persist all the way up to scission. The authors of Ref. [284] were inspired by recent experimental results and theoretical arguments for the presence of a constant nuclear temperature below the critical pairing energy [397, 398]. Following theoretical expectations that the nascent fragments aquire their individual properties well before scission, they claimed that the dinuclear system on the way from the outer saddle to scission behaves like two coupled thermostats [399, 400]. In general, the temperature of the heavier fragment is expected to be lower, because the nuclear temperature is known to be grossly proportional to $A^{-2/3}$ [401] in the superfluid regime. This trend may eventually only be inverted by strong shell effects in mass splits close to symmetry. Since the nascent fragments cannot reach thermal equilibrium, essentially all intrinsic excitation energy moves to the heavy fragment, because it has the lower temperature.

CONTENTS   53

The GEF code [283] that considers this process of entropy-driven energy sorting reproduces the measured data quite well, see Fig. 65.

A priori, it is doubtful, whether the energy-sorting mechanism that was introduced above can be invoked for explaining the insensitivity of the prompt-neutron yield in the light fission-fragment group to the initial excitation energy at the higher excitation energies of the systems shown in Fig. 66.

For the understanding of the data shown in Fig. 66 it is necessary to recall the properties of the fissioning system that have an influence on the prompt neutron emission. With increasing initial excitation energy, the energy available for prompt neutron emission is no longer dominated by the surplus of deformation energy of the fragments at scission compared to the ground-state deformation, but it contains an increasingly important contribution from intrinsic excitation energy at scission. With increasing intrinsic excitation energy, pairing correlations vanish, and the influence of shell effects on the fissioning system diminishes. All this, in turn, modifies the characteristics of the level densities that determine the thermodynamical properties of the system. In detail, the level density shows a transition from the superfluid regime to the independent-particle scenario [397, 398] at the critical pairing energy ($\approx 10\,\mathrm{MeV}$). Thus, the nuclear temperature is not constant any more, and a pre-requisite for the energy-sorting mechanism is not given. The reduction of shell effects leads to a change of the relative yields of the fission channels. In the actinides, the yields of the asymmetric fission channels with their characteristic shapes determined by the relevant fragment shells decrease, while the symmetric fission channel that is favored by the macroscopic nuclear properties takes over. Thus, the shapes of the nascent fragments are no longer influenced by shell effects. As a consequence, the saw-tooth structure in $\bar{\nu}(A)$ is expected to vanish. This is indeed the case for the data from the highest excitation energy in Fig. 66. Moreover, with increasing excitation energy, multi-chance fission sets in (see Figs. 49–50), and, thus, the mass-dependent prompt-neutron multiplicities are a superposition of several contributions, originating from fission of different isotopes at different excitation energies.

Finally, it is noteworthy that the total prompt-neutron multiplicity grows only by about one unit when the incoming-proton energy increases from $20\,\mathrm{MeV}$ to $55\,\mathrm{MeV}$. Thus, only a small part ($\sim 10\,\mathrm{MeV}$) of the additional bombarding energy ($35\,\mathrm{MeV}$) is found in the total excitation energy of the fragments. It may be assumed that the missing energy ($\sim 20\,\mathrm{MeV}$) is consumed by pre-saddle neutron emission, leading to multi-chance fission, and by the emission of

neutrons between saddle and scission [402]. These two processes may appreciably reduce the intrinsic excitation energy of the nascent fragments before scission, with the consequence that the energy-sorting mechanism extends to higher initial excitation energies than expected. Thus, the energy-sorting mechanism may indeed be responsible to some extent for the constant prompt-neutron multiplicity in the light fragment group found in Fig. 66.

To further study this phenomenon experimentally, the use of multi-nucleon transfer reactions would be an ideal tool to measure the excitation-energy dependence of $\bar{\nu}(A)$ (or $M_{post}(A)$) for nuclei further away from the β-stability line. Such experiments are now planned with the JAEA prompt-fission setup, complemented with an array of neutron detectors.

4.6.2. Prompt γ-ray emission from fission fragments.
Most prompt γ rays are emitted following the prompt-neutron emission. The γ-ray energy/multipolarity and multiplicity carry information on the spins of the fragments, which are important for understanding the mechanism of spin generation during fission.

The recent application of highly-efficient, multi-detector $\sim 4\pi$ γ-ray calorimeters in fission studies allowed to obtain a more detailed information. As an example of data from the Crystall Ball setup (see, Sec. 3.2.2), Fig. 67 shows the γ-ray spectra from ^{252}Cf(sf), measured in coincidence with FFs detected in a GIC (Section 3.1.1) [403, 182]. It is seen that the γ-ray spectrum for fission fragments with a mass split around $A_\mathrm{L}/A_\mathrm{H}$=120/132 does not follow the linearly decreasing trend as a function of energy (in logarithmic scale), as it is seen for example for the mass splits around $A_\mathrm{L}/A_\mathrm{H}$=108/144, but shows a hump centered around E_γ=6 MeV. In the further experiments at the CB, the origin of this hump was assigned to heavy fragments in the vicinity of $A\sim132$ by systematically changing the fissioning nuclei and searching for the high-energy structure as a function of the mass split [404]. An explanation of the high-energy component was proposed within the statistical-model framework [405, 182], whereby the small value of the level-density parameter around $A\sim132$ for fission fragments of ^{252}Cf [392] F(see Fig. 63(c) as an example for ^{233}U(n$_\mathrm{th}$,f)) generated the enhancement of the γ-ray spectra between 4 and 8 MeV.

At the LANSCE spallation source, thanks to the enhanced sensitivity of the DANCE γ-ray calorimeter (Section 3.2.2), the prompt γ-ray measurements could be extended up to $E_\gamma\sim9$ MeV as shown in Fig. 68, which provides unfolded γ-ray spectra for the neutron-induced-fission reactions ^{235}U(n,f), ^{239}Pu(n,f), and for ^{252}Cf(sf) [199]. In these spectra, the yields are normalized to each other in the γ-ray energy range

CONTENTS   54
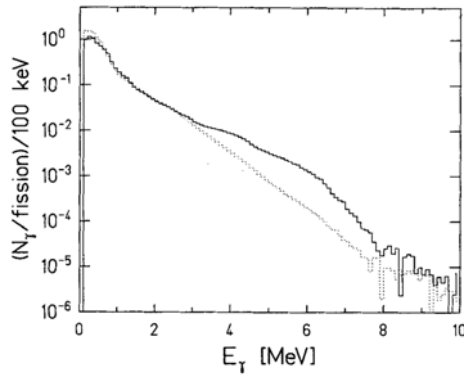
Figure 67. Normalized γ-ray energy spectrum for ^{252}Cf(sf) [182]. The full line is the spectrum in coincidence with fragment mass splits of $(118 < A_L < 122)/(130 < A_H < 134)$. The dotted line is the one in coincidence with $(106 < A_L < 110)/(142 < A_H < 146)$. The figure is taken from [182].

Figure 68. (Color online) The comparison of the unfolded γ-ray energy distributions for the reactions ^{235}U(n,f) (red circles), ^{239}Pu(n,f) (blue squares), and for ^{252}Cf(sf) (black triangles), obtained at DANCE. Figure is taken from [199].

of $1 < E_\gamma < 4$ MeV. Despite the similarity of the shape in this energy interval, distinctly different features can be seen in the spectra above 5 MeV. Since this is the energy region where the γ rays associated with fragments around ^{132}Sn would be more strongly generated (see Fig. 67 for ^{252}Cf(sf)), the difference in the spectra between these nuclei suggests the reaction-dependence of populating the relevant states in FFs'. It is also mentioned in Ref. [199] that pygmy dipole resonances [406, 407] could be the candidates for such states. An alternative possibility is the reaction dependence of the level-density parameters [182, 405] and/or initial excitation energies [408] of fragments around $A \sim 132$ as discussed in the context of Fig. 67. In passing we note that, even with a nearly 4π solid-angle coverage, quite complex corrections for the detector response are essential, via some 'unfolding' procedure with specific assumptions, see e.g. [199].

At KVI(Groningen), the measurements of fission γ rays for ^{252}Cf(sf) were extended up to $E_\gamma = 20$ MeV, using a large-volume γ-ray setup consisting of ten BaF$_2$ (2.6 liter each) and one NaI detectors (diameter 255 mm×length 355 mm) [405]. Fission fragments were detected using PPACs, giving a rough estimate of the fragment masses. A hump structure associated with the giant dipole resonance (GDR) decay was clearly observed for every mass-split bin, and an attempt of its description was undertaken via statistical-model calculations, see details in Ref. [405].

Very recently, a collaboration led by the JAEA fission group performed a dedicated measurement of the γ-ray spectra up to $\sim$20 MeV in thermal-neutron-induced fission of ^{235}U [409]. The experiment was performed at the cold-neutron beam line (PF1B) of the high-flux reactor at ILL, Grenoble [410]. Two large-volume LaBr$_3$(Ce) detectors (diameter
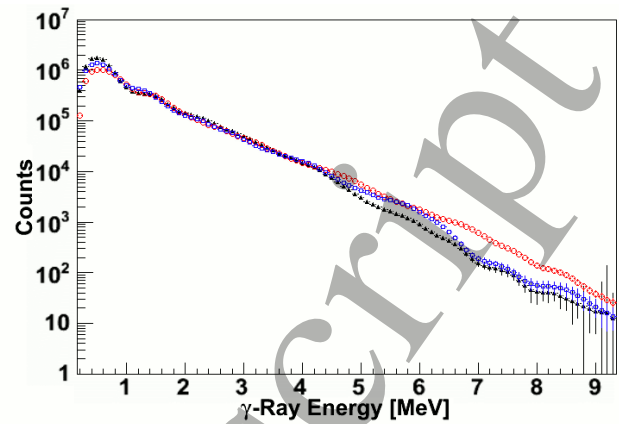
102 mm×thickness 127 mm) [411] coupled with multi-wire proportional counters for fission fragments were used. Although the data analysis is underway, enough coincidence events between FFs and γ rays were registered as to reveal the hump structure around $E_\gamma = 15$ MeV associated with the GDR decay as well as local peaks at $\sim$4 and 6 MeV [409].

Prompt γ-ray spectra for the reactions ^{235}U(n$_{th}$,f) [60], ^{241}Pu(n$_{th}$,f)[61], and ^{252}Cf(sf) [62] were measured by the JRC-IRMM group and collaborators down to the low γ-ray energy region of $E_\gamma \sim 0.1$ MeV using a twin Frisch-gridded ionization chamber coupled with different combinations of high-resolution large-size scintillation crystals of LaBr$_3$, CeBr$_3$ and LaCl$_3$. The experiments were performed at the cold-neutron beam from the 10 MW research reactor of the Budapest Neutron Center [412]. The measured γ-ray multiplicity for ^{241}Pu(n$_{th}$,f) in the low-energy region below $E_\gamma = 0.75$ MeV is shown in Fig. 69. The pronounced periodic structures could be seen for the first time in this reaction, similarly to those observed in 1970's for ^{235}U(n$_{th}$,f), ^{239}Pu(n$_{th}$,f) and ^{252}Cf(sf) [413, 414]. This interesting observation is in contrast to the evaluated data from ENDF/B-VII.1 library [415], see the smoothly varying dotted line in Fig. 69, which does not show any structures and has a much lower magnitude in comparison to the new measurement. In future studies, it would be interested to extract such low-energy spectra for each mass split of the fissionig nucleus.

4.7. Spallation-fission studies for ADS

Spallation reactions, that means interactions of high-energy protons or other light particles with heavy target nuclei, have gained an increasing interest
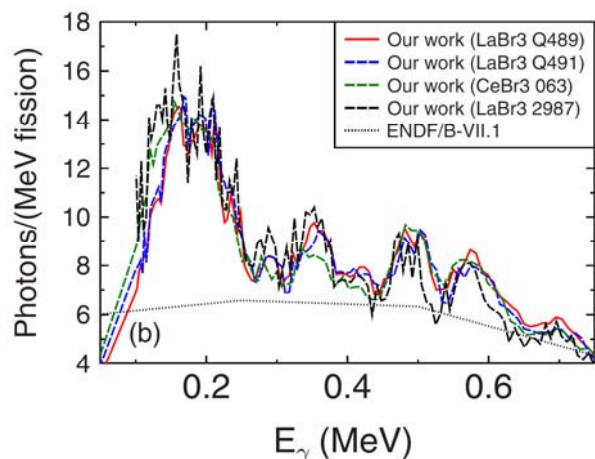
Figure 69. (Color online) The prompt-fission γ-ray spectrum for the reaction ^{241}Pu(n$_{th}$,f) taken with different sets of LaBr$_3$ and CeBr$_3$ detectors. Evaluated data from [415] are shown by the dotted line. Figure is taken from [61].

in the development of accelerator-driven systems (ADS) [416] for the incineration of nuclear waste, in the development of spallation neutron sources [417], in astrophysics [418], and in the preparation of radioactive beams [234, 419, 420]. Thus, by the initiative of Armbruster a campaign of systematic measurements was started in 1996 at GSI, Darmstadt. These studies were performed in inverse kinematics with primary beams, delivered by the SIS18 accelerator, ranging from ^{56}Fe to ^{238}U, interacting with liquid hydrogen and deuterium targets. The fragment separator FRS was used for a full unambiguous identification of the reaction products in Z and A by the ΔE - TOF - Bρ method and for the measurement of their velocity component in beam direction. One product per reaction inside the angular acceptance of the FRS (15 mrad around the beam direction) was detected. The aim was to obtain isotopic production cross sections for a number of systems with an accuracy of about 10% and for an improved understanding of reaction mechanisms at energies up to $1\,A\,$GeV in order to interpolate to other systems and for developing adequate nuclear-reaction models.

In the spallation of the heaviest projectiles, such as ^{197}Au [422, 423], ^{208}Pb [424, 425, 426, 427, 428] and ^{238}U [429, 430, 431, 432, 254, 433], fission was found to form a large fraction of the reaction products. Due to the full identification of all residues in Z and A and the measurement of their kinematical properties, a precise and rather complete information on the reaction process was obtained that provided also valuable information on the fission properties for a large number of nuclei below uranium over a large range of excitation energy.

As an example, Fig. 70 shows a comprehensive
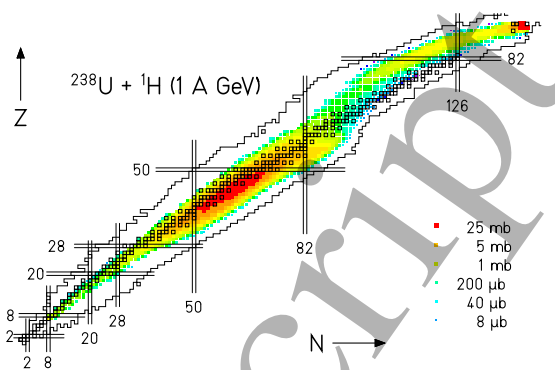
Figure 70. (Color online) Nuclides produced in the reaction ^{238}U $(1\,A\,$GeV$)$ + ^{1}H. The measured cross sections are shown on the chart of the nuclides in a logarithmic color scale. The figure is taken from Ref. [421].
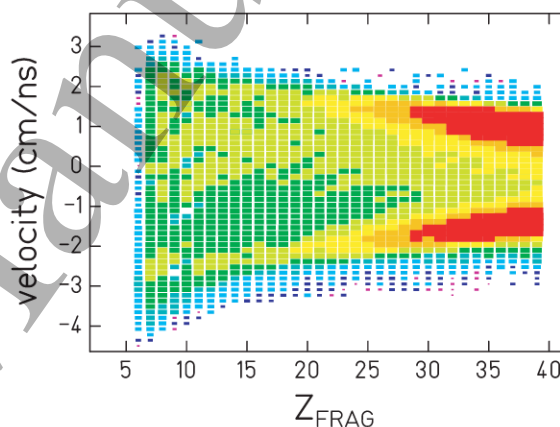
Figure 71. (Color online) Two-dimensional cluster plot of the experimental longitudinal velocities of residues produced in the interaction of $1\,A\,$GeV ^{238}U projectiles with a hydrogen target, including the titanium windows and thermal insulation (87.3 mg/cm^2 H$_2$ + 36.3 mg/cm^2 Ti + 8.3 mg/cm^2 Mylar). The velocity is presented in the beam frame. The figure is taken from Ref. [420] with kind permission of The European Physical Journal (EPJ).

overview of the production of hundreds of nuclei in the spallation of ^{238}U projectiles at $1\,A\,$GeV in an hydrogen target. One can clearly distinguish two main regions: firstly, the predominantly neutron-deficient isotopes of elements above $Z \approx 70$ up to neptunium originating from spallation and consecutive evaporation of light particles [429]. The second extended region includes predominantly neutron-rich isotopes around $Z = 45$, which are produced via symmetric fission [430, 431, 432]. The production extends towards lighter nuclei, reaching down to the detection threshold at $Z = 7$.

The measured velocity distribution of the reaction products is particularly interesting for characterizing the process that is responsible for the production of the

CONTENTS   56

lighter residues. Fig. 71 shows that the Z-dependent velocities below $Z = 40$ are dominated by two ridges in forward and backward direction, respectively. They evolve continuously towards the lighter elements. Note that the broad ridge between the outer narrow ridges with a mean value around $0.5\,\mathrm{cm/ns}$ corresponds to residues produced in the titanium backing of the liquid hydrogen target by multifragmentation [434], thus demonstrating the sensitivity of the experiment to the reaction mechanism. The velocity difference between the forward and the backward component reflects the Coulomb repulsion of the reaction productions (e.g. of the emerging fission fragments), while the mean velocity corresponds to the velocity of the decaying spallation residue that correlates with the impact parameter [429]. The pattern of Fig. 71 is compatible with the population of a spherical shell in velocity space with Z-dependent radius by the binary decay of a heavy nucleus, only slightly lighter than ^{238}U, from which only a forward and a backward portion are measured due to the angular cut of the FRS [432].

This experiment delivered unprecedented detailed information on the binary decay processes of a moderately excited heavy nucleus. The data provide a convincing justification and even demonstrate the need for a unified view of fission and evaporation, as proposed by Moretto and Wozniak [435], while they are traditionally considered as two different processes, described by different formalism that are not compatible. Moreover, they demonstrate that the energy of about $1\,\mathrm{GeV}$ (center-of-mass) is not sufficient for a sizable amount of multifragmentation to occur. Note that the heavy counterparts of the light charged particles appear in the heavy spallation-evaporation component.

A systematic comparison of the nuclide production as a function of the target mass has also been performed for the fission of $1\,A\,\mathrm{GeV}$ ^{208}Pb in reactions with hydrogen, deuterium and titanium [426] and for the fission of $1\,A\,\mathrm{GeV}$ ^{238}U in the same targets [436].

Besides the determination of the individual fission-fragment nuclide cross sections, the experimental conditions in inverse kinematics are also very favorable for measuring the total fission cross section with high precision. This has been exploited in Refs. [437, 438] to determine the total fission cross sections in the reactions ^{208}Pb + ^{1}H at $500\,A\,\mathrm{MeV}$ and ^{238}U + ^{1}H at 545 and $935\,A\,\mathrm{MeV}$ as well as ^{181}Ta + ^{1}H at 300, 500, 800, and $1000\,A\,\mathrm{MeV}$, respectively. In these experiments, both fission fragments were detected with a set-up similar to the one used in Ref. [40] that was able to determine the atomic numbers of both fission fragments.

In continuation of this experimental program, very recently an even more complete characterization of the fission fragments, namely the identification of both fission fragment in Z and A, has been achieved for the system ^{208}Pb + ^{1}H at $500\,A\,\mathrm{MeV}$ [439] by using the same set-up as the SOFIA experiment [71].

The results of these experiments have been and are still being employed for benchmarking and for improving nuclear-reaction models, see for example the intercomparison of model codes for spallation reactions, organized by the IAEA [440], whereby a realistic description of the fission process is of eminent importance.

5. Future developments in fission techniques

5.1. Fission of secondary RIBs at relativistic energies at GSI/FAIR and RIKEN

Fission at SOFIA(GSI) The SOFIA experiment (see Section 3.5.1) has presently only exploited a small part of its potential, while many more systems are accessible to the measurement of the fission-fragment charge/mass distributions via low-energy electromagnetic-induced fission as demonstrated in Fig. 21. In particular, fission of neutron-deficient systems from mercury to polonium is a very promising research topic. SOFIA offers the unique possibility for a systematic survey of the structure effects in this region of the chart of the nuclides, first observed in the βDF of ^{180}Hg [16]. Importantly, in contrast to βDF, the SOFIA-like approach is not restricted to odd-odd nuclei.

Recently, the ALADIN magnet has been replaced by the superconducting dipole GLAD [441], which has a higher field strength. This will make the resolution of position-sensitive detectors to deduce the magnetic rigidity of the fission fragments less crucial in future experiments.

There are plans to extend the choice of systems to be investigated by using a long-lived ^{242}Pu primary beam. This would give access to heavier actinides up to americium. When the future installations at the R3B set-up [442], namely the neutron detector NEULAND [443] and the gamma calorimeter CALIFA [444] will become available for the SOFIA experiment, prompt neutrons and the total energy of the prompt γ rays emitted during the fission process can also be measured directly.

Fission in an electron-ion collider ELISe at FAIR On a longer-term scale, the planned installation of the electron–ion scattering experiment ELISe [445, 446] at the International Facility for Antiproton and Ion Research(FAIR) [447] could allow yet another type of experiments on low-energy fission in inverse kinematics with relativistic secondary beams. In this approach, the RIBs, provided by the future

CONTENTS   57

separator Super-FRS and stored in a dedicated storage ring, will be collided in-ring with a beam of relativistic electrons (0.2 to 0.5 GeV), causing the RIB's excitation via in-elastic scattering and their subsequent fission by means of the (e,e'f) fission mechanism. The measurement of fission fragments in coincidence with an inelastically scattered electron will allow an accurate determination of the excitation energy of the fissioning nucleus, provided a precise determination of the electron energy is performed.

In passing we note that a similar concept of the use of electron scattering from (the low-energy) RIBs is pursued by the SCRIT (Self-Confining Radioactive Isotope Target) collaboration at RIBF-RIKEN, see Ref. [448] and references therein. However, at present, only the experiments with low-energy FFs produced by photofission of ^{238}U and extracted via the ISOL method are considered, for example, for FF charge-radii measurements.

The feasibility of the fission experiments at both facilities is crucially dependent on whether the necessary luminosity can actually be achieved.

Measurements of fission-barrier heights with neutron-rich RIBs via the (p,2pf) reactions with SAMURAI at RIBF-RIKEN The electromagnetic excitation of secondary RIBs in a heavy target that was used in the SOFIA experiment populates a rather broad range of excitation energies, which cannot be narrowed down (see Fig. 17). Therefore, it is considered to exploit the quasi-free (p,2p) scattering channel in collisions of relativistic RIBs with an hydrogen target, where the excitation energy can be determined by measuring the scattered protons. Provided the fission happens in the (p,2pf) channel, the simultaneous measurement of two coincident protons also allows to reduce the random background for proton-FF coincidences. This is the approach taken by the SAMURAI (Superconducting Analyser for MUlti particles from RAdio Isotope beams) collaboration at RIKEN [449] for their planned fission experiments aimed to experimentally determine fission-barrier heights in the neutron-rich nuclei north east of the doubly magic ^{208}Pb [450]. In the experiment, heavy secondary beams will be produced by spallation of a relativistic primary ^{238}U beam (similar to the SOFIA approach) and identified using the magnetic separator BigRIPS [451], before they impact on the secondary hydrogen target installed in front of the large-acceptance spectrometer SAMURAI. The two fission fragments will be detected and analyzed with SAMURAI, while a specially designed silicon tracker at the target position will be exploited to measure protons. One of the difficulties of this approach at RIKEN is that the energy of the primary ^{238}U beam is $\sim 350\,A\,$MeV, which is not as high as at

FRS at GSI, where a beam of $1\,A\,$GeV is used. The lower primary-beam energy results in a lower energy of the secondary beams, which does not allow to obtain fully stripped secondary heavy-ion beams. This, in turn, creates extra difficulties for an unambiguous determination of the fissioning parent nuclei due to their overlapping A/Q values.

5.2. Fission of post-accelerated RIBs in transfer-induced reactions in inverse kinematics at energies around the Coulomb barrier at HIE-ISOLDE (CERN)

A broad range of possibilities for fission and surrogate-reaction type of measurements in inverse kinematics for long isotopic chains of pre-actinide and actinide beams opens up at the ISOL-type radioactive-ion-beam facilities.

The HIE-ISOLDE, a presently performed upgrade to higher intensities and energies up to $10\,A\,$MeV of the existing REX-ISOLDE facility at CERN [452], matches well this kind of experiments. In this approach, the d(RIB,pf) type of inverse-kinematics reaction will be exploited, whereby a post-accelerated radioactive beam from HIE-ISOLDE with an energy around the Coulomb barrier ($\sim$4–5 $A\,$MeV) will be shot on e.g. a deuteron-enriched target. The RIB's excitation to energies close to the top of the fission barrier will occur due to neutron transfer, leading to fission of the resulting compound nucleus. The fission fragments will be measured in coincidence with the outgoing proton by using an active-target approach ACTAR, see details in the approved proposal [453].

In a separate future development, the former Heidelberg TSR storage ring is planned to be moved to HIE-ISOLDE [454]. The use of an internal target and of an additional charge breeder in order to match to the limited magnetic rigidity of the storage ring would help to improve the quality of the experiments by achieving a better precision of the excitation energy after nucleon transfer and by avoiding parasitic reactions in target backings and contaminants [455].

5.3. Recent technical developments for neutron-induced fission research

Historically, neutrons for fission studies were generated by research reactors, such as e.g. the high-flux reactor at the Institute of Laue-Langevin, which reaches a core flux of 1.5×10^{15} n/cm^2/s under 58 MW operation [410]. Several other reactors, such as the Kyoto University Research Reactor [388] and the Budapest Research Reactor [412] are also used for fission research. The recent extensive use of neutron spallation sources opens further possibilities for more detailed and precise fission studies, see also Sec. 3.2.3.

CONTENTS   58

5.3.1. *Prospective fission studies with the FIPPS spectrometer at ILL* The very successful EXILL campaign (see Section 3.2.2) will be perpetuated at ILL with the commissioning and first experiments at the new dedicated instrument called FIPPS (FIssion Product Prompt γ-ray Spectrometer) [456] in the first quarter of 2017. A clover Ge detector array will surround targets irradiated with a halo-free pencil beam of thermal neutrons. In a first phase, a fission trigger will improve the separation between prompt fission γ rays and delayed decay γ rays. In a second phase, the Ge detector array will be complemented by a recoil-tagging system to sort the fission γ rays according to the mass (and nuclear charge) of one of the fragments. A gas-filled recoil separator [457], equipped with a time-projection chamber for individual ray tracing of each recoil event [456], is foreseen to provide simultaneously high acceptance and satisfactory resolution. Moreover, the Ge detector array can be complemented by ancillary detectors such as neutron detectors for the simultaneous study of many fission observables. The target handling at FIPPS is foreseen to accept all kinds of actinide targets, so future systematic studies of these fission systems are solely limited by the availability of appropriate target material (^{229}Th, ^{232,233,235}U, ^{239,241}Pu, ^{242m}Am, ^{243,245,247}Cm, ^{249,251}Cf).

5.3.2. *Neutrons for Science(NSF) facility at SPIRAL(GANIL)* The Neutrons-for-Science (NFS) facility is a component of the SPIRAL2 complex, which is dedicated to the production of very intense radioactive ion beams. It is presently under construction at GANIL in Caen, France [458, 459]. At NFS, a high-power superconducting LINear Accelerator of GANIL (LINAG) will supply deuteron (maximum 40 MeV) and proton (33 MeV) beams to produce neutrons via two different nuclear reactions. A mono-energetic neutron beam up to $E_n \sim 31$ MeV will be produced by the reaction ^{7}Li(p,n)^{7}Be with a thin lithium target of 1–3 mm thickness. On the other hand, neutrons having a 'white' spectrum with 14 MeV on average in zero-degree direction and 40 MeV at the maximum will be generated in the deuteron break-up reaction by impinging the deuteron beam into a thick (10 mm) carbon or beryllium target. A continuous spectrum is generated with an average energy of around 14 MeV at zero degrees, and the impinging deuteron is stopped in the target. The flight-path length, thus the detector-setup position, can be changed between 5 m and 30 m. According to simulations, the use of beryllium instead of carbon allows to gain a factor of 2 in the neutron yield [459].

One of the planned fission measurements at the NFS facility is based on a new 2v-2E fission setup

called FALSTAFF [460]. The kinetic energies will be obtained by using ionization chambers, which also have a ΔE section to measure the FFs energy loss to provide the nuclear charge of light fission fragments. The start and stop signals for the velocity measurements are obtained by detecting electrons, generated when fission fragments pass through a foil and multiplied by a dedicated MWPC designed as a secondary-electron detector.

5.4. Future photofission experiments with brilliant, tunable, high-intensity γ-ray beams

In the near future, next-generation Compton backscattered γ-ray facilities, such as MEGa-ray at LLNL(US) [461] and ELI-NP (Bucharest, Romania) [42], are expected to provide beams with spectral fluxes of $\sim 10^6$ γ/(eV s) and high energy resolution of $\Delta E \approx 1$ keV [214]. The deep sub-barrier photofission studies at such facilities will be an ideal tool for reliable characterization of complex multi-humped potential-energy surfaces in the heavy actinides, including the precise evaluation of the barrier parameters.

6. Some of the open questions in fission studies

There is still a number of open questions in fission. Some of those that are considered to be the most important ones are listed in this section. Not all were addressed in this review, because some are rather old and still cannot be tackled due to unavailable technical capabilities. It is foreseeable, however, that technical progress will allow to address many of those in the near future.

6.1. Fission-fragment properties in scarcely-explored regions

As evidenced by Fig. 5, there is now a rather continuous coverage of fission-fragment properties in low-energy fission from ^{178}Hg to the heaviest elements. However, good-quality and comprehensive data (FF distributions with unambiguous identification in Z and A, total kinetic energies, eventually in coincidence with prompt γ rays and neutrons) only exist for a limited number of nuclei in the actinides rather close to the β-stability line.

The present data in the lead region, albeit considerably extended in the recent years, are very incomplete and give only a fragmentary view. Systematic studies of structural effects in the fission-fragment properties in this region over a broader range of N/Z and excitation energies are highly desirable for establishing a complete empirical systematics that would allow to verify the recent comprehensive theoretical predictions [272, 270]. Such data would test

CONTENTS   59

the potential-energy surface for these light systems, where the shape of the nucleus at the fission barrier is already very close to the shape at scission.

In the region of the heavy elements with masses of $A \sim 240$–260, the studies of the neutron-rich isotopes are of a paramount importance to probe the increasing effects of the ^{132}Sn-like fragments on fission. For example, the sharp change of FFMDs between ^{256}Fm and ^{258}Fm (see Fig. 5) still remains a theoretical and experimental challenge. Furthermore, since fission data in this region exist only for SF decay, the excitation-energy dependence of FFMDs as well as of the fission-barrier heights should be explored in future experiments and compared to calculations [9, 462]. To obtain such fission data, MNT-induced reactions in direct kinematics, described in Section 4.3.1, would be useful, especially by using accessible (but extremely exotic) radioactive actinide targets, e.g. ^{254}Es. To explore more exotic nuclei, however, it is essential to increase the sensitivity of the detection setup, especially the ΔE-E telescope, to identify weak transfer channels generated by populating the neutron-rich nuclei.

By moving towards the region of superheavy nuclei with masses above $\sim$270, in the recent years important new systematic features of the FF mass distributions and fission half-lives have been established [35, 36]. The dominant role of the spherical nuclear shells with Z = 50 and N = 82 and the deformed neutron shell at N = 88 on the mass distributions in low-energy fission have been deduced up to ^{306}122. These are the same shells that have been invoked to be responsible for the asymmetric fission of the lighter actinides [78]. Multimodal (symmetric and asymmetric) fission was found to be present in the range from $A \approx 256$ to $A \approx 276$. Improved precision and a better coverage of fissioning system in this region are hampered by low production rates, an admixture of quasifission and the limited choice of projectile and target combinations to produce such heavy nuclei.

6.2. Needs for signatures of fission dynamics

In the last decade, important progress has been achieved in the measurement and the interpretation of the fission-fragment mass distributions. In this domain, the most comprehensive calculations of the nuclear shape evolution have been made by Möller and Randrup, within the macroscopic-microscopic framework [271] with the Brownian shape-motion method [272]. Their model has yielded remarkably good results in the extended region of fission from around ^{180}Hg [17, 264] up to heavy elements [273, 317, 320]. These calculations are carried out in the limit of highly dissipative collective motion where inertial effects are absent and, furthermore, the method

employs a schematic dissipation tensor. Consequently, neither time scales nor fragment kinetic energies can be addressed at the present stage. The rather good success of this model indicates that the FFMDs seem to reflect mostly the properties of the potential-energy surface, while being rather insensitive to dynamical aspects of the fission process. This would mean that a better understanding of the fission dynamics requires data of different nature. The latter may include the high-resolution simultaneous measurements of several fission observables, like A and Z of the fission fragments, their kinetic energies and angular distributions, as well as the characteristics of prompt neutrons and γ rays for various systems, including the evolution as a function of the initial excitation energy. Specific types of such measurements will be mentioned in the following sections.

6.3. Fission-fragment angular momentum

It is known since long that fission fragments carry a considerable amount of angular momentum [383]. However, there still exist competing theoretical ideas on how the angular momentum of the fission fragments is generated: thermal excitation [435, 463, 464, 465] and/or quantum-mechanical uncertainty [466] of angular-momentum-bearing modes and Coulomb excitation after scission [467]. Also a strong direct coupling between the elongation and all other collective degrees of freedom was considered [468]. Recently, also the importance of the quantum-mechanical uncertainty of the orbital angular momentum has been stressed [469, 470]. The different scenarios have important implications on the fission time [468].

A final decision cannot be made on the basis of the present experimental knowledge. As discussed in the recent review [283], the available data are incomplete, and often not very precise. In particular, results for fragment-mass-dependent γ-ray multiplicities $\bar{M}_\gamma(A)$ are contradictory. More complete and more precise data may help to discriminate between the different ideas. Although a direct experimental proof seems to be difficult, a comparison of measured correlations of the energies and the emission angles of the prompt γ rays emitted from the two fragments with elaborate models may help to solve this question. These models should couple the above-mentioned scenarios for the generation of angular momentum [435, 463, 464, 465, 466, 467] with advanced descriptions of the de-excitation process (e.g. [471, 472, 473]).

6.4. Dissipation and time scales in fission

Dissipation is driving many phenomena in fission, for example odd-even effects, energy sharing, particle emission, and - eventually - fission times. But pinning

CONTENTS   60

down the precise nature of dissipative processes, in particular in low-energy fission, is a difficult task. Some signatures that are intimately connected with dissipation are very pronounced. For example, the prompt neutron and γ-ray emission is driven by the dissipated energy, and the odd-even effect in fission-fragment Z distributions has been related to the degree of pair breaking (quasi-particle excitations) at scission [474, 475, 476]. However, the direct relation to dissipation is generally obscured by other contributions or additional effects. The fragment excitation energy partly consists of other contributions, for example the deformation energy of the nascent fragments and collective excitations, and the odd-even effect is further influenced by the transport of thermal energy between the nascent fragments [21] and possibly by pair breaking at neck rupture [475].

The quantitative interpretation of the odd-even effect in terms of intrinsic excitation energy at scission is still uncertain. A more systematic investigation, for example a better experimental coverage of the excitation-energy dependence of the odd-even effect may help to improve this situation.

Despite a long history of dedicated studies, the fission time scale remains one of the most controversial and least understood in fission. Following the 1992' review by Hilscher and Rossner [22], a comprehensive summary of experimental methods and the discussion of ensuing results was given by Jacquet and Morjean in 2009 in Ref. [26]. We refer the reader to this study for further details, while here we will only stress the main conclusions, some of which could be considered as highly arguable and require further efforts. On the experimental side, four nuclear clock techniques are extensively used for such studies: a) the measurements of the pre-scission prompt particle emission, e.g. neutrons [22, 296], γ rays [23], and charged particles [297]; b) fission mass-angle distributions [18]; c) the fission probablity [298]; and d) atomic methods (the crystal blocking technique, e.g. [24, 25] and the filling of vacancies in the inner electronic shells in the fission fragments [27]). As was already known for a while, and as strongly stressed in the review [26], it is difficult to reconcile the relatively short fission time scales, of the order of $\sim 10^{-20}$ s, deduced from e.g. prompt particle emission, with the much longer (by orders of magnitude) times, derived by the atomic techniques. On the analysis and interpretation side, the review [26] also critically discussed a range of approaches on the extraction of the fission times from the measured prompt particle multiplicities, including the statistical framework with or without the inclusion of friction effects, the Langevin calculations and others. Specifically, a strong sensitivity to many parameters and assumptions, often fitted to different

sets of data and/or observables, was highlighted in [26]. Furthermore, as argued by the authors of [26], the discrepancy in deduced fission times could possibly be explained by a poor sensitivity of pre-scission studies to the very long component in fission, which is expected to occur also theoretically, at least in some studies, as e.g. claimed by the work [477]. However, the recent investigation [300] questioned whether the sensitivity argument can explain this discrepancy.

The issue of incompatibility between the shorter fission times measured by the MAD method [18] and by the atomic techniques [24], when both techniques were applied to the similar type of reactions, was further raised by the ANU group. In particular, their study [18] strongly called for dedicated efforts to clarify the analysis of the data in the crystal blocking method, with the aim to resolve this controversial topic, which is very important for the production of the superheavy elements.

Another open question in fission is the temperature dependence of the nuclear dissipation. Presently, the attempts to use both temperature-dependent and temperature-independent friction are in use, see e.g. Figs.11-13 and relevant references in [26], or some of the recent results derived from the experiments in inverse kinematics, discussed in Sec. 4.2.3. We believe that use of inverse kinematic technique, which allows to produce nuclei in ideal conditions for studies of dissipation, namely the high excitation energy and low angular momentum, is a very promising technique for addressing this important question.

7. Summary and Conclusions

The aim of this review is to summarize considerable progress in fission research, which has been extensively undergoing for the last couple of decades. The recent substantial technological advances in production and detection techniques of exotic nuclei opened up new regions of the Chart of Nuclides, which were hardly accessible by the previous fission studies, and which are situated further away from the traditional area of fission in the actinides and trans-actinides along the β-stability line.

In particular, an extended region of very neutron-deficient mercury-to-thorium isotopes became accessible for the first time for the *low-energy* fission studies, by means of Coulomb-excitation in reactions at relativistic energies in inverse kinematics at SOFIA/FRS at GSI and via the β-delayed fission of selectively laser-ionized and mass-separated radioactive beams at ISOLDE(CERN). Along with the use of traditional fusion-fission reactions with heavy ions, which lead to higher excitation energies, these complementary techniques allow to probe both the isospin and the energy

CONTENTS   61

dependence of fission in this region of nuclei, previously scarcely accessible for such investigations. Due to a very different neutron-to-proton ratio in this region, new fission phenomena could be expected, which was indeed demonstrated by a surprising discovery of a new region of asymmetric fission around ^{180}Hg (N/Z=1.25) in the experiments at ISOLDE. Following these studies, extensive research activities, both on the experimental and on the theory sides, have been initiated by different fission groups around the world; they are summarized in this review.

The unprecedented high-quality data for fission fragments, completely identified in Z and A, by means of reactions in inverse kinematics at FRS(GSI) and VAMOS(GANIL), meet the needs for highly requested higher-precision nuclear data for fast-neutron-induced fission and spallation reactions that allow to estimate the radioactive inventory and the heat production in Generation IV reactors and accelerator-driven systems (ADS), respectively. These novel techniques directly provide the required data and stimulate and constrain the development of appropriate nuclear-reaction models.

A renewed interest to fission studies via few- and/or multi-nucleon transfer reactions with light and heavy ions at energies in the vicinity of the Coulomb barrier opened up new possibilities to probe the excitation-energy dependence of fission probability and fission-fragment mass distributions in the region of neutron-rich isotopes north-east of ^{235}U. By using advanced detection techniques, the fission of long isotopic chains of several elements with $Z=90$-100 could now be systematically investigated, which provides unique data both for basic nuclear science and for nuclear industry. The use of such approaches gives new insights on e.g. the crucial role of multi-chance fission for the proper understanding of experimental fission-fragment mass distributions.

During the last two decades, a substantial progress with the synthesis of the new elements in complete-fusion reactions with heavy ions was reached, whereby the Chart of Nuclides was extended up to the element Og (Oganesson, $Z=118$). In the course of these studies, many new cases of spontaneously-fissioning isotopes were discovered, which are summarised in this review. The systematics of spontaneous-fission half-lives provide a unique proof for the long-predicted increased nuclear stability around the deformed neutron shell at $N=162$, and also the first hints of the enhanced stability by approaching the predicted spherical neutron shell at $N=184$. The important role of orientation effects and of the competition between fusion-fission and quasifission, which strongly reduces the probability of the production of even heavier nuclei, is highlighted.

While the main emphasis of this review was put on the fission-fragment mass and charge distributions, several important complementary fission observables were also analyzed, such as the prompt-neutron and γ-ray energy spectra and multiplicities. A substantial progress in their understanding is anticipated in future studies, due to the advent of modern detection techniques in fission studies, such as the use of highly-efficient γ-ray calorimeters and neutron-detector arrays. Such experiments are expected to provide detailed information on such open questions in fission studies, as e.g. the generation of angular momentum, energy sharing between fragments, fission time scale.

Although this review is primarily dedicated to the experimental advances in nuclear-fission research, several theoretical considerations and results were also mentioned, without any claim for completeness. This was done, because we think that a common view that includes theory is needed to assess the progress in our understanding of nuclear fission.

Some of the open questions addressed in Section 6 are presently tackled by well-focused experiments, whereby novel techniques play an important role. But others require more complex and precise measurements of many different observables in coincidence that cannot yet be realized with the available techniques. These questions and probably some others that will come up will guide the development of experimental fission research in longer terms.

8. Acknowledgments

9. References

[1] Hahn, O. and Strassmann, F. *Naturwissenschaften* **27**, 11–15 (1939).

[2] Karpov, A. V., Kelić, A., and Schmidt, K.-H. *Journal of Physics G: Nuclear and Particle Physics* **35**(3), 035104 (2008).

[3] Bohr, N. and Wheeler, J. A. *Phys. Rev.* **56**, 426–450 Sep (1939).

CONTENTS   62

[4] Strutinsky, V. M. *Nuclear Physics A* **95**(2), 420 – 442 (1967).

[5] Strutinsky, V. M. *Nuclear Physics A* **122**(1), 1 – 33 (1968).

[6] Brack, M., Damgaard, J., Jensen, A. S., Pauli, H. C., Strutinsky, V. M., and Wong, C. Y. *Rev. Mod. Phys.* **44**, 320–405 Apr (1972).

[7] Brosa, U., Grossmann, S., and Müller, A. *Physics Reports* **197**(4), 167 – 262 (1990).

[8] Wagemans, C., editor. *The Nuclear Fission Process.* CRC Press, (1991).

[9] Möller, P., Sierk, A. J., Ichikawa, T., Iwamoto, A., and Mumpower, M. *Phys. Rev. C* **91**, 024310 Feb (2015).

[10] Andreyev, A. N., Huyse, M., and Van Duppen, P. *Rev. Mod. Phys.* **85**, 1541–1559 Oct (2013).

[11] Martin, J.-F., Taieb, J., Chatillon, A., Bélier, G., Boutoux, G., Ebran, A., Gorbinet, T., Grente, L., Laurent, B., Pellereau, E., Alvarez-Pol, H., Audouin, L., Aumann, T., Ayyad, Y., Benlliure, J., Casarejos, E., Cortina Gil, D., Caamaño, M., Farget, F., Fernández Domínguez, B., Heinz, A., Jurado, B., Kelić-Heil, A., Kurz, N., Nociforo, C., Paradela, C., Pietri, S., Ramos, D., Rodríguez-Sànchez, J.-L., Rodríguez-Tajes, C., Rossi, D., Schmidt, K.-H., Simon, H., Tassan-Got, L., Vargas, J., Voss, B., and Weick, H. *The European Physical Journal A* **51**(12), 1–8 (2015).

[12] Itkis, M., Okolovich, V., Rusanov, A., and Smirenkin, G. *Sov. J. Part. Nucl. Phys.* **19**, 301 (1988).

[13] Itkis, M., Kondrat'ev, N., Kotlov, Y., Mul'gin, S., Okolovich, V., Rusanov, A., and Smirenkin, G. *Sov. J. Nucl. Phys.* **47**, 4 (1988).

[14] Itkis, M., Kondrat'ev, N., Mul'gin, S., Okolovich, V., Rusanov, A., and Smirenkin, G. *Sov. J. Nucl. Phys.* **52**, 601 (1990).

[15] Itkis, M., Kondrat'ev, N., Mul'gin, S., Okolovich, V., Rusanov, A., and Smirenkin, G. *Sov. J. Nucl. Phys.* **53**, 757 (1991).

[16] Andreyev, A. N., Elseviers, J., Huyse, M., Van Duppen, P., Antalic, S., Barzakh, A., Bree, N., Cocolios, T. E., Comas, V. F., Diriken, J., Fedorov, D., Fedosseev, V., Franchoo, S., Heredia, J. A., Ivanov, O., Köster, U., Marsh, B. A., Nishio, K., Page, R. D., Patronis, N., Seliverstov, M., Tsekhanovich, I., Van den Bergh, P., Van De Walle, J., Venhart, M., Vermote, S., Veselský, M., Wagemans, C., Ichikawa, T., Iwamoto, A., Möller, P., and Sierk, A. J. *Phys. Rev. Lett.* **105**, 252502 Dec (2010).

[17] Ghys, L., Andreyev, A. N., Huyse, M., Van Duppen, P., Sels, S., Andel, B., Antalic, S., Barzakh, A., Capponi, L., Cocolios, T. E., Derkx, X., De Witte, H., Elseviers, J., Fedorov, D. V., Fedosseev, V. N., Heßberger, F. P., Kalaninová, Z., Köster, U., Lane, J. F. W., Liberati, V., Lynch, K. M., Marsh, B. A., Mitsuoka, S., Möller, P., Nagame, Y., Nishio, K., Ota, S., Pauwels, D., Page, R. D., Popescu, L., Radulov, D., Rajabali, M. M., Randrup, J., Rapisarda, E., Rothe, S., Sandhu, K., Seliverstov, M. D., Sjödin, A. M., Truesdale, V. L., Van Beveren, C., Van den Bergh, P., Wakabayashi, Y., and Warda, M. *Phys. Rev. C* **90**, 041301 Oct (2014).

[18] du Rietz, R., Hinde, D. J., Dasgupta, M., Thomas, R. G., Gasques, L. R., Evers, M., Lobanov, N., and Wakhle, A. *Phys. Rev. Lett.* **106**, 052701 Feb (2011).

[19] Nadtochy, P. N., Ryabov, E. G., Gegechkori, A. E., Anischenko, Y. A., and Adeev, G. D. *Phys. Rev. C* **89**, 014616 Jan (2014).

[20] Bouzid, B., Asghar, M., Djebara, M., and Medkour, M. *Journal of Physics G: Nuclear and Particle Physics* **24**(5), 1029 (1998).

[21] Jurado, B. and Schmidt, K.-H. *Journal of Physics G: Nuclear and Particle Physics* **42**(5), 055101 (2015).

[22] Hilscher, D. and Rossner, H. *Ann. Phys. Fr.* **17**, 471–552 June (1992).

[23] Paul, P. and Thoennessen, M. *Annu. Rev. Nucl. Part. Sci.* **44**, 65–108 (1994).

[24] Andersen, J. U., Chevallier, J., Forster, J. S., Karamian, S. A., Vane, C. R., Beene, J. R., Galindo-Uribarri, A., del Campo, J. G., Krause, H. F., Padilla-Rodal, E., Radford, D., Broude, C., Malaguti, F., and Uguzzoni, A. *Phys. Rev. Lett.* **99**, 162502 Oct (2007).

[25] Morjean, M., Jacquet, D., Charvet, J. L., L'Hoir, A., Laget, M., Parlog, M., Chbihi, A., Chevallier, M., Cohen, C., Dauvergne, D., Dayras, R., Drouart, A., Escano-Rodriguez, C., Frankland, J. D., Kirsch, R., Lautesse, P., Nalpas, L., Ray, C., Schmitt, C., Stodel, C., Tassan-Got, L., Testa, E., and Volant, C. *Phys. Rev. Lett.* **101**, 072701 Aug (2008).

[26] Jacquet, D. and Morjean, M. *Progress in Particle and Nuclear Physics* **63**(1), 155 – 185 (2009).

[27] Frégeau, M. O., Jacquet, D., Morjean, M., Bonnet, E., Chbihi, A., Frankland, J. D., Rivet, M. F., Tassan-Got, L., Dechery, F., Drouart, A., Nalpas, L., Ledoux, X., Parlog, M., Ciortea, C., Dumitriu, D., Fluerasu, D., Gugiu, M., Gramegna, F., Kravchuk, V. L., Marchi, T., Fabris, D., Corsi, A., and Barlini, S. *Phys. Rev. Lett.* **108**, 122701 Mar (2012).

[28] Chatillon, A., Taieb, J., Martin, J.-F., Pellereau, E., Boutoux, G., Gorbinet, T., Grente, L., Belier, G., Laurent, B., Alvarez-Pol, H., Ayyad, Y., Benlliure, J., Caamaño, M., Audouin, L., Casarejos, E., Cortina-Gil, D., Farget, F., Fernandez-Dominguez, B., Heinz, A., Jurado, B., Kelić-Heil, A., Kurz, N., Lindberg, S., Loeher, B., Nociforo, C., Paradela, C., Pietri, S., Ramos, D., Rodriguez-Sanchez, J.-L., Rodriguez-Tajes, C., Rossi, D., Schmidt, K.-H., Simon, H., Tassan-Got, L., Toernqvist, H., Vargas, J., Voss, B., Weick, B., and Yan, Y. *EPJ Web of Conf.* **111**, 08001 (2016).

[29] Gönnenwein, F. *Seminar on Fission VI*, chapter 1. Corsendonk Priory, Belgium (2007).

[30] Tudora, A., Hambsch, F.-J., Giubega, G., and Visan, I. *Nuclear Physics A* **929**, 260 – 292 (2014).

[31] Hoffman, D. C. *Nucl. Phys. A* **502**, 21 – 40 (1989).

[32] Hoffman, D. C. and Lane, M. R. *Radiochimica Acta* **70/71**, 135–145 (1995).

[33] Gönnenwein, F. In *Contribution to the École Joliot Curie, 2014*, (2014).

[34] Kailas, S. and Mahata, K. *Pramana* **83**(6), 851–884 (2014).

[35] Itkis, M. G., Vardaci, E., Itkis, I. M., Knyazheva, G. N., and Kozulin, E. M. *Nuclear Physics A* **944**, 204 – 237 (2015). Special Issue on Superheavy Elements.

[36] Oganessian, Y. T. and Utyonkov, V. K. *Reports on Progress in Physics* **78**(3), 036301 (2015).

[37] Heßberger, F. P. *The European Physical Journal A* **53**(4), 75 (2017).

[38] Flerov, G. N. and Petrjak, K. A. *Phys. Rev.* **58**, 89–89 Jul (1940).

[39] Rodríguez-Tajes, C., Farget, F., Derkx, X., Caamaño, M., Delaune, O., Schmidt, K.-H., Clément, E., Dijon, A., Heinz, A., Roger, T., Audouin, L., Benlliure, J., Casarejos, E., Cortina, D., Doré, D., Fernández-Domínguez, B., Jacquot, B., Jurado, B., Navin, A., Paradela, C., Ramos, D., Romain, P., Salsac, M. D., and Schmitt, C. *Phys. Rev. C* **89**, 024614 Feb (2014).

[40] Schmidt, K.-H., Steinhäuser, S., Böckstiegel, C., Grewe, A., Heinz, A., Junghans, A., Benlliure, J., Clerc, H. G., de Jong, M., Müller, J., Pfützner, M., and Voss, B. *Nucl. Phys. A* **665**(34), 221 – 267 (2000).

[41] Schmidt, K.-H., Benlliure, J., and Junghans, A. R. *Nucl. Phys. A* **693**, 169–189 (2001).

[42] *ELI-NP: http://www.eli-np.ro/.*

CONTENTS   63

[43] Metropolis, N., Bivins, R., Storm, M., Miller, J. M., Friedlander, G., and Turkevich, A. *Phys. Rev.* **110**, 204–219 Apr (1958).

[44] Myers, W. D. *Nuclear Physics A* **296**(1), 177 – 188 (1978).

[45] Konecny, E., Specht, H., and Weber, J. *Physics Letters B* **45**(4), 329 – 331 (1973).

[46] Weber, J., Britt, H. C., Gavron, A., Konecny, E., and Wilhelmy, J. B. *Phys. Rev. C* **13**, 2413–2420 Jun (1976).

[47] Hulet, E. K., Wild, J. F., Dougan, R. J., Lougheed, R. W., Landrum, J. H., Dougan, A. D., Schadel, M., Hahn, R. L., Baisden, P. A., Henderson, C. M., Dupzyk, R. J., Sümmerer, K., and Bethune, G. R. *Phys. Rev. Lett.* **56**, 313–316 Jan (1986).

[48] Hulet, E. K., Wild, J. F., Dougan, R. J., Lougheed, R. W., Landrum, J. H., Dougan, A. D., Baisden, P. A., Henderson, C. M., Dupzyk, R. J., Hahn, R. L., Schädel, M., Sümmerer, K., and Bethune, G. R. *Phys. Rev. C* **40**, 770–784 Aug (1989).

[49] Hulet, E. K., Lougheed, R. W., Landrum, J. H., Wild, J. F., Hoffman, D. C., Weber, J., and Wilhelmy, J. B. *Phys. Rev. C* **21**, 966–971 Mar (1980).

[50] Powers, J. A., Wogman, N. A., and Cobble, J. W. *Phys. Rev.* **152**, 1096–1102 Dec (1966).

[51] Nethaway, D. R., Prindle, A. L., Myers, W. A., Fuqua, W. C., and Kantelo, M. V. *Phys. Rev. C* **16**, 1907–1918 Nov (1977).

[52] Glendenin, L. E., Gindler, J. E., Henderson, D. J., and Meadows, J. W. *Phys. Rev. C* **24**, 2600–2605 Dec (1981).

[53] Crouch, E. A. C. *Atomic Data and Nuclear Data Tables* **19**(5), 417 – 532 (1977).

[54] Laurec, J., Adam, A., de Bruyne, T., Bauge, E., Granier, T., Aupiais, J., Bersillon, O., Petit, G. L., Authier, N., and Casoli, P. *Nuclear Data Sheets* **111**(12), 2965 – 2980 (2010).

[55] Naik, H., Goswami, A., Kim, G. N., Lee, M. W., Kim, K. S., Suryanarayana, S. V., Kim, E. A., Shin, S. G., and Cho, M.-H. *Phys. Rev. C* **86**, 054607 Nov (2012).

[56] Naik, H., Mukerji, S., Crasta, R., Suryanarayana, S. V., Sharma, S. C., and Goswami, A. *Nuclear Physics A* **941**, 16 – 37 (2015).

[57] Nishinaka, I., Nakahara, H., and Nagame, Y. *The European Physical Journal A* **33**(2), 231–236 (2007).

[58] Hambsch, F.-J., Oberstedt, S., Tudora, A., Vladuca, G., and Ruskov, I. *Nuclear Physics A* **726**(34), 248 – 264 (2003).

[59] Hambsch, F.-J., Bryś, T., Gamboni, T., Geerts, W., Göök, A., Matei, C., Oberstedt, S., and Vidali, M. *EPJ Web of Conferences* **62**, 02001 (2013).

[60] Oberstedt, A., Belgya, T., Billnert, R., Borcea, R., Bryś, T., Geerts, W., Göök, A., Hambsch, F.-J., Kis, Z., Martinez, T., Oberstedt, S., Szentmiklosi, L., Takàcs, K., and Vidali, M. *Phys. Rev. C* **87**, 051602 May (2013).

[61] Oberstedt, S., Billnert, R., Belgya, T., Bryś, T., Geerts, W., Guerrero, C., Hambsch, F.-J., Kis, Z., Moens, A., Oberstedt, A., Sibbens, G., Szentmiklosi, L., Vanleeuw, D., and Vidali, M. *Phys. Rev. C* **90**, 024618 Aug (2014).

[62] Oberstedt, A., Billnert, R., Hambsch, F.-J., and Oberstedt, S. *Phys. Rev. C* **92**, 014618 Jul (2015).

[63] Oberstedt, S., Billnert, R., Hambsch, F. J., Lebois, M., Oberstedt, A., and Wilson, J. N. *The European Physical Journal A* **51**(12), 1–9 (2015).

[64] Moll, E., Schrader, H., Siegert, G., Asghar, M., Bocquet, J. P., Bailleul, G., Gautheron, J. P., Greif, J., Crawford, G. I., Chauvin, C., Ewald, H., Wollnik, H., Armbruster, P., Fiebig, G., Lawin, H., and Sistemich, K. *Nuclear Instruments and Methods* **123**(3), 615 – 617 (1975).

[65] Armbruster, P., Asghar, M., Bocquet, J. P., Decker, R., Ewald, H., Greif, J., Moll, E., Pfeiffer, B., Schrader, H., Schussler, F., Siegert, G., and Wollnik, H. *Nuclear Instruments and Methods* **139**, 213 – 222 (1976).

[66] Bail, A., Serot, O., Mathieu, L., Litaize, O., Materna, T., Köster, U., Faust, H., Letourneau, A., and Panebianco, S. *Phys. Rev. C* **84**, 034605 Sep (2011).

[67] Martin, F., Sage, C., Kessedjian, G., Sérot, O., Amouroux, C., Bacri, C., Bidaud, A., Billebaud, A., Capellan, N., Chabod, S., Doligez, X., Faust, H., Köster, U., Letourneau, A., Materna, T., Mathieu, L., Méplan, O., and Panebianco, S. *Nuclear Data Sheets* **119**, 328 – 330 (2014).

[68] Chebboubi, A., Kessedjian, G., Litaize, O., Serot, O., Faust, H., Bernard, D., Blanc, A., Köster, U., Méplan, O., Mutti, P., and Sage, C. *EPJ Web of Conferences* **111**, 08003 (2016).

[69] Chebboubi, A., Kessedjian, G., Litaize, O., Serot, O., Faust, H., Bernard, D., Blanc, A., Köster, U., Méplan, O., Mutti, P., and Sage, C. In *Proc. 14th Int. Conf. Nucl. Reaction Mechanisms, Varenna, 15-19 June 2015*, (2015).

[70] Grabitz, P., Andrianov, V., Bishop, S., Blanc, A., Dubey, S., Echler, A., Egelhof, P., Faust, H., Gönnenwein, F., Gomez-Guzman, J. M., Köster, U., Kraft-Bermuth, S., Mutterer, M., Scholz, P., and Stolte, S. *Journal of Low Temperature Physics* **184**(3), 944–951 (2016).

[71] Boutoux, G., Bélier, G., Chatillon, A., Ebran, A., Gorbinet, T., Laurent, B., Martin, J.-F., Pellereau, E., Taieb, J., Audouin, L., Tassan-Got, L., Jurado, B., Álvarez-Pol, H., Ayyad, Y., Benlliure, J., Caamaño, M., Cortina-Gil, D., Fernández-Domínguez, B., Paradela, C., Rodriguez-Sanchez, J.-L., Vargas, J., Casarejos, E., Heinz, A., Kelić-Heil, A., Kurz, N., Nociforo, C., Pietri, S., Prochazka, A., Rossi, D., Schmidt, K.-H., Simon, H., Voss, B., Weick, H., and Winfield, J. *Physics Procedia* **47**, 166 – 171 (2013). Scientific Workshop on Nuclear Fission Dynamics and the Emission of Prompt Neutrons and Gamma Rays, Biarritz, France, 28-30 November 2012.

[72] Lang, W., Clerc, H.-G., Wohlfarth, H., Schrader, H., and Schmidt, K.-H. *Nuclear Physics A* **345**(1), 34 – 71 (1980).

[73] Britt, H. C., Hoffman, D. C., van der Plicht, J., Wilhelmy, J. B., Cheifetz, E., Dupzyk, R. J., and Lougheed, R. W. *Phys. Rev. C* **30**, 559–565 Aug (1984).

[74] Léguillon, R., Nishio, K., Hirose, K., Makii, H., Nishinaka, I., Orlandi, R., Tsukada, K., Smallcombe, J., Chiba, S., Aritomo, Y., Ohtsuki, T., Tatsuzawa, R., Takaki, N., Tamura, N., Goto, S., Tsekhanovich, I., Petrache, C. M., and Andreyev, A. N. *Physics Letters B* **761**, 125 – 130 (2016).

[75] Nishio, K., Hirose, K., Leguillon, R., Makii, H., Nishinaka, I., Orlandi, R., Smallcombe, J., Tsukada, K., Chiba, S., Ohtsuki, T., Tatsuzawa, R., and Takaki, N. *Physics Procedia* **64**, 140 – 144 (2015). Scientific Workshop on Nuclear Fission Dynamics and the Emission of Prompt Neutrons and Gamma Rays, THEORY-3.

[76] Unik, J. P., Gindler, J. E., Glendenin, L. E., Flynn, K. F., Gorski, A., and Sjoblom, R. K. In *Proc. Symp. Phys. Chem. Fission, Rochester 1973*, volume 2, 19. IAEA, Vienna, (1974).

[77] Nagame, Y. Nakahara, H. *Radiochimica Acta* **100**, 605–614 April (2012).

[78] Wilkins, B. D., Steinberg, E. P., and Chasman, R. R. *Phys. Rev. C* **14**, 1832–1863 Nov (1976).

[79] Konecny, E., Specht, H. J., and Weber, J. In *Proc. Symp. Phys. Chem. Fission, Rochester 1973*, volume 2, 3. IAEA, Vienna, (1974).

[80] Specht, H. J. *Physica Scripta* **10**(A), 21 (1974).

[81] Schmidt, K.-H., Heinz, A., Clerc, H.-G., Blank, B., Brohm,

CONTENTS   64

T., Czajkowski, S., Donzaud, C., Geissel, H., Hanelt, E., Irnich, H., Itkis, M. C., de Jong, M., Junghans, A., Magel, A., Münzenberg, G., Nickel, F., Pfützner, M., Piechaczek, A., Röhl, C., Scheidenberger, C., Schwab, W., Steinhäuser, S., Sümmerer, K., Trinder, W., Voss, B., and Zhdanov, S. V. *Physics Letters B* **325**(34), 313 – 316 (1994).

[82] Taieb, J. *private communication.*

[83] Savajols, H. *Nuclear Instruments and Methods in Physics Research Section B: Beam Interactions with Materials and Atoms* **204**, 146 – 153 (2003). 14th International Conference on Electromagnetic Isotope Separators and Techniques Related to their Applications.

[84] Caamaño, M., Delaune, O., Farget, F., Derkx, X., Schmidt, K.-H., Audouin, L., Bacri, C.-O., Barreau, G., Benlliure, J., Casarejos, E., Chbihi, A., Fernández-Domínguez, B., Gaudefroy, L., Golabek, C., Jurado, B., Lemasson, A., Navin, A., Rejmund, M., Roger, T., Shrivastava, A., and Schmitt, C. *Phys. Rev. C* **88**, 024605 Aug (2013).

[85] Caamaño, M., Farget, F., Delaune, O., Schmidt, K.-H., Schmitt, C., Audouin, L., Bacri, C.-O., Benlliure, J., Casarejos, E., Derkx, X., Fernández-Domínguez, B., Gaudefroy, L., Golabek, C., Jurado, B., Lemasson, A., Ramos, D., Rodríguez-Tajes, C., Roger, T., and Shrivastava, A. *Phys. Rev. C* **92**, 034606 Sep (2015).

[86] Elseviers, J., Andreyev, A. N., Huyse, M., Van Duppen, P., Antalic, S., Barzakh, A., Bree, N., Cocolios, T. E., Comas, V. F., Diriken, J., Fedorov, D., Fedosseev, V. N., Franchoo, S., Ghys, L., Heredia, J. A., Ivanov, O., Köster, U., Marsh, B. A., Nishio, K., Page, R. D., Patronis, N., Seliverstov, M. D., Tsekhanovich, I., Van den Bergh, P., Van De Walle, J., Venhart, M., Vermote, S., Veselský, M., and Wagemans, C. *Phys. Rev. C* **88**, 044321 Oct (2013).

[87] Liberati, V., Andreyev, A. N., Antalic, S., Barzakh, A., Cocolios, T. E., Elseviers, J., Fedorov, D., Fedoseeev, V. N., Huyse, M., Joss, D. T., Kalaninová, Z., Köster, U., Lane, J. F. W., Marsh, B., Mengoni, D., Molkanov, P., Nishio, K., Page, R. D., Patronis, N., Pauwels, D., Radulov, D., Seliverstov, M., Sjödin, M., Tsekhanovich, I., Van den Bergh, P., Van Duppen, P., Venhart, M., and Veselský, M. *Phys. Rev. C* **88**, 044322 Oct (2013).

[88] Truesdale, V. L., Andreyev, A. N., Ghys, L., Huyse, M., Van Duppen, P., Sels, S., Andel, B., Antalic, S., Barzakh, A., Capponi, L., Cocolios, T. E., Derkx, X., De Witte, H., Elseviers, J., Fedorov, D. V., Fedosseev, V. N., Heßberger, F. P., Kalaninová, Z., Köster, U., Lane, J. F. W., Liberati, V., Lynch, K. M., Marsh, B. A., Mitsuoka, S., Nagame, Y., Nishio, K., Ota, S., Pauwels, D., Popescu, L., Radulov, D., Rapisarda, E., Rothe, S., Sandhu, K., Seliverstov, M. D., Sjödin, A. M., Van Beveren, C., Van den Bergh, P., and Wakabayashi, Y. *Phys. Rev. C* **94**, 034308 Sep (2016).

[89] Nishio, K., Ikezoe, H., Nishinaka, I., Mitsuoka, S., Hirose, K., Ohtsuki, T., Watanabe, Y., Aritomo, Y., and Hofmann, S. *Phys. Rev. C* **82**, 044604 Oct (2010).

[90] Swiatecki, W. J. *Physica Scripta* **24**(1B), 113 (1981).

[91] Hinde, D. J., Dasgupta, M., Leigh, J. R., Mein, J. C., Morton, C. R., Newton, J. O., and Timmers, H. *Phys. Rev. C* **53**, 1290–1300 Mar (1996).

[92] Toke, J., Bock, R., Dai, G. X., Gobbi, A., Gralla, S., Hildenbrand, K. D., Kuzminski, J., Müller, W. F. J., Olmi, A., Stelzer, H., Back, B. B., and Bjørnholm, S. *Nuclear Physics A* **440**(2), 327 – 365 (1985).

[93] Schmitt, H. W., Neiler, J. H., and Walter, F. J. *Phys. Rev.* **141**, 1146–1160 Jan (1966).

[94] Wagemans, C., Dematté, L., Pommé, S., and Schillebeeckx, P. *Nuclear Physics A* **597**(2), 188 – 196 (1996).

[95] Gorodisskiy, D. M., Mulgin, S. I., Okolovich, V. N., Rusanov, A. Y., and Zhdanov, S. V. *Physics Letters B* **548**(12), 45 – 51 (2002).

[96] Mulgin, S. I., Okolovich, V. N., and Zhdanova, S. V. *Physics Letters B* **462**(12), 29 – 33 (1999).

[97] Mulgin, S. I., Zhdanov, S. V., Kondratiev, N. A., Kovalchuk, K. V., and Rusanov, A. Y. *Nuclear Physics A* **824**(14), 1 – 23 (2009).

[98] Frégeau, M. O., Oberstedt, S., Gamboni, T., Geerts, W., Hambsch, F.-J., and Vidali, M. *Nuclear Instruments and Methods in Physics Research Section A: Accelerators, Spectrometers, Detectors and Associated Equipment* **817**, 35 – 41 (2016).

[99] Schmitt, H. W., Kiker, W. E., and Williams, C. W. *Phys. Rev.* **137**, B837–B847 (1965).

[100] Weissenberger, E., Geltenbort, P., Oed, A., Gönnenwein, F., and Faust, H. *Nucl. Instrum. Methods A* **248**(23), 506 – 515 (1986).

[101] Neidel, H.-O. and Henschel, H. *Nuclear Instruments and Methods* **178**(1), 137 – 148 (1980).

[102] Bohne, W., Galster, W., Grabisch, K., and Morgenstern, H. *Nuclear Instruments and Methods in Physics Research Section A: Accelerators, Spectrometers, Detectors and Associated Equipment* **240**(1), 145 – 151 (1985).

[103] Wild, J. F., van Aarle, J., Westmeier, W., Lougheed, R. W., Hulet, E. K., Moody, K. J., Dougan, R. J., Koop, E. A., Glaser, R. E., Brandt, R., and Patzelt, P. *Phys. Rev. C* **41**, 640–646 Feb (1990).

[104] Caïtucoli, F., Asghar, M., Leroux, B., Barreau, G., Hamadache, K., Sicre, A., Doan, T. P., and Allab, M. *Nuclear Physics A* **394**(3), 360 – 368 (1983).

[105] Wagemans, C., Allaert, E., Deruytter, A., Barthélémy, R., and Schillebeeckx, P. *Phys. Rev. C* **30**, 218–223 Jul (1984).

[106] Schmidt, R. and Henschel, H. *Nuclear Physics A* **395**(1), 29 – 43 (1983).

[107] Shaughnessy, D. A., Gregorich, K. E., Adams, J. L., Lane, M. R., Laue, C. A., Lee, D. M., McGrath, C. A., Ninov, V., Patin, J. B., Strellis, D. A., Sylwester, E. R., Wilk, P. A., and Hoffman, D. C. *Phys. Rev. C* **65**, 024612 (2002).

[108] Yanez, R., Yao, L., King, J., Loveland, W., Tovesson, F., and Fotiades, N. *Phys. Rev. C* **89**, 051604 May (2014).

[109] Straede, C., Budtz-Jørgensen, C., and Knitter, H.-H. *Nuclear Physics A* **462**(1), 85 – 108 (1987).

[110] Ryzhov, I. V., Yavshits, S. G., Tutin, G. A., Kovalev, N. V., Saulski, A. V., Kudryashev, N. A., Onegin, M. S., Vaishnene, L. A., Gavrikov, Y. A., Grudzevich, O. T., Simutkin, V. D., Pomp, S., Blomgren, J., Österlund, M., Andersson, P., Bevilacqua, R., Meulders, J. P., and Prieels, R. *Phys. Rev. C* **83**, 054603 May (2011).

[111] Al-Adili, A., Hambsch, F.-J., Pomp, S., and Oberstedt, S. *Phys. Rev. C* **86**, 054601 Nov (2012).

[112] Al-Adili, A., Hambsch, F.-J., Pomp, S., Oberstedt, S., and Vidali, M. *Phys. Rev. C* **93**, 034603 Mar (2016).

[113] Göök, A., Hambsch, F.-J., and Vidali, M. *Phys. Rev. C* **90**, 064611 Dec (2014).

[114] Budtz-Jørgensen, C., Knitter, H.-H., Straede, C., Hambsch, F.-J., and Vogt, R. *Nuclear Instruments and Methods in Physics Research Section A: Accelerators, Spectrometers, Detectors and Associated Equipment* **258**(2), 209 – 220 (1987).

[115] Simon, G., Trochon, J., Brisard, F., and Signarbieux, C. *Nuclear Instruments and Methods in Physics Research Section A: Accelerators, Spectrometers, Detectors and Associated Equipment* **286**(1), 220 – 229 (1990).

[116] Paradela, C., Tassan-Got, L., Audouin, L., Berthier, B., Duran, I., Ferrant, L., Isaev, S., Le Naour, C., Stephan, C., Tarrío, D., Trubert, D., Abbondanno, U., Aerts, G., Álvarez, H., Álvarez-Velarde, F., Andriamonje,

CONTENTS   65

S., Andrzejewski, J., Assimakopoulos, P., Badurek, G., Baumann, P., Bečvář, F., Berthoumieux, E., Calviño, F., Calviani, M., Cano-Ott, D., Capote, R., Carrapiço, C., Cennini, P., Chepel, V., Chiaveri, E., Colonna, N., Cortes, G., Couture, A., Cox, J., Dahlfors, M., David, S., Dillmann, I., Domingo-Pardo, C., Dridi, W., Eleftheriadis, C., Embid-Segura, M., Ferrari, A., Ferreira-Marques, R., Fujii, K., Furman, W., Goncalves, I., González-Romero, E., Gramegna, F., Guerrero, C., Gunsing, F., Haas, B., Haight, R., Heil, M., Herrera-Martinez, A., Igashira, M., Jericha, E., Kadi, Y., Käppeler, F., Karadimos, D., Karamanis, D., Kerveno, M., Koehler, P., Kossionides, E., Krtička, M., Lampoudis, C., Leeb, H., Lindote, A., Lopes, I., Lozano, M., Lukic, S., Marganiec, J., Marrone, S., Martínez, T., Massimi, C., Mastinu, P., Mengoni, A., Milazzo, P. M., Moreau, C., Mosconi, M., Neves, F., Oberhummer, H., O'Brien, S., Oshima, M., Pancin, J., Papachristodoulou, C., Papadopoulos, C., Patronis, N., Pavlik, A., Pavlopoulos, P., Perrot, L., Pigni, M. T., Plag, R., Plompen, A., Plukis, A., Poch, A., Praena, J., Pretel, C., Quesada, J., Rauscher, T., Reifarth, R., Rubbia, C., Rudolf, G., Rullhusen, P., Salgado, J., Santos, C., Sarchiapone, L., Savvidis, I., Tagliente, G., Tain, J. L., Tavora, L., Terlizzi, R., Vannini, G., Vaz, P., Ventura, A., Villamarin, D., Vincente, M. C., Vlachoudis, V., Vlastou, R., Voss, F., Walter, S., Wiescher, M., and Wisshak, K. *Phys. Rev. C* **82**, 034601 Sep (2010).

[117] Calviani, M., Cennini, P., Karadimos, D., Ketlerov, V., Konovalov, V., Furman, W., Goverdowski, A., Vlachoudis, V., and Zanini, L. *Nuclear Instruments and Methods in Physics Research Section A: Accelerators, Spectrometers, Detectors and Associated Equipment* **594**(2), 220 – 227 (2008).

[118] Frégeau, M. O., Oberstedt, S., Bryš, T., Gamboni, T., Geerts, W., Hambsch, F.-J., Oberstedt, A., and Vidali, M. *Nuclear Instruments and Methods in Physics Research Section A: Accelerators, Spectrometers, Detectors and Associated Equipment* **791**, 58 – 64 (2015).

[119] Beliuskina, O., Strekalovsky, A. O., Aleksandrov, A. A., Aleksandrova, I. A., Devaraja, H. M., Heinz, C., Heinz, S., Hofmann, S., Ilich, S., Imai, N., Kamanin, D. V., Kis, M., Knyazheva, G. N., Kozhuharov, C., Kuznetsova, E. A., Maurer, J., Mishinsky, G. V., Pomorski, M., Pyatkov, Yu. V., Strekalovsky, O. V., Trger, M., and Zhuchko, V. E. *Eur. Phys. J. A* **53**(2), 32 (2017).

[120] Nishio, K., Ikezoe, H., Mitsuoka, S., Nishinaka, I., Nagame, Y., Watanabe, Y., Ohtsuki, T., Hirose, K., and Hofmann, S. *Phys. Rev. C* **77**, 064607 Jun (2008).

[121] Nishio, K., Hofmann, S., Heßberger, F. P., Ackermann, D., Antalic, S., Aritomo, Y., Comas, V. F., Düllmann, C. E., Gorshkov, A., Graeger, R., Hagino, K., Heinz, S., Heredia, J. A., Hirose, K., Ikezoe, H., Khuyagbaatar, J., Kindler, B., Kojouharov, I., Lommel, B., Mann, R., Mitsuoka, S., Nagame, Y., Nishinaka, I., Ohtsuki, T., Popeko, A. G., Saro, S., Schädel, M., Türler, A., Watanabe, Y., Yakushev, A., and Yeremin, A. V. *Phys. Rev. C* **82**, 024611 Aug (2010).

[122] Khuyagbaatar, J., Nishio, K., Hofmann, S., Ackermann, D., Block, M., Heinz, S., Heßberger, F. P., Hirose, K., Ikezoe, H., Kinlder, B., Lommel, B., Makii, H., Mitsuoka, S., Nishinaka, I., Ohtsuki, T., Wakabayashi, Y., and Yan, S. *Phys. Rev. C* **86**, 064602 Dec (2012).

[123] Nishio, K., Mitsuoka, S., Nishinaka, I., Makii, H., Wakabayashi, Y., Ikezoe, H., Hirose, K., Ohtsuki, T., Aritomo, Y., and Hofmann, S. *Phys. Rev. C* **86**, 034608 Sep (2012).

[124] Nishio, K., Andreyev, A. N., Chapman, R., Derkx, X.,

Düllmann, C. E., Ghys, L., Heßberger, F., Hirose, K., Ikezoe, H., Khuyagbaatar, J., Kindler, B., Lommel, B., Makii, H., Nishinaka, I., Ohtsuki, T., Pain, S., Sagaidak, R., Tsekhanovich, I., Venhart, M., Wakabayashi, Y., and Yan, S. *Physics Letters B* **748**, 89 – 94 (2015).

[125] Hirose, K. and Nishio, K. *to be submitted* (2016).

[126] Hinde, D. J., Thomas, R. G., du Rietz, R., Diaz-Torres, A., Dasgupta, M., Brown, M. L., Evers, M., Gasques, L. R., Rafiei, R., and Rodriguez, M. D. *Phys. Rev. Lett.* **100**, 202701 May (2008).

[127] Hinde, D. J., du Rietz, R., Dasgupta, M., Thomas, R. G., and Gasques, L. R. *Phys. Rev. Lett.* **101**, 092701 Aug (2008).

[128] Rafiei, R., Thomas, R. G., Hinde, D. J., Dasgupta, M., Morton, C. R., Gasques, L. R., Brown, M. L., and Rodriguez, M. D. *Phys. Rev. C* **77**, 024606 Feb (2008).

[129] Thomas, R. G., Hinde, D. J., Duniec, D., Zenke, F., Dasgupta, M., Brown, M. L., Evers, M., Gasques, L. R., Rodriguez, M. D., and Diaz-Torres, A. *Phys. Rev. C* **77**, 034610 Mar (2008).

[130] Lin, C. J., du Rietz, R., Hinde, D. J., Dasgupta, M., Thomas, R. G., Brown, M. L., Evers, M., Gasques, L. R., and Rodriguez, M. D. *Phys. Rev. C* **85**, 014611 Jan (2012).

[131] du Rietz, R., Williams, E., Hinde, D. J., Dasgupta, M., Evers, M., Lin, C. J., Luong, D. H., Simenel, C., and Wakhle, A. *Phys. Rev. C* **88**, 054618 Nov (2013).

[132] Williams, E., Hinde, D. J., Dasgupta, M., du Rietz, R., Carter, I. P., Evers, M., Luong, D. H., McNeil, S. D., Rafferty, D. C., Ramachandran, K., and Wakhle, A. *Phys. Rev. C* **88**, 034611 Sep (2013).

[133] Hammerton, K., Kohley, Z., Hinde, D. J., Dasgupta, M., Wakhle, A., Williams, E., Oberacker, V. E., Umar, A. S., Carter, I. P., Cook, K. J., Greene, J., Jeung, D. Y., Luong, D. H., McNeil, S. D., Palshetkar, C. S., Rafferty, D. C., Simenel, C., and Stiefel, K. *Phys. Rev. C* **91**, 041602 Apr (2015).

[134] Khuyagbaatar, J., Hinde, D. J., Carter, I. P., Dasgupta, M., Düllmann, C. E., Evers, M., Luong, D. H., du Rietz, R., Wakhle, A., Williams, E., and Yakushev, A. *Phys. Rev. C* **91**, 054608 May (2015).

[135] Itkis, M. G., Calabretta, L., Hanappe, F., Itkis, Y. M., Kelic, A., Kondratiev, N. A., Kozulin, E. M., Oganessian, Y. T., Pokrovsky, I. V., Prokhorova, E. V., Rudolf, G., Rusanov, A. Y., and Stuttge, L. *Nuclear Physics A* **654**(1, Supplement 1), 870c – 877c (1999).

[136] Pokrovsky, I. V., Calabretta, L., Itkis, M. G., Kondratiev, N. A., Kozulin, E. M., Maiolino, C., Prokhorova, E. V., Rusanov, A. Y., and Tretyakova, S. P. *Phys. Rev. C* **60**, 041304 Sep (1999).

[137] Kondratiev, N., Kozulin, E., Pokrovski, I., and Prokhorova, E. V. *Proceedings of the Fourth International Conference on Dynamical Aspects of Nuclear Fission (DANF98), Casta-Papiernicka, Slovak Republic, 1998* , 431 (2000).

[138] Pokrovsky, I. V., Itkis, M. G., Itkis, J. M., Kondratiev, N. A., Kozulin, E. M., Prokhorova, E. V., Salamatin, V. S., Pashkevich, V. V., Mulgin, S. I., Rusanov, A. Y., Zhdanov, S. V., Chubarian, G. G., Hurst, B. J., Schmitt, R. P., Agodi, C., Bellia, G., Calabretta, L., Lukashin, K., Maiolino, C., Kelic, A., Rudolf, G., Stuttge, L., and Hanappe, F. *Phys. Rev. C* **62**, 014615 Jun (2000).

[139] Chizhov, A. Y., Itkis, M. G., Itkis, I. M., Kniajeva, G. N., Kozulin, E. M., Kondratiev, N. A., Pokrovsky, I. V., Sagaidak, R. N., Voskressensky, V. M., Yeremin, A. V., Corradi, L., Gadea, A., Latina, A., Stefanini, A. M., Szilner, S., Trotta, M., Vinodkumar, A. M., Beghini, S., Montagnoli, G., Scarlassara, F., Rusanov, A. Y.,

CONTENTS   66

Hanappe, F., Dorvaux, O., Rowley, N., and Stuttgé, L. *Phys. Rev. C* **67**, 011603 Jan (2003).

[140] Kniajeva, G. N., Krupa, L., Bogachev, A. A., Chubarian, G. G., Dorvaux, O., Itkis, I. M., Itkis, M. G., Kliman, J., Khlebnikov, S., Kondratiev, N. A., Kozulin, E. M., Lyapin, V., Materna, T., Pokrovsky, I. V., Rubchenya, V. A., Trzaska, W. H., Vakhtin, D., and Voskressenski, V. M. *Nuclear Physics A* **734, Supplement**, E25 – E28 (2004). Proceedings of the Eighth International Conference on Nucleus-Nucleus Collisions (NN2003).

[141] Rubchenya, V. A., Trzaska, W. H., Itkis, I. M., Itkis, M. G., Kliman, J., Kniajeva, G. N., Kondratiev, N. A., Kozulin, E. M., Krupa, L., Pokrovski, I. V., Voskressenski, V. M., Hanappe, F., Materna, T., Dorvaux, O., Stuttge, L., Chubarian, G., Khlebnikov, S. V., Vakhtin, D. N., and Lyapin, V. G. *Nuclear Physics A* **734**, 253 – 256 (2004). Proceedings of the Eighth International Conference On Nucleus-Nucleus Collisions.

[142] Knyazheva, G. N., Kozulin, E. M., Sagaidak, R. N., Chizhov, A. Y., Itkis, M. G., Kondratiev, N. A., Voskressensky, V. M., Stefanini, A. M., Behera, B. R., Corradi, L., Fioretto, E., Gadea, A., Latina, A., Szilner, S., Trotta, M., Beghini, S., Montagnoli, G., Scarlassara, F., Haas, F., Rowley, N., Gomes, P. R. S., and Toledo, A. S. d. *Phys. Rev. C* **75**, 064602 Jun (2007).

[143] Prokhorova, E. V., Bogachev, A. A., Itkis, M. G., Itkis, I. M., Knyazheva, G. N., Kondratiev, N. A., Kozulin, E. M., Krupa, L., Oganessian, Y. T., Pokrovsky, I. V., Pashkevich, V. V., and Rusanov, A. Y. *Nuclear Physics A* **802**(14), 45 – 66 (2008).

[144] Kozulin, E. M., Bogachev, A. A., Itkis, M. G., Itkis, I. M., Knyazheva, G. N., Kondratiev, N. A., Krupa, L., Pokrovsky, I. V., and Prokhorova, E. V. *Instruments and Experimental Techniques* **51**(1), 44–58 (2011).

[145] Kozulin, E. M., Knyazheva, G. N., Itkis, I. M., Itkis, M. G., Bogachev, A. A., Chernysheva, E. V., Krupa, L., Hanappe, F., Dorvaux, O., Stuttgé, L., Trzaska, W. H., Schmitt, C., and Chubarian, G. *Phys. Rev. C* **90**, 054608 Nov (2014).

[146] Itkis, I. M., Kozulin, E. M., Itkis, M. G., Knyazheva, G. N., Bogachev, A. A., Chernysheva, E. V., Krupa, L., Oganessian, Y. T., Zagrebaev, V. I., Rusanov, A. Y., Gönnenwein, F., Dorvaux, O., Stuttgé, L., Hanappe, F., Vardaci, E., and de Goés Brennand, E. *Phys. Rev. C* **83**, 064613 Jun (2011).

[147] Dubey, R., Sugathan, P., Jhingan, A., Kaur, G., Mukul, I., Mohanto, G., Siwal, D., Saneesh, N., Banerjee, T., Thakur, M., Mahajan, R., Kumar, N., and Chatterjee, M. B. *Physics Letters B* **752**, 338 – 343 (2016).

[148] Shamlath, A., Shareef, M., Prasad, E., Sugathan, P., Thomas, R. G., Jhingan, A., Appannababu, S., Nasirov, A. K., Vinodkumar, A. M., Varier, K. M., Yadav, C., Babu, B. R. S., Nath, S., Mohanto, G., Mukul, I., Singh, D., and Kailas, S. *Nuclear Physics A* **945**, 67 – 79 (2016).

[149] Mukul, I., Nath, S., Golda, K. S., Jhingan, A., Gehlot, J., Prasad, E., Kalkal, S., Naik, M. B., Banerjee, T., Varughese, T., Sugathan, P., Madhavan, N., and Pal, S. *Phys. Rev. C* **92**, 054606 Nov (2015).

[150] Appannababu, S., Thomas, R. G., Danu, L. S., Rath, P. K., Gupta, Y. K., John, B. V., Nayak, B. K., Biswas, D. C., Saxena, A., Mukherjee, S., and Choudhury, R. K. *Phys. Rev. C* **83**, 067601 Jun (2011).

[151] Ghosh, T. K., Pal, S., Sinha, T., Chattopadhyay, S., Golda, K. S., and Bhattacharya, P. *Nuclear Instruments and Methods in Physics Research Section A: Accelerators, Spectrometers, Detectors and Associated Equipment* **540**(23), 285 – 294 (2005).

[152] Ghosh, T. K., Pal, S., Sinha, T., Chattopadhyay, S., Bhattacharya, P., Biswas, D. C., and Golda, K. S. *Phys. Rev. C* **70**, 011604 Jul (2004).

[153] Ghosh, T. K., Banerjee, K., Bhattacharya, C., Bhattacharya, S., Kundu, S., Mali, P., Meena, J. K., Mukherjee, G., Mukhopadhyay, S., Rana, T. K., Bhattacharya, P., and Golda, K. S. *Phys. Rev. C* **79**, 054607 May (2009).

[154] Ghosh, T. K., Pal, S., Sinha, T., Majumdar, N., Chattopadhyay, S., Bhattacharya, P., Saxena, A., Sahu, P. K., Golda, K. S., and Datta, S. K. *Phys. Rev. C* **69**, 031603 Mar (2004).

[155] Prasad, E., Varier, K. M., Thomas, R. G., Sugathan, P., Jhingan, A., Madhavan, N., Babu, B. R. S., Sandal, R., Kalkal, S., Appannababu, S., Gehlot, J., Golda, K. S., Nath, S., Vinodkumar, A. M., Ajith Kumar, B. P., John, B. V., Mohanto, G., Musthafa, M. M., Singh, R., Sinha, A. K., and Kailas, S. *Phys. Rev. C* **81**, 054608 May (2010).

[156] Yadav, C., Thomas, R. G., Choudhury, R. K., Sugathan, P., Jhingan, A., Appannababu, S., Golda, K. S., Singh, D., Mukul, I., Gehlot, J., Prasad, E., and Wollersheim, H. J. *Phys. Rev. C* **86**, 034606 Sep (2012).

[157] Banerjee, K., Ghosh, T. K., Bhattacharya, S., Bhattacharya, C., Kundu, S., Rana, T. K., Mukherjee, G., Meena, J. K., Sadhukhan, J., Pal, S., Bhattacharya, P., Golda, K. S., Sugathan, P., and Singh, R. P. *Phys. Rev. C* **83**, 024605 Feb (2011).

[158] Pullanhiotan, S. *Journal of Physics: Conference Series* **755**(1), 012007 (2016).

[159] Sugathan, P., Jhingan, A., Golda, K. S., Varughese, T., Venkataramanan, S., Saneesh, N., Satyanarayana, V. V., Suman, S. K., Antory, J., Shanti, R., Singh, K., Saini, S. K., Gupta, A., Kothari, A., Barua, P., Kumar, R., Zacharias, J., Singh, R. P., Behera, B. R., Mandal, S. K., Govil, I. M., and Bhowmik, R. K. *Pramana* **83**(5), 807–815 (2014).

[160] Tripathi, R., Sodaye, S., Sudarshan, K., Nayak, B. K., Jhingan, A., Pujari, P. K., Mahata, K., Santra, S., Saxena, A., Mirgule, E. T., and Thomas, R. G. *Phys. Rev. C* **92**, 024610 Aug (2015).

[161] Matsuda, M., Nakanoya, T., Hanashima, S., and Takeuchi, S. *Nuclear Instruments and Methods in Physics Research Section A: Accelerators, Spectrometers, Detectors and Associated Equipment* **654**(1), 45 – 51 (2011).

[162] Jhingan, A. *Pramana* **85**(3), 483–495 (2015).

[163] Back, B. B., Hansen, O., Britt, H. C., and Garrett, J. D. *Phys. Rev. C* **9**, 1924–1947 May (1974).

[164] Back, B. B., Britt, H. C., Hansen, O., Leroux, B., and Garrett, J. D. *Phys. Rev. C* **10**, 1948–1965 Nov (1974).

[165] Gavron, A., Britt, H. C., Konecny, E., Weber, J., and Wilhelmy, J. B. *Phys. Rev. C* **13**, 2374–2384 Jun (1976).

[166] Petit, M., Aiche, M., Barreau, G., Boyer, S., Carjan, N., Czajkowski, S., Dassié, D., Grosjean, C., Guiral, A., Haas, B., Karamanis, D., Misicu, S., Rizea, C., Saintamon, F., Andriamonje, S., Bouchez, E., Gunsing, F., Hurstel, A., Lecoz, Y., Lucas, R., Theisen, C., Billebaud, A., Perrot, L., and Bauge, E. *Nuclear Physics A* **735**(34), 345 – 371 (2004).

[167] Kessedjian, G., Jurado, B., Aiche, M., Barreau, G., Bidaud, A., Czajkowski, S., Dassié, D., Haas, B., Mathieu, L., Audouin, L., Capellan, N., Tassan-Got, L., Wilson, J. N., Berthoumieux, E., Gunsing, F., Theisen, C., Serot, O., Bauge, E., Ahmad, I., Greene, J. P., and Janssens, R. V. F. *Physics Letters B* **692**(5), 297 – 301 (2010).

[168] Desai, V. V., Nayak, B. K., Saxena, A., Biswas, D. C., Mirgule, E. T., John, B., Santra, S., Gupta, Y. K., Danu, L. S., Prajapati, G. K., Joshi, B. N., Mukhopadhyay, S., Kailas, S., Pujari, P. K., Kumar, A.,

CONTENTS 67

Patel, D., Mukherjee, S., and Prajapati, P. M. *Phys. Rev. C* **87**, 034604 Mar (2013).

[169] Hughes, R. O., Beausang, C. W., Ross, T. J., Burke, J. T., Casperson, R. J., Cooper, N., Escher, J. E., Gell, K., Good, E., Humby, P., McCleskey, M., Saastimoinen, A., Tarlow, T. D., and Thompson, I. J. *Phys. Rev. C* **90**, 014304 Jul (2014).

[170] Casperson, R. J., Burke, J. T., Scielzo, N. D., Escher, J. E., McCleskey, E., McCleskey, M., Saastamoinen, A., Spiridon, A., Ratkiewicz, A., Blanc, A., Kurokawa, M., and Pizzone, R. G. *Phys. Rev. C* **90**, 034601 Sep (2014).

[171] Csige, L., Csatlós, M., Faestermann, T., Gulyás, J., Habs, D., Hertenberger, R., Hunyadi, M., Krasznahorkay, A., Maier, H. J., Thirolf, P. G., and Wirth, H.-F. *Phys. Rev. C* **85**, 054306 May (2012).

[172] Escher, J. E., Burke, J. T., Dietrich, F. S., Scielzo, N. D., Thompson, I. J., and Younes, W. *Rev. Mod. Phys.* **84**, 353–397 Mar (2012).

[173] Simutkin, V. D., Pomp, S., Blomgren, J., Österlund, M., Bevilacqua, R., Andersson, P., Ryzhov, I. V., Tutin, G. A., Yavshits, S. G., Vaishnene, L. A., Onegin, M. S., Meulders, J. P., and Prieels, R. *Nuclear Data Sheets* **119**, 331 – 333 (2014).

[174] Oed, A., Geltenbort, P., Brissot, R., Gönnenwein, F., Perrin, P., Aker, E., and Engelhardt, D. *Nuclear Instruments and Methods in Physics Research* **219**(3), 569 – 574 (1984).

[175] Kanno, I., Nakagome, Y., and Kimura, I. *Journal of Nuclear Science and Technology* **25**(2), 111–119 (1988).

[176] Nishio, K., Nakagome, Y., Kanno, I., and Kimura, I. *Journal of Nuclear Science and Technology* **32**(5), 404–414 (1995).

[177] Boucheneb, N., Asghar, M., Barreau, G., Doan, T. P., Leroux, B., Sicre, A., Geltenbort, P., and Oed, A. *Nuclear Physics A* **535**(1), 77 – 93 (1991).

[178] Pollitt, A.J., Smith, A.G., Tsekhanovich, I., Dare, J.A., and Murray, L. *EPJ Web of Conferences* **93**, 02018 (2015).

[179] Meierbachtol, K., Tovesson, F., Shields, D., Arnold, C., Blakeley, R., Bredeweg, T., Devlin, M., Hecht, A. A., Heffern, L. E., Jorgenson, J., Laptev, A., Mader, D., O'Donnell, J. M., Sierk, A., and White, M. *Nuclear Instruments and Methods in Physics Research Section A: Accelerators, Spectrometers, Detectors and Associated Equipment* **788**, 59 – 66 (2015).

[180] Metag, V., Habs, D., Helmer, K., v. Helmolt, U., Heyng, H. W., Kolb, B., Pelte, D., Schwalm, D., Hennerici, W., Hennrich, H. J., Himmele, G., Jaeschke, E., Repnow, R., Wahl, W., Simon, R. S., and Albrecht, R. *The Darmstadt-Heidelberg-crystal-ball*, 163–178. Springer Berlin Heidelberg, Berlin, Heidelberg (1983).

[181] Kopach, Y. N., Singer, P., Mutterer, M., Klemens, M., Hotzel, A., Schwalm, D., Thirolf, P., Hesse, M., and Gönnenwein, F. *Phys. Rev. Lett.* **82**, 303–306 Jan (1999).

[182] Hotzel, A., Thirolf, P., Ender, C., Schwalm, D., Mutterer, M., Singer, P., Klemens, M., Theobald, J. P., Hesse, M., Gönnenwein, F., and Ploeg, H. *Zeitschrift für Physik A Hadrons and Nuclei* **356**(3), 299–308 (1996).

[183] de France, G., Blanc, A., Drouet, F., Jentschel, M., Köster, U., Mutti, P., Régis, J.M., Simpson, G., Soldner, T., Stezowski, O., Ur, C.A., Urban, W., and Vancrayenest, A. *EPJ Web of Conferences* **66**, 02010 (2014).

[184] Materna, T. *et al.*. In *ND2016 International Coference on Nuclear Data for Science and Technology, 11-16.Sep. Bruges, Belgium*, (2016).

[185] *J-PARC: https://j-parc.jp/index-e.html*.

[186] *LANSCE: http://lansce.lanl.gov/*.

[187] *n-TOF: https://ntof-exp.web.cern.ch/ntof-exp/*.

[188] Guerrero, C., Tsinganis, A., Berthoumieux, E., Barbagallo, M., Belloni, F., Gunsing, F., Weiß, C., Chiaveri, E., Calviani, M., Vlachoudis, V., Altstadt, S., Andriamonje, S., Andrzejewski, J., Audouin, L., Bécares, V., Bečvář, F., Billowes, J., Boccone, V., Bosnar, D., Brugger, M., Calviño, F., Cano-Ott, D., Carrapiço, C., Cerutti, F., Chin, M., Colonna, N., Cortés, G., Cortés-Giraldo, M. A., Diakaki, M., Domingo-Pardo, C., Duran, I., Dressler, R., Dzysiuk, N., Eleftheriadis, C., Ferrari, A., Fraval, K., Ganesan, S., García, A. R., Giubrone, G., Göbel, K., Gómez-Hornillos, M. B., Gonçalves, I. F., González-Romero, E., Griesmayer, E., Gurusamy, P., Hernández-Prieto, A., Jenkins, D. G., Jericha, E., Kadi, Y., Käppeler, F., Karadimos, D., Kivel, N., Koehler, P., Kokkoris, M., Krtička, M., Kroll, J., Lampoudis, C., Langer, C., Leal-Cidoncha, E., Lederer, C., Leeb, H., Leong, L. S., Losito, R., Manousos, A., Marganiec, J., Martínez, T., Massimi, C., Mastinu, P. F., Mastromarco, M., Meaze, M., Mendoza, E., Mengoni, A., Milazzo, P. M., Mingrone, F., Mirea, M., Mondalaers, W., Papaevangelou, T., Paradela, C., Pavlik, A., Perkowski, J., Plompen, A., Praena, J., Quesada, J. M., Rauscher, T., Reifarth, R., Riego, A., Roman, F., Rubbia, C., Sabate-Gilarte, M., Sarmento, R., Saxena, A., Schillebeeckx, P., Schmidt, S., Schumann, D., Steinegger, P., Tagliente, G., Tain, J. L., Tarrío, D., Tassan-Got, L., Valenta, S., Vannini, G., Variale, V., Vaz, P., Ventura, A., Versaci, R., Vermeulen, M. J., Vlastou, R., Wallner, A., Ware, T., Weigand, M., Wright, T., and Žugec, P. *The European Physical Journal A* **49**(2), 1–15 (2013).

[189] Calviani, M., Meaze, M. H., Colonna, N., Praena, J., Abbondanno, U., Aerts, G., Alvarez, H., Alvarez-Velarde, F., Andriamonje, S., Andrzejewski, J., Assimakopoulos, P., Audouin, L., Badurek, G., Barbagallo, M., Baumann, P., Bečvář, F., Belloni, F., Berthier, B., Berthoumieux, E., Calviño, F., Cano-Ott, D., Capote, R., Carrapiço, C., Cennini, P., Chepel, V., Chiaveri, E., Cortes, G., Couture, A., Cox, J., Dahlfors, M., David, S., Dillmann, I., Domingo-Pardo, C., Dridi, W., Duran, I., Eleftheriadis, C., Embid-Segura, M., Ferrant, L., Ferrari, A., Ferreira-Marques, R., Fujii, K., Furman, W., Galanopoulos, S., Giubrone, G., Gonçalves, I., Gonzalez-Romero, E., Goverdovski, A., Gramegna, F., Guerrero, C., Gunsing, F., Haas, B., Haight, R., Heil, M., Herrera-Martinez, A., Igashira, M., Jericha, E., Käppeler, F., Kadi, Y., Karadimos, D., Karamanis, D., Ketlerov, V., Kerveno, M., Koehler, P., Konovalov, V., Kossionides, E., Krtička, M., Lampoudis, C., Lederer, C., Leeb, H., Lindote, A., Lopes, I., Lozano, M., Lukic, S., Marganiec, J., Marrone, S., Martínez, T., Massimi, C., Mastinu, P., Mendoza, E., Mengoni, A., Milazzo, P. M., Moreau, C., Mosconi, M., Neves, F., Oberhummer, H., O'Brien, S., Pancin, J., Papachristodoulou, C., Papadopoulos, C., Paradela, C., Patronis, N., Pavlik, A., Pavlopoulos, P., Perrot, L., Pigni, M. T., Plag, R., Plompen, A., Plukis, A., Poch, A., Pretel, C., Quesada, J., Rauscher, T., Reifarth, R., Rosetti, M., Rubbia, C., Rudolf, G., Rullhusen, P., Salgado, J., Santos, C., Sarchiapone, L., Sarmento, R., Savvidis, I., Schillebeeckx, P., Stephan, C., Tagliente, G., Tain, J. L., Tassan-Got, L., Tavora, L., Terlizzi, R., Vannini, G., Variale, V., Vaz, P., Ventura, A., Villamarin, D., Vincente, M. C., Vlachoudis, V., Vlastou, R., Voss, F., Walter, S., Wiescher, M., and Wisshak, K. *Phys. Rev. C* **85**, 034616 Mar (2012).

[190] Diakaki, M., Karadimos, D., Vlastou, R., Kokkoris, M., Demetriou, P., Skordis, E., Tsinganis, A., Abbondanno, U., Aerts, G., Álvarez, H., Alvarez-Velarde, F., Andriamonje, S., Andrzejewski, J., Assimakopoulos,

CONTENTS 68

P., Audouin, L., Badurek, G., Baumann, P., Bečvář, F., Berthoumieux, E., Calviani, M., Calviño, F., Cano-Ott, D., Capote, R., Carrillo de Albornoz, A., Cennini, P., Chepel, V., Chiaveri, E., Colonna, N., Cortes, G., Couture, A., Cox, J., David, S., Dolfini, R., Domingo-Pardo, C., Dorochenko, A., Dridi, W., Duran, I., Eleftheriadis, C., Embid-Segura, M., Ferrant, L., Ferrari, A., Ferreira-Marques, R., Fitzpatrick, L., Frais-Koelbl, H., Fuji, K., Furman, W., Goncalves, I., Gallino, R., Gonzalez-Romero, E., Goverdovski, A., Gramegna, F., Griesmayer, E., Guerrero, C., Gunsing, F., Haas, B., Haight, R., Heil, M., Herrera-Martinez, A., Igashira, M., Ioannidis, K., Isaev, S., Jericha, E., Kadi, Y., Käppeler, F., Karamanis, D., Kerveno, M., Ketlerov, V., Koehler, P., Kolokolov, D., Konovalov, V., Krtička, M., Lamboudis, C., Leeb, H., Lindote, A., Lopes, I., Lozano, M., Lukic, S., Marganiec, J., Marques, L., Marrone, S., Massimi, C., Mastinu, P., Mengoni, A., Milazzo, P. M., Moreau, C., Mosconi, M., Neves, F., Oberhummer, H., O'Brien, S., Oshima, M., Pancin, J., Papadopoulos, C., Paradela, C., Patronis, N., Pavlik, A., Pavlopoulos, P., Perrot, L., Plag, R., Plompen, A., Plukis, A., Poch, A., Pretel, C., Quesada, J., Rauscher, T., Reifarth, R., Rosetti, M., Rubbia, C., Rudolf, G., Rullhusen, P., Salgado, J., Sarchiapone, L., Savvidis, I., Sedysheva, M., Stamoulis, K., Stephan, C., Tagliente, G., Tain, J. L., Tassan-Got, L., Tavora, L., Terlizzi, R., Vannini, G., Vaz, P., Ventura, A., Villamarin, D., Vincente, M. C., Vlachoudis, V., Voss, F., Wendler, H., Wiescher, M., and Wisshak, K. *Phys. Rev. C* **93**, 034614 Mar (2016).

[191] Guerrero, C., Abbondanno, U., Aerts, G., Álvarez, H., Álvarez-Velarde, F., Andriamonje, S., Andrzejewski, J., Assimakopoulos, P., Audouin, L., Badurek, G., Baumann, P., Bečvá, F., Berthoumieux, E., Calviño, F., Calviani, M., Cano-Ott, D., Capote, R., Carrapiço, C., Cennini, P., Chepel, V., Chiaveri, E., Colonna, N., Cortes, G., Couture, A., Cox, J., Dahlfors, M., David, S., Dillmann, I., Domingo-Pardo, C., Dridi, W., Duran, I., Eleftheriadis, C., Ferrant, L., Ferrari, A., Ferreira-Marques, R., Fujii, K., Furman, W., Goncalves, I., González-Romero, E., Gramegna, F., Gunsing, F., Haas, B., Haight, R., Heil, M., Herrera-Martinez, A., Igashira, M., Jericha, E., Käppeler, F., Kadi, Y., Karadimos, D., Kerveno, M., Koehler, P., Kossionides, E., Krtička, M. Lampoudis, C., Leeb, H., Lindote, A., Lopes, I., Lozano, M., Lukic, S., Marganiec, J., Marrone, S., Martínez, T., Massimi, C., Mastinu, P., Mendoza, E., Mengoni, A., Milazzo, P., Moreau, C., Mosconi, M., Neves, F., Oberhummer, H., OBrien, S., Pancin, J., Papachristodoulou, C., Papadopoulos, C., Paradela, C., Patronis, N., Pavlik, A., Pavlopoulos, P., Perrot, L., Pigni, M. T., Plag, R., Plompen, A., Plukis, A., Poch, A., Praena, J., Pretel, C., Quesada, J., Rauscher, T., Reifarth, R., Rubbia, C., Rudolf, G., Rullhusen, P., Salgado, J., Santos, C., Sarchiapone, L., Savvidis, I., Stephan, C., Tagliente, G., Tain, J. L., Tassan-Got, L., Tavora, L., Terlizzi, R., Vannini, G., Vaz, P., Ventura, A., Villamarin, D., Vicente, M., Vlachoudis, V., Vlastou, R., Voss, F., Walter, S., Wiescher, M., and Wisshak, K. *Nuclear Instruments and Methods in Physics Research Section A: Accelerators, Spectrometers, Detectors and Associated Equipment* **608**(3), 424 – 433 (2009).

[192] Weiß, C., Chiaveri, E., Girod, S., Vlachoudis, V., Aberle, O., Barros, S., Bergström, I., Berthoumieux, E., Calviani, M., Guerrero, C., Sabaté-Gilarte, M., Tsinganis, A., Andrzejewski, J., Audouin, L., Bacak, M., Balibrea-Correa, J., Barbagallo, M., Bécares, V., Beinrucker, C., Belloni, F., Bečvá, F., Billowes, J.,

Bosnar, D., Brugger, M., Caamaño, M., Calviño, F., Cano-Ott, D., Cerutti, F., Colonna, N., Cortés, G., Cortés-Giraldo, M., Cosentino, L., Damone, L., Deo, K., Diakaki, M., Domingo-Pardo, C., Dupont, E., Durán, I., Dressler, R., Fernández-Domínguez, B., Ferrari, A., Ferreira, P., Finocchiaro, P., Frost, R., Furman, V., Ganesan, S., Gheorghe, A., Glodariu, T., Göbel, K., Gonçalves, I. F., González-Romero, E., Goverdovski, A., Griesmayer, E., Gunsing, F., Harada, H., Heftrich, T., Heinitz, S., Hernández-Prieto, A., Heyse, J., Jenkins, D. G., Jericha, E., Kadi, Y., Käppeler, F., Katabuchi, T., Kavrigin, P., Ketlerov, V., Khryachkov, V., Kimura, A., Kivel, N., Kokkoris, M., Krtika, M., Leal-Cidoncha, E., Lederer, C., Leeb, H., Lerendegui, J., Licata, M., Meo, S. L., López, D., Losito, R., Macina, D., Marganiec, J., Martínez, T., Massimi, C., Mastinu, P. F., Mastromarco, M., Matteucci, F., Mendoza, E., Mengoni, A., Milazzo, P. M., Mingrone, F., Mirea, M., Montesano, S., Musumarra, A., Nolte, R., Pinto, R. P., Paradela, C., Patronis, N., Pavlik, A., Perkowski, J., Porras, I., Praena, J., Quesada, J. M., Rauscher, T., Reifarth, R., Riego-Perez, A., Robles, M. S., Rubbia, C., Ryan, J., Saxena, A., Schillebeeckx, P., Schmidt, S., Schumann, D., Sedyshev, P., Smith, G., Stamatopoulos, A., Steinegger, P., Suryanarayana, S. V., Tagliente, G., Tain, J. L., Tarifeño-Saldivia, A., Tassan-Got, L., Valenta, S., Vannini, G., Variale, V., Vaz, P., Ventura, A., Vlastou, R., Wallner, A., Warren, S., Weigand, M., Wright, T., and Zugec, P. *Nuclear Instruments and Methods in Physics Research Section A: Accelerators, Spectrometers, Detectors and Associated Equipment* **799**, 90 – 98 (2015).

[193] *STEFF: http://t2.lanl.gov/fiesta2014/presentations/Smith.pdf.*

[194] Lisowski, P. W. and Schoenberg, K. F. *Nuclear Instruments and Methods in Physics Research Section A: Accelerators, Spectrometers, Detectors and Associated Equipment* **562**(2), 910 – 914 (2006). Proceedings of the 7th International Conference on Accelerator Applications (AccApp05).

[195] Tovesson, F., Hill, T. S., Mocko, M., Baker, J. D., and McGrath, C. A. *Phys. Rev. C* **79**, 014613 Jan (2009).

[196] Nelson, Ronald O. *EPJ Web of Conferences* **93**, 06002 (2015).

[197] Heil, M., Reifarth, R., Fowler, M. M., Haight, R. C., Käppeler, F., Rundberg, R. S., Seabury, E. H., Ullmann, J. L., Wilhelmy, J. B., and Wisshak, K. *Nuclear Instruments and Methods in Physics Research Section A: Accelerators, Spectrometers, Detectors and Associated Equipment* **459**(12), 229 – 246 (2001).

[198] Chyzh, A., Wu, C. Y., Kwan, E., Henderson, R. A., Gostic, J. M., Bredeweg, T. A., Haight, R. C., Hayes-Sterbenz, A. C., Jandel, M., O'Donnell, J. M., and Ullmann, J. L. *Phys. Rev. C* **85**, 021601 Feb (2012).

[199] Chyzh, A., Wu, C. Y., Kwan, E., Henderson, R. A., Gostic, J. M., Bredeweg, T. A., Couture, A., Haight, R. C., Hayes-Sterbenz, A. C., Jandel, M., Lee, H. Y., O'Donnell, J. M., and Ullmann, J. L. *Phys. Rev. C* **87**, 034620 Mar (2013).

[200] Chyzh, A., Wu, C. Y., Kwan, E., Henderson, R. A., Bredeweg, T. A., Haight, R. C., Hayes-Sterbenz, A. C., Lee, H. Y., O'Donnell, J. M., and Ullmann, J. L. *Phys. Rev. C* **90**, 014602 Jul (2014).

[201] Wu, C. Y., Chyzh, A., Kwan, E., Henderson, R. A., Gostic, J. M., Carter, D., Bredeweg, T. A., Couture, A., Jandel, M., and Ullmann, J. L. *Nuclear Instruments and Methods in Physics Research Section A: Accelerators, Spectrometers, Detectors and Associated Equipment* **694**, 78 – 81 (2012).

[202] Tovesson, F., (2016). Private communication.

CONTENTS 69

[203] Lee, H. Y. In *Proceedings of the Fifth International Conference on Fission and Properties of Nuetron-rich Nuclei: ICFN5*, 430 – 436. World Scientific, (2013).

[204] Haight, R. C., Lee, H. Y., Taddeucci, T. N., O'Donnell, J. M., Perdue, B. A., Fotiades, N., Devlin, M., Ullmann, J. L., Laptev, A., Bredeweg, T., Jandel, M., Nelson, R. O., Wender, S. A., White, M. C., Wu, C. Y., Kwan, E., Chyzh, A., Henderson, R., and Gostic, J. *Journal of Instrumentation* **7**(03), C03028 (2012).

[205] Heffner, M., Asner, D. M., Baker, R. G., Baker, J., Barrett, S., Brune, C., Bundgaard, J., Burgett, E., Carter, D., Cunningham, M., Deaven, J., Duke, D. L., Greife, U., Grimes, S., Hager, U., Hertel, N., Hill, T., Isenhower, D., Jewell, K., King, J., Klay, J., Kleinrath, V., Kornilov, N., Kudo, R., Laptev, A. B., Leonard, M., Loveland, W., Massey, T. N., McGrath, C., Meharchand, R., Montoya, L., Pickle, N., Qu, H., Riot, V., Ruz, J., Sangiorgio, S., Seilhan, B., Sharma, S., Snyder, L., Stave, S., Tatishvili, G., Thornton, R. T., Tovesson, F., Towell, D., Towell, R. S., Watson, S., Wendt, B., Wood, L., and Yao, L. *Nuclear Instruments and Methods in Physics Research Section A: Accelerators, Spectrometers, Detectors and Associated Equipment* **759**, 50 – 64 (2014).

[206] Ikeda, Y. *Nuclear Instruments and Methods in Physics Research Section A: Accelerators, Spectrometers, Detectors and Associated Equipment* **600**(1), 1 – 4 (2009).

[207] Igashira, M., Kiyanagi, Y., and Oshima, M. *Nuclear Instruments and Methods in Physics Research Section A: Accelerators, Spectrometers, Detectors and Associated Equipment* **600**(1), 332 – 334 (2009).

[208] Kino, K., Furusaka, M., Hiraga, F., Kamiyama, T., Kiyanagi, Y., Furutaka, K., Goko, S., Harada, H., Harada, M., Kai, T., Kimura, A., Kin, T., Kitatani, F., Koizumi, M., Maekawa, F., Meigo, S., Nakamura, S., Ooi, M., Ohta, M., Oshima, M., Toh, Y., Igashira, M., Katabuchi, T., and Mizumoto, M. *Nuclear Instruments and Methods in Physics Research Section A: Accelerators, Spectrometers, Detectors and Associated Equipment* **626−627**, 58 – 66 (2011).

[209] Kimura, A., Fujii, T., Fukutani, S., Furutaka, K., Goko, S., Hara, K. Y., Harada, H., Hirose, K., ichi Hori, J., Igashira, M., Kamiyama, T., Katabuchi, T., Kin, T., Kino, K., Kitatani, F., Kiyanagi, Y., Koizumi, M., Mizumoto, M., Nakamura, S., Ohta, M., Oshima, M., Takamiya, K., and Toh, Y. *Journal of Nuclear Science and Technology* **49**(7), 708–724 (2012).

[210] Katabuchi, T., Matsuhashi, T., Terada, K., Arai, T., Furutaka, K., Hara, K. Y., Harada, H., Hirose, K., ichi Hori, J., Igashira, M., Kamiyama, T., Kimura, A., Kino, K., Kitatani, F., Kiyanagi, Y., Koizumi, M., Mizumoto, M., Nakamura, S., Oshima, M., and Toh, Y. *Nuclear Instruments and Methods in Physics Research Section A: Accelerators, Spectrometers, Detectors and Associated Equipment* **764**, 369 – 377 (2014).

[211] Katabuchi, T., Matsuhashi, T., Terada, K., Igashira, M., Mizumoto, M., Hirose, K., Kimura, A., Iwamoto, N., Hara, K. Y., Harada, H., Hori, J.-i., Kamiyama, T., Kino, K., Kitatani, F., Kiyanagi, Y., Nakamura, S., and Toh, Y. *Phys. Rev. C* **91**, 037603 Mar (2015).

[212] Hirose, K., Nishio, K., Makii, H., Nishinaka, I., Ota, S., Nagayama, T., Tamura, N., Goto, S., Andreyev, A., Vermeulen, M., Gilespie, S., Barton, C., Kimura, A., Harada, H., Meigo, S., Chiba, S., and Ohtsuki, T. *Nuclear Instruments and Methods in Physics Research Section A: Accelerators, Spectrometers, Detectors and Associated Equipment* , – (2016). in press.

[213] Reifarth, R., Esch, E.-I., Alpizar-Vicente, A., Bond, E. M., Bredeweg, T. A., Glover, S. E., Greife, U., Hatarik, R., Haight, R. C., Kronenberg, A., O'Donnell, J. M., Rundberg, R., Schwantes, J. M., Ullmann, J. L., Vieira, D. J., Wilhelmy, J. B., and Wouters, J. M. *Nuclear Instruments and Methods in Physics Research Section B: Beam Interactions with Materials and Atoms* **241**(14), 176 – 179 (2005). The Application of Accelerators in Research and IndustryProceedings of the Eighteenth International Conference on the Application of Accelerators in Research and Industry (CAARI 2004) Eighteenth International Conference on the Application of Accelerators in Research and Industry.

[214] Csige, L., Filipescu, D. M., Glodariu, T., Gulyás, J., Günther, M. M., Habs, D., Karwowski, H. J., Krasznahorkay, A., Rich, G. C., Sin, M., Stroe, L., Tesileanu, O., and Thirolf, P. G. *Phys. Rev. C* **87**, 044321 Apr (2013).

[215] Miyamoto, S., Asano, Y., Amano, S., Li, D., Imasaki, K., Kinugasa, H., Shoji, Y., Takagi, T., and Mochizuki, T. *Radiation Measurements* **41, Supplement 2**, S179 – S185 (2006). The 3rd International Workshop on Radiation Safety at Synchrotron Radiation Sources.

[216] Amano, S., Horikawa, K., Ishihara, K., Miyamoto, S., Hayakawa, T., Shizuma, T., and Mochizuki, T. *Nuclear Instruments and Methods in Physics Research Section A: Accelerators, Spectrometers, Detectors and Associated Equipment* **602**(2), 337 – 341 (2009).

[217] Litvinenko, V. N., Burnham, B., Emamian, M., Hower, N., Madey, J. M. J., Morcombe, P., O'Shea, P. G., Park, S. H., Sachtschale, R., Straub, K. D., Swift, G., Wang, P., Wu, Y., Canon, R. S., Howell, C. R., Roberson, N. R., Schreiber, E. C., Spraker, M., Tornow, W., Weller, H. R., Pinayev, I. V., Gavrilov, N. G., Fedotov, M. G., Kulipanov, G. N., Kurkin, G. Y., Mikhailov, S. F., Popik, V. M., Skrinsky, A. N., Vinokurov, N. A., Norum, B. E., Lumpkin, A., and Yang, B. *Phys. Rev. Lett.* **78**, 4569–4572 Jun (1997).

[218] Mueller, J. M., Ahmed, M. W., Davis, B., Hall, J. M., Henshaw, S. S., Johnson, M. S., Karwowski, H. J., Markoff, D., Myers, L. S., Perdue, B. A., Stave, S., Tompkins, J. R., Tuffley, M. J., and Weller, H. R. *Phys. Rev. C* **85**, 014605 Jan (2012).

[219] Mueller, J. M., Ahmed, M. W., France, R. H., Johnson, M. S., Karwowski, H. J., Myers, L. S., Randrup, J., Sikora, M. H., Spraker, M. C., Stave, S., Tompkins, J. R., Vogt, R., Weller, H. R., Whisnant, C. S., and Zimmerman, W. R. *Phys. Rev. C* **89**, 034615 Mar (2014).

[220] Ghys, L., Andreyev, A. N., Antalic, S., Huyse, M., and Van Duppen, P. *Phys. Rev. C* **91**, 044314 Apr (2015).

[221] Veselský, M., Andreyev, A. N., Antalic, S., Huyse, M., Möller, P., Nishio, K., Sierk, A. J., Van Duppen, P., and Venhart, M. *Phys. Rev. C* **86**, 024308 Aug (2012).

[222] Kaji, D., Morimoto, K., Haba, H., Ideguchi, E., Koura, H., and Morita, K. *Journal of the Physical Society of Japan* **85**(1), 015002 (2016).

[223] Wilson, G. *Phys. Rev. C* **XX**, XX Sep (2016).

[224] Konki, J., Khuyagbaatar, J., Uusitalo, J., Greenlees, P., Auranen, K., Badran, H., Block, M., Briselet, R., Cox, D., Dasgupta, M., Nitto, A. D., Dllmann, C., Grahn, T., Hauschild, K., Herzn, A., Herzberg, R.-D., Heberger, F., Hinde, D., Julin, R., Juutinen, S., Jger, E., Kindler, B., Krier, J., Leino, M., Lommel, B., Lopez-Martens, A., Luong, D., Mallaburn, M., Nishio, K., Pakarinen, J., Papadakis, P., Partanen, J., Peura, P., Rahkila, P., Rezynkina, K., Ruotsalainen, P., Sandzelius, M., Sarn, J., Scholey, C., Sorri, J., Stolze, S., Sulignano, B., Theisen, C., Ward, A., Yakushev, A., and Yakusheva, V. *Physics Letters B* **764**, 265 – 270 (2017).

[225] Seaborg, G. T. *Phys. Rev.* **85**, 157–158 Jan (1952).

[226] Bjørnholm, S. and Lynn, J. E. *Rev. Mod. Phys.* **52**, 725–

CONTENTS 70

931 Oct (1980).

[227] Wheeler, J. A. *Niels Bohr and the Deparment of Physics*, 163. Pergamon, London (1955).

[228] Rodríguez-Guzmán, R. and Robledo, L. M. *The European Physical Journal A* **52**(11), 348 (2016).

[229] Prasad, E., Hinde, D. J., Ramachandran, K., Williams, E., Dasgupta, M., Carter, I. P., Cook, K. J., Jeung, D. Y., Luong, D. H., McNeil, S., Palshetkar, C. S., Rafferty, D. C., Simenel, C., Wakhle, A., Khuyagbaatar, J., Düllmann, C. E., Lommel, B., and Kindler, B. *Phys. Rev. C* **91**, 064605 Jun (2015).

[230] Shaughnessy, D. A., Adams, J. L., Gregorich, K. E., Lane, M. R., Laue, C. A., Lee, D. M., McGrath, C. A., Patin, J. B., Strellis, D. A., Sylwester, E. R., Wilk, P. A., and Hoffman, D. C. *Phys. Rev. C* **61**, 044609 Mar (2000).

[231] Shaughnessy, D. A., Gregorich, K. E., Lane, M. R., Laue, C. A., Lee, D. M., McGrath, C. A., Strellis, D. A., Sylwester, E. R., Wilk, P. A., and Hoffman, D. C. *Phys. Rev. C* **63**, 037603 (2001).

[232] Lane, J. F. W., Andreyev, A. N., Antalic, S., Ackermann, D., Gerl, J., Heßberger, F. P., Hofmann, S., Huyse, M., Kettunen, H., Kleinböhl, A., Kindler, B., Kojouharov, I., Leino, M., Lommel, B., Münzenberg, G., Nishio, K., Page, R. D., Šáro, i. c. v., Schaffner, H., Taylor, M. J., and Van Duppen, P. *Phys. Rev. C* **87**, 014318 Jan (2013).

[233] Andreyev, A. N., Antalic, S., Ackermann, D., Bianco, L., Franchoo, S., Heinz, S., Heßberger, F. P., Hofmann, S., Huyse, M., Kalaninová, Z., Kojouharov, I., Kindler, B., Lommel, B., Mann, R., Nishio, K., Page, R. D., Ressler, J. J., Streicher, B., Saro, S., Sulignano, B., and Van Duppen, P. *Phys. Rev. C* **87**, 014317 Jan (2013).

[234] Kugler, E. *Hyp. Int.* **129**, 23–42 (2000).

[235] Fedosseev, V. N., Berg, L. E., Fedorov, D. V., Fink, D., J., L. O., Losito, R., Marsh, B. A., Rossel, R. E., Rothe, S., Seliverstov, M. D., Sjodin, A. M., and Wendt, K. D. A. *Review of Scientific Instruments* **83**(2), 02A903 (2012).

[236] Marsh, B. A., Fedosseev, V. N., Fink, D. A., Day Goodacre, T., Rossel, R. E., Rothe, S., Fedorov, D. V., Imai, N., Seliverstov, M. D., and Molkanov, P. *Hyperfine Interactions* **227**(1), 101–111 (2014).

[237] Rothe, S., Andreyev, A. N., Antalic, S., Borschevsky, A., Capponi, L., Cocolios, T., De Witte, H., Eliav, E., Fedorov, D., Fedosseev, V., Fink, D., Fritzsche, S., Ghys, L., Huyse, M., Imai, N., Kaldor, U., Kudryavtsev, Y., Koster, U., Lane, J., and Lassen, J. *Nature communications* **4**, **1835**, 1 (2013).

[238] Greiner, D. E., Crawford, H., Lindstrom, P. J., Kidd, J. M., Olson, D. L., Schimmerling, W., and Symons, T. J. M. *Phys. Rev. C* **31**, 416–420 Feb (1985).

[239] Justice, M. L., Blumenfeld, Y., Colonna, N., Delis, D. N., Guarino, G., Hanold, K., Meng, J. C., Peaslee, G. F., Wozniak, G. J., and Moretto, L. G. *Phys. Rev. C* **49**, R5–R9 Jan (1994).

[240] Polikanov, S., Brüchle, W., Folger, H., Jäger, E., Krogulski, T., Schädel, M., Schimpf, E., Wirth, G., Aumann, T., Kratz, J. V., Stiel, E., and Trautmann, N. *Zeitschrift für Physik A Hadrons and Nuclei* **350**(3), 221–227 (1994).

[241] Bernas, M., Czajkowski, S., Armbruster, P., Geissel, H., Dessagne, P., Donzaud, C., Faust, H.-R., Hanelt, E., Heinz, A., Hesse, M., Kozhuharov, C., Miehe, C., Münzenberg, G., Pfützner, M., Röhl, C., Schmidt, K.-H., Schwab, W., Stéphan, C., Sümmerer, K., Tassan-Got, L., and Voss, B. *Physics Letters B* **331**(12), 19 – 24 (1994).

[242] Rubehn, T., Müller, W. F. J., Bassini, R., Begemann-Blaich, M., Blaich, T., Ferrero, A., Groß, C., Imme, G., Iori, I., Kunde, G. J., Kunze, W. D., Lindenstruth, V.,

Lynen, U., Möhlenkamp, T., Moretto, L. G., Ocker, B., Pochodzalla, J., Raciti, G., Reito, S., Sann, H., Schüttauf, A., Seidel, W., Serfling, V., Trautmann, W., Trzcinski, A., Verde, G., Wörner, A., Zude, E., and Zwieglinski, B. *Zeitschrift für Physik A Hadrons and Nuclei* **353**(2), 197–204 (1995).

[243] Rubehn, T., Bassini, R., Begemann-Blaich, M., Blaich, T., Ferrero, A., Groß, C., Immé, G., Iori, I., Kunde, G. J., Kunze, W. D., Lindenstruth, V., Lynen, U., Möhlenkamp, T., Moretto, L. G., Müller, W. F. J., Ocker, B., Pochodzalla, J., Raciti, G., Reito, S., Sann, H., Schüttauf, A., Seidel, W., Serfling, V., Trautmann, W., Trzcinski, A., Verde, G., Wörner, A., Zude, E., and Zwieglinski, B. *Phys. Rev. C* **53**, 3143–3146 Jun (1996).

[244] Rubehn, T., Bassini, R., Begemann-Blaich, M., Blaich, T., Ferrero, A., Groß, C., Immé, G., Iori, I., Kunde, G. J., Kunze, W. D., Lindenstruth, V., Lynen, U., Möhlenkamp, T., Moretto, L. G., Müller, W. F. J., Ocker, B., Pochodzalla, J., Raciti, G., Reito, S., Sann, H., Schüttauf, A., Seidel, W., Serfling, V., Trautmann, W., Trzcinski, A., Verde, G., Wörner, A., Zude, E., and Zwieglinski, B. *Phys. Rev. C* **53**, 993–996 Feb (1996).

[245] Armbruster, P., Bernas, M., Czajkowski, S., Geissel, H., Aumann, T., Dessagne, P., Donzaud, C., Hanelt, E., Heinz, A., Hesse, M., Kozuharov, C., Miehe, C., Münzenberg, G., Pfützner, M., Schmidt, K. H., Schwab, W., Stéphan, C., Sümmerer, K., Tassan-got, L., and Voss, B. *Zeitschrift für Physik A Hadrons and Nuclei* **355**(1), 191–201 (1996).

[246] Hesse, M., Bernas, M., Armbruster, P., Aumann, T., Czajkowski, S., Dessagne, P., Donzaud, C., Geissel, H., Hanelt, E., Heinz, A., Kozhuharov, C., Miehé, C., Münzenberg, G., Pfützner, M., Röhl, C., Schmidt, K. H., Schwab, W., Stéphan, C., Sümmerer, K., and Tassan-Got, L. *Zeitschrift für Physik A Hadrons and Nuclei* **355**(1), 69–75 (1996).

[247] C. Donzaud, S. Czajkowski, P. Armbruster, M. Bernas, C. Böckstiegel, Ph. Dessagne, H. Geissel, E. Hanelt, A. Heinz, C. Kozhuharov, Ch. Miehé, G. Münzenberg, M. Pfützner, W. Schwab, C. Stéphan, K. Sümmerer, L. Tassan-Got, and B. Voss. *Eur. Phys. J. A* **1**(4), 407– 426 (1998).

[248] Enqvist, T., Benlliure, J., Farget, F., Schmidt, K.-H., Armbruster, P., Bernas, M., Tassan-Got, L., Boudard, A., Legrain, R., Volant, C., Böckstiegel, C., de Jong, M., and Dufour, J. P. *Nuclear Physics A* **658**(1), 47 – 66 (1999).

[249] Grente, L. *private communication*.

[250] Schmidt, K.-H., Brohm, T., Clerc, H.-G., Dornik, M., Fauerbach, M., Geissel, H., Grewe, A., Hanelt, E., Junghans, A., Magel, A., Morawek, W., Münzenberg, G., Nickel, F., Pfützner, M., Scheidenberger, C., Sümmerer, K., Vieira, D., Voss, B., and Ziegler, C. *Physics Letters B* **300**(4), 313 – 316 (1993).

[251] de Jong, M., Ignatyuk, A. V., and Schmidt, K.-H. *Nuclear Physics A* **613**(4), 435 – 444 (1997).

[252] Grente, L., Taeb, J., Chatillon, A., Martin, J.-F., Pellereau, É., Boutoux, G., Gorbinet, T., Bélier, G., Laurent, B., Alvarez-Pol, H., Ayyad, Y., Benlliure, J., Caamao, M., Audouin, L., Casarejos, E., Cortina-Gil, D., Farget, F., Fernndez-Domnguez, B., Heinz, A., Jurado, B., Keli-Heil, A., Kurz, N., Lindberg, S., Löher, B., Nociforo, C., Paradela, C., Pietri, S., Ramos, D., Rodriguez-Sanchez, J.-L., Rodrguez-Tajes, C., Rossi, D., Schmidt, K.-H., Simon, H., Tassan-Got, L., Törnqvist, H., Vargas, J., Voss, B., Weick, H., and Yan, Y. *EPJ Web of Conferences* **122**, 01006 (2016).

[253] Benlliure, J., Grewe, A., de Jong, M., Schmidt, K.-H., and Zhdanov, S. *Nuclear Physics A* **628**(3), 458 – 478 (1998).

CONTENTS 71

[254] Casarejos, E., Benlliure, J., Pereira, J., Armbruster, P., Bernas, M., Boudard, A., Czajkowski, S., Enqvist, T., Legrain, R., Leray, S., Mustapha, B., Pravikoff, M., Rejmund, F., Schmidt, K.-H., Stéphan, C., Taieb, J., Tassan-Got, L., Volant, C., and Wlazlo, W. *Phys. Rev. C* **74**, 044612 Oct (2006).

[255] Boudard, A., Cugnon, J., David, J.-C., Leray, S., and Mancusi, D. *Phys. Rev. C* **87**, 014606 Jan (2013).

[256] Kelic, A., Ricciardi, M. V., and Schmidt, K.-H. In *Joint ICTP-IAEA Advanced Workshop on Model Codes for Spallation Reactions,* Filges, D., Leray, S., Yariv, Y., Mengoni, A., Stanculescu, A., and Mank, G., editors, volume Report INDC(NDS)-0530. IAEA, (2008).

[257] Badhwar, G. D. *Nuclear Instruments and Methods* **109**(1), 119 – 123 (1973).

[258] Farget, F. *private communication.*

[259] Delaune, O. *Technique de la cinématique inverse pour l'étude des rendements isotopiques des fragments de fission aux énergies GANIL.* PhD thesis, Université de Caen, (2012).

[260] Hofmann, S. *Journal of Physics G: Nuclear and Particle Physics* **42**(11), 114001 (2015).

[261] Balantekin, A. B. and Takigawa, N. *Rev. Mod. Phys.* **70**, 77–100 Jan (1998).

[262] Elseviers, J., Andreyev, A. N., Antalic, S., Barzakh, A., Bree, N., Cocolios, T. E., Comas, V. F., Diriken, J., Fedorov, D., Fedosseyev, V. N., Franchoo, S., Heredia, J. A., Huyse, M., Ivanov, O., Köster, U., Marsh, B. A., Page, R. D., Patronis, N., Seliverstov, M., Tsekhanovich, I., Van den Bergh, P., Van De Walle, J., Van Duppen, P., Venhart, M., Vermote, S., Veselský, M., and Wagemans, C. *Phys. Rev. C* **84**, 034307 Sep (2011).

[263] Ichikawa, T., Iwamoto, A., Möller, P., and Sierk, A. J. *Phys. Rev. C* **86**, 024610 Aug (2012).

[264] Möller, P., Randrup, J., and Sierk, A. J. *Phys. Rev. C* **85**, 024306 Feb (2012).

[265] Panebianco, S., Sida, J.-L., Goutte, H., Lemaître, J.-F., Dubray, N., and Hilaire, S. *Phys. Rev. C* **86**, 064601 Dec (2012).

[266] Andreev, A. V., Adamian, G. G., and Antonenko, N. V. *Phys. Rev. C* **86**, 044315 Oct (2012).

[267] Andreev, A. V., Adamian, G. G., Antonenko, N. V., and Andreyev, A. N. *Phys. Rev. C* **88**, 047604 (2013).

[268] Andreev, A. V., Adamian, G. G., and Antonenko, N. V. *Phys. Rev. C* **93**, 034620 Mar (2016).

[269] Warda, M., Staszczak, A., and Nazarewicz, W. *Phys. Rev. C* **86**, 024601 Aug (2012).

[270] McDonnell, J. D., Nazarewicz, W., Sheikh, J. A., Staszczak, A., and Warda, M. *Phys. Rev. C* **90**, 021302 Aug (2014).

[271] Möller, P., Madland, D. G., Sierk, A. J., and Iwamoto, A. *Nature* **409**(6822), 785 – 790 (2001).

[272] Möller, P. and Randrup, J. *Phys. Rev. C* **91**, 044316 Apr (2015).

[273] Randrup, J. and Möller, P. *Phys. Rev. Lett.* **106**, 132503 Mar (2011).

[274] Sierk, A. J. *Phys. Rev. C* **33**, 2039–2053 Jun (1986).

[275] Böckstiegel, C., Steinhäuser, S., Schmidt, K.-H., Clerc, H.-G., Grewe, A., Heinz, A., de Jong, M., Junghans, A., Müller, J., and Voss, B. *Nuclear Physics A* **802**(14), 12 – 25 (2008).

[276] Hoffman, D. In *Proc. Symp. Phys. Chem. Fission, Jülich 1979*, volume 2, 275. IAEA, Vienna, (1980).

[277] Mosel, U. and Schmitt, H. W. *Phys. Rev. C* **4**, 2185–2201 Dec (1971).

[278] Schmitt, H. and Mosel, U. *Nuclear Physics A* **186**(1), 1 – 14 (1972).

[279] Scharnweber, D., Mosel, U., and Greiner, W. *Phys. Rev. Lett.* **24**, 601–603 Mar (1970).

[280] Itkis, M. G., Okolovich, V. N., Rusanov, A. Y., and Smirenkin, G. N. *Zeitschrift für Physik A Atoms and Nuclei* **320**(3), 433–441 (1985).

[281] Böckstiegel, C., Steinhäuser, S., Benlliure, J., Clerc, H.-G., Grewe, A., Heinz, A., de Jong, M., Junghans, A. R., Müller, J., and Schmidt, K.-H. *Physics Letters B* **398**(34), 259 – 263 (1997).

[282] Schmidt, K.-H., Jurado, B., and Amouroux, C. *JEFF Report* **24** (2014).

[283] Schmidt, K.-H., Jurado, B., Amouroux, C., and Schmitt, C. *Nuclear Data Sheets* **131**, 107 – 221 (2016). Special Issue on Nuclear Reaction Data.

[284] Schmidt, K.-H. and Jurado, B. *Phys. Rev. Lett.* **104**, 212501 May (2010).

[285] Ramos, D., Rodríguez-Tajes, C., Caamaño, M., Farget, F., Audouin, L., Benlliure, J., Casarejos, E., Clement, E., Cortina, D., Delaune, O., Derkx, X., Dijon, A., Doré, D., Fernández-Domínguez, B., de France, G., Heinz, A., Jacquot, B., Navin, A., Paradela, C., Rejmund, M., Roger, T., Salsac, M. D., and Schmitt, C. *EPJ Web of Conf.* **111**, 10001 (2016).

[286] Bocquet, J. P. and Brissot, R. *Nuclear Physics A* **502**, 213 – 232 (1989).

[287] Steinhäuser, S., Benlliure, J., Böckstiegel, C., Clerc, H.-G., Heinz, A., Grewe, A., de Jong, M., Junghans, A., Müller, J., Pfützner, M., and Schmidt, K.-H. *Nuclear Physics A* **634**(12), 89 – 111 (1998).

[288] Pellereau, E. *Ph. D. thesis, Université de Paris Sud* (2013).

[289] Caamaño, M., Rejmund, F., and Schmidt, K.-H. *Journal of Physics G: Nuclear and Particle Physics* **38**(3), 035101 (2011).

[290] Tracy, B. L., Chaumont, J., Klapisch, R., Nitschke, J. M., Poskanzer, A. M., Roeckl, E., and Thibault, C. *Phys. Rev. C* **5**, 222–234 Jan (1972).

[291] Pommé, S., Jacobs, E., Persyn, K., Frenne, D. D., Govaert, K., and Yoneama, M.-L. *Nuclear Physics A* **560**(2), 689 – 714 (1993).

[292] Ricciardi, M. V., Ignatyuk, A. V., Kelić, A., Napolitani, P., Rejmund, F., Schmidt, K.-H., and Yordanov, O. *Nuclear Physics A* **733**(34), 299 – 318 (2004).

[293] Ricciardi, M., Schmidt, K.-H., Kelic-Heil, A., and Napolitani, P. *arXiv:1007.0386v1 [nucl-ex]* (2010).

[294] Grangé, P. and Weidenmüller, H. A. *Physics Letters B* **96**(1), 26 – 30 (1980).

[295] Hilscher, D., Rossner, H., Cramer, B., Gebauer, B., Jahnke, U., Lehmann, M., Schwinn, E., Wilpert, M., Wilpert, T., Frobeen, H., Mordhorst, E., and Scobel, W. *Phys. Rev. Lett.* **62**, 1099–1102 Mar (1989).

[296] Hinde, D. J., Hilscher, D., Rossner, H., Gebauer, B., Lehmann, M., and Wilpert, M. *Phys. Rev. C* **45**, 1229–1259 Mar (1992).

[297] Ramachandran, K., Chatterjee, A., Navin, A., Mahata, K., Shrivastava, A., Tripathi, V., Kailas, S., Nanal, V., Pillay, R. G., Saxena, A., Thomas, R. G., Kumar, S., and Sahu, P. K. *Phys. Rev. C* **73**, 064609 Jun (2006).

[298] Jing, K. X., Phair, L. W., Moretto, L. G., Rubehn, T., Beaulieu, L., Fan, T. S., and Wozniak, G. J. *Physics Letters B* **518**(34), 221 – 228 (2001).

[299] Nadtochy, P. N., Ryabov, E. G., Gegechkori, A. E., Anischenko, Y. A., and Adeev, G. D. *Phys. Rev. C* **85**, 064619 Jun (2012).

[300] Sikdar, A. K., Ray, A., and Chatterjee, A. *Phys. Rev. C* **93**, 041604 Apr (2016).

[301] Jurado, B., Schmitt, C., Schmidt, K.-H., Benlliure, J., and Junghans, A. R. *Nuclear Physics A* **757**(34), 329 – 348 (2005).

[302] Gontchar, I. I. and Ponomarenko, N. A. *Physics of Atomic Nuclei* **70**(12), 1999–2015 (2007).

[303] Gontchar, I. I., Ponomarenko, N. A., and Litnevsky, A. L.

CONTENTS   72

Physics of Atomic Nuclei **71**(7), 1143–1148 (2008).

[304] Ye, W. and Tian, J. *Phys. Rev. C* **91**, 064603 Jun (2015).

[305] Jurado, B., Schmitt, C., Schmidt, K.-H., Benlliure, J., and Junghans, A. R. *Nuclear Physics A* **747**(1), 14 – 43 (2005).

[306] Jurado, B., Schmitt, C., Schmidt, K.-H., Benlliure, J., Enqvist, T., Junghans, A. R., Kelić, A., and Rejmund, F. *Phys. Rev. Lett.* **93**, 072501 Aug (2004).

[307] Ignatyuk, A. V., Kudyaev, G. A., Junghans, A., de Jong, M., Clerc, H.-G., and Schmidt, K.-H. *Nuclear Physics A* **593**(4), 519 – 534 (1995).

[308] Benlliure, J., Armbruster, P., Bernas, M., Boudard, A., Enqvist, T., Legrain, R., Leray, S., Rejmund, F., Schmidt, K.-H., Stéphan, C., Tassan-Got, L., and Volant, C. *Nuclear Physics A* **700**(12), 469 – 491 (2002).

[309] Benlliure, J., Casarejos, E., Pereira, J., and Schmidt, K.-H. *Phys. Rev. C* **74**, 014609 Jul (2006).

[310] Schmitt, C., Schmidt, K.-H., Kelić, A., Heinz, A., Jurado, B., and Nadtochy, P. N. *Phys. Rev. C* **81**, 064602 Jun (2010).

[311] Schmitt, C., Nadtochy, P. N., Heinz, A., Jurado, B., Kelić, A., and Schmidt, K.-H. *Phys. Rev. Lett.* **99**, 042701 Jul (2007).

[312] Ayyad, Y., Benlliure, J., Rodríguez-Sánchez, J. L., Bacquias, A., Boudard, A., Casarejos, E., Enqvist, T., Fernandez, M., Henzl, V., Henzlova, V., Jurado, B., Kelić-Heil, A., Kurtukian, T., Lukić, S., Nadtochy, P., Pérez-Loureiro, D., Pleskač, R., Farget, F., Ricciardi, M. V., Schmidt, K.-H., Schmitt, C., and Ngoc, S. N. *Phys. Rev. C* **91**, 034601 Mar (2015).

[313] Lestone, J. P. and McCalla, S. G. *Phys. Rev. C* **79**, 044611 Apr (2009).

[314] Aritomo, Y. and Chiba, S. *Phys. Rev. C* **88**, 044614 Oct (2013).

[315] Sato, K., Iwamoto, A., Harada, K., Yamaji, S., and Yoshida, S. *Zeitschrift für Physik A Atoms and Nuclei* **288**(4), 383–390 (1978).

[316] Ignatyuk, A. V., Smirenkin, G. N., and Tishin, A. S. *Soviet Journal of Nuclear Physics* **21**, 255 (1975).

[317] Randrup, J. and Möller, P. *Phys. Rev. C* **88**, 064606 Dec (2013).

[318] Lestone, J. *Nuclear Data Sheets* **112**(12), 3120 – 3134 (2011).

[319] Nishio, K. In *ND2016 International Coference on Nuclear Data for Science and Technology, 11-16.Sep. Bruges, Belgium*, (2016).

[320] Möller, P. and Schmitt, C. *Eur. Phys. J. A* **53**(1), 7 (2017).

[321] Duke, D. L., Tovesson, F., Laptev, A. B., Mosby, S., Hambsch, F.-J., Bryś, T., and Vidali, M. *Phys. Rev. C* **94**, 054604 Nov (2016).

[322] Ethvignot, T., Devlin, M., Duarte, H., Granier, T., Haight, R. C., Morillon, B., Nelson, R. O., O'Donnell, J. M., and Rochman, D. *Phys. Rev. Lett.* **94**, 052701 Feb (2005).

[323] Thirolf, P. G. and Habs, D. *Progress in Particle and Nuclear Physics* **49**(2), 325 – 402 (2002).

[324] Butler, P. A. and Nazarewicz, W. *Rev. Mod. Phys.* **68**, 349–421 Apr (1996).

[325] Specht, H. J., Fraser, J. F., Milton, J. C. D., and Davies, W. G. *IAEA 2nd Symp. on the Physics and Chemistry of Fission, Vienna, 1969* , 363 (1969).

[326] Glässel, P., Rösler, H., and Specht, H. J. *Nuclear Physics A* **256**(2), 220 – 242 (1976).

[327] Hunyadi, M., Gassmann, D., Krasznahorkay, A., Habs, D., Thirolf, P. G., Csatlós, M., Eisermann, Y., Faestermann, T., Graw, G., Gulyás, J., Hertenberger, R., Maier, H. J., Máté, Z., Metz, A., and Chromik, M. J. *Physics Letters B* **505**(14), 27 – 35 (2001).

[328] Möller, P. and Nix, J. In *Proc. Symp. Phys. Chem. Fission, Rochester 1973*, volume 1, 103. IAEA, Vienna, (1974).

[329] Möller, P., Nilsson, S. G., and Sheline, R. K. *Physics Letters B* **40**(3), 329 – 332 (1972).

[330] Howard, W. and Möller, P. *Atomic Data and Nuclear Data Tables* **25**(3), 219 – 285 (1980).

[331] Bengtsson, R., Ragnarsson, I., Åberg, S., Gyurkovich, A., Sobiczewski, A., and Pomorski, K. *Nuclear Physics A* **473**(1), 77 – 110 (1987).

[332] Ćwiok, S., Nazarewicz, W., Saladin, J. X., Płóciennik, W., and Johnson, A. *Physics Letters B* **322**(4), 304 – 310 (1994).

[333] Ichikawa, T., Möller, P., and Sierk, A. J. *Phys. Rev. C* **87**, 054326 May (2013).

[334] Berger, J. F., Girod, M., and Gogny, D. *Nuclear Physics A* **502**, 85 – 104 (1989).

[335] Rutz, K., Maruhn, J. A., Reinhard, P.-G., and Greiner, W. *Nuclear Physics A* **590**(3), 680 – 702 (1995).

[336] McDonnell, J. D., Nazarewicz, W., and Sheikh, J. A. *Phys. Rev. C* **87**, 054327 May (2013).

[337] Kortelainen, M., McDonnell, J., Nazarewicz, W., Reinhard, P.-G., Sarich, J., Schunck, N., Stoitsov, M. V., and Wild, S. M. *Phys. Rev. C* **85**, 024304 Feb (2012).

[338] Csatlós, M., Krasznahorkay, A., Thirolf, P. G., Habs, D., Eisermann, Y., Faestermann, T., Graw, G., Gulyás, J., Harakeh, M. N., Hertenberger, R., Hunyadi, M., Maier, H. J., Máté, Z., Schaile, O., and Wirth, H.-F. *Physics Letters B* **615**(34), 175 – 185 (2005).

[339] Krasznahorkay, A., Habs, D., Hunyadi, M., Gassmann, D., Csatlós, M., Eisermann, Y., Faestermann, T., Graw, G., Gulyás, J., Hertenberger, R., Maier, H. J., Máté, Z., Metz, A., Ott, J., Thirolf, P., and van der Werf, S. Y. *Physics Letters B* **461**(12), 15 – 21 (1999).

[340] Krasznahorkay, A., Hunyadi, M., Harakeh, M. N., Csatlós, M., Faestermann, T., Gollwitzer, A., Graw, G., Gulyás, J., Habs, D., Hertenberger, R., Maier, H. J., Máté, Z., Rudolph, D., Thirolf, P., Timár, J., and Valnion, B. D. *Phys. Rev. Lett.* **80**, 2073–2076 Mar (1998).

[341] Csige, L., Csatlós, M., Faestermann, T., Gácsi, Z., Gulyás, J., Habs, D., Hertenberger, R., Krasznahorkay, A., Lutter, R., Maier, H. J., Thirolf, P. G., and Wirth, H.-F. *Phys. Rev. C* **80**, 011301 Jul (2009).

[342] Nishio, K., Ikezoe, H., Nagame, Y., Mitsuoka, S., Nishinaka, I., Duan, L., Satou, K., Goto, S., Asai, M., Haba, H., Tsukada, K., Shinohara, N., Ichikawa, S., and Ohsawa, T. *Phys. Rev. C* **67**, 014604 Jan (2003).

[343] Lyles, B. F., Bernstein, L. A., Burke, J. T., Dietrich, F. S., Escher, J., Thompson, I., Bleuel, D. L., Clark, R. M., Fallon, P., Gibelin, J., Macchiavelli, A. O., McMahan, M. A., Phair, L., Rodriguez-Vieitez, E., Wiedeking, M., Beausang, C. W., Lesher, S. R., Darakchieva, B., and Evtimova, M. *Phys. Rev. C* **76**, 014606 Jul (2007).

[344] Czeszumska, A., Angell, C. T., Burke, J. T., Scielzo, N. D., Norman, E. B., Austin, R. A. E., Boutoux, G., Casperson, R. J., Chodash, P., Hughes, R. O., Mattoon, C. M., Méot, V., Munson, J., Phair, L., Ressler, J. J., Roig, O., Ross, T. J., Swanberg, E., and Wang, B. *Phys. Rev. C* **87**, 034613 Mar (2013).

[345] Burke, J. T., Bernstein, L. A., Escher, J., Ahle, L., Church, J. A., Dietrich, F. S., Moody, K. J., Norman, E. B., Phair, L., Fallon, P., Clark, R. M., Deleplanque, M. A., Descovich, M., Cromaz, M., Lee, I. Y., Macchiavelli, A. O., McMahan, M. A., Moretto, L. G., Rodriguez-Vieitez, E., Stephens, F. S., Ai, H., Plettner, C., Beausang, C., and Crider, B. *Phys. Rev. C* **73**, 054604 May (2006).

[346] Lesher, S. R., Burke, J. T., Bernstein, L. A., Ai, H., Beausang, C. W., Bleuel, D. L., Clark, R. M., Dietrich,

CONTENTS 73

F. S., Escher, J. E., Fallon, P., Gibelin, J., Goldblum, B. L., Lee, I. Y., Macchiavelli, A. O., McMahan, M. A., Moody, K. J., Norman, E. B., Phair, L., Rodriguez-Vieitez, E., Scielzo, N. D., and Wiedeking, M. *Phys. Rev. C* **79**, 044609 Apr (2009).

[347] Ressler, J. J., Burke, J. T., Escher, J. E., Angell, C. T., Basunia, M. S., Beausang, C. W., Bernstein, L. A., Bleuel, D. L., Casperson, R. J., Goldblum, B. L., Gostic, J., Hatarik, R., Henderson, R., Hughes, R. O., Munson, J., Phair, L. W., Ross, T. J., Scielzo, N. D., Swanberg, E., Thompson, I. J., and Wiedeking, M. *Phys. Rev. C* **83**, 054610 May (2011).

[348] Nayak, B. K., Saxena, A., Biswas, D. C., Mirgule, E. T., John, B. V., Santra, S., Vind, R. P., Choudhury, R. K., and Ganesan, S. *Phys. Rev. C* **78**, 061602 Dec (2008).

[349] Desai, V. V., Nayak, B. K., Saxena, A., Mirgule, E. T., and Suryanarayana, S. V. *Phys. Rev. C* **88**, 014613 Jul (2013).

[350] Desai, V. V., Nayak, B. K., Saxena, A., and Mirgule, E. T. *Phys. Rev. C* **89**, 024606 Feb (2014).

[351] Pal, A., Santra, S., Nayak, B. K., Mahata, K., Desai, V. V., Chattopadhyay, D., and Tripathi, R. *Phys. Rev. C* **91**, 054618 May (2015).

[352] Scielzo, N. D., Escher, J. E., Allmond, J. M., Basunia, M. S., Beausang, C. W., Bernstein, L. A., Bleuel, D. L., Burke, J. T., Clark, R. M., Dietrich, F. S., Fallon, P., Gibelin, J., Goldblum, B. L., Lesher, S. R., McMahan, M. A., Norman, E. B., Phair, L., Rodriquez-Vieitez, E., Sheets, S. A., Thompson, I. J., and Wiedeking, M. *Phys. Rev. C* **81**, 034608 Mar (2010).

[353] Beer, H. and Macklin, R. L. *Astrophys. J.* **331**, 1047–1057 August (1988).

[354] Voignier, J., Joly, S., and Grenier, G. *Nucl. Sci. Eng.* **112**, 87–94 (1992).

[355] Boutoux, G., Jurado, B., Méot, V., Roig, O., Mathieu, L., Aïche, M., Barreau, G., Capellan, N., Companis, I., Czajkowski, S., Schmidt, K.-H., Burke, J. T., Bail, A., Daugas, J. M., Faul, T., Morel, P., Pillet, N., Théroine, C., Derkx, X., Sérot, O., Matéa, I., and Tassan-Got, L. *Physics Letters B* **712**(45), 319 – 325 (2012).

[356] Bokhovko, M. V. *et al.*. Fiz-Energ Institut, Obninsk Reports, No. 2169, 1991, p. 91.

[357] Wisshak, K., Voss, F., Arlandini, C., Käppeler, F., and Kazakov, L. *Phys. Rev. C* **61**, 065801 May (2000).

[358] Macklin, R. *et al.*. Los Alamos Scientific Lab. Report, No. LA-7479-MS, 1978.

[359] Wisshak, K., Voss, F., Käppeler, F., and Kazakov, L. *Phys. Rev. C* **73**, 015807 Jan (2006).

[360] Ducasse, Q., Jurado, B., Aiche, M., Marini, P., Mathieu, L., Görgen, A., Guttormsen, M., Larsen, A. C., Tornyi, T., Wilson, J. N., Barreau, G., Boutoux, G., Czajkowski, S., Giacoppo, F., Gunsing, F., Hagen, T. W., Lebois, M., Lei, J., Méot, V., Morillon, B., Moro, A. M., Renstrøm, T., Roig, O., Rose, S. J., Sérot, O., Siem, S., Tsekhanovich, I., Tveten, G. M., and Wiedeking, M. *Phys. Rev. C* **94**, 024614 Aug (2016).

[361] Lei, J. and Moro, A. M. *Phys. Rev. C* **92**, 044616 Oct (2015).

[362] Smolańczuk, R., Skalski, J., and Sobiczewski, A. *Phys. Rev. C* **52**, 1871–1880 Oct (1995).

[363] Smolańczuk, R. *Phys. Rev. C* **56**, 812–824 Aug (1997).

[364] Agbemava, S. E., Afanasjev, A. V., Nakatsukasa, T., and Ring, P. *Phys. Rev. C* **92**, 054310 Nov (2015).

[365] Utyonkov, V. K., Brewer, N. T., Oganessian, Y. T., Rykaczewski, K. P., Abdullin, F. S., Dmitriev, S. N., Grzywacz, R. K., Itkis, M. G., Miernik, K., Polyakov, A. N., Roberto, J. B., Sagaidak, R. N., Shirokovsky, I. V., Shumeiko, M. V., Tsyganov, Y. S., Voinov, A. A., Subbotin, V. G., Sukhov, A. M., Sabel'nikov, A. V., Vostokin, G. K., Hamilton, J. H., Stoyer, M. A., and Strauss, S. Y. *Phys. Rev. C* **92**, 034609 Sep (2015).

[366] Oganessian, Y. *Journal of Physics G: Nuclear and Particle Physics* **34**(4), R165 (2007).

[367] Möller, P., Nix, J. R., Myers, W. D., and Swiatecki, W. J. *Atomic Data and Nuclear Data Tables* **59**(2), 185 – 381 (1995).

[368] Leigh, J. R., Dasgupta, M., Hinde, D. J., Mein, J. C., Morton, C. R., Lemmon, R. C., Lestone, J. P., Newton, J. O., Timmers, H., Wei, J. X., and Rowley, N. *Phys. Rev. C* **52**, 3151–3166 Dec (1995).

[369] Reisdorf, W., Hessberger, F. P., Hildenbrand, K. D., Hofmann, S., Münzenberg, G., Schmidt, K. H., Schneider, J. H. R., Schneider, W. F. W., Sümmerer, K., Wirth, G., Kratz, J. V., and Schlitt, K. *Phys. Rev. Lett.* **49**, 1811–1815 Dec (1982).

[370] Bjørnholm, S. and Swiatecki, W. J. *Nuclear Physics A* **391**(2), 471 – 504 (1982).

[371] Bock, R., Chu, Y. T., Dakowski, M., Gobbi, A., Grosse, E., Olmi, A., Sann, H., Schwalm, D., Lynen, U., Müller, W., Bjørnholm, S., Esbensen, H., Wölfli, W., and Morenzoni, E. *Nuclear Physics A* **388**(2), 334 – 380 (1982).

[372] Shen, W. Q., Albinski, J., Gobbi, A., Gralla, S., Hildenbrand, K. D., Herrmann, N., Kuzminski, J., Müller, W. F. J., Stelzer, H., Tke, J., Back, B. B., Bjørnholm, S., and Sørensen, S. P. *Phys. Rev. C* **36**, 115–142 Jul (1987).

[373] Blocki, J. P., Feldmeier, H., and Swiatecki, W. J. *Nuclear Physics A* **459**(1), 145 – 172 (1986).

[374] Aritomo, Y., Hagino, K., Nishio, K., and Chiba, S. *Phys. Rev. C* **85**, 044614 Apr (2012).

[375] Nishio, Katsuhisa. *EPJ Web of Conferences* **62**, 03001 (2013).

[376] Nix, J. R. *Nuclear Physics A* **130**(2), 241 – 292 (1969).

[377] Zagrebaev, V. and Greiner, W. *Journal of Physics G: Nuclear and Particle Physics* **31**(7), 825 (2005).

[378] Aritomo, Y., Wada, T., Ohta, M., and Abe, Y. *Phys. Rev. C* **59**, 796–809 Feb (1999).

[379] Itkis, M. G., Aÿstö, J., Beghini, S., Bogachev, A. A., Corradi, L., Dorvaux, O., Gadea, A., Giardina, G., Hanappe, F., Itkis, I. M., Jandel, M., Kliman, J., Khlebnikov, S. V., Kniajeva, G. N., Kondratiev, N. A., Kozulin, E. M., Krupa, L., Latina, A., Materna, T., Montagnoli, G., Oganessian, Y. T., Pokrovsky, I. V., Prokhorova, E. V., Rowley, N., Rubchenya, V. A., Rusanov, A. Y., Sagaidak, R. N., Scarlassara, F., Stefanini, A. M., Stuttge, L., Szilner, S., Trotta, M., Trzaska, W. H., Vakhtin, D. N., Vinodkumar, A. M., Voskressenski, V. M., and Zagrebaev, V. I. *Nuclear Physics A* **734**, 136 – 147 (2004). Proceedings of the Eighth International Conference On Nucleus-Nucleus Collisions.

[380] Itkis, M. G., Bogachev, A. A., Itkis, I. M., Kliman, J., Knyazheva, G. N., Kondratiev, N. A., Kozulin, E. M., Krupa, L., Oganessian, Y. T., Pokrovsky, I. V., Prokhorova, E. V., and Rusanov, A. Y. *Nuclear Physics A* **787**(14), 150 – 159 (2007). Proceedings of the Ninth International Conference on Nucleus-Nucleus Collisions (NN2006).

[381] Bass, R. *Nuclear Physics A* **231**(1), 45 – 63 (1974).

[382] Wakhle, A., Simenel, C., Hinde, D. J., Dasgupta, M., Evers, M., Luong, D. H., du Rietz, R., and Williams, E. *Phys. Rev. Lett.* **113**, 182502 Oct (2014).

[383] Vandenbosch, R. and Huizenga, J. R. *Nuclear Fission.* Academic Press, (1973).

[384] Hoffman, D. C. and Hoffman, M. M. *Annual Review of Nuclear Science* **24**(1), 151–208 (1974).

[385] Nishio, K., Nakashima, M., Kimura, I., and Nakagome, Y. *Journal of Nuclera Science and Technology* **35**(9), 631–642 (1998).

CONTENTS 74

[386] Nishio, K., Nakagome, Y., Yamamoto, H., and Kimura, I. *Nuclear Physics A* **632**(4), 540 – 558 (1998).

[387] Tsuchiya, C., Nakagome, Y., Yamana, H., Moriyama, H., Nishio, K., Kanno, I., Shin, K., and Kimura, I. *Journal of Nuclera Science and Technology* **37**(11), 941–948 (2000).

[388] *KURRI: http://www.rri.kyoto-u.ac.jp/en.*

[389] Nishio, K., Yamamoto, H., Kanno, I., Kimura, I., and Nakagome, Y. *Nuclear Instruments and Methods in Physics Research Section A: Accelerators, Spectrometers, Detectors and Associated Equipment* **385**(1), 171 – 178 (1997).

[390] D.G. Madland, J. N. *Nuclear Science and Engineering* **81**, 213–271 (1982).

[391] Iljinov, A. S., Mebel, M. V., Bianchi, N., Sanctis, E. D., Guaraldo, C., Lucherini, V., Muccifora, V., Polli, E., Reolon, A., and Rossi, P. *Nuclear Physics A* **543**(3), 517 – 557 (1992).

[392] Budtz-Jørgensen, C. and Knitter, H.-H. *Nuclear Physics A* **490**(2), 307 – 328 (1988).

[393] Gilbert, A. and Cameron, A. *Canadian Journal of Physics* **43**(8), 1446 – 1496 (1965).

[394] Müller, R., Naqvi, A. A., Käppeler, F., and Dickmann, F. *Phys. Rev. C* **29**, 885–905 Mar (1984).

[395] Naqvi, A. A., Käppeler, F., Dickmann, F., and Müller, R. *Phys. Rev. C* **34**, 218–225 Jul (1986).

[396] Mouatassim, S., Costa, G. J., Guillaume, G., Heusch, B., Huck, A., and Moszyski, M. *Nuclear Instruments and Methods in Physics Research Section A: Accelerators, Spectrometers, Detectors and Associated Equipment* **359**(3), 530 – 536 (1995).

[397] Schmidt, K.-H. and Jurado, B. *Phys. Rev. C* **86**, 044322 Oct (2012).

[398] Moretto, L. G., Larsen, A. C., Giacoppo, F., Guttormsen, M., and Siem, S. *Journal of Physics: Conference Series* **580**(1), 012048 (2015).

[399] Schmidt, K.-H. and Jurado, B. *Phys. Rev. C* **83**, 061601 Jun (2011).

[400] Schmidt, K.-H. and Jurado, B. *Phys. Rev. C* **83**, 014607 Jan (2011).

[401] Bucurescu, D. and Egidy, T. v. *Phys. Rev. C* **72**, 067304 Dec (2005).

[402] Ye, W. and Wang, N. *Phys. Rev. C* **86**, 034605 Sep (2012).

[403] Glässel, P., Schmid-Fabian, R., Schwalm, D., Habs, D., and v. Helmolt, H. U. *Nuclear Physics A* **502**, 315 – 324 (1989).

[404] Fitzgerald, J. B., Habs, D., Heller, F., Reiter, P., Schwalm, D., Thirolf, P., and Wiswesser, A. *Zeitschrift für Physik A Hadrons and Nuclei* **355**(4), 401–405 (1996).

[405] van der Ploeg, H., Bacelar, J. C. S., Buda, A., Laurens, C. R., van der Woude, A., Gaardho/je, J. J., Żelazny, Z., van 't Hof, G., and Kalantar-Nayestanaki, N. *Phys. Rev. C* **52**, 1915–1923 Oct (1995).

[406] Adrich, P., Klimkiewicz, A., Fallot, M., Boretzky, K., Aumann, T., Cortina-Gil, D., Pramanik, U. D., Elze, T. W., Emling, H., Geissel, H., Hellström, M., Jones, K. L., Kratz, J. V., Kulessa, R., Leifels, Y., Nociforo, C., Palit, R., Simon, H., Surówka, G., Sümmerer, K., and Waluś, W. *Phys. Rev. Lett.* **95**, 132501 Sep (2005).

[407] Klimkiewicz, A., Paar, N., Adrich, P., Fallot, M., Boretzky, K., Aumann, T., Cortina-Gil, D., Pramanik, U. D., Elze, T. W., Emling, H., Geissel, H., Hellström, M., Jones, K. L., Kratz, J. V., Kulessa, R., Nociforo, C., Palit, R., Simon, H., Surówka, G., Sümmerer, K., Vretenar, D., and Waluś, W. *Phys. Rev. C* **76**, 051603 Nov (2007).

[408] Hofman, D. J., Back, B. B., Montoya, C. P., Schadmand, S., Varma, R., and Paul, P. *Phys. Rev. C* **47**, 1103–1107 (1993).

[409] Makii, H. In *ND2016 International Coference on Nuclear Data for Science and Technology, 11-16.Sep. Bruges, Belgium,* (2016).

[410] *ILL: https://www.ill.eu/.*

[411] Makii, H., Ota, S., Ishii, T., Wakabayashi, Y., Furutaka, K., Nishio, K., Nishinaka, I., Chiba, S., Igashira, M., and Czeszumska, A. *Nuclear Instruments and Methods in Physics Research Section A: Accelerators, Spectrometers, Detectors and Associated Equipment* **797**, 83 – 93 (2015).

[412] *BNC: http://www.bnc.hu/.*

[413] Verbinski, V. V., Weber, H., and Sund, R. E. *Phys. Rev. C* **7**, 1173–1185 Mar (1973).

[414] Peelle, R. W. and Maienschein, F. C. *Phys. Rev. C* **3**, 373–390 Jan (1971).

[415] *ENDF/B-VII.1 Evaluated Nuclear Data File ZA=92235,MF= 15, MT=18 (2011), http://www.nndc.bnl.gov/exfor/endf00.jsp.*

[416] Nifenecker, H., David, S., Loiseaux, J. M., and Meplan, O. *Nuclear Instruments and Methods in Physics Research Section A: Accelerators, Spectrometers, Detectors and Associated Equipment* **463**(3), 428 – 467 (2001). Accelerator driven systems.

[417] Carpenter, J. M. *Nuclear Instruments and Methods* **145**(1), 91 – 113 (1977).

[418] Silberberg, R. and Tsao, C. H. *Physics Reports* **191**(6), 351 – 408 (1990).

[419] Bricault, P. G., Dombsky, M., Schmor, P. M., and Stanford, G. *Nucl. Instrum. Methods B* **126**, 231 (1997).

[420] Ricciardi, V. M., Lukić, S., Kelić, A., Schmidt, K.-H., and Veselsky, M. *The European Physical Journal Special Topics* **150**(1), 321–324 (2007).

[421] Armbruster, P., Benlliure, J., Bernas, M., Boudard, A., Casarejos, E., Czajkowski, S., Enqvist, T., Leray, S., Napolitani, P., Pereira, J., Rejmund, F., Ricciardi, M.-V., Schmidt, K.-H., Stéphan, C., Taieb, J., Tassan-Got, L., and Volant, C. *Phys. Rev. Lett.* **93**, 212701 Nov (2004).

[422] Rejmund, F., Mustapha, B., Armbruster, P., Benlliure, J., Bernas, M., Boudard, A., Dufour, J. P., Enqvist, T., Legrain, R., Leray, S., Schmidt, K.-H., Stéphan, C., Taieb, J., Tassan-Got, L., and Volant, C. *Nuclear Physics A* **683**(14), 540 – 565 (2001).

[423] Benlliure, J., Armbruster, P., Bernas, M., Boudard, A., Dufour, J. P., Enqvist, T., Legrain, R., Leray, S., Mustapha, B., Rejmund, F., Schmidt, K.-H., Stéphan, C., Tassan-Got, L., and Volant, C. *Nuclear Physics A* **683**(14), 513 – 539 (2001).

[424] Wlazło, W., Enqvist, T., Armbruster, P., Benlliure, J., Bernas, M., Boudard, A., Czájkowski, S., Legrain, R., Leray, S., Mustapha, B., Pravikoff, M., Rejmund, F., Schmidt, K.-H., Stéphan, C., Taieb, J., Tassan-Got, L., and Volant, C. *Phys. Rev. Lett.* **84**, 5736–5739 Jun (2000).

[425] Enqvist, T., Wlazło, W., Armbruster, P., Benlliure, J., Bernas, M., Boudard, A., Czajkowski, S., Legrain, R., Leray, S., Mustapha, B., Pravikoff, M., Rejmund, F., Schmidt, K.-H., Stéphan, C., Taieb, J., Tassan-Got, L., and Volant, C. *Nuclear Physics A* **686**(14), 481 – 524 (2001).

[426] Enqvist, T., Armbruster, P., Benlliure, J., Bernas, M., Boudard, A., Czajkowski, S., Legrain, R., Leray, S., Mustapha, B., Pravikoff, M., Rejmund, F., Schmidt, K.-H., Stéphan, C., Taieb, J., Tassan-Got, L., Vivés, F., Volant, C., and Wlazo, W. *Nuclear Physics A* **703**(1), 435 – 465 (2002).

[427] Audouin, L., Tassan-Got, L., Armbruster, P., Benlliure, J., Bernas, M., Boudard, A., Casarejos, E., Czajkowski, S., Enqvist, T., Fernández-Domínguez, B., Jurado, B., Legrain, R., Leray, S., Mustapha, B., Pereira, J.,

CONTENTS

75

Pravikoff, M., Rejmund, F., Ricciardi, M.-V., Schmidt, K.-H., Stéphan, C., Taieb, J., Volant, C., and Wlazlo, W. *Nuclear Physics A* **768**(12), 1 – 21 (2006).

[428] Fernández-Domínguez, B., Armbruster, P., Audouin, L., Benlliure, J., Bernas, M., Boudard, A., Casarejos, E., Czajkowski, S., Ducret, J. E., Enqvist, T., Jurado, B., Legrain, R., Leray, S., Mustapha, B., Pereira, J., Pravikoff, M., Rejmund, F., Ricciardi, M. V., Schmidt, K.-H., Stéphan, C., Taieb, J., Tassan-Got, L., Volant, C., and Wlazlo, W. *Nuclear Physics A* **747**(24), 227 – 267 (2005).

[429] Taïeb, J., Schmidt, K.-H., Tassan-Got, L., Armbruster, P., Benlliure, J., Bernas, M., Boudard, A., Casarejos, E., Czajkowski, S., Enqvist, T., Legrain, R., Leray, S., Mustapha, B., Pravikoff, M., Rejmund, F., Stéphan, C., Volant, C., and Wlazlo, W. *Nuclear Physics A* **724**(34), 413 – 430 (2003).

[430] Bernas, M., Armbruster, P., Benlliure, J., Boudard, A., Casarejos, E., Czajkowski, S., Enqvist, T., Legrain, R., Leray, S., Mustapha, B., Napolitani, P., Pereira, J., Rejmund, F., Ricciardi, M.-V., Schmidt, K.-H., Stéphan, C., Taieb, J., Tassan-Got, L., and Volant, C. *Nuclear Physics A* **725**, 213 – 253 (2003).

[431] Bernas, M., Armbruster, P., Benlliure, J., Boudard, A., Casarejos, E., Enqvist, T., Kelic, A., Legrain, R., Leray, S., Pereira, J., Rejmund, F., Ricciardi, M.-V., Schmidt, K.-H., Stéphan, C., Taieb, J., Tassan-Got, L., and Volant, C. *Nuclear Physics A* **765**(12), 197 – 210 (2006).

[432] Ricciardi, M. V., Armbruster, P., Benlliure, J., Bernas, M., Boudard, A., Czajkowski, S., Enqvist, T., Kelić, A., Leray, S., Legrain, R., Mustapha, B., Pereira, J., Rejmund, F., Schmidt, K.-H., Stéphan, C., Tassan-Got, L., Volant, C., and Yordanov, O. *Phys. Rev. C* **73**, 014607 Jan (2006).

[433] Pereira, J., Benlliure, J., Casarejos, E., Armbruster, P., Bernas, M., Boudard, A., Czajkowski, S., Enqvist, T., Legrain, R., Leray, S., Mustapha, B., Pravikoff, M., Rejmund, F., Schmidt, K.-H., Stéphan, C., Taïeb, J., Tassan-Got, L., Volant, C., and Wlazlo, W. *Phys. Rev. C* **75**, 014602 Jan (2007).

[434] Napolitani, P., Schmidt, K.-H., and Tassan-Got, L. *Journal of Physics G: Nuclear and Particle Physics* **38**(11), 115006 (2011).

[435] Moretto, L. G. and Wozniak, G. J. *Pramana, J. Phys.* **33**, 209–253 (1989).

[436] Pereira, J., Armbruster, P., Benlliure, J., and Schmidt, K.-H. *Phys. Rev. C* **75**, 044604 Apr (2007).

[437] Schmidt, K.-H., Jurado, B., Pleskač, R., Ricciardi, M. V., Benlliure, J., Boudard, A., Casarejos, E., Enqvist, T., Farget, F., Bacquias, A., Fernandez, M., Giot, L., Henzl, V., Henzlova, D., Kelić-Heil, A., Kurtukian, T., Leray, S., Lukić, S., Ngoc, S. N., Nadtochy, P., Perez, D., and Schmitt, C. *Phys. Rev. C* **87**, 034601 Mar (2013).

[438] Ayyad, Y., Benlliure, J., Casarejos, E., Álvarez-Pol, H., Bacquias, A., Boudard, A., Caamaño, M., Enqvist, T., Föhr, V., Kelić-Heil, A., Kezzar, K., Leray, S., Mancusi, D., Paradela, C., Pérez-Loureiro, D., Pleskač, R., Rodríguez-Sánchez, J. L., and Tarrío, D. *Phys. Rev. C* **89**, 054610 May (2014).

[439] Rodríguez-Sánchez, J. L., Benlliure, J., Taïeb, J., Álvarez-Pol, H., Audouin, L., Ayyad, Y., Bélier, G., Boutoux, G., Casarejos, E., Chatillon, A., Cortina-Gil, D., Gorbinet, T., Heinz, A., Kelić-Heil, A., Laurent, B., Martin, J.-F., Paradela, C., Pellereau, E., Pietras, B., Ramos, D., Rodríguez-Tajes, C., Rossi, D. M., Simon, H., Vargas, J., and Voss, B. *Phys. Rev. C* **91**, 064616 Jun (2015).

[440] Filges, D., Leray, S., Yariv, Y., Mengoni, A., Stanculescu, A., and Mank, G. In *Proceedings of the Joint ICTP-IAEA Advanced Workshop on Model Codes for Spallation Reactions, ICTP Trieste, Italy, 4-8 February 2008, IAEA INDC(NDS)-0530*, volume 2, 181–221. IAEA Vienna, (1956).

[441] Dael, A., Gastineau, B., Ducret, J. E., and Vysotsky, V. S. *IEEE Transactions on Applied Superconductivity* **12**(1), 353–357 Mar (2002).

[442] *A next generation experimental setup for studies of Reactions with Relativistic Radioactive Beams: https://www.gsi.de/r3b/*.

[443] *Technical Report for the Design, Construction and Commissioning of NeuLAND: The High-Resolution Neutron Time-of-Flight Spectrometer for R^3B: https://www.gsi.de/neuland/*.

[444] Cortina-Gil, D., Alvarez-Pol, H., Aumann, T., Avdeichikov, V., Bendel, M., Benlliure, J., Bertini, D., Bezbakh, A., Bloch, T., Böhmer, M., Borge, M. J. G., Briz, J. A., Cabanelas, P., Casarejos, E., Gallardo, M. C., Cederkäll, J., Chulkov, L., Dierigl, M., Julio, D. D., Durán, I., Fiori, E., Fomichev, A., Galaviz, D., Gascón, M., Gernhäuser, R., Gerl, J., Golubev, P., Golovkov, M., González, D., Gorshkov, A., Heinz, A., Heil, M., Henning, W., Ickert, G., Ignatov, A., Jakobsson, B., Johansson, H. T., Kröll, T., Krücken, R., Krupko, S., Kurz, N., Bleis, T. L., Löher, B., Nacher, E., Nilsson, T., Parrilla, C., Perea, A., Pietralla, N., Pietras, B., Reifarth, R., del Rio, J. S., Savran, D., Sidorchuk, S., Simon, H., Schnorrenberger, L., Tengblad, O., Teubig, P., Thies, R., Vilán, J., von Schmid, M., Winkel, M., Winkler, S., Wamers, F., and Yañez, P. *Nuclear Data Sheets* **120**, 99 – 101 (2014).

[445] Simon, H. *Nucl. Phys. A* **787**(14), 102 – 109 (2007).

[446] Antonov, A. N., Gaidarov, M. K., Ivanov, M. V., Kadrev, D. N., Aïche, M., Barreau, G., Czajkowski, S., Jurado, B., Belier, G., Chatillon, A., Granier, T., Taieb, J., Doré, D., Letourneau, A., Ridikas, D., Dupont, E., Berthoumieux, E., Panebianco, S., Farget, F., Schmitt, C., Audouin, L., Khan, E., Tassan-Got, L., Aumann, T., Beller, P., Boretzky, K., Dolinskii, A., Egelhof, P., Emling, H., Franzke, B., Geissel, H., Kelic-Heil, A., Kester, O., Kurz, N., Litvinov, Y., Münzenberg, G., Nolden, F., Schmidt, K.-H., Scheidenberger, C., Simon, H., Steck, M., Weick, H., Enders, J., Pietralla, N., Richter, A., Schrieder, G., Zilges, A., Distler, M. O., Merkel, H., Müller, U., Junghans, A. R., Lenske, H., Fujiwara, M., Suda, T., Kato, S., Adachi, T., Hamieh, S., Harakeh, M. N., Kalantar-Nayestanaki, N., Wörtche, H., Berg, G. P. A., Koop, I. A., Logatchov, P. V., Otboev, A. V., Parkhomchuk, V. V., Shatilov, D. N., Shatunov, P. Y., Shatunov, Y. M., Shiyankov, S. V., Shvartz, D. I., Skrinsky, A. N., Chulkov, L. V., Danilin, B. V., Korsheninnikov, A. A., Kuzmin, E. A., Ogloblin, A. A., Volkov, V. A., Grishkin, Y., Lisin, V. P., Mushkarenkov, A. N., Nedorezov, V., Polonski, A. L., Rudnev, N. V., Turinge, A. A., Artukh, A., Avdeichikov, V., Ershov, S. N., Fomichev, A., Golovkov, M., Gorshkov, A. V., Grigorenko, L., Klygin, S., Krupko, S., Meshkov, I. N., Rodin, A., Sereda, Y., Seleznev, I., Sidorchuk, S., Syresin, E., Stepantsov, S., Ter-Akopian, G., Teterev, Y., Vorontsov, A. N., Kamerdzhiev, S. P., Litvinova, E. V., Karataglidis, S., Rodriguez, R. A., Borge, M. J. G., Ramirez, C. F., Garrido, E., Sarriguren, P., Vignote, J. R., Prieto, L. M. F., Herraiz, J. L., de Guerra, E. M., Udias-Moinelo, J., Soriano, J. E. A., Rojo, A. M. L., Caballero, J. A., Johansson, H. T., Jonson, B., Nilsson, T., Nyman, G., Zhukov, M., Golubev, P., Rudolph, D., Hencken, K., Jourdan, J., Krusche, B., Rauscher, T., Kiselev, D., Trautmann, D., Al-Khalili, J., Catford,

CONTENTS   76

W., Johnson, R., Stevenson, P. D., Barton, C., Jenkins, D., Lemmon, R., Chartier, M., Cullen, D., Bertulani, C. A., and Heinz, A. *Nuclear Instruments and Methods in Physics Research Section A: Accelerators, Spectrometers, Detectors and Associated Equipment* **637**(1), 60 – 76 (2011).

[447] *FAIR: https://www.gsi.de/fair/*.

[448] Ohnishi, T., Ichikawa, S., Koizumi, K., Kurita, K., Miyashita, Y., Ogawara, R., Tamaki, S., Togasaki, M., and Wakasugi, M. *Nuclear Instruments and Methods in Physics Research Section B: Beam Interactions with Materials and Atoms* **317, Part B**, 357 – 360 (2013). {XVIth} International Conference on ElectroMagnetic Isotope Separators and Techniques Related to their Applications, December 27, 2012 at Matsue, Japan.

[449] Kobayashi, T., Chiga, N., Isobe, T., Kondo, Y., Kubo, T., Kusaka, K., Motobayashi, T., Nakamura, T., Ohnishi, J., Okuno, H., Otsu, H., Sako, T., Sato, H., Shimizu, Y., Sekiguchi, K., Takahashi, K., Tanaka, R., and Yoneda, K. *Nuclear Instruments and Methods in Physics Research Section B: Beam Interactions with Materials and Atoms* **317, Part B**, 294 – 304 (2013). {XVIth} International Conference on ElectroMagnetic Isotope Separators and Techniques Related to their Applications, December 27, 2012 at Matsue, Japan.

[450] Mücher, D. *et al.,*. In *RIKEN Accel. Prog. Rep.*, volume 48, (2015).

[451] Kubo, T. *Nuclear Instruments and Methods in Physics Research Section B: Beam Interactions with Materials and Atoms* **204**, 97 – 113 (2003). 14th International Conference on Electromagnetic Isotope Separators and Techniques Related to their Applications.

[452] Borge, M. J. G. *Nuclear Instruments and Methods in Physics Research Section B: Beam Interactions with Materials and Atoms* **376**, 408 – 412 (2016). Proceedings of the {XVIIth} International Conference on Electromagnetic Isotope Separators and Related Topics (EMIS2015), Grand Rapids, MI, U.S.A., 11-15 May 2015.

[453] Veselský, M. *et al.,*. In *ISOLDE proposal, https://cds.cern.ch/record/1603070/files/INTC-CLL-012.pdf*, (2013).

[454] Grieser, M., Litvinov, Y. A., Raabe, R., Blaum, K., Blumenfeld, Y., Butler, P. A., Wenander, F., Woods, P. J., Aliotta, M., Andreyev, A., Artemyev, A., Atanasov, D., Aumann, T., Balabanski, D., Barzakh, A., Batist, L., Bernardes, A. P., Bernhardt, D., Billowes, J., Bishop, S., Borge, M., Borzov, I., Bosch, F., Boston, A. J., Brandau, C., Catford, W., Catherall, R., Cederkäll, J., Cullen, D., Davinson, T., Dillmann, I., Dimopoulou, C., Dracoulis, G., Düllmann, C. E., Egelhof, P., Estrade, A., Fischer, D., Flanagan, K., Fraile, L., Fraser, M. A., Freeman, S. J., Geissel, H., Gerl, J., Greenlees, P., Grisenti, R. E., Habs, D., von Hahn, R., Hagmann, S., Hausmann, M., He, J. J., Heil, M., Huyse, M., Jenkins, D., Jokinen, A., Jonson, B., Joss, D. T., Kadi, Y., Kalantar-Nayestanaki, N., Kay, B. P., Kiselev, O., Kluge, H. J., Kowalska, M., Kozhuharov, C., Kreim, S., Kröll, T., Kurcewicz, J., Labiche, M., Lemmon, R. C., Lestinsky, M., Lotay, G., Ma, X. W., Marta, M., Meng, J., Mücher, D., Mukha, I., Müller, A., Murphy, A. J. S., Neyens, G., Nilsson, T., Nociforo, C., Nörtershäuser, W., Page, R. D., Pasini, M., Petridis, N., Pietralla, N., Pfützner, M., Podolyák, Z., Regan, P., Reed, M. W., Reifarth, R., Reiter, P., Repnow, R., Riisager, K., Rubio, B., Sanjari, M. S., Savin, D. W., Scheidenberger, C., Schippers, S., Schneider, D., Schuch, R., Schwalm, D., Schweikhard, L., Shubina, D., Siesling, E., Simon, H., Simpson, J., Smith, J., Sonnabend, K., Steck, M., Stora, T., Stöhlker, T., Sun, B., Surzhykov, A., Suzaki, F., Tarasov, O., Trotsenko, S., Tu, X. L., Van Duppen, P., Volpe, C., Voulot, D., Walker, P. M., Wildner, E., Winckler, N., Winters, D. F. A., Wolf, A., Xu, H. S., Yakushev, A., Yamaguchi, T., Yuan, Y. J., Zhang, Y. H., and Zuber, K. *The European Physical Journal Special Topics* **207**(1), 1–117 (2012).

[455] Jurado, B. habilitation, University of Bordeaux, 2015.

[456] Blanc, A., Chebboubi, A., de France, G., Drouet, F., Faust, H., Jentschel, M., Kessedjian, G., Köster, U., Leoni, S., Materna, T., Mutti, P., Panebianco, S., Sage, C., Simpson, G., Soldner, T., Ur, C. A., Urban, W., and Vancraeyenest, A. *EPJ Web of Conferences* **93**, 01015 (2015).

[457] Chebboubi, A., Kessedjian, G., Faust, H., Blanc, A., Jentschel, M., Köster, U., Materna, T., Méplan, O., Sage, C., and Serot, O. *Nuclear Instruments and Methods in Physics Research Section B: Beam Interactions with Materials and Atoms* **376**, 120 – 124 (2016). Proceedings of the {XVIIth} International Conference on Electromagnetic Isotope Separators and Related Topics (EMIS2015), Grand Rapids, MI, U.S.A., 11-15 May 2015.

[458] Ledoux, X. and Aïche, M. In *International Conference on Nuclear Data for Science and Technology*, 459–462. EDP Science, (2008).

[459] Doré, D., Farget, F., Lecolley, F.-R., Ledoux, X., Lehaut, G., Materna, T., Pancin, J., Panebianco, S., and the FALSTAFF and NFS Collaborations. *EPJ Web of Conferences* **42**, 01001 (2013).

[460] Panebianco, Stefano, Doré, Diane, Farget, Fanny, Lecolley, Francois-René, Lehaut, Grégory, Materna, Thomas, Pancin, Julien, and Papaevangelou, Thomas. *EPJ Web of Conferences* **69**, 00021 (2014).

[461] Barty, C., (2015). Nuclear photonics with laser-based gamma rays; http://spie.org/newsroom/3681-nuclear-photonics-with-laser-based-gamma-rays.

[462] Sheikh, J. A., Nazarewicz, W., and Pei, J. C. *Phys. Rev. C* **80**, 011302 Jul (2009).

[463] Mişicu, i. m. c., Săndulescu, A., Ter-Akopian, G. M., and Greiner, W. *Phys. Rev. C* **60**, 034613 Aug (1999).

[464] Shneidman, T. M., Adamian, G. G., Antonenko, N. V., Ivanova, S. P., Jolos, R. V., and Scheid, W. *Physics of Atomic Nuclei* **66**(2), 206–217 (2003).

[465] Gönnenwein, F., Tsekanovich, I., and Rubchenya, V. *International Journal of Modern Physics E* **16**(02), 410–424 (2007).

[466] Bonneau, L., Quentin, P., and Mikhailov, I. N. *Phys. Rev. C* **75**, 064313 Jun (2007).

[467] Hoffman, M. M. *Phys. Rev.* **133**, B714–B723 Feb (1964).

[468] Bulgac, A., Magierski, P., Roche, K. J., and Stetcu, I. *Phys. Rev. Lett.* **116**, 122504 Mar (2016).

[469] Kadmensky, S. G. *Physics of Atomic Nuclei* **71**(7), 1193–1199 (2008).

[470] Kadmensky, S. G., Lyubashevsky, D. E., and Titova, L. V. *Bulletin of the Russian Academy of Sciences: Physics* **75**(7), 989–993 (2011).

[471] Vogt, R. and Randrup, J. *Phys. Rev. C* **87**, 044602 Apr (2013).

[472] Stetcu, I., Talou, P., Kawano, T., and Jandel, M. *Phys. Rev. C* **90**, 024617 Aug (2014).

[473] Litaize, O., Serot, O., and Berge, L. *The European Physical Journal A* **51**(12), 177 (2015).

[474] Nifenecker, H., Mariolopoulos, G., Bocquet, J. P., Brissot, R., Hamelin, M. C., Crançon, J., and Ristori, C. *Zeitschrift für Physik A Atoms and Nuclei* **308**(1), 39–49 (1982).

[475] Medkour, G., Asghar, M., Djebara, M., and Bouzid, B. *Journal of Physics G: Nuclear and Particle Physics* **23**(1), 103 (1997).

CONTENTS 77

[476] Rejmund, F., Ignatyuk, A., Junghans, A., and Schmidt, K.-H. *Nuclear Physics A* **678**(3), 215 – 234 (2000).

[477] Gontchar, I., Morjean, M., and Basnary, S. *EPL (Europhysics Letters)* **57**(3), 355 (2002).